

NAVAL POSTGRADUATE SCHOOL

Monterey, California



DISSERTATION

THESIS

54385

PASSIVE MULTIPATH TARGET TRACKING
IN AN INHOMOGENEOUS ACOUSTIC MEDIUM

by

Amnon Shefi

December 1987

Dissertation Supervisor: C. W. Therrien

Approved for public release; distribution is unlimited

T239237

REPORT DOCUMENTATION PAGE

a. REPORT SECURITY CLASSIFICATION Unclassified		1b. RESTRICTIVE MARKINGS	
a. SECURITY CLASSIFICATION AUTHORITY		3. DISTRIBUTION / AVAILABILITY OF REPORT Approved for public release, distribution is unlimited	
b. DECLASSIFICATION / DOWNGRADING SCHEDULE			
PERFORMING ORGANIZATION REPORT NUMBER(S)		5. MONITORING ORGANIZATION REPORT NUMBER(S)	
a. NAME OF PERFORMING ORGANIZATION Naval Postgraduate School	6b. OFFICE SYMBOL (If applicable) Code 62	7a. NAME OF MONITORING ORGANIZATION Naval Postgraduate School	
c. ADDRESS (City, State, and ZIP Code) Monterey, California 93943-5000		7b. ADDRESS (City, State, and ZIP Code) Monterey, California 93943-5000	
a. NAME OF FUNDING / SPONSORING ORGANIZATION	8b. OFFICE SYMBOL (If applicable)	9. PROCUREMENT INSTRUMENT IDENTIFICATION NUMBER	
c. ADDRESS (City, State, and ZIP Code)		10. SOURCE OF FUNDING NUMBERS	
		PROGRAM ELEMENT NO.	PROJECT NO.
		TASK NO.	WORK UNIT ACCESSION NO.
11. TITLE (Include Security Classification) Passive Multipath Target Tracking in an Inhomogeneous Acoustic Medium			
12. PERSONAL AUTHOR(S) Zannon Shafi			
a. TYPE OF REPORT D. Dissertation	13b. TIME COVERED FROM _____ TO _____	14. DATE OF REPORT (Year, Month, Day) December 1987	15. PAGE COUNT 238
16. SUPPLEMENTARY NOTATION			
COSATI CODES		18. SUBJECT TERMS (Continue on reverse if necessary and identify by block number)	
FIELD	GROUP	SUB-GROUP	
		Multipath, passive, tracking, acoustic, underwater, inhomogeneous, ocean, 2-D function inversion, multi-model estimation, ranging, maneuvering target	
17. ABSTRACT (Continue on reverse if necessary and identify by block number)			
<p>Tracking a maneuvering acoustic source using multipath (MP) arrivals in an inhomogeneous (IH) ocean medium is investigated. Errors introduced by a horizontally stratified sound speed profile are quantitatively evaluated. A new method of converting MP time difference of arrivals to depth and range which accounts for the IH effect is developed and evaluated. A 3-D target tracker previously used in MP tracking is modified in order to remove estimation biases and improve computational efficiency. Tracking performance is demonstrated using extensive simulation and shown to be greatly improved.</p>			
20. DISTRIBUTION / AVAILABILITY OF ABSTRACT <input checked="" type="checkbox"/> UNCLASSIFIED/UNLIMITED <input type="checkbox"/> SAME AS RPT. <input type="checkbox"/> DTIC USERS		21. ABSTRACT SECURITY CLASSIFICATION Unclassified	
22a. NAME OF RESPONSIBLE INDIVIDUAL Charles W. Therrien		22b. TELEPHONE (Include Area Code) (408) 646-3347	22c. OFFICE SYMBOL 62Ti

Approved for public release; distribution is unlimited

Passive Multipath Target Tracking
in an Inhomogeneous Acoustic Medium

by

Amnon Shefi
Commander, Israeli Navy
B.S., Technion, Haifa, Israel, 1971

Submitted in partial fulfillment of the
requirements for the degree of

DOCTOR OF PHILOSOPHY
IN ELECTRICAL ENGINEERING

from the

NAVAL POSTGRADUATE SCHOOL

December, 1987

1/1

ABSTRACT

Tracking a maneuvering acoustic source using multipath (MP) arrivals in an inhomogeneous (IH) ocean medium is investigated. Errors introduced by a horizontally stratified sound speed profile are quantitatively evaluated. A new method of converting MP time difference of arrivals to depth and range which accounts for the IH effect is developed and evaluated. A 3-D target tracker previously used in MP tracking is modified in order to remove estimation biases and improve computational efficiency. Tracking performance is demonstrated using extensive simulation and shown to be greatly improved.

712515
20185
-1

TABLE OF CONTENTS

	Page
I. INTRODUCTION	25
A. BACKGROUND - PASSIVE TARGET TRACKING	25
1. T.M.A. - Target Motion Analysis	25
2. Wavefront Curvature	26
3. Multipath Tracking	26
B. THE BASIC MULTIPATH METHOD	27
1. The Travel Time Differences	27
2. Time Delay Estimation	29
3. Target Tracking	30
C. REVIEW OF PAST WORK	33
1. MP Target Tracking	33
a. Hassab	33
b. Singer	33
c. Moose	33
2. Time Delay Estimation and Source Localization	34
3. Acoustic Propagation and Modeling	34
D. PROBLEM STATEMENT	35

1.	The Inhomogeneous Ocean Medium	35
2.	Realistic Receiver and Delay Estimation	38
a.	Limited Resolution	38
b.	Nonidentifiable Paths	38
c.	Nonnegative Noise	38
3.	Tracker Modification	38
4.	Evaluation	38
E.	SCOPE AND OUTLINE	39
II.	THREE DIMENSIONAL MANEUVERING TARGET TRACKER	41
A.	INTRODUCTION	41
B.	TARGET DESCRIPTION	42
1.	Horizontal Plane	42
2.	Depth	42
3.	Command Noise Augmentation	43
4.	Cylindrical Coordinate Observations	44
5.	Linearization and Decoupling	46
C.	MULTI-MODEL ESTIMATION	48
1.	Concept	48
2.	The Multi-Model Estimator Equations	49
3.	Estimation Factors	54
a.	Hypothesized Commands	54
b.	Basic State Separation	58
c.	Smoother Order	66

d.	Coordinate Linearization and Decoupling	68
e.	Measurement Noise	68
D.	IMPROVEMENTS AND MODIFICATION	69
1.	Adaptive Command Bank	70
a.	Concept	70
b.	Complete Model Updating	71
2.	Second Order Target Model	76
3.	Second Order Smoother	78
4.	Improved Measurement Noise Model	78
a.	Dependence on SNR	78
b.	Nonnegative Time Delay	80
c.	Depth Range and Bearing Noise	81
E.	SIMULATION	82
1.	Model Description	82
2.	Description of the Output Plots	86
3.	Parameters Selection	87
F.	SIMULATION RESULTS	89
G.	SUMMARY OF TRACKER EVALUATION	97
III.	INHOMOGENEOUS REALISTIC MULTIPATH DEPTH AND RANGE MEASUREMENTS	98
A.	INTRODUCTION	98
B.	REALISTIC MEDIUM AND RECEIVER EFFECTS	98
1.	Propagation Loss and Reflections	98
a.	Spreading Loss	99

b.	Absorption Loss	100
c.	Reflections From the Boundaries	100
2.	Inhomogeneous Medium	102
a.	Speed of Sound Variations	102
b.	Ray Tracing	103
c.	Effect on MP	107
(1)	Time Delay	106
(2)	Lack of Closed Form Solution - the Eigenray Problem	107
(3)	Loss of Direct Ray	107
3.	Ocean Data	108
4.	Receiver and Delay Estimator Effects	108
a.	Bandwidth and Delay Resolution	109
b.	Nonidentifiable Path	109
5.	Instrumentation Outline	110
6.	Resulting Ambiguity	111
7.	Graphical Representation of the Medium and Receiver Effects	114
a.	Introduction	114
b.	Case Definition	114
c.	TDOA Surfaces	115
C.	IMPROVED FILTER	121
1.	Concept Overview	121
2.	Direct Function	122

a.	The Eigneray Model	122
b.	Generation of Direct Function Table	123
c.	Interpolation	124
d.	Implementation	127
3.	TDOA of Inhomogeneous Surfaces	127
4.	2-D Function Inversion	129
a.	Overview	129
b.	TDOA Search	134
c.	DR Search	138
d.	Localized Search	140
e.	The Local Search Algorithm (LSA)	141
f.	The Inversion	144
(1)	Initiation of the Search Process	144
(2)	Interpolation	144
(3)	Ambiguity Resolution	147
(4)	Failure Handling	147
(5)	Prefilter Performance Monitoring	149
g.	2-D Function Inversion Summary	149
IV.	IMPROVED PREFILTER PERFORMANCE	151
A.	MOTIVATION	151
B.	PREFILTER EVALUATION SCHEME	154
C.	EVALUATION RESULTS	155
1.	Effects of Grid Size	156

2.	Bilinear Interpolation	160
3.	The Effects of Acoustic Medium Inhomogeneity	160
4.	Finite Delay Resolution	162
5.	Delay Estimation Bias	166
6.	Effects of Range Independent Noise	168
7.	Effects of Range Dependent Noise	170
8.	Effect of Bottom Depth Error	172
D.	SUMMARY OF PREFILTER EVALUATION	176
V.	OVERALL PERFORMANCE EVALUATION	177
A.	INTRODUCTION	177
B.	INTEGRATED SYSTEM FUNCTIONAL PERFORMANCE	177
C.	TRACKING IN AN INHOMOGENEOUS MEDIUM	182
D.	EFFECTS OF ERRONEOUS SVP	186
E.	SUMMARY OF SIMULATION RESULTS	190
VI.	CONCLUSION	191
	APPENDIX A: TRANSITION MATRICES	195
	APPENDIX B: CONDITIONAL MEAN ESTIMATE	198
	APPENDIX C: COMMAND UPDATE TRANSIENT	200
	APPENDIX D: DELAY ESTIMATION ERRORS	201
	APPENDIX E: DETAILED DATA DEFINITION AND SELECTION	208
	APPENDIX F: THE EIGENRAY ACOUSTIC MODEL	216
	APPENDIX G: THE LOCAL SEARCH ALGORITHM	221

LIST OF REFERENCES 231
INITIAL DISTRIBUTION LIST 234

LIST OF TABLES

	Page
2.1 CYLINDRICAL COORDINATES VARIABLES	44
2.2 MM VARIABLE DEFINITION	51
2.3 NOISE PARAMETERS	89
3.1 LSA INTERFACE VARIABLES	143
4.1 INTERPOLATION EVALUATION GRIDS	157
E.1 DEPTH DATA GRID DATA	215
E.2 GRID DATA	215

LIST OF FIGURES

Fig. 1.1 Multipath propagation	28
Fig. 1.2 MP tracking system	32
Fig. 1.3 IH MP propagation	37
Fig. 2.1 Cylindrical coordinates	45
Fig. 2.2 Multi-model block diagram	50
Fig. 2.3 Conditional mean estimate	55
Fig. 2.4 Command estimation bias	57
Fig. 2.5 State position seperation	62
Fig. 2.6 Weight vector history	64
Fig. 2.7 Model update block diagram	74
Fig. 2.8 Complete model update	75
Fig. 2.9 Tracking of an updating model	77
Fig. 2.10 Second order model tracking	79
Fig. 2.11 Simulation block diagram	84
Fig. 2.12 Plot sampling rate	88
Fig. 2.13 Run-1: Range dependent DR noise	90
Fig. 2.14 Run-2: Low TDOA noise $p = 1$	92
Fig. 2.15 Run-2: Bearing and XY plots	93
Fig. 2.16 Run-3: Range dependent noise, SNR_0 of 70 dB	94

Fig. 2.17 Run-4: Range dependent noise, SNR_0 of 60 dB	95
Fig. 2.18 Run-5: High Range dependent noise, SNR_0 of 50 dB	96
Fig. 3.1 Reflection from a boundary	100
Fig. 3.2 Acoustic ray path	104
Fig. 3.3 Unresolvable ACF peaks t_0t_1	112
Fig. 3.4 Resolvable ACF peaks t_1t_2	112
Fig. 3.5 Ideal TDOA surface (U1111)	116
Fig. 3.6 Modified TDOA surface, homogeneous medium (S1111)	118
Fig. 3.7 Modified TDOA near the surface (S2251)	119
Fig. 3.8 Finite resolution TDOA and bounce count (C1111)	120
Fig. 3.9 Linear interpolation	126
Fig. 3.10 Inhomogeneous TDOA surface (A2251)	128
Fig. 3.11 Inhomogeneous and unresolvable TDOA (C2251)	130
Fig. 3.12 Graphical inversion	131
Fig. 3.13 Depth range mappings	133
Fig. 3.14 Non-unique triangle selection	135
Fig. 3.15 Ambiguous triangle selection	137
Fig. 3.16 Unique valid DR triangle set	139
Fig. 3.17 System block diagram	142
Fig. 3.18 Outward and Inward search	145
Fig. 4.1 Nonlinear inversion bias	153
Fig. 4.2 Inversion performance evaluation	154
Fig. 4.3 A 50×500 m DR grid interpolation error	158

Fig. 4.4 A 100×1000 m DR grid interpolation error	159
Fig. 4.5 Bilinear interpolation error	161
Fig. 4.6 Effect of medium inhomogeneity (A2251)	163
Fig. 4.7 Inhomogeneity error	164
Fig. 4.8 Effect of finite inhomogeneity and delay resolution	165
Fig. 4.9 TDOA constant bias error ($t_1 + 1$ ms)	167
Fig. 4.10 Range independent TDOA and DR noise (1 ms)	169
Fig. 4.11 Range independent TDOA noise (5 ms)	171
Fig. 4.12 Range dependent TDOA noise	173
Fig. 4.13 Effect of bottom depth error	175
Fig. 5.1 Run-6: Tracking of a maneuvering target	179
Fig. 5.2 Run-6: Bearing and XY plot	180
Fig. 5.3 Run-7: Failure Due to reduced search area size	181
Fig. 5.4 Run-8: Tracking in an inhomogeneous medium	183
Fig. 5.5 Run-9: Effect of IH and TDOA noise	184
Fig. 5.6 Run-10: Correction for medium inhomogeneity	185
Fig. 5.7 Run 10a Correction for medium inhomogeneity with low noise	187
Fig. 5.8 Run-11: Effect of small errors in SVP	188
Fig. 5.9 Run-12: Effect of large BT errors	189
Fig. D.1 Range dependent TDOA noise type 2 (low)	204
Fig. D.2 Range dependent TDOA noise type 2 (high)	205
Fig. D.3 Nonnegative bias	206
Fig. F.1 Bounce count with missing horizontal rays	220

Fig. F.2 Grid without horizontal rays 220
Fig. G.1 Examples of characteristic digits 223
Fig. G.2 Vectors for inside test 226

LIST OF VARIABLES

A	The <i>MM</i> conditional model probability matrix
<i>AF</i>	Averaging factor
<i>AN</i>	Averaging number constant. <i>AN1</i> ... <i>AN9</i>
<i>a</i>	Autoregressive gain
<i>A_R</i>	Target horizontal (<i>x, y, R</i>) motion time constant
<i>A_D</i>	Target depth motion time constant
<i>a_i</i>	Path gain
B	Bearing state vector $\begin{bmatrix} B \\ \dot{B} \\ w'_b \end{bmatrix}$
<i>B</i>	Bandwidth [Hz]
<i>C</i>	Speed of sound [m/sec]
<i>D</i>	Depth [m]
<i>D_g</i>	Vector of depth grid values [m]
<i>D_{g0}</i>	Initial depth of the grid [m]
<i>D_o</i>	Observer depth, from ocean surface [m]
<i>D_w</i>	Water depth, surface to bottom [m]
<i>D_u</i>	Command quantization correction factor
<i>D_c</i>	Drag coefficient [N/(m/sec)]
\mathcal{E}	Error
EI	State bank deviation
$E\{x\}$	Expectation operation

F	Steady state command to state deviation transformation
G	Kalman gain matrix
<i>g</i>	Scalar Kalman gain
g	Speed of sound gradient [sec^{-1}]
H	Observation matrix
<i>i</i>	Index
<i>j</i>	Index
<i>k</i>	<i>MM</i> update time
<i>m</i>	Mass [Kg]
<i>N</i>	Number of models in multi-model (<i>MM</i>) estimator
N	Raw vector ($1 \times N$) of 1's
<i>N_d</i>	Number of depth steps in DR grid (length of vector <i>D_g</i>)
<i>N_r</i>	Number of range steps in DR grid (length of vector <i>R_g</i>)
<i>N_o</i>	Noise spectral level
<i>p</i>	Acoustic pressure [N/m^2]
P	Kalman filter error covariance matrix
<i>P_r</i>	Probability of unchanging command
<i>p</i>	Range dependence power
Q	Direct function TDOA array
<i>q_{ij}</i>	Quad of depth <i>D_g[i]</i> , range <i>R_g[j]</i> , TDOA <i>t₁[i, j]</i> and TDOA <i>t₂[i, j]</i> corresponding to point [<i>ij</i>] on the <i>DR</i> grid

R	Range horizontal, from observer to source [m]
R_{op}	Range estimation output [m]
r	Real part of acoustic impedance [Kg m^2 /sec]
R_{ray}	Ray radius [m]
\mathbf{R}_g	Vector of range grid values [m]
R_{go}	Initial range of the grid [m]
S	Ray path length [m] or signal spectral density
S	salinity [parts per thousand]
T_h	Thrust [N]
T	Sample time [sec]
T_0, T_1, T_2	Travel time [sec]
t	Modified TDOA [sec]
T	Temperature [$^{\circ}$ C]
U	Speed Command [m/sec]
U_i	Command hypothesis of filter i
UI	$1 \times N$ command bank vector $ U_1 U_2 \dots U_N $
U_r	Range speed command [m/sec]
U_b	Cross range speed command [m/sec]
U_d	Depth position command [m]
U'_d	Depth speed command [m/sec]
U_H	U hypothesis [m/sec]
U_c	Command bank center $\frac{U_{min} + U_{max}}{2}$ [m/sec]

U_s	Command bank separation $U_{max} - U_{min}$ [m/sec]
$\mathbf{u}(t, r)$	Acoustic particle velocity [m/sec]
U_{cd}	$U_{center\ deviation} = U_c - U_{actual}$
v	Measurement noise
w	Singer process noise input, white [m/sec ³ , or scaled in eventual speed m/sec]
w'	Singer acceleration, colored [m/sec ² or scaled in eventual speed m/sec]
W_i	Hypothesis weight (Probability)
\mathbf{W}	$N \times 1$ Hypothesis weight (Probability) vector $ W_1, W_2 \dots W_N ^T$
\mathbf{W}_{op}	Output weight vector
x	Position (either generic or Cartesian x)
\mathbf{X}	State vector $\begin{bmatrix} x \\ \dot{x} \\ \ddot{x} \end{bmatrix}$ (or $\begin{bmatrix} x \\ \dot{x} \\ \ddot{x} \\ \dot{w} \end{bmatrix}$)
\mathbf{X}_i	State vector of filter i
\mathbf{X}_I	$(3 \times N)$ State bank matrix $[\mathbf{X}_1 \mathbf{X}_2 \dots \mathbf{X}_N]$
χ	Imaginary part of acoustic impedance
χ_m	Acoustic source distribution [sec ⁻¹]
y	Cartesian coordinate
\mathbf{Z}	Observation vector
z	Observation scalar or the Z transform variable.
Z	Acoustic impedance $\left[\frac{N \cdot sec}{m^3} \right]$

α	System time constant [sec^{-1}]
α_D	System time constant, depth channel [sec^{-1}]
α_R	System time constant, range channel [sec^{-1}]
α_w	System time constant singer noise [sec^{-1}]
α_B	System time constant bearing [sec^{-1}]
β	Ray angle [RAD]
Γ	Control gain matrix
Γ	Reflection coefficient (Γ_P -pressure; Γ_I - intensity)
ΔU	Command bank step size $UI[2] - UI[1]$ [m/sec]
ΔX	$XI[2] - XI[1]$ Adjacent state difference vector
ϕ	State transition matrix
Ψ	Process noise gain matrix
σ	Standard deviation (STD)
σ_i	STD of TDOA i
σ_w	Singer input white noise variance [m/sec^3] or scaled in eventual speed [m/sec]
σ_v	Measurement noise variance [m or deg]
τ	Time Difference of Arrivals TDOA
τ_o	Actual τ
∇	Del operator.
ρ_o	Density [Kg/m^3]
φ	Velocity potential [m^2/sec]

ρ

Slant range from observer to source [m]

θ

Command Markov probability transition matrix

$$\theta[i, j] = \begin{cases} P_r & i = j \\ \frac{1}{N-1}(1 - P_r) & i \neq j \end{cases}$$

LIST OF ABBREVIATIONS

ACF	Autocorrelation Function
AF	Averaging Factor
An	Averaging number const $An = \frac{1}{\ln(1/a)} = \frac{1}{\alpha T}$
BC	Bounce count
CPA	Closest Point of Approach
CRLB	Cramer Rao lower bound
DR	Depth Range
MM	Multi-model Estimator
MMS	Minimum mean square
MP	Multipath
ms	milli-sec
Rx	Receiver
SNR	Signal to Noise Ratio
STD	Standard Deviation
SVP	Sound Velocity Profile
TDOA	Time Difference of Arrivals
Tx	Transmitter (or source)
WKB	Wentzel, Kramers, Brillouin (approximation)
$X \sim N(m, \sigma^2)$	X is a normally distributed random variable where mean = m and variance σ^2
ZZLB	Ziv Zakai lower bound

ACKNOWLEDGMENTS

The author wishes to acknowledge the help and contribution of Professor C. W. Therrien as my advisor in the conduct of this research and for his help during the writing of the dissertation.

Gratitude is also extended to Professors Garret, Kirk, Hamming, McLellen, Ziomek and to Dr. Friedlander. As members of my doctoral committee they demonstrated interest in the research and lent their knowledge and experience in many hours of formal seminars and informal discussions.

The support of Mr. A. Novick and Mission Sciences Corporation in providing the SMART acoustic eigenray model was crucial for this study and is greatly appreciated.

Mrs. and Mr. Allen typeset this document in \TeX . Their dedication and proficiency, for which I am very thankful, produced a very fine looking document.

APL GRAFSTAT which was used in this research has been made available to the Naval Postgraduate School by IBM on a test bed agreement. We are grateful to Dr. P. D. Welch of IBM for arranging this agreement.

DEDICATION

This work is dedicated to my parents who made everything possible for me; to my wife who makes everything enjoyable; to my children who make everything worthwhile; and to the Israeli Navy for providing me with the opportunity to learn.

I. INTRODUCTION

A. **BACKGROUND - PASSIVE TARGET TRACKING**

Passive tracking is based on reception and analysis of signals emitted from a target at an unknown time and location. Range measurement to the target, usually based on knowledge of the travel time and speed of the signal, is not possible. The lack of range information makes the tracking of targets, which are free to change their range, a challenge. Our interest in passive target tracking is primarily for acoustic tracking of targets in the ocean. However, the problem of passive localization is encountered in fields like radio astronomy and seismology as well as in passive sonar. Several passive tracking techniques have evolved over the years; some of these will be briefly reviewed here.

1. T.M.A - Target Motion Analysis

Target motion analysis is a range estimation technique devised for World War II submarines. Typical targets were surface ships and the measurements were primarily sonar bearing. Occasional course and speed estimates derived from periscope peeks were used as well, but mainly for initialization. The method is based on hypothesizing constant course and speed targets. The range of the target whose trajectory would have produced bearing measurements which best fit the actually observed bearing data is selected as the estimate. The observability problem is partially solved by maneuvering the observing platform while assuming the target maintains its course and speed. Own ship maneuvering is a lengthy operation and the assumption is that the target maintains course and speed only of limited validity. The important points to note about TMA are:

- No direct or indirect measurement of range.
- Range estimates limited to nonmaneuvering targets.
- Lengthy own ship maneuver requirement.
- Lengthy solution development time.
- Very accurate bearing measurements needed.

2. Wavefront Curvature

Wavefront curvature is an indirect range measurement technique. It is based on the assumption that the acoustic waves propagate in spherical wavefronts. Signals from an array of at least three spatially separated receivers are delayed in time to affect focusing. The amount of delay, which is the travel time difference of arrival (TDOA) required for a given array length, is then translated into target range. The performance depends on the length of the array baseline, the precision of both the sensor location along the array and the time delay measurements.

A number of implementations exist with array baselines varying from a few tens of meters in integrated systems, to hundreds of meters in large multi-platform distributed configurations. The range measurement, which is independent, can however be further combined with other measurements like target bearing or Doppler in order to reduce the ranging error. The important features of this method are:

- Truly independent measurement of range.
- Requirement for multiple sensors precisely located over a large baseline.
- Applicability to maneuvering targets.

3. Multipath Tracking

Multipath (MP) tracking is similar in principle to wavefront curvature. Here travel time differences to a single receiver via different paths, are measured

using autocorrelation techniques. The paths most commonly used are the direct path and those reflected from the surface and bottom of the ocean. The reflected paths can be viewed as paths to imaginary virtual receivers in mirror image locations, one above the water and the other below the bottom. In this sense, the single receiver acts like an array of three receivers (see Section C.2).

As in the wavefront methods, the travel time differences depend on the target's depth and range and on the array baseline, here determined by the water column. If propagation is assumed to be along straight lines, the inverse dependence of target position on travel time differences is relatively simple. It provides a mapping of time delays to range and depth. The range and depth observations thus obtained can again be combined with other available target measurements in order to reduce the error. The main features of multipath tracking are therefore:

- Independent measurement of range and depth.
- Compact single receiver configuration.
- Applicability to maneuvering targets.
- Dependence on ocean propagation conditions.

The MP method has enjoyed a growing amount of attention in recent years due to the advantages stated above and the continued improvement in time delay estimation. Compensating for the dependence of the method on ocean conditions is the main subject of this work.

B. THE BASIC MULTIPATH METHOD

1. The Travel Time Differences

The acoustic medium of the ocean is confined between the distinct surface and bottom boundaries. The medium thus provides multiple reflective paths along which sound can travel between two given points. The sound travel time along

those different paths will differ by an amount dependent in a known manner on the geometry of the scenario.

Consider the direct and single reflection paths shown in Fig. 1.1, under the following assumptions:

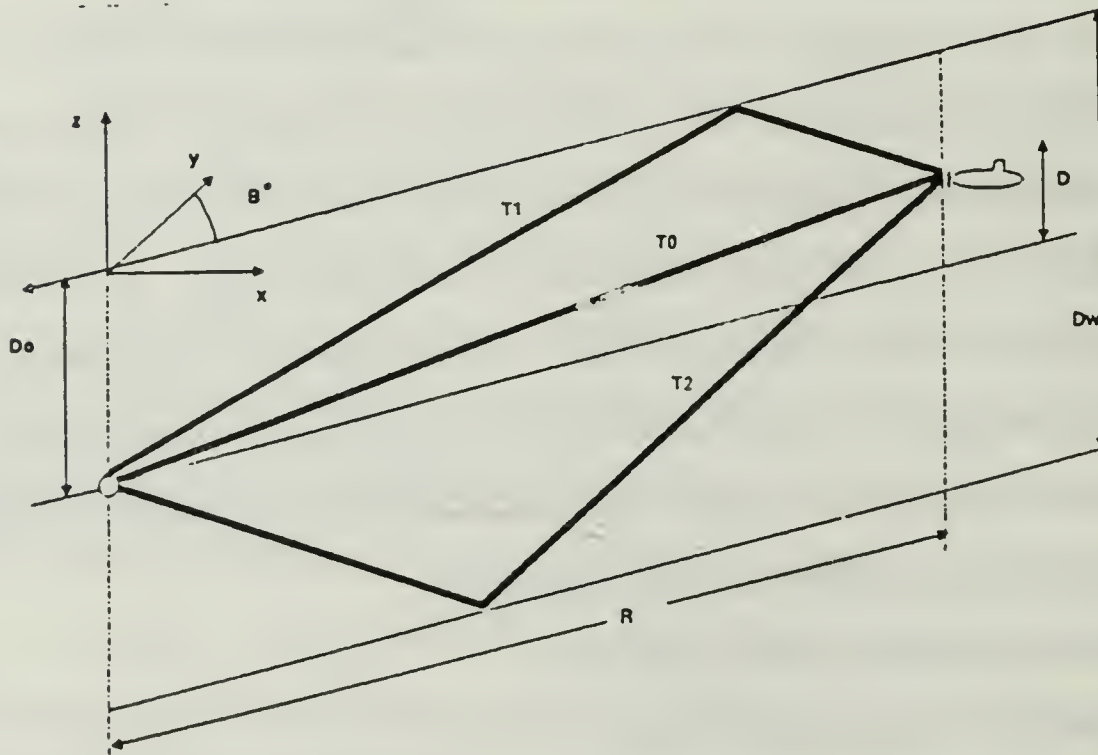


Fig. 1.1 Multipath propagation.

- A. The sound propagates along straight lines.
- B. The bottom and surface are ideal rigid and pressure release boundaries, respectively.
- C. The travel time differences can be analyzed, resolved, and associated with the corresponding paths.

The following relations then exist between the target depth D and range R position, measured relative to the observer, and the travel time differences τ_1 and τ_2 :

$$\tau_1 = T_1 - T_0 = \frac{1}{C} \cdot \left[(R^2 + D^2 + 4D_0^2 - 4D_0D)^{1/2} - \rho \right] \quad (1.1a)$$

and

$$\tau_2 = T_2 - T_0 = \frac{1}{C} \left[(R^2 + D^2 + 4(D_w - D_0)^2 - 4(D_w - D_0)D)^{1/2} - \rho \right] \quad (1.1b)$$

Where T_0, T_1, T_2 are the travel times of the direct, surface, and bottom paths, respectively; D_w is the water depth (surface to bottom); D_o is the observer depth (surface to observer); ρ is the slant range given by $(R^2 + D^2)^{1/2}$ and C is the speed of sound. These relation can be inverted to express the slant range, the depth and the range as functions of the travel time differences. The results are

$$\rho = \frac{4 \left[(D_w - D_0) \cdot D_0^2 + D_0(D_w - D_0)^2 \right] - C^2 T_2^2 D_0 + T_1^2 (D_w - D_0)}{2C [T_1(D_w - D_0) + T_2 D_0]} \quad (1.2a)$$

$$D = \frac{1}{4(D_w - D_0)} \cdot [C^2 T_2^2 + 2CT_2 \rho - 4(D_w - D_0)^2] \quad (1.2b)$$

and

$$R = (\rho^2 - D^2)^{1/2}. \quad (1.2c)$$

Eq. (1.1) and Eq. (1.2), referred to in this work as the direct and inverse functions respectively, were derived by Hassab in Ref. 1.

2. Time Delay Estimation

The signal $y'(t)$ at the receiver is modeled as a sum of replicas of the original signal $x(t)$, each multiplied by the path gain a_i , and time shifted by the path travel time T_i , that is,

$$y'(t) = \sum_{i=0}^N a_i \cdot x(t - T_i) \quad (1.3)$$

The signal $y(t)$, which is the signal $y'(t)$ time shifted by the travel time of the first arrival T_0 , that is,

$$y(t) = y'(t - T_0) \quad (1.4)$$

can be expressed in terms of the TDOAs τ_i as

$$y(t) = \sum_{i=0}^N a_i x(t - T_0 - T_i) = \sum_{i=0}^N a_i x(t - \tau_i) \quad (1.5)$$

where $\tau_i = T_i - T_0$. If the source of the target's acoustic emission is propeller cavitation noise, as is the case for broadband MP, then the original signal $x(t)$ is a broadband random process. The autocorrelation of its received version $y(t)$ will exhibit peaks at time lags equal to τ_i . The autocorrelation can be easily computed at discrete time lags using a sampled version of the received signal. As long as the ACF peaks are resolvable, they can be interpolated between the discrete lags providing the required continuous time delay measurement. The measured delays can be further smoothed using a time delay tracker.

In the narrowband case, low frequency tonals emitted by target machinery can be received at long range. Since the autocorrelation function of such sinusoids is periodic, the ACF approach is impractical. A different approach has been applied to this situation which is based on standing waves generated by the tonals in the water column. The sound field intensity is sensed by a number of receivers placed along a vertical array. A technique called field matching is used to select a target position which will give rise to a sound field that best matches the measured intensity. The effort in this work concentrates on the broadband case.

3. Target Tracking

The MP depth and range measurements are contaminated with noise. Sources of the noise include acoustical noise which distorts the autocorrelation

of the received signal, errors and fluctuations of the MP conditions in the ocean, and errors in the receiver and signal processor. To estimate the actual position from the noisy measurements, a target tracker is employed. The tracker fits the measurements with an estimate that, on the average, minimizes the squared error between the actual and estimated position. Such a tracker, also referred to as an *estimator, observer, or filter*, may also use other available measurements like bearing and Doppler.

Many trackers of the type described above are available. These range from simple averaging trackers to large banks of Kalman filters. The trackers differ primarily in the measurements they use and the complexity of the assumed target model.

A typical complete MP measurement and tracking system is shown in Fig. 1.2. Estimated TDOAs are converted to depth and range by the prefilter. Depth and range are then combined with bearing to form a 3-D target position measurement which is filtered by the target tracker.

Current MP tracking methodology is lacking in the following areas:

- The methods assume straight line propagation which is true only in a homogeneous medium. This assumption is largely in error for the realistic inhomogeneous (IH) case. This causes large errors in the transformation of time delays to depth and range.
- The assumption that path and delays are easily associable is wrong for many practical cases. A significant amount of detailed oceanographic data is required in order to identify the multiple paths. This information is not typically available in an actual target tracking situation.
- Receiver time delay resolution is not perfect but limited by the bandwidth of the signal and the receiver. This affects the performance whenever the geometry yields two or more multipaths with similar travel times. Three such typical geometries are :

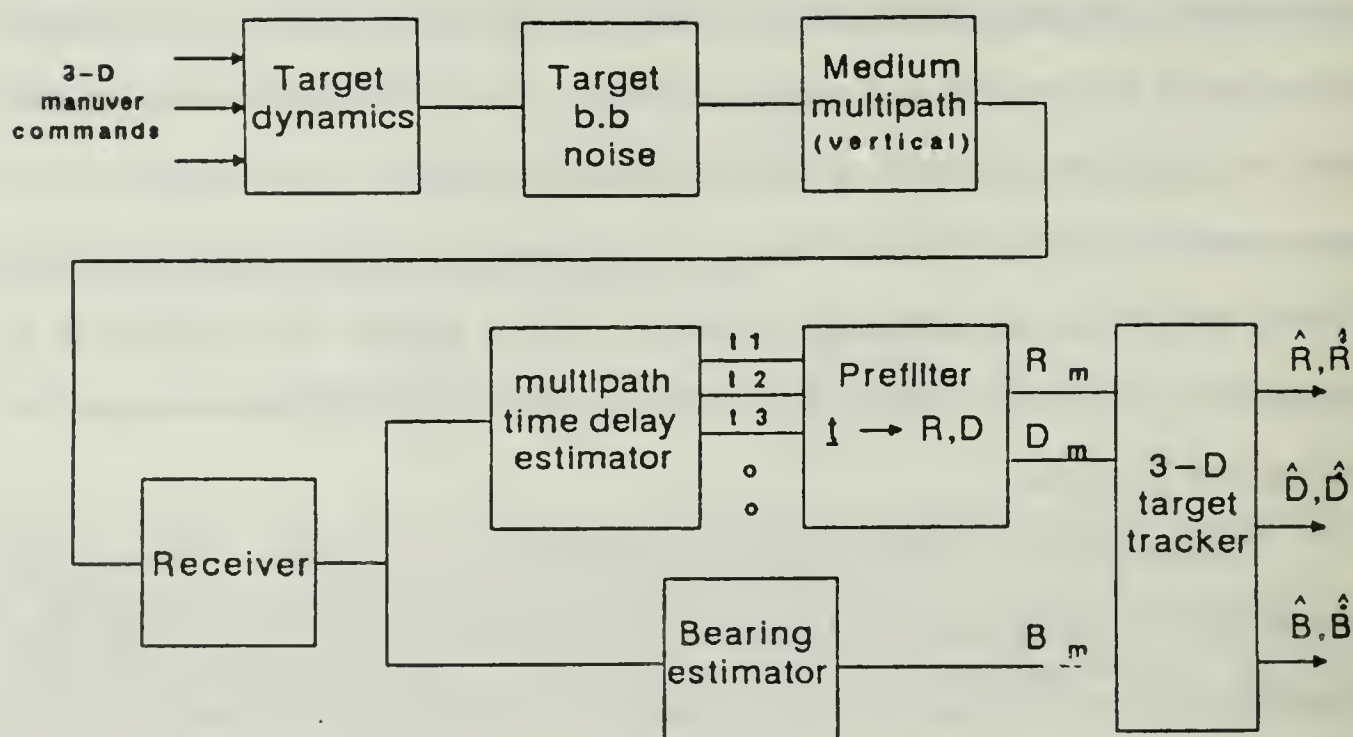


Fig. 1.2. MP tracking system.

- Long range, where all paths tend to be of same length.
- Target or observer close to the surface or bottom where the direct path and the reflected path have similar length.
- Target and observer at symmetrically opposing depths such that the bottom and surface paths have similar travel times.
- The lack of exact knowledge of bottom depth and structure limits both the time delay measurement and the exact translation to depth and range.
- Other effects including slanted bottom, and the anisotropic nature of the bottom which may have different slopes at different directions.

Our work seeks to address some of these effects, in particular the first three.

C. REVIEW OF PAST WORK

1. MP Target Tracking

a. Hassab

In 1976 Hassab published an original work titled "Passive tracking of moving source by a single observer in shallow water" [Ref. 1] which was the starting point for the research in the area. In this work, the use of measured travel time differences as inputs to a target tracking filter was established. The tracker was realized in cartesian coordinates using an extended Kalman filter and assuming a nonmaneuvering target. Earlier work by Hassab [Ref.2] dealt with the very process of measuring the travel time differences using a technique based on the cepstrum.

b. Singer

In the early T.M.A algorithm the development of a range solution was halted when a target maneuver was detected (a "Zig Zag" in World War II jargon). The maneuvers were detected when constant tracking errors indicated a mismatch between the actual target and its model. With the application of Kalman filters to target tracking, the maneuvering command uncertainty was represented as a white gaussian process noise. Singer [3] improved the model by coloring (low pass filtering) the command noise to correspond to the expected maneuver dynamics.

c. Moose

In the 1970's multiple model (multiple hypothesis) methods were introduced [4] to address the maneuvering problem. Here a number of target models based on different hypothesized maneuvers are computed in parallel, and combined in a Bayesian manner to form the overall estimate.

This approach was applied to both airborne and underwater targets by Moose [5,11] and his colleagues McCabe [6], Gholson [7], Van Landingham [8], Dailey [9], and Caputi [10]. Three main issues related to MP tracking were addressed

in this work, which is ongoing; They are the selection of a particular coordinate system, the account for target maneuver, and the bias associated with the nonlinear transformation of TDOAs to depth and range. Performance evaluations were carried out in Moose's work but both the simulation and tracking were done without taking account for the effects of the IH acoustic medium and the realistic delay estimation process.

2. Time Delay Estimation and Source Localization.

The area of time delay estimation has received enormous attention in the last twenty years. Among the contributors are Schultheiss [13], Ianniello [14], Wienstien [15], Friedlander [16, 17], and others. Work in this area covered the topics of estimation instrumentation, theoretical and experimental error bounds, estimation resolution, continuous delay reconstruction from sampled time sequences, and more. A very good summary is presented in Refs. 15 and 16.

Use of TDOA for source localization was investigated by Schultheiss for a variety of receiving array configurations. In his work [18] lower bounds on achievable error using bandlimited signals is developed using the Cramér Rao lower bound (CRLB) and Ziv Zakai lower bound (ZZLB). In the Ph.D. dissertation by his student Hamilton [19] the lower bound for the MP localization error variance is also developed. Hamilton also establishes the relation between the wavefront curvature and the multipath ranging using reflected mirror images of the receiver.

3. Acoustic Propagation and Modeling

The basic form of sound propagation in an inhomogeneous medium where the speed of sound is a function of depth has long been known. The development of the associated approximations and the resulting ray acoustics are presented, for example, in Ref. 20 by Ziomek.

Numerous computer models have been developed to compute sound propagation in the ocean based on ray acoustics, starting from analog computer simulations which were used for ray tracing, and proceeding up to very large and sophisticated numerical models which account for many of the special effects of the ocean medium. A classic model in this category is the Generic Sonar Model developed by Weinberg [21].

Only a few models address the problem of finding the rays traveling between two given end points, the eigenray problem. A recent model of this kind is SMART (SMall Acoustic Ray Tracer) developed by Novick [22].

Research on the nature of reflection from the bottom and the surface of the ocean also dates back to World War II. Contributors in this field include, for example, Clay and Medwin [23]. Recent work in this area reveals the interrelationship between the various oceanographic processes, for example, internal waves, surface interaction of the ocean and the atmosphere, and shear waves induced in the bottom of the ocean by a sound field. The limitation of simplified partial, lumped models for these phenomena is becoming apparent.

D. PROBLEM STATEMENT

This thesis research seeks to address the following issues:

- To account for the complex effects of the inhomogeneous (vertically stratified) ocean medium on broadband MP tracking.
- To investigate the impact and account for the effects of a realistic receiver and time delay estimator on the overall tracking process.

In addition our work includes:

- Modification of the state of the art target tracking algorithm to decrease some of its estimation bias.

- Evaluation of the complete tracking algorithm using a realistic environment, and target simulation considering all main sources of estimation errors.

The main contributions and key discussions of each of the foregoing issues are given below.

1. The Inhomogeneous Ocean Medium

The real ocean is acoustically inhomogeneous, in that among other effects, the speed of sound varies with depth. This variation significantly effects the MP propagation and travel time as shown in Fig. 1.3 where the receiver (Rx) is at range = 0. Note that the direct path between the source and the receiver is completely eliminated due to the ray bending in Fig. 1.3b (an exhaustive search for the eigen rays was conducted for this plot and the resultant eigenrays are plotted). The effects, believed to be analyzed quantitatively here for the first time, are shown to render the assumption of straight line propagation to be of limited practical use. Accounting for this effect is difficult since the inverse function, which transforms travel time differences to depth and range is not readily computable by existing acoustic models. *Devising an inversion method to account for the IH effects on the MP tracking is a main goal of this research.*

The acoustic energy attenuates as it propagates through the water, and many factors contribute to this loss including spreading, absorption, and reflection. While these losses and their impact on the time delay estimation noise are relatively well understood, they were nevertheless never considered in past simulations. Inclusion of the reflection and spreading effects to increase the reliability of the simulation is another part of the effort to better account for the effects of the medium.

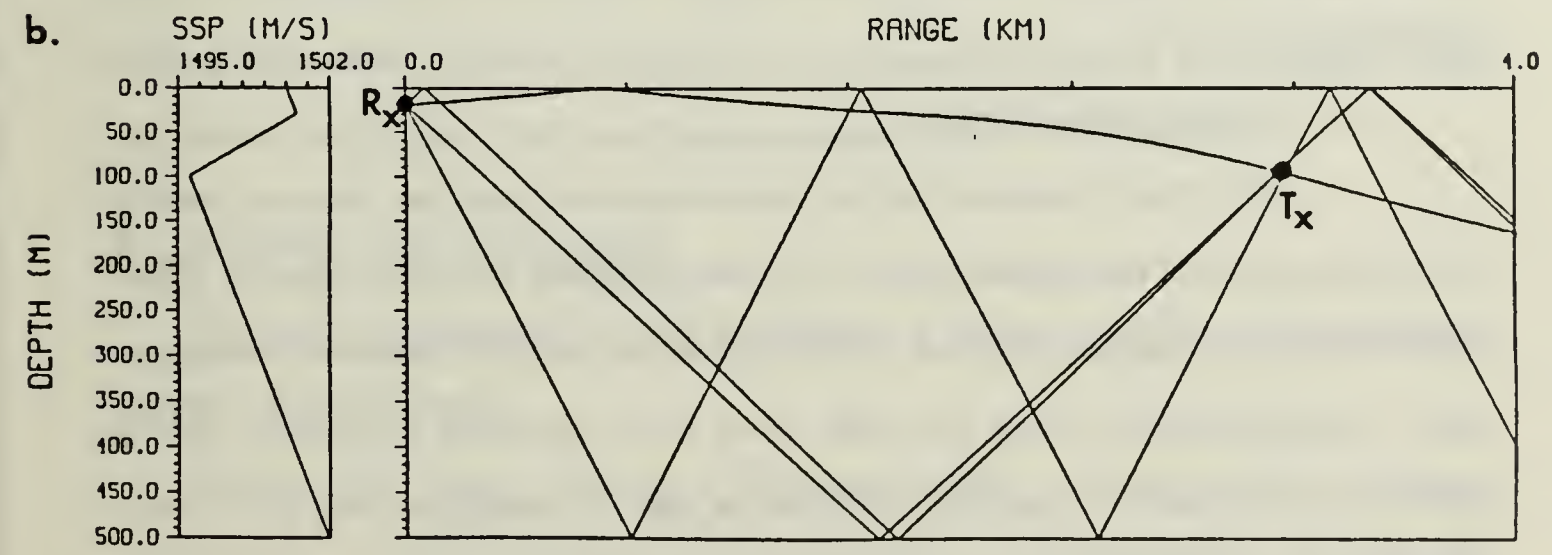
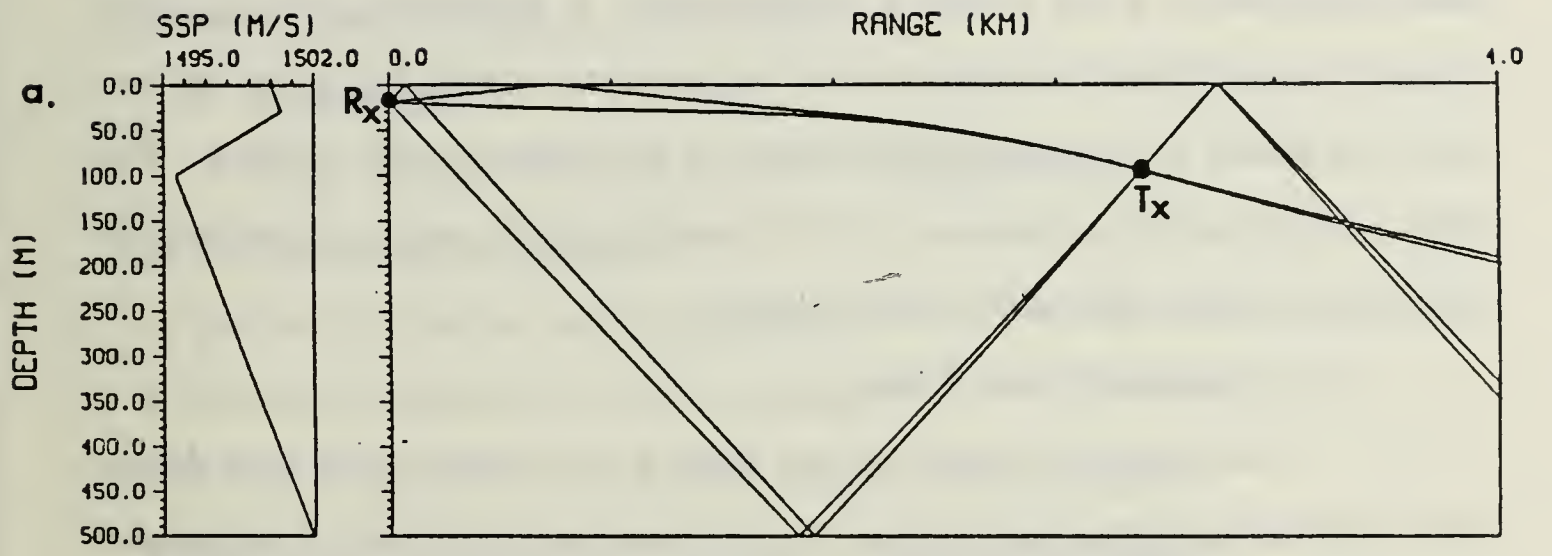


Fig. 1.3. IH MP propagation, a. with direct path, b. without direct path.

2. Realistic Receiver and Delay Estimation

a. Limited Resolution

The finite bandwidth of the target signal and receiver limit the time delay resolution to a few tenths of a millisecond. A significant amount of this research was dedicated to prediction and improvement of this limitation but less work was aimed at investigating the details of its impact on MP tracking. The effect of this limited resolution on the MP tracker and the means to overcome it are another subject addressed by this research.

b. Nonidentifiable Paths

The polarity of the ACF can support association of the time delays with their corresponding paths when the MP structure is known to be simple. However, when the structure is complex and/or unknown, such as in cases where there is a lack of direct path due to ray bending, the simple association is not possible. The ability to associate delay with paths, assumed in previous work, is *not* assumed here.

c. Nonnegative Noise

The even symmetry of the autocorrelation function does not enable the measurement of time delay polarity. In the multipath situation, there is a first arrival followed by lagging replicas. This justifies the use of the positive time delays only. The implication is that the delay noise is not normally distributed as was assumed in the past. A distribution which is zero for negative delay is a better description and it leads to a nonzero delay estimation bias error.

3. Tracker Modification

In the maneuvering target tracker introduced by Moose, the conditional mean of some hypotheses commands is used as the estimate. This estimate is biased if the hypotheses commands are not symmetrically centered around the

actual value. Removing this bias is difficult since modification of the hypotheses disrupts a recursion used in the estimation process. Modification of the tracker to remove the bias without disrupting the recursion or introducing large estimation transients is one of the goals of the research.

4. Evaluation

Many elements are involved in MP tracking, namely

- The target and its dynamics.
- The medium and its multipath structure.
- The receiver and the time delay analyzer.
- The conversion from time delays to position measurement.
- The actual acquisition and tracking of a maneuvering target.

Evaluation of the system performance is done in two steps. First, each and every component is evaluated separately. This is done under simulated conditions, which are determined for each component based on the analysis of the overall system operation. Then and only then, the integrated system is evaluated, using the results of the individual component evaluation as 'reference data'.

E. SCOPE AND OUTLINE

This work approaches the MP tracking as a system problem. The remaining chapters are as follows.

Chapter Two deals with the 3-D target tracker. A state-of-the-art tracker is described. An idealized receiver delay analyzer and homogeneous straight line propagation are assumed. The algorithm provides a good starting point in terms of its treatment of a 3-D maneuvering target. New interpretation and analysis is provided for certain aspects of the estimation mechanism, leading to a modification and improvement. A systems approach, not used in previous work, is applied to

evaluate the performance of the modified tracker. Some of the parameters and algorithms used for the simulation are not discussed in detail here, since they result from the removal of the above idealized assumptions which is explained in Chapter Three.

Chapter Three addresses the main source of tracking error, namely the IH medium together with the effects of a realistic receiver and delay analyzer. The nature of the problem is described and the proposed solution is discussed in detail. The performance of the method is then evaluated and analyzed in detail.

Chapter Four presents a detailed evaluation and analysis of the performance of the new inversion prefilter.

Chapter Five resumes the overall system performance analysis, this time without idealized assumptions and using the new inversion algorithm and the improved tracker.

The work is summarized in Chapter Six where conclusions and recommended extensions are presented.

II. THREE DIMENSIONAL MANEUVERING TARGET TRACKER

A. INTRODUCTION

The three dimensional (3-D) target tracker developed in this chapter is based on a state-of-the-art design by Moose, and McCabe. The modified Kalman filter which forms the central portion of the tracker was recently investigated by Saez [Ref. 24], in conjunction with this study. In his work, Saez includes a detailed review of the tracker, results of which are briefly repeated here for completeness and to establish notation.

The emphasis in this section is on improvements of the tracker design and a new overall systems approach to the performance evaluation. The modifications include an adaptive, instead of a fixed, command hypothesis bank and an advancing smoother. Both modifications are intended to reduce tracking biases. The investigation also includes the use of a second instead of a third order target model. This was found to reduce computational load without sacrificing estimation accuracy.

A realistic new model for the time delay estimation noise is used in evaluating the performance. The model incorporates propagation effects as well the effects of some inaccuracies in the time delay estimation. This enables a more realistic evaluation of the overall performance for the homogeneous case, which will be extended in Chapters Three through Five to the IH case.

A range and bearing coordinate decoupling approximation was introduced in the original tracker by McCabe [Ref. 6] to linearize the model. An interesting interpretation of this procedure provides an explanation for errors in tracking non-maneuvering targets that occur at short ranges.

B. TARGET DESCRIPTION

1. Horizontal Plane

A second order physical model is used to describe target motion in the X and Y directions of the horizontal plane. Controlling the motion is a command which forms the third degree of freedom in each axis. If $Th(t)$ is the command thrust in Newtons (N) and D_c is the drag in [N per m/sec] the differential equation for each axis which follows from Newton's second law is

$$Th(t) - D_c \dot{x}(t) = m\ddot{x}(t). \quad (2.1)$$

This equation can be rewritten as

$$\ddot{x}(t) = -\alpha (U(t) - \dot{x}(t)) \quad (2.2)$$

where $\alpha = D_c/m$ [sec⁻¹] is the reciprocal of the system's damping time constant, and $U = Th(t)/D_c$ [m/sec] is the speed command, i.e., the speed at which the platform will move when steady state is reached. If it is assumed that $\dot{X}(0) = X(0) = 0$ and that the command is a constant U then the solution is :

$$\dot{x}(t) = U(1 - e^{-\alpha t}) \quad (2.3)$$

$$x(t) = U \left(t + \frac{1}{\alpha} (e^{-\alpha t} - 1) \right) \quad (2.4)$$

2. Depth

Because of the reduced dynamics expected for underwater targets in the depth channel, the target's motion in depth was modeled as a first order system. The command U_d [m] can therefore be represented in terms of the steady state depth, and the differential equation along the depth axis is

$$\dot{D}(t) = \alpha_d (U_d - D(t)). \quad (2.5)$$

The solution of Eq.(2.5) is given by

$$D(t) = D_{(o)}e^{-\alpha_d t} + U_d \cdot (1 - e^{-\alpha_d t}). \quad (2.6)$$

3. Command Noise Augmentation

Eq. (2.2) describes target motion in response to a known control U . However the control (command) is not known to the observer, especially if the target is maneuvering. Singer partially accounts for this by adding a colored noise component w' to the command. This noise w' is modeled by a first order recursive filter driven by a normally distributed white noise input w .

$$\dot{w}'(t) = -\alpha_w w'(t) + w(t) \quad (2.7)$$

The lowpass model was chosen since it represents a maneuver which typically takes at least a few seconds to complete. The command is thus modeled in the observer by the sum of an assumed command U and the random noise w' , that is, $U_{observer} = U + w'(t)$. This description suggests estimation of the command U by the multi-model (MM) estimator described in Section C.

In order to maintain a complete system state description, the coloring LP filter and its state w' are combined into the target state equations. Both the command U and the the noise w are represented in units of the resulting steady state speed. The differential equations are then represented in discrete form by the following set of (3-D) Cartesian motion difference equations.

$$X_n = \phi X_{n-1} + \Gamma U_x + \Psi w_x \quad (2.8a)$$

$$Y_n = Y_n \phi Y_{n-1} + \Gamma U_y + \Psi w_y \quad (2.8b)$$

$$D_n = a_d D_{n-1} + (1 - a_d)U_d \quad (2.8c)$$

where

$$\mathbf{X} = (x \quad \dot{x} \quad w'_x)^T$$

$$\mathbf{Y} = (y \quad \dot{y} \quad w'_y)^T$$

and the components of the matrices ϕ, Γ, Ψ are detailed in Appendix A, and $a_d = e^{-\alpha_d T}$. Note that since the equations are linear and decoupled, a change in target course at a constant speed is modeled here as an acceleration along one axis and a deceleration along another.

4. Cylindrical Coordinate Observations

Most surveillance and tracking sensors produce measurements relative to their own position and orientation. The same is true in the MP case, where range and depth are indirectly deduced from the travel time differences across the vertical plane. Bearing is measured by beamforming; here sonar azimuthal beams are formed using travel time differences across the horizontal plane. Thus, the natural measurements are in the cylindrical coordinate system of range, depth and bearing. These are relative to the observing sensor which is therefore set at the origin. The detailed set of variables used to describe the positions of the observer and the target in the ocean is shown in Fig. 2.1 and defined in Table 2.1.

TABLE 2.1

CYLINDRICAL COORDINATES VARIABLES

D_o	Observer depth measured from surface.
D_w	Depth of the water.
D	Depth of target relative to observer.
R	Horizontal range of target relative to observer.
B	Bearing (azimuthal target angle relative to north).
\dot{B}	Bearing rate.
U_r	Speed command in range direction.
U_b	Speed command in cross range direction.
U_d	Depth position command.
U'_d	Depth speed $\alpha_d(U_d - D)$
ρ	Slant range.

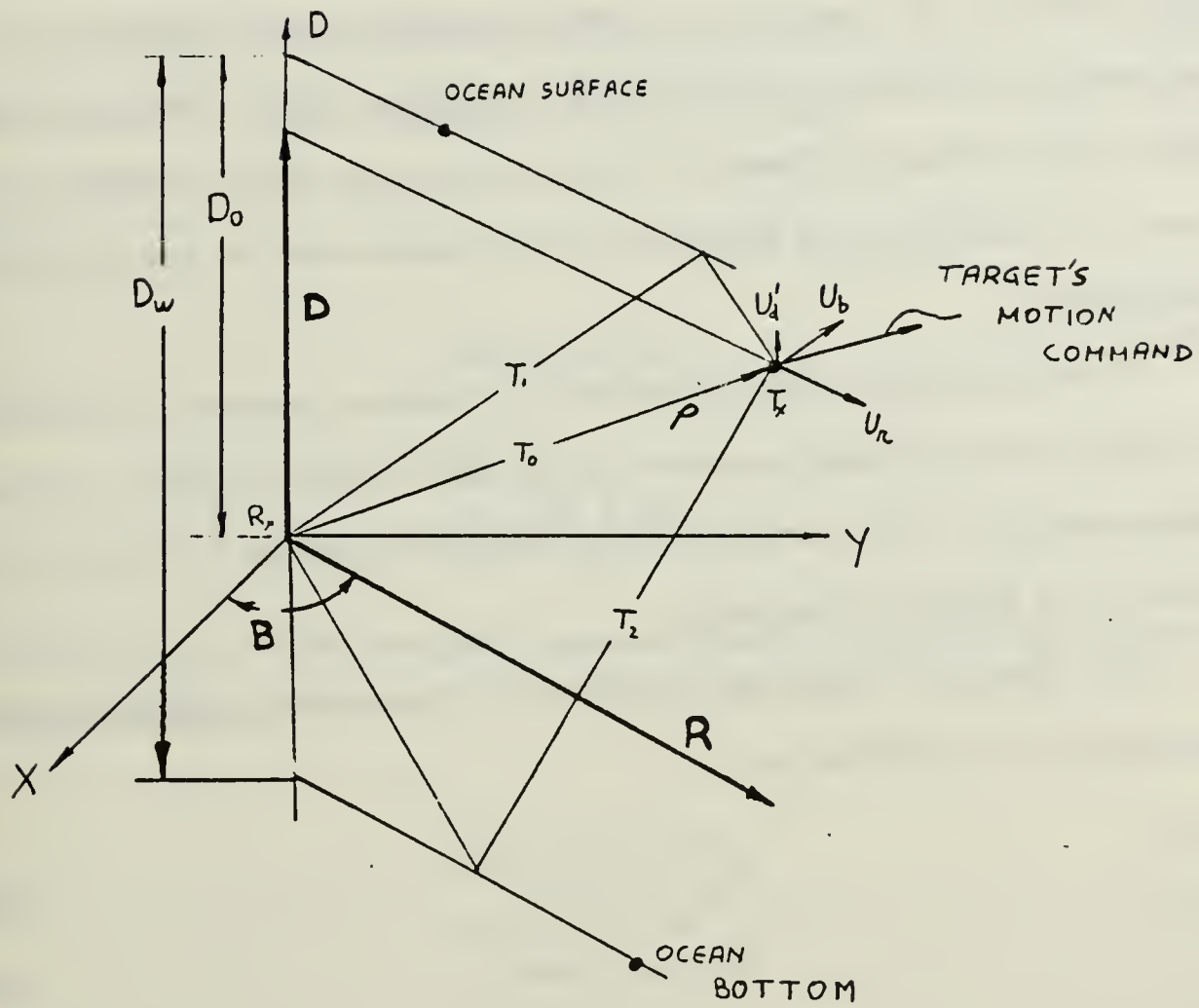


Fig. 2.1 Cylindrical coordinates.

5. Linearization and Decoupling

In order to use the cylindrical measurements as observations for the Cartesian target model of Eq. (2.8), the measurements have to be transformed. This leads to a coupled, nonlinear observer. Two possible approaches have been applied to this problem in the past. One is based on conversion and linearization of the measurements, and leads to the extended Kalman filter, (EKF). This approach was applied to MP tracking by Hassab [1]. The other was introduced by Moose [5] and is based on a decoupling and linearization of the state equations, using discretized approximations.

Investigation of the two approaches [7] indicated a preference for the second since taking account of target maneuvers in the EKF seemed to require a very large computational load. The second approach, developed in detail by McCabe in [6], is based on the following main steps.

The Cartesian target state description is transformed to cylindrical coordinates using the transformation:

$$R = (x^2 + y^2)^{1/2} \quad (2.9a)$$

$$B = \tan^{-1} (y/x) \quad (2.9b)$$

$$D = D. \quad (2.9c)$$

In the bearing channel, the range is assumed constant for the duration of the sampling period. The speed maneuver commands U_x and U_y along the X and Y directions are replaced by commands along the range and cross range (bearing) coordinates U_r and U_b respectively.

Range and bearing coordinate coupling is thus reduced to a parametric relation. This requires the bearing channel matrices to be recomputed only when

the range changes by more than some given ratio and no more than once per iteration. The resulting state equations are

$$D_n = a_d D_{n-1} + (1 - a_d) U d_{n-1} \quad (2.10a)$$

$$\mathbf{R}_n = \phi_r \mathbf{R}_{n-1} + \Gamma_r U_{r \ n-1} + \Psi_R w_r \quad (2.10b)$$

$$\mathbf{B}_n = \phi_b \mathbf{B}_{n-1} + \Gamma_b U_{b \ n-1} + \Psi_b w_b \quad (2.10c)$$

where

$$\mathbf{R} = (R \dot{R} w'_r)^T \quad (2.11)$$

and

$$\mathbf{B} = (B \dot{B} w'_b)^T. \quad (2.12)$$

Each channel of the three decoupled channels (depth, range, bearing) is observed by a scalar z defined as

$$z_{dn} = d_n + v_{0|n} \quad (2.13a)$$

$$z_{rn} = R_n + v_{rn} \quad (2.13b)$$

$$z_{bn} = B_n + v_{bn} \quad (2.13c)$$

where v_d , v_r , and v_b are the observation noises. The components ϕ_b , Γ_b , Ψ_b of the cross range matrices are range dependent and presented in Appendix A. The subtle terminology – preference of the term “cross range” to “bearing” – used by McCabe, is significant. It is indicative of the fact that while the bearing variable is used, a constant cross range rate motion is actually being modeled as the basic nonmaneuvering case. The command U_b is a speed command in the cross range direction and *not* a bearing rate command. While the former is a constant, the

latter is range-dependent. Similarly the range rate command U_r reflects an assumed constant range rate for the nonmaneuvering case. This again is an incorrect assumption for a target moving along any straight line other than the line of sight. The impact of these assumptions will become more apparent in the next section.

C. MULTI-MODEL ESTIMATION

1. Concept

Use of the classic Kalman filter as an observer for a maneuvering target is possible only if provision is made for the unknown maneuver command. The method suggested by Singer does not suffice in itself since it dictates maintaining high Kalman gain; this inhibits effective measurement noise filtration.

A better procedure is known as the Multi-Model (MM) [43] and was first applied to the MP tracking problem by Moose. In the MM a number (N) of commands are hypothesized to form a command bank vector \mathbf{UI} defined as:

$$\mathbf{UI} = (U_1, U_2 \dots U_N). \quad (2.14a)$$

The bank is ideally centered around the mean command value and the commands in the bank are evenly spread to span the full range of possible commands. A corresponding bank of Kalman filters (models) is formed and each filter in the bank separately tracks the target using its particular hypothesized command and the common measurement Z . The estimated states \mathbf{X}_i from all the filters in the bank are combined to form a conditional mean which is used as the overall estimator output. The conditional mean depends on the discrete command probability distribution represented by the weight vector \mathbf{W} defined as

$$\mathbf{W} = (W_1 \ W_2 \ \dots \ W_N)^T \quad (2.14b)$$

where the weight W_i is the conditional probability (weight) that a command U_i was exercised in the previous time period given all past observations z_n . The expression for the estimated state \mathbf{X} is $\sum_{i=1}^N \mathbf{X}_i W_i$.

The discrete distribution of \mathbf{W} can be computed recursively if the command is modeled as a semi-markov process with a known probability transition matrix θ . The conditional probability of each command, given the past position measurements *and* the hypothesis, is computable using the Kalman filter's error propagation matrix \mathbf{P} . A diagonal matrix \mathbf{A} with elements $a[i, i]$ set proportional to the conditional probability of the innovation given the hypothesis i is also used in the recursion which is given below. An overall block diagram of the resulting estimator is shown on Fig. 2.2. The development of the basic estimator is reviewed in detail in Ref. 24 and will not be repeated here except for the resulting estimator equations. Emphasis in the following sections will be directed towards the more recent evaluation and modification of the algorithm and to its application to the IH multipath tracking problem.

2. The Multi-Model Estimator Equations

The equations are written in a generic form for a 3×1 state vector \mathbf{X} representing either range \mathbf{R} or bearing \mathbf{B} . The specific state vectors, observation scalars and the corresponding matrices can be substituted to develop either the range or bearing equations. The depth is estimated by means of a first order smoother (similar to Eq. (2.10a)). The variables and their definitions are given in Table 2.2.

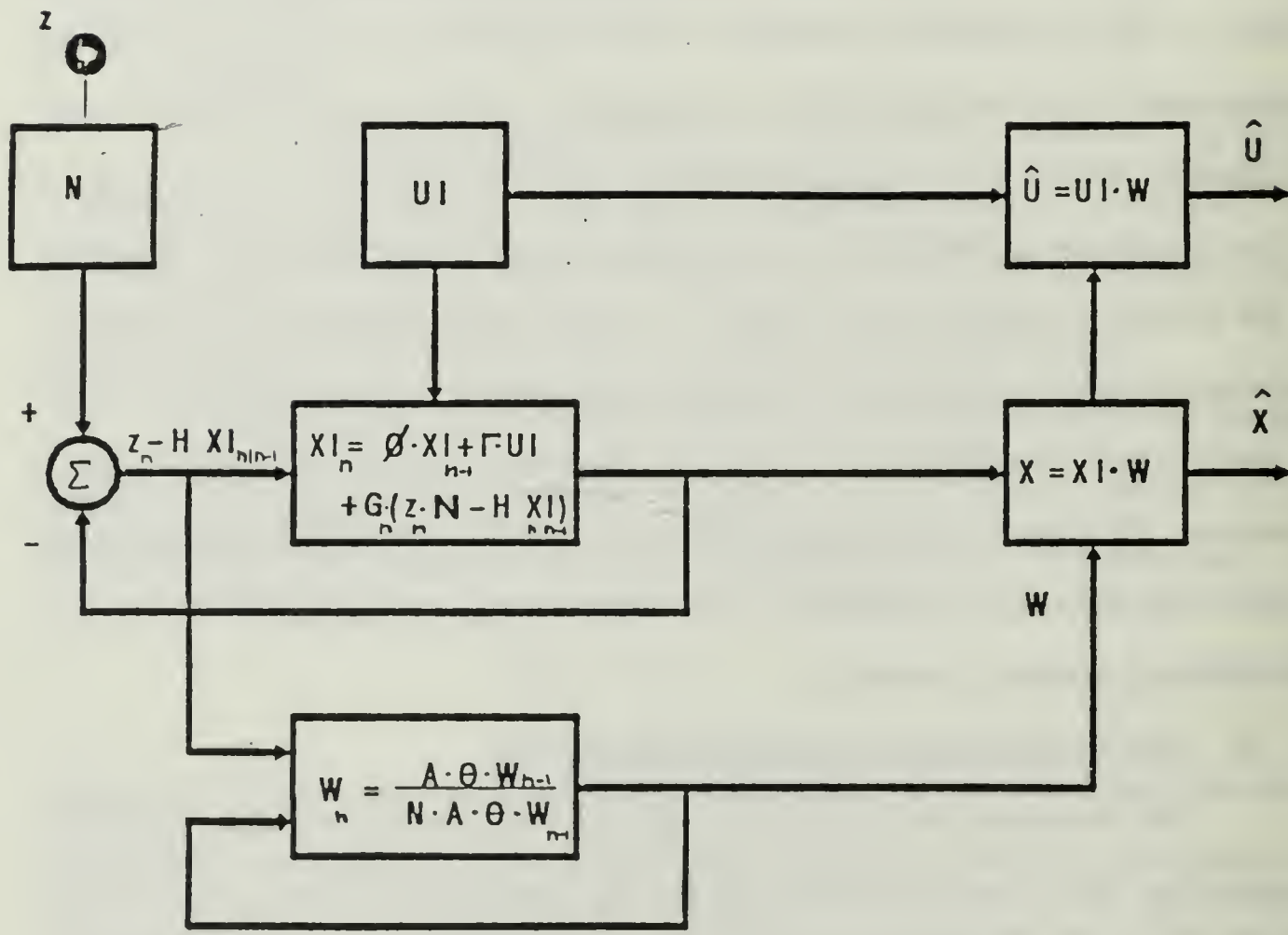


Fig. 2.2 Multi-Model Block Diagram

TABLE 2.2

MM VARIABLE DEFINITIONS

ϕ	3×3 state transition matrix.
Γ	3×1 control gain vector.
Ψ	3×1 Singer process noise gain vector.
H	3×1 observation matrix $H = [1, 0, 0]$.
G	3×1 Kalman gain matrix.
X_n	3×1 state vector $X = \begin{bmatrix} x \\ \dot{x} \\ w'_x \end{bmatrix}$ at time n .
X_i $n_1 n_2$	3×1 estimate of filter i in the bank at time n_1 given past observations $z_1, z_2 \dots z_{n_2}$
z	The observation scalar.
N	Number of models in the bank.
\mathbf{N}	$1 \times N$ a vector of 1's.
\mathbf{XI}	$3 \times N$ state bank matrix. $\mathbf{XI}[i j]$ is the i -th component of the state vector X_j of the j -th model, i.e., $\mathbf{XI} = [X_1 X_2 \dots X_N]$. The matrix is time index like X_i above.
U_i	The assumed command of the i^{th} filter in the bank.
\mathbf{UI}	$1 \times N$ command bank, evenly spanning the $U_{\min} - U_{\max}$ interval of allowable commands, $\mathbf{UI} = [U_1, U_2, \dots, U_N]$.
U_{\min}	Minimum command in the bank.
U_{\max}	Maximum command in the bank.
U_s	Command bank separation $U_{\max} - U_{\min}$.
ΔU	1×1 command bank step size $\mathbf{UI}[2] - \mathbf{UI}[1]$.
U_c	Center of command bank $(U_{\max} - U_{\min})/2$.
v	1×1 zero mean gaussian measurement noise $v \sim N(0, \sigma_v^2)$.
σ_v	1×1 measurement noise standard deviation.
w	1×1 Singer white process noise input.
σ_I	1×1 standard deviation of the conditional innovation distribution given the hypothesis.
σ_u	Standard deviation of the command quantization error.
\mathbf{D}_u	3×3 command quantization error matrix.
\mathbf{W}	$N \times 1$ hypothesis command probability (weight) vector. $\mathbf{W} = [W_1 \ W_2 \ \dots \ W_N]$
θ	$N \times N$ command Markov probability transition matrix, $\theta_{[i,j]}$ - the probability that command j will change to command i in one step. $\theta_{[i,j]} = \begin{cases} P_r & i = j \\ \frac{1}{N-1}(1 - P_r) & i \neq j \end{cases}$ where P_r is the probability of unchanging command.
\mathbf{A}	$N \times N$ conditional innovation probability matrix.
X_{op}, U_{op}, W_{op}	Smoothed output of the estimates $\hat{X}, \hat{U}, \hat{W}$
a	Smoothing coefficient

The estimation equations are presented in the order of their use in the recursion. The Kalman filter equations are

$$\mathbf{XI}_{n|n-1} = \phi \cdot \mathbf{XI}_{n-1|n-1} + \Gamma \cdot \mathbf{UI} \quad (2.15)$$

$$\mathbf{P}_{n|n-1} = \phi \mathbf{P}_{n-1|n-1} \phi^T + \mathbf{D}_u + \Psi \sigma_w^2 \Psi^T \quad (2.16)$$

$$\mathbf{G}_n = \mathbf{P}_{n|n-1} \mathbf{H}^T [\mathbf{H} \mathbf{P}_{n|n-1} \mathbf{H}^T + \sigma_v^2]^{-1} \quad (2.17)$$

$$\mathbf{P}_{n|n} = [\mathbf{I} - \mathbf{G}_n \mathbf{H}] \mathbf{P}_{n|n-1} \quad (2.18)$$

$$\mathbf{XI}_{n|n} = \mathbf{XI}_{n|n-1} + \mathbf{G}_n (z_n \cdot \mathbf{N} - \mathbf{H} \cdot \mathbf{XI}_{n|n-1}) \quad (2.19)$$

Note that the state of the multiple-model \mathbf{XI} is the $3 \times N$ state bank matrix whose columns represent the states of the individual filters in the bank. The corresponding command \mathbf{UI} is an $N \times 1$ row vector which represents the entire command bank. \mathbf{D}_u is the command quantization error matrix and is computed once as

$$\mathbf{D}_u = \Gamma \frac{\Delta U^2}{12} \Gamma^T. \quad (2.20)$$

Since Eq.(2.15) through (2.19) are common to all the filters, the classical single channel Kalman gain vector \mathbf{G}_n can be computed once and used for all the filters.

The adaptive command estimation equations are

$$\sigma_{I_n}^2 = \mathbf{H} \mathbf{P}_{n|n-1} \mathbf{H}^T + \sigma_v^2 \quad (2.21)$$

$$\mathbf{A}_{[i,j]_n} = \begin{cases} e^{-(z_n \cdot \mathbf{N} - \mathbf{H} \cdot \mathbf{XI}_{[1,i]_n})^2 / 2\sigma_{I_n}^2} & i = j \\ 0 & i \neq j \end{cases} \quad (2.22)$$

$$\mathbf{W}'_n = [\mathbf{N} \ \mathbf{A} \ \theta \ \mathbf{W}_{n-1}]^{-1} \ \mathbf{A} \theta \mathbf{W}_{n-1} \quad (2.23a)$$

$$\mathbf{W}_n = a_w \mathbf{W}_{n-1} + (1 - a_w) \mathbf{W}'_n \quad (2.23b)$$

where the vector of conditional command probability \mathbf{W} is recursively computed. The conditional command probability \mathbf{W} is then used to compute the conditional mean estimates $\hat{\mathbf{X}}$ and \hat{U} of the state and command banks \mathbf{XI} and \mathbf{UI} respectively.

$$\hat{U}_n = \mathbf{UI} \cdot \mathbf{W}_n \quad (2.24)$$

$$\hat{\mathbf{X}}_n = \mathbf{XI}_n \cdot \mathbf{W}_n \quad (2.25)$$

Additional first order smoothing is applied to the MM estimate in the form of

$$(\mathbf{X}_{op})_n = a_x(\mathbf{X}_{op})_{n-1} + (1 - a_x)\hat{\mathbf{X}}_n \quad (2.26)$$

$$(U_{op})_n = a_u(U_{op})_{n-1} + (1 - a_u)\hat{U}_n \quad (2.27)$$

$$(\mathbf{W}_{op})_n = a_w(\mathbf{W}_{op})_{n-1} + (1 - a_w)\mathbf{W}_n \quad (2.28)$$

where the subscript *op* stands for "output".

A high initial Kalman gain is insured by setting the initial conditions as follows:

for $i = 1, 2, \dots, N$

$$\mathbf{XI}_{0|0}[1, i] = z_0 \quad (2.29)$$

$$\mathbf{XI}_{0|0}[2, i] = \frac{1}{T}(z_1 - z_0) \quad (2.30)$$

$$\mathbf{XI}_{0|0}[3, i] = 0 \quad (2.31)$$

$$\mathbf{P}_{0|0}[1, 1] = \sigma_v^2 \times 10 \quad (2.32)$$

$$\mathbf{P}_{0|0}[2, 2] = \frac{\sigma_v^2}{T^2} \quad (2.33)$$

$$\mathbf{P}_{0|0}[1, 2] = \mathbf{P}_{0|0}[2, 1] = \frac{10 \times \sigma_v^2}{T} \quad (2.34)$$

$$\mathbf{P}_{0|0}[1, 3] = \mathbf{P}_{0|0}[3, 1] = \frac{10\sigma^2}{T^2} \quad (2.35)$$

$$\mathbf{P}_{0|0}[3, 3] = 0 \quad (2.36)$$

$$\mathbf{W}_0 = \frac{1}{N}[1, 1, \dots, 1] \quad (2.37)$$

3. Estimation Factors

Some factors in the estimation process emerged as dominant when the observer performance was evaluated over a variety of conditions. These factors are reviewed in this section.

a. Hypothesized Commands

The use of a conditional mean between the set of hypothesized command parameters in the estimator leads to the dependence of the estimate on the validity and accuracy of the hypotheses and the nature (distribution) of the measurement noise. This effect can be demonstrated by the following simplified example. Consider an unknown scalar parameter U which is to be estimated from a single observation $z = U + n$ where n is a random variable with zero mean normal distribution $n \sim (0, \sigma^2)$. If one assumes a discrete model for U with two equally likely possible hypotheses U_1 and U_2 and $U_2 > U_1$, then the Bayes mean-square estimate is given by the conditional mean

$$\hat{U} = E \{U|z\} = \sum_{i=1}^2 U_i \cdot P(U_i|z) = \sum_{i=1}^2 U_i \cdot \frac{f(z|U_i) \cdot P(U_i)}{f_z} \quad (2.38)$$

where f is the probability density function of z . This estimate is shown in appendix B to yield

$$\hat{U} = U_c + \frac{U_s}{2} \tanh \left[\frac{U_s}{2\sigma^2} (z - U_c) \right] \quad (2.39)$$

where U_c and U_s are the center and separation of the hypothesis command bank defined by

$$U_c = \frac{U_1 + U_2}{2} \quad (2.40)$$

$$U_s = U_2 - U_1 \quad (2.41)$$

$$U_1 = -10; U_2 = 10; \text{STD} = 10$$

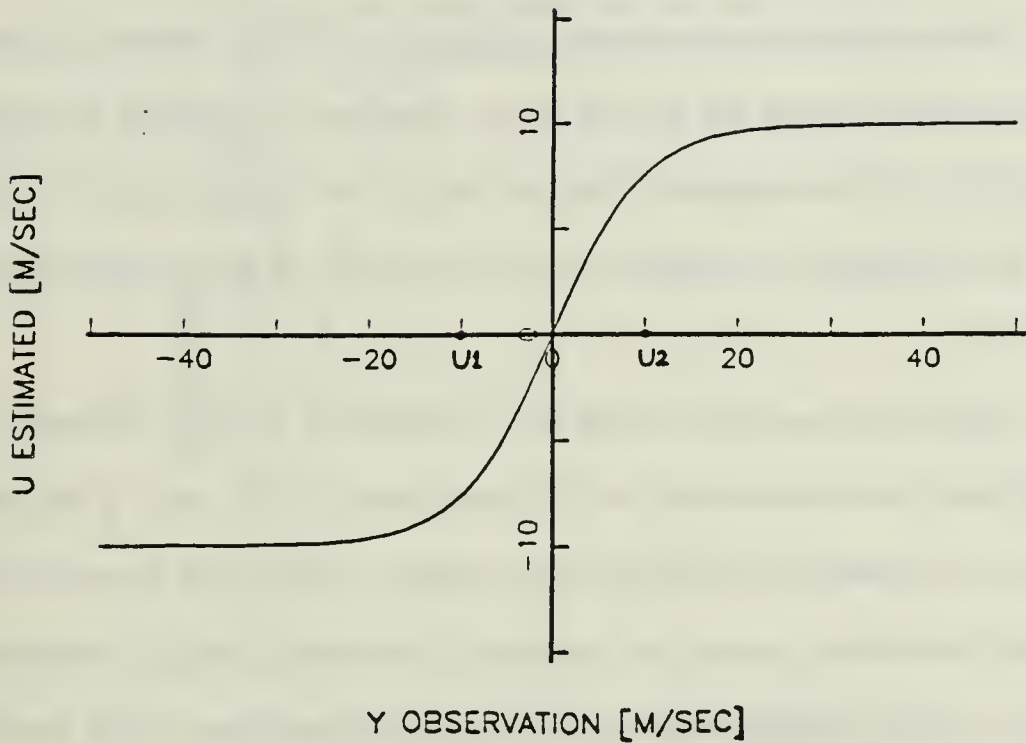


Fig. 2.3. Conditional mean estimate.

The dependence of the estimates on U_c and U_s , and on the noise distribution variance σ is clearly seen in Eq. (2.39). The function $U(z)$ defined by Eq. (2.39) is plotted in Fig. 2.3. The bias $\mathcal{E} = E \{ \hat{U} - U \}$ of the estimator is given by:

$$\mathcal{E} = E \left\{ U_c + \frac{U_s}{2} \tanh \left[\frac{U_s}{2\sigma^2} (U + n - U_c) \right] - U \right\} \quad (2.42)$$

which after rearranging and extracting the constants from the expectation gives

$$\mathcal{E} = U_c - U + \frac{U_s}{2} E \left\{ \tanh \frac{U_s}{2\sigma^2} (U + n - U_c) \right\}. \quad (2.43)$$

Given that $U_c = U$ the conditional bias can be shown to be zero as follows. Substituting $U = U_c$ into Eq. (2.43) gives the bias as

$$\mathcal{E} = \frac{U_s}{2} E \left\{ \tanh \left(\frac{U_s}{2\sigma^2} n \right) \right\}. \quad (2.44)$$

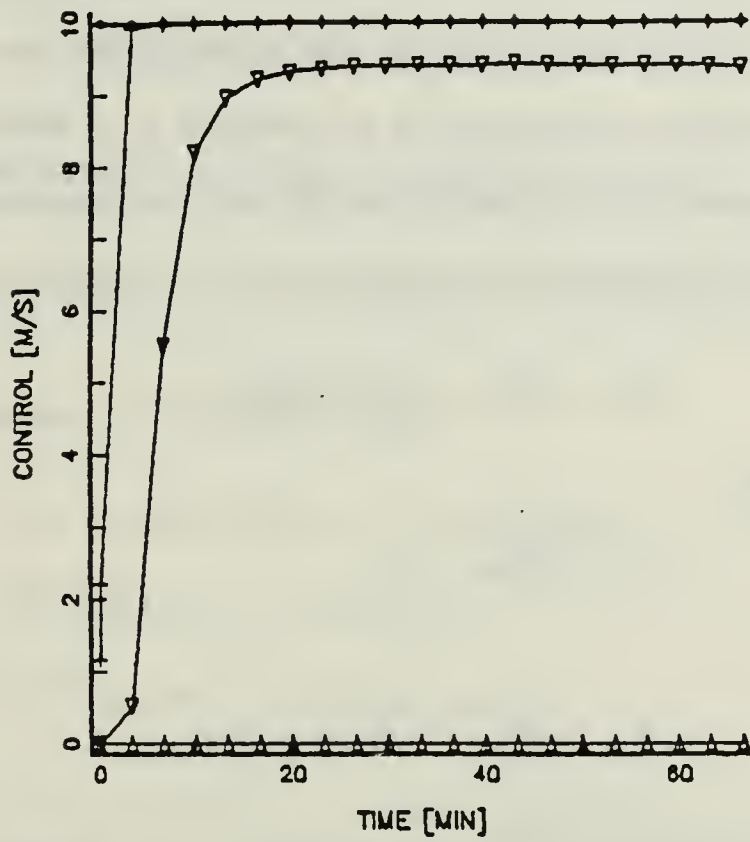
Since the $\tanh(x)$ function is odd and the density function of n is even, the expectation in Eq. (2.43) is zero.

However the bias is non-zero when $U_c \neq U$, i.e., when the hypothesis bank is not centered around the actual value. This can be realized for example by investigating Fig. 2.3 for values of U larger than U_2 or smaller than U_1 . If $U_c \neq U$ then U will be incorrectly estimated with the amount of error depending on the deviation $U - U_c$.

This simple analysis which can be extended to the MM case, provides a new insight into the operation of the MM estimator and its bias. If the command bank is to cover all possible commands of a target which could move at full speed both incoming (decreasing range) and outgoing (increasing range), its center should be set to zero speed. While a choice of $U_c = 0$ will produce good results when averaged over all possible target scenarios, it will produce a bias E for every specific scenario with average command $E\{U\} \neq U_c$. As long as the target is moving in one direction (inward or outward) the center of the hypothesis bank will be very different from the average command. This will give rise to an estimation bias.

In the example shown in Fig. 2.4 the command U of a target driven by a true command of 10 m/sec is estimated using a bank of 7 filters evenly spanning the range -15 to $+15$ m/sec centered around 0 m/sec. The resulting steady state command bias is 0.8 m/sec as shown in Fig. 2.4a. The position error resulting from the command bias is 150 m (Fig. 2.4b).

a. ACTUAL CONTROL • SPEED +; ESTIMATED CONTROL ▽



b. RANGE ERROR

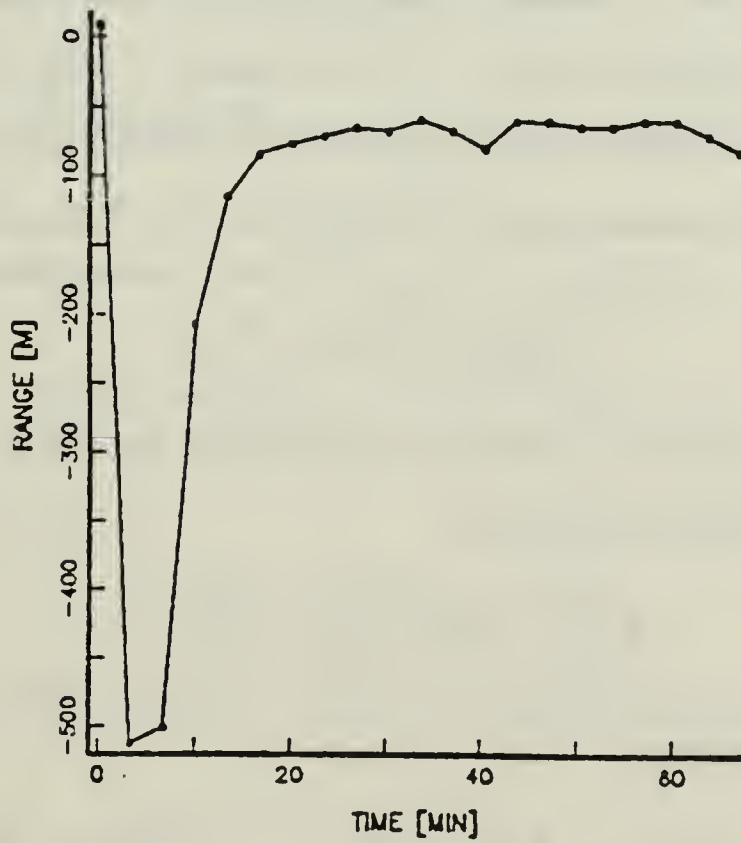


Fig. 2.4. Command estimation bias.

b. Basic State Separation

The dependence of the MM performance on the hypotheses separation warrants some further investigation. The measurement and the evaluation of the conditional mean are performed in the position $x(z)$ domain. The system dynamics as represented in the transition matrix and the Kalman filter translate a hypothesized command to a hypothesized position. In particular, consider a system

$$\mathbf{X}_n = \phi \mathbf{X}_{n-1} + \Gamma U + \Psi w_{n-1} \quad (2.45)$$

with an observation

$$z_n = \mathbf{H} \mathbf{X}_n + v_n \quad (2.46)$$

modeled by

$$\hat{\mathbf{X}}_n = \phi \hat{\mathbf{X}}_{n-1} + \Gamma U_H + \Psi w_{n-1} \quad (2.47)$$

U_H represents the hypothesized constant command here assumed to be different than the actual constant command U . The observation noise v and process noise w are both normally distributed with $v \sim N(0, \sigma_v^2)$ and $w \sim N(0, \sigma_w^2)$. The variables ϕ, Γ and \mathbf{H} are the transition, control gain, and observation matrices respectively. The goal is to find the mean steady state deviation \mathcal{E} of $\hat{\mathbf{X}}$ from \mathbf{X} , i.e.,

$$\mathcal{E} = \lim_{n \rightarrow \infty} E \left\{ \hat{\mathbf{X}}_{n|n} - \mathbf{X}_n \right\} \quad (2.48)$$

resulting from the mismatch between the model (U_H) and the actual system (U).

The Kalman prediction is

$$\hat{\mathbf{X}}_{n|n-1} = \phi \hat{\mathbf{X}}_{n-1|n-1} + \Gamma U_H \quad (2.49)$$

and its average is given by

$$E \left\{ \hat{\mathbf{X}}_{n|n-1} \right\} = \phi E \left\{ \hat{\mathbf{X}}_{n-1|n-1} \right\} + \Gamma U_H. \quad (2.50)$$

The Kalman estimate $\hat{\mathbf{X}}_{n|n}$ is

$$\hat{\mathbf{X}}_{n|n} = (\mathbf{I} - \mathbf{G}_n \mathbf{H}) \hat{\mathbf{X}}_{n|n-1} + \mathbf{G}_n z_n \quad (2.51)$$

which after substitution of Eq. (2.45) and (2.46) becomes

$$\hat{\mathbf{X}}_{n|n} = (\mathbf{I} - \mathbf{G}_n \mathbf{H}) \hat{\mathbf{X}}_{n|n-1} + \mathbf{G}_n \mathbf{H} (\phi \mathbf{X}_{n-1} + \Gamma U + \Psi w_{n-1}) + \mathbf{G}_n v_n. \quad (2.52)$$

Taking the expectation of Eq. (2.52) yields

$$\begin{aligned} E \left\{ \hat{\mathbf{X}}_{n|n} \right\} &= (\mathbf{I} - \mathbf{G}_n \mathbf{H}) E \left\{ \hat{\mathbf{X}}_{n|n-1} \right\} + \mathbf{G}_n \mathbf{H} \phi E \left\{ \mathbf{X}_{n-1} \right\} + \mathbf{G}_n \mathbf{H} \Gamma U \\ &\quad + \mathbf{G}_n \mathbf{H} \Psi E \left\{ w_{n-1} \right\} + \mathbf{G}_n E \left\{ v_n \right\} \end{aligned} \quad (2.53)$$

and since $E\{w_n\} = E\{v_n\} = 0$ Eq. (2.53) becomes

$$E \left\{ \hat{\mathbf{X}}_{n|n} \right\} = (\mathbf{I} - \mathbf{G}_n \mathbf{H}) E \left\{ \hat{\mathbf{X}}_{n|n-1} \right\} + \mathbf{G}_n \mathbf{H} \phi E \left\{ \mathbf{X}_{n-1} \right\} + \mathbf{G}_n \mathbf{H} \Gamma U. \quad (2.54)$$

If Eq. (2.50) is substituted into Eq. (2.54) the result is:

$$E \left\{ \hat{\mathbf{X}}_{n|n} \right\} = (\mathbf{I} - \mathbf{G}_n \mathbf{H}) (\phi E \left\{ \mathbf{X}_{n-1|n-1} \right\} + \Gamma U_H) + \mathbf{G}_n \mathbf{H} (\phi E \left\{ \mathbf{X}_{n-1} \right\} + \Gamma U). \quad (2.55)$$

Now taking the expectation of both sides of Eq. (2.45) gives

$$E \left\{ \mathbf{X}_n \right\} = \phi E \left\{ \mathbf{X}_{n-1} \right\} + \Gamma U + \Psi E \left\{ w_{n-1} \right\} \quad (2.56)$$

and since $E\{w_n\} = 0$,

$$E \left\{ \mathbf{X}_n \right\} = \phi E \left\{ \mathbf{X}_{n-1} \right\} + \Gamma U. \quad (2.57)$$

Subtracting Eq. (2.57) from Eq. (2.55), rearranging terms and substituting \mathcal{E}_n defined as

$$\mathcal{E}_n = E \left\{ \hat{\mathbf{X}}_{n|n} - \mathbf{X}_n \right\} = E \left\{ \hat{\mathbf{X}}_{n|n} \right\} - E \left\{ \mathbf{X}_n \right\} \quad (2.58)$$

results in

$$E \{ \mathcal{E}_n \} = (\mathbf{I} - \mathbf{G}_n \mathbf{H}) \phi E \{ \mathcal{E}_{n-1} \} + (\mathbf{I} - \mathbf{G}_n \mathbf{H}) \mathbf{\Gamma} (U_H - U). \quad (2.59)$$

At the steady state we can substitute $\mathcal{E} = \mathcal{E}_\infty$ for both \mathcal{E}_n and \mathcal{E}_{n-1} as well as $\mathbf{G} = \mathbf{G}_\infty$ for \mathbf{G}_n , in Eq. (2.59) and therefore obtain

$$\mathcal{E} = (\mathbf{I} - \mathbf{G}\mathbf{H}) \phi \mathcal{E} + (\mathbf{I} - \mathbf{G}\mathbf{H}) \mathbf{\Gamma} (U_H - U) \quad (2.60)$$

or alternatively

$$[\mathbf{I} - (\mathbf{I} - \mathbf{G}\mathbf{H}) \phi] \mathcal{E} = (\mathbf{I} - \mathbf{G}\mathbf{H}) \mathbf{\Gamma} (U_H - U). \quad (2.61)$$

The desired transformation of the speed command hypothesis deviation $U_H - U$ to the steady state average state deviation is thus found to be

$$\mathcal{E} = [\mathbf{I} - (\mathbf{I} - \mathbf{G}\mathbf{H}) \phi]^{-1} (\mathbf{I} - \mathbf{G}\mathbf{H}) \mathbf{\Gamma} (U_H - U) \quad (2.62)$$

which has the simple form

$$\mathcal{E} = \mathbf{F} (U_H - U) \quad (2.63)$$

where

$$\mathbf{F} = [\mathbf{I} - (\mathbf{I} - \mathbf{G}\mathbf{H}) \phi]^{-1} (\mathbf{I} - \mathbf{G}\mathbf{H}) \mathbf{\Gamma}. \quad (2.64)$$

In the MM the hypothesized commands in the bank deviate from the actual command value. This command deviation translates into the deviation of the corresponding states from the actual state according to Eq. (2.63). The separation of the states in the bank is therefore dependent on the command separation, the system matrices and the steady state Kalman gain.

The dominance of the Kalman gain in Eq. (2.64) is clearly evident. A simple scalar example will demonstrate the effect. Consider an attempt to estimate a slowly varying constant x defined by the model

$$x_n = ax_{n-1} + U + w_{n-1} \quad (2.65)$$

where w is a process noise $w \sim N(0, \sigma_w^2)$ and a has a positive value close to but less than 1. The observation is defined by

$$z_n = Hx_n + v_n \quad (2.66)$$

where $H = 1$ and v is the observation noise $v \sim N(0, \sigma_v^2)$. If the model

$$\hat{x}_{n|n-1} = a\hat{x}_{n-1|n-1} + U_H + w_{n-1} \quad (2.67)$$

is used for the Kalman filter estimate then, the model mismatch $U_H - U$ will give rise to a steady state position deviation. Substituting $\phi = a, \Gamma = 1, H = 1$ into Eq. (2.62) gives the steady state position deviation

$$E = \frac{1-g}{1-(1-g)a} (U_H - U) \quad (2.68)$$

where g is the positive scalar steady state Kalman gain which depends on the variances ratio of the process and the measurement noise. The deviation, as indicated by Eq. (2.68), will vary from a minimum of 0 (for the highest gain case of $g = 1$) to a maximum of $\frac{U_H - U}{1-a}$ (for the lowest gain case of $g = 0$).

For the MM the ϕ, Γ, H matrices and the allowable range of maneuver commands are assumed known. Under such conditions the only control the MM designer has over the state separation is the Kalman gain. A high gain gives heavy weight to the new measurement which is common to all the filters; this tends to

keep the filters states close together since their differences are not emphasized. A low gain gives higher weight to the different individual channel predictions thus allowing the states to grow apart. The states diverge until their average innovation is large enough to compensate via the Kalman gain for the command mismatch.

An example is given in Fig. 2.5a showing the positions of the two extremes and the center filters in the bank. The Kalman gain (position component) was $G(1) = 0.073$ when the position deviation of the first filter was 1.4km. Fig. 2.5b shows a similar case with higher gain $G(1) = 0.041$. Note that the separation between the first and center tracks is increased to 2.9Km (note the different scale).

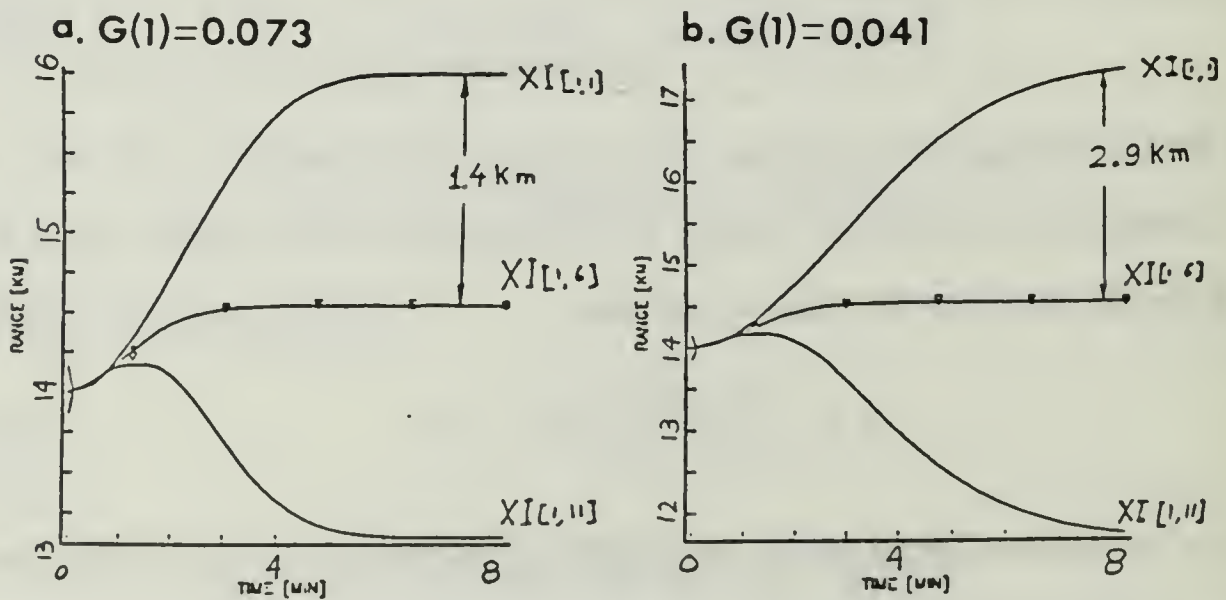


Fig. 2.5. State position separation.

In Fig. 2.6 a 3-D plot showing the weight vector \mathbf{W} as a function of time. A sharp and well defined peak (a) leads to a less noisy and overall better maneuver tracking performance. This is the case if most of the measurements z (Eq. (2.13)) fall within the interval spanned by the state bank \mathbf{XI} , and if the innovation variance σ_I is of the order of the position separation. If many of the measurements fall outside the interval spanned by \mathbf{XI} , as is the case when the gain is too high, then a less well defined peak is formed. Such a case is shown in Fig. 2.6b where the resulting "hesitation" and noisy nature of the weight vector may eventually lead to loss of track.

On the basis of the forgoing discussion, it can be seen that in order to minimize the estimation bias one should take the following actions. First one has to ensure that the state bank spans the expected spread of position measurements. This can be done by tuning the Kalman gain. Secondly one should maintain the center of the hypothesis bank close to the actual command. This can be done by adaptively relocating the command bank center U_c defined as:

$$U_c = \frac{1}{N} \sum_{i=1}^N U_i \quad (2.69)$$

around the estimated command value. Adaptive recentering has not been attempted in previous work with the MM tracking filter.

Trimming the Kalman gain, is done by means of an optimized correction factor \mathbf{D}_u . Athans and Chang [4] refer to the optimization as "more of an art than a science." and Ref. 9 attempts to derive an analytical expression for \mathbf{D}_u^* .

* The argument made there is that each model in the bank is subject to an additional command uncertainty in the interval $\pm \frac{\Delta U}{2}$ around the discrete value. This is of limited validity since the command uncertainty for every channel is over the entire interval $U_{max} - U_{min}$. However the Singer noise component which is added to the \mathbf{D}_u compensates by maintaining a high enough Kalman gain.

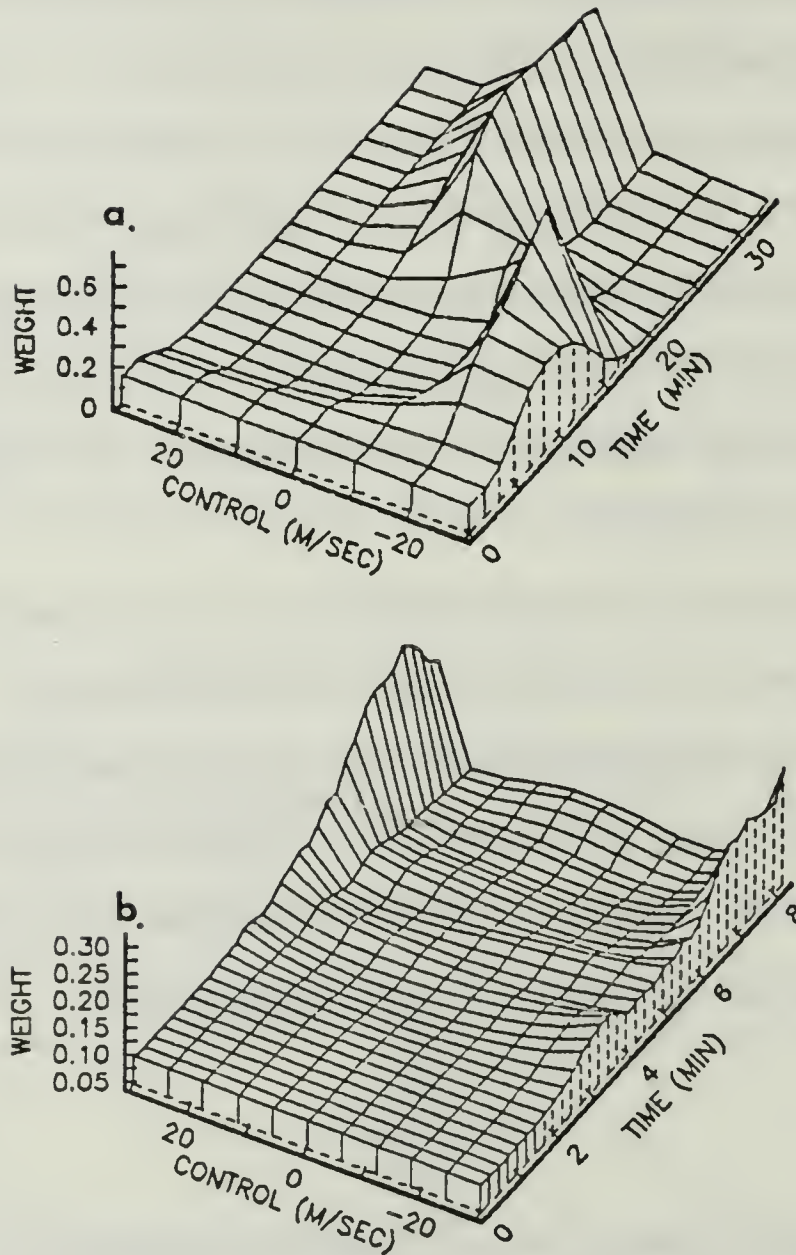


Fig. 2.6. Weight vector history.

Gain control by means of the D_u factor reduces the need for the Singer state component w' , which was devised partially for the same purpose. Our approach, which was found to be more effective is discussed in Section D. Adaptively recentering the command bank, was a more involved procedure than it seem to be at first. The method is also described in Section D.

To complete the discussion Eq. (2.63) is now extended to case of a complete MM state bank with N channels. Recall from Table 2.2 that the state bank matrix has the form

$$\mathbf{XI} = [\mathbf{X}_1 | \mathbf{X}_2 | \dots | \mathbf{X}_N] \quad (2.69)$$

where $\mathbf{X}_1, \mathbf{X}_2, \dots, \mathbf{X}_N$ are the state vectors for the individual filters, and that the command bank vector has the form

$$\mathbf{UI} = [U_1, U_2, \dots, U_N] \quad (2.70)$$

where U_1, U_2, \dots, U_N are the corresponding commands. The state bank deviation matrix defined as

$$\mathcal{E}\mathbf{I} = [\mathcal{E}_1, \mathcal{E}_2, \dots, \mathcal{E}_N] = [\mathbf{X}_1 - \mathbf{X}, \mathbf{X}_2 - \mathbf{X}, \dots, \mathbf{X}_N - \mathbf{X}] \quad (2.71)$$

is given by

$$\mathcal{E}\mathbf{I} = \mathbf{XI} - \mathbf{X} \cdot \mathbf{N} \quad (2.72)$$

where

$$\mathbf{N} = [1, 1, \dots, 1]. \quad (2.73)$$

It follows from Eq. (2.63) that the error for the i^{th} filter is given by

$$\mathcal{E}_i = \mathbf{F}(U_i - U) \quad (2.74)$$

and thus $\mathcal{E}\mathbf{I}$ is also given by

$$\mathcal{E}\mathbf{I} = [\mathbf{F}(U_1 - U), \mathbf{F}(U_2 - U), \dots, \mathbf{F}(U_N - U)] \quad (2.75)$$

$$\mathcal{E}\mathbf{I} = \mathbf{F}(\mathbf{UI} - U \cdot \mathbf{N}) \quad (2.75)$$

namely

$$\mathbf{XI} - \mathbf{X} \cdot \mathbf{N} = \mathbf{F}(\mathbf{UI} - \mathbf{UN}). \quad (2.76)$$

Now if each control U_i is changed by the same amount ΔU , then the change in the entire command bank $\Delta \mathbf{UI}$ is $\Delta U \cdot \mathbf{N}$ and the new command vector will be given by $\mathbf{UI} + \Delta U \cdot \mathbf{N}$. From Eq. (2.63) the corresponding change in the state bank matrix is given by

$$\Delta \mathbf{XI} = \mathbf{F} \cdot \Delta \mathbf{UI} = \mathbf{F} \cdot \Delta U \cdot \mathbf{N}. \quad (2.77)$$

The foregoing discussion implies that for an evenly spaced command the state bank matrix is also evenly spaced along the position speed and acceleration axis, the state spacing ΔX is given by

$$\Delta \mathbf{X} = \mathbf{F} \cdot \Delta U. \quad (2.78)$$

Eq. (2.78) compared very favorably with simulation results (the predicted deviation was within $\pm 0.01\%$ of the simulation result.) and turned out to be very useful in ridding the MM tracker from one of its inherent biases (in Section D).

c. Smoother Order

A first order averager, Eq. (2.26), (2.27), and (2.28) was added to smooth the filter output in order to reduce the output variance. The price paid for the smoothing is a tracking lag error for targets of constant speed [9]. This results from the mismatch between the target model (second order) and the averager (first order). The steady state error E can be derived using the final value theorem

$$x_\infty = \lim_{z \rightarrow 1} \frac{z-1}{z} \mathcal{X}(z) \quad (2.79)$$

where $\mathcal{X}(z)$ is the z transform of x_n . Consider the scalar, constant rate target position x_n given by

$$x_n = U_o \cdot nu(n). \quad (2.80)$$

where $u(n)$ is the unit step function and U_0 is the rate parameter [position units/sample time T], and a smoothing filter of the form

$$y_n = ay_{n-1} + (1-a)x_n. \quad (2.81)$$

The observation z is here assumed to be noise free so that $z_n = x_n$. The smoothing filter produces a lag error E [position units] defined as

$$E_n = y_n - x_n. \quad (2.82)$$

whose value at steady state is sought. The analysis in the \mathcal{Z} domain proceeds as follows. Let $\mathcal{H}_{(z)}$ be the system response and $\mathcal{X}_{(z)}, \mathcal{Y}_{(z)}$ be the \mathcal{Z} transformations of x_n and y_n . Then

$$\mathcal{X}_{(z)} = -z \cdot \frac{d}{dz} [U_0 \cdot U_{(z)}] = \frac{U_0 z}{(z-1)^2} \quad (2.83)$$

$$\mathcal{H}_{(z)} = \frac{1 - az^{-1}}{1 - a} \quad (2.84)$$

$$E_{(z)} = \mathcal{Y}_{(z)} - \mathcal{X}_{(z)} = (H_{(z)} - 1)\mathcal{X}_{(z)} = \frac{U_0 a}{1-a} \cdot \frac{1}{z-1}. \quad (2.85)$$

Applying Eq. (2.79) yields the steady state error

$$E_\infty = \lim_{z \rightarrow 1} \frac{z-1}{z} \frac{aU_0}{(1-a)(z-1)} = \frac{aU_0}{1-a} \cdot \lim_{z \rightarrow 1} \frac{1}{z}. \quad (2.86)$$

and the steady state lag error is thus

$$E_\infty = \frac{a}{1-a} \cdot U_0 \quad (2.87)$$

indicating large errors for heavy smoothing (a close to 1).

In the time domain Eq. (2.81) averages the past estimated value $X(n-1)$ with the current measurement of $x(n)$. This produces an error even for the case of no measurement noise since the position x is different at the two successive time samples. This intuitive understanding of the source of the error led to the development of the improved advancing smoother discussed in Section D.

d. Coordinate Linearization and Decoupling

An important aspect of the coordinate decoupling and linearization is that the target helmsman commands in the decoupled system are attached to a moving coordinate system, namely the target range and cross range. The drawback of such a system is that a (nonmaneuvering) target moving with constant velocity along any straight line other than the line of sight has to be described as maneuvering since its range and cross-range speeds are constantly changing. However in the MM the probability that the command will not change is assumed to be very high (P_r close to 1).

These two opposing assumptions produce an error which is more pronounced at short ranges where range and cross range accelerations are higher. At short ranges the normalized range rate (range rate/range) is also large. This implies that there is a need to update the bearing channel transition matrix more frequently. Under the foregoing condition the advantages of this linearization and decoupling approach are marginal.

A potential remedy to the coordinate linearization problem may be to return to an XY Cartesian system or to adaptively modify the probability transition matrix ϕ to reflect a predicted linear motion. These ideas were not pursued further however in order to concentrate effort on the IH effects of the MP tracking.

e. Measurement Noise

In passive localization, TDOA from the target via different acoustical paths to separate parts of a sonar array are converted to depth, range and bearing information. The process is error prone both in the time delay estimation and in the transformation to target position (range depth bearing). This is one of the major topics addressed in this research and most of Chapter Three is devoted to

this problem. However the noise dependence on range affects the evaluation of the target tracker itself, and so is described briefly here.

The time delay estimation error depends on the signal to noise ratio (SNR) of the received signal. The SNR in turn depends on the transmission loss and therefore indirectly on the range. Thus, the delay noise is *range dependent*.*

In addition, the time delay estimation limits the estimated delay to positive values. An improved noise model is used for the tracker performance evaluation. This noise model is described in the Section D.

D. IMPROVEMENTS AND MODIFICATION

The following modifications of the tracker were introduced to improve it and evaluate its performance with respect to the issues discussed in Section C.

- An adaptive instead of a fixed hypothesis bank was incorporated.
- A second instead of a third order system was incorporated in the model. The second order system was demonstrated as sufficient for the target when the steady state Kalman gain is adjusted by the correction factor D_u (see eq. (2.16), (2.17), (2.20)).
- A new second order smoothing algorithm was developed and used to replace the first order smoother.

The modified tracker was than evaluated with

- A more realistic range dependent and nonnegative noise.
- Emphasis on range bearing coordinate decoupling and linearization at short ranges.

* With this limitation in mind the disadvantage of the coordinate linearization, discussed above, at short ranges is further emphasized.

1. Adaptive Command Bank

a. Concept

The problem addressed by this modification is the bias error arising from a hypotheses bank which is not symmetric around the actual command. A possible solution to this problem, cited earlier, is to adaptively recenter the hypothesis bank around the actual value. Recall that when the center U_c of the command bank (referred to here as “the center” for convenience) is equal to the value of the true command, this bias is removed. Since the actual value of the command is not known, our algorithm uses the command estimate U_{op} instead. The main idea is therefore to periodically recenter the command bank around the estimated command value.

A straightforward implementation is to average the estimated control over a time interval long compared to the system and the observer time constants and to feed back the average as the new center. Specifically the difference between the estimated command U_{op} and the center U_c is averaged using an autoregressive filter to produce the center deviation U_{cd} .

$$U_{cd\ n} = aU_{cd\ n-1} + (1 - a)(U_{op\ n-1} - U_{c\ n}) \quad (2.88)$$

This average value is used to dynamically shift the center and the complete command bank.

$$U_{c\ n+1} = U_{c\ n} + U_{cd\ n} \quad (2.89)$$

$$UI_{n+1} = UI_n + U_{cd\ n} \quad (2.90)$$

Although this method was implemented, its performance was poor for the following reason. The combination of the command hypothesis UI and the weight vector

\mathbf{W} is a discrete description of the command probability distribution estimated by the Bayesian recursion (Eq. (2.23)). Updating the command hypothesis vector but keeping the weight vector unchanged effectively modifies the command distribution and disrupts the recursive command estimation.

Further, the command bank yields, over some time, a corresponding bank of hypothesized states in the form of the matrix \mathbf{XI} which based on Eq. (2.76) is

$$\mathbf{XI} = |\mathcal{E}_1 \mathcal{E}_2 \dots \mathcal{E}_N| + \mathbf{X} \cdot \mathbf{N} = \mathbf{F}(\mathbf{UI} + U \cdot \mathbf{N}).$$

Different states correspond to the new updated command bank. Shifting the command hypotheses bank introduces an undesirable transient in the state vectors of the filters. This transient seriously degrades the tracking. Furthermore, the feedback of the state vector's transient into the recursive command estimation process (Eq. (2.22) and (2.23a)), may lead to instability of the entire tracker.

It is clear therefore that updating the command bank center alone disrupts the recursive estimation process unless there is a corresponding update of the weight vector \mathbf{W} and the state matrix \mathbf{XI} . In simulation recentering the command bank without updating the weight vector and the state matrix resulted in complete divergence of the command estimate.

b. Complete Model Updating

An alternative approach was devised where the complete model was updated and the instability was eliminated. The method was as follows:

- The update was restricted to occur at discrete events in time when the averaged deviation of the center U_c from the estimate U_{op} reached a preset threshold.
- The commands and the command center were restricted to take on a set of discrete quantized equally-spaced values. Updating was done by shifting the entire bank up or down one position.

- The complete model including command and state banks, and the weight vector were updated.

The time discretization was intended to prevent the continuous dynamic feedback which led to instability. The time constant used for the exponential command deviation averaging was set larger than both the system and the MM estimator time constants. This was done to ensure complete transient recovery from one update before another update is allowed.

The model update was implemented in a cyclic manner. The least likely filter in the bank, i.e., the one corresponding to the command furthest away from the estimated command, is dropped. A new and more likely command is added at the closer end of the bank. The probability of the new channel is initially set to that of the one that is dropped, so that the total probability $\sum_{i=1}^N W_i$ is kept equal to 1. If the update takes place at time k then

$$UI_{k+} = UI_{k-} \pm \Delta U \cdot N \quad (2.9i)$$

where the subscripts k^- and k^+ represent the control prior to and after the update and the sign of ΔU depends on the sign of the averaged center deviation U_{cd} (Eq. (2.88)).

A block diagram of the modified MM is shown in Fig. 2.7 and Fig. 2.8 shows an example of a model update process assuming the update takes place at time index $n = k$. The variables at time k^- , i.e., just prior to the update, are shown in Fig. 2.8a; the variables immediately after the update (time k^+) are shown in Fig. 2.8b. Prior to the update the bank is centered around $U_c = 0$ and spans the interval -15 to $+15$ [m/sec] as shown along the horizontal axis. The second (lower) horizontal axis represents the first component (position) of the state vectors of all filters in the bank (this is the first row of XI) before the

update. This spans the interval 8.5 to 11.5 km. During the update the first hypothesis $(U_1)_{k-} = -15$ m/sec is dropped and a new hypothesis $(U_7)_{k+}$ is added at +20 m/sec with a corresponding state position $\mathbf{XI}[1, 7]_{k+}$ at 12 km (Fig. 2.8b). The weights W_i (conditional probabilities) for all the filters except that of the new one are shifted one position. This is done in order to maintain the correspondence with the hypotheses. The new filter assumes the weight of the filter that is dropped (0.01 in the example shown). The command bank is now properly centered around 5 m/sec. The command estimation transient is shown in Appendix C to be given by

$$\hat{U}_{transient} = \mathbf{N} \Delta U (W_1)_{k-} \quad (2.92)$$

For the specific case in Fig. 2.8 this transient is therefore

$$\hat{U}_{transient} = 7 \cdot 5 \cdot 0.01 = 0.35 \text{m/sec. .}$$

This minor transient is further smoothed by the output smoother and its effect on the output U_{op} is negligible.

The command in the bank and the center U_c are restricted to the evenly spaced discrete values. The center update is further limited to a one position shift up or down from its current position on the discretized scale. The command bank update is thus implemented by means of the linear shift given by Eq. (2.91). Since the states of the bank are also evenly spread over the state scales (position, speed and acceleration). The corresponding update of the states matrix \mathbf{XI} can thus be implemented by means of a linear shift as follows

$$\mathbf{XI}_{k+} = \mathbf{XI}_{k-} \pm \Delta \mathbf{X} \cdot \mathbf{N} \quad (2.93)$$

where $\Delta \mathbf{X}$ is the constant vector $\mathbf{F} \cdot \Delta U \cdot \mathbf{N}$ (Eq. (2.78)). *The complete model is thus updated by a simple one position shift.* The shift is linear for the command

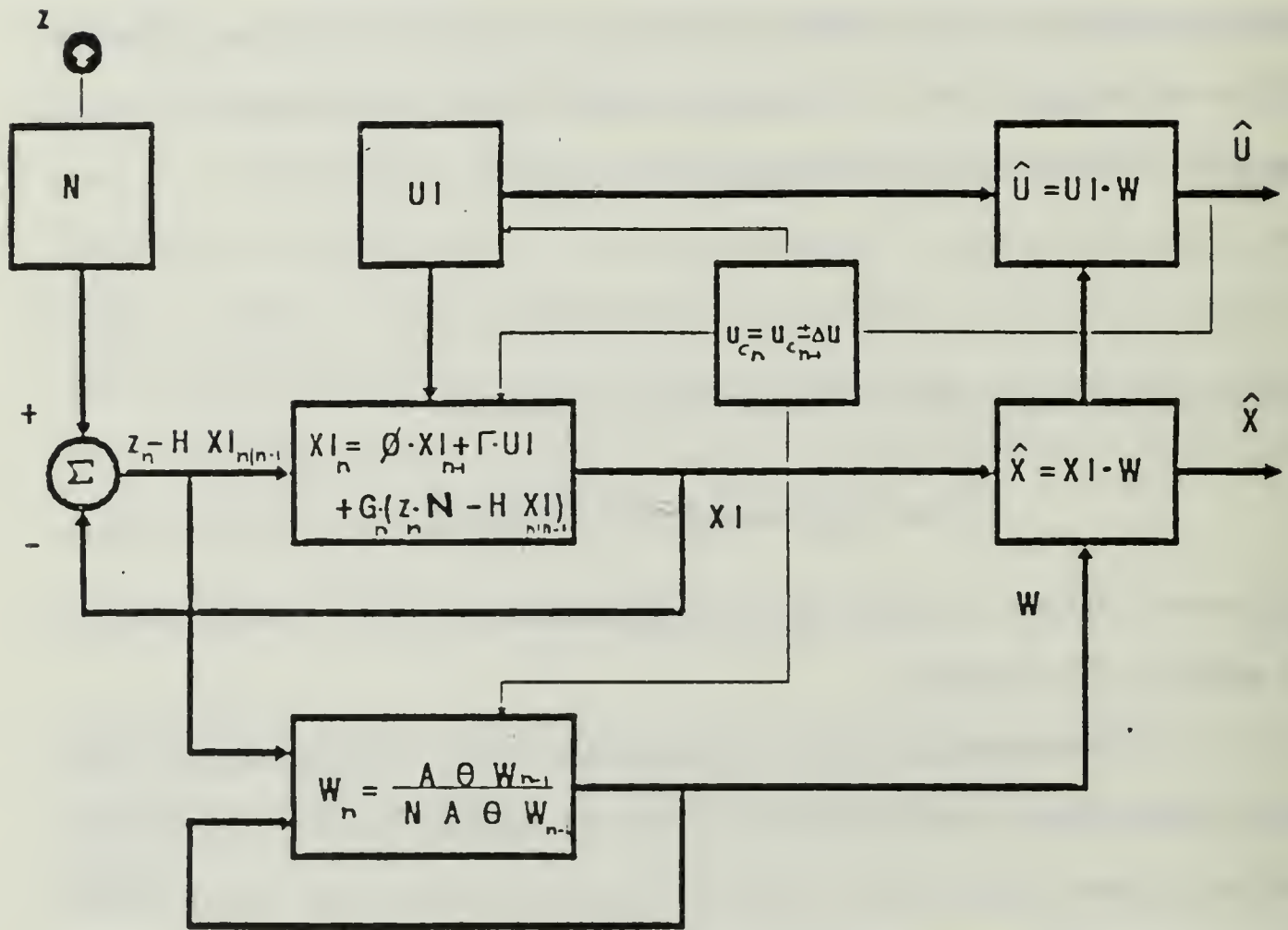


Fig. 2.7. Model update block diagram.

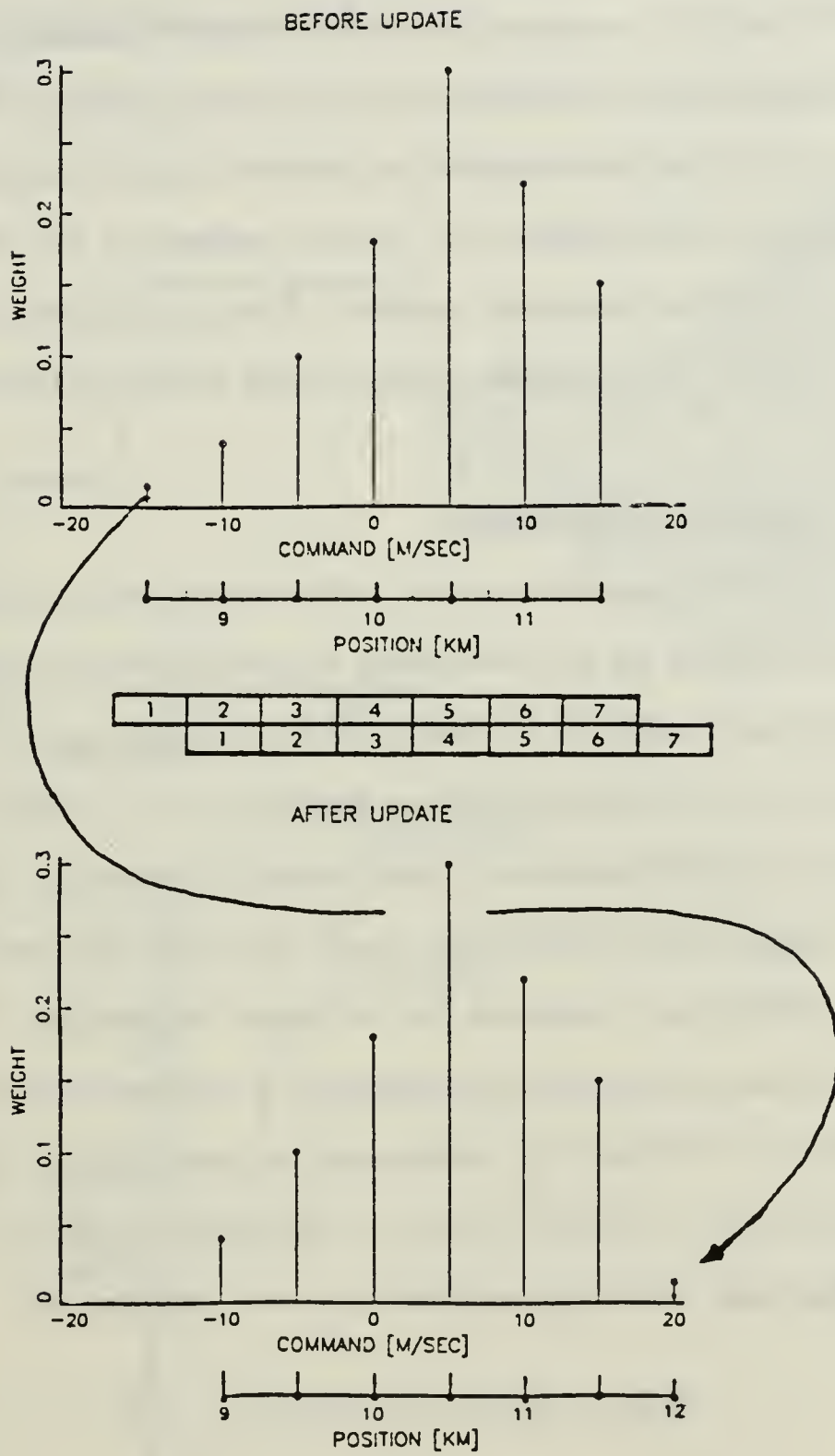


Fig. 2.8. Complete model update.

UI and the state XI, and circular for the weight vector W. The simplicity of the model update procedure (which requires no computation) resulted from the constraint of the center U_c to assume values on the discrete command scale.

Tracking with the complete adaptive model (updating UI, W and XI) is shown in Fig. 2.9. Notice the command and position biases developing just prior to the update 2.9c which is reduced by the two updates at the 18th and 35th minute, and the almost unnoticeable transient. Further persistence of the same target motion would lead to additional updates which would eventually reduce the bias completely.

2. Second Order Target Model

In Eq. (2.8) the second order target model was augmented to a third order model in order to account for the uncertainty in the maneuver command. Practically this augmentation effected the tracking by increasing the error covariance matrix P which in turn increases the Kalman gain (Eq. (2.14)). Since the Kalman gain is so critical in the MM estimator it is additionally trimmed by the factor D_u .

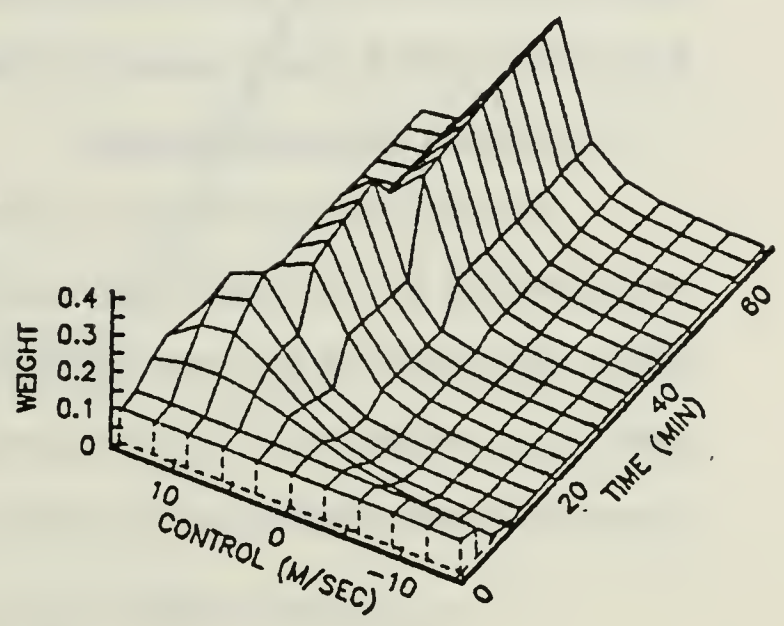
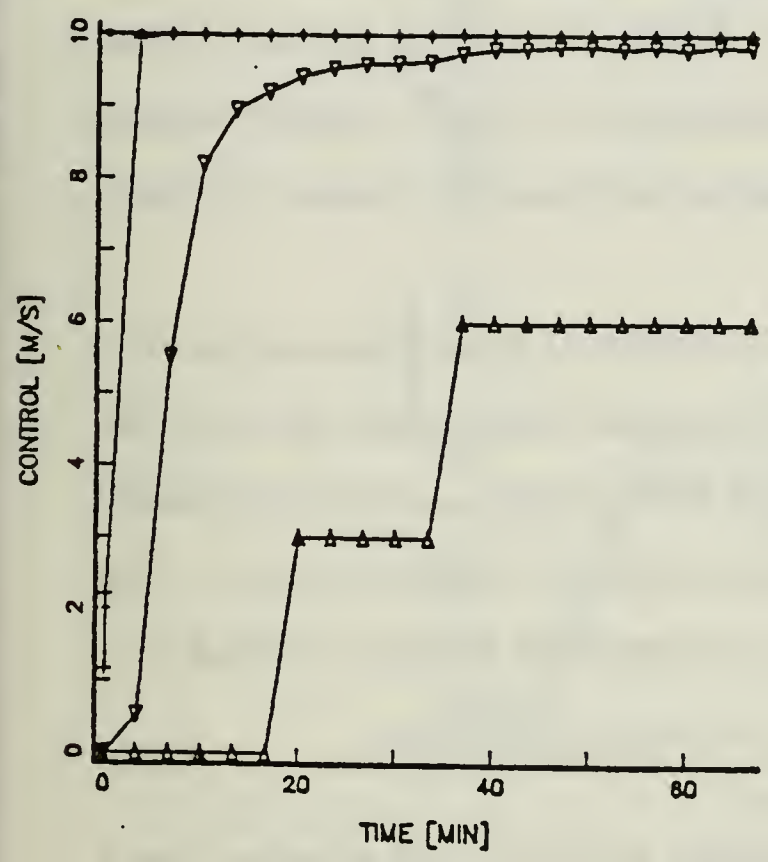
In the original third order Singer model the third state variable w was the only state variable that accounted for the target acceleration. In the MM the command (and the corresponding acceleration) is separately estimated as the independent state U . With both the acceleration estimate and the Kalman gain handled otherwise the use of the third state w is redundant and can be eliminated. Elimination of this state results in the following second order model

$$\mathbf{XI}_2 \mathbf{H}_2 = \phi_2 \mathbf{XI}_2 \mathbf{H}_2 + \Gamma_2 U_{n-1} \quad (2.94)$$

Where $\mathbf{XI}_2 \mathbf{H}_2$ and Γ_2 are the first two rows of XI, H and Γ respectively, and ϕ_2 is the 2×2 upper left block part of ϕ (see Eq. (2.15)). This configuration will save computation time and simplify the gain adjustment procedure.

ACTUAL: CONTROL • SPEED +; ESTIMATED CONTROL ▽ CENTER Δ

ADAPTIVE WEIGHTS



RANGE ERROR

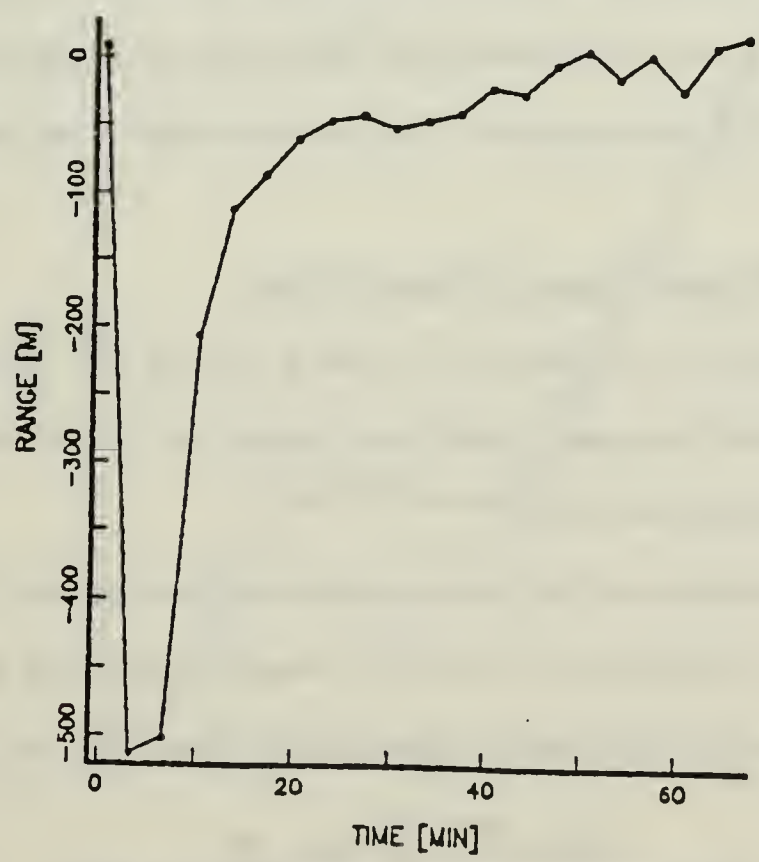


Fig. 2.9. Tracking of an updating model.

Fig. 2.10 compares the tracking of a third order model with steady state Kalman position gain $G[1] = 0.041$ to the tracking of a second order model with practically the same position gain ($G[1] = 0.042$). The gain of the second order model is controlled by σ_u which affects the gain via $D_u = \Gamma\sigma_u^2\Gamma^T$. The performance of the two models is similar except the third order system has a larger overshoot.

3. Second Order Smoother

An improved second order smoother referred to as an *advancing smoother* was introduced [25] in order to reduce the constant speed target lag error (Eq. (2.75)). The basic idea is to average the new filter output $\hat{x}_{n|n}$ with the predicted point $\hat{x}_{n|n-1}$ rather than with the previous estimated position $\hat{x}_{n-1|n-1}$. The current estimated speed is used to generate the predicted position according to

$$(\mathbf{X}_{op})_n = a \cdot [1, T, 0] \cdot (\mathbf{X}_{op})_{n-1} + (1 - a)[1, 0, 0]\hat{\mathbf{X}}[1]n. \quad (2.95)$$

If carried out to the full extent, this principle would turn the smoother into a Kalman filter by itself. The need for this additional smoothing, which is usually handled by means of a reduced Kalman gain, results from the optimizing the gains to meet the overall MM requirements. This forces the additional external smoothing.

4. Improved Measurement Noise Model

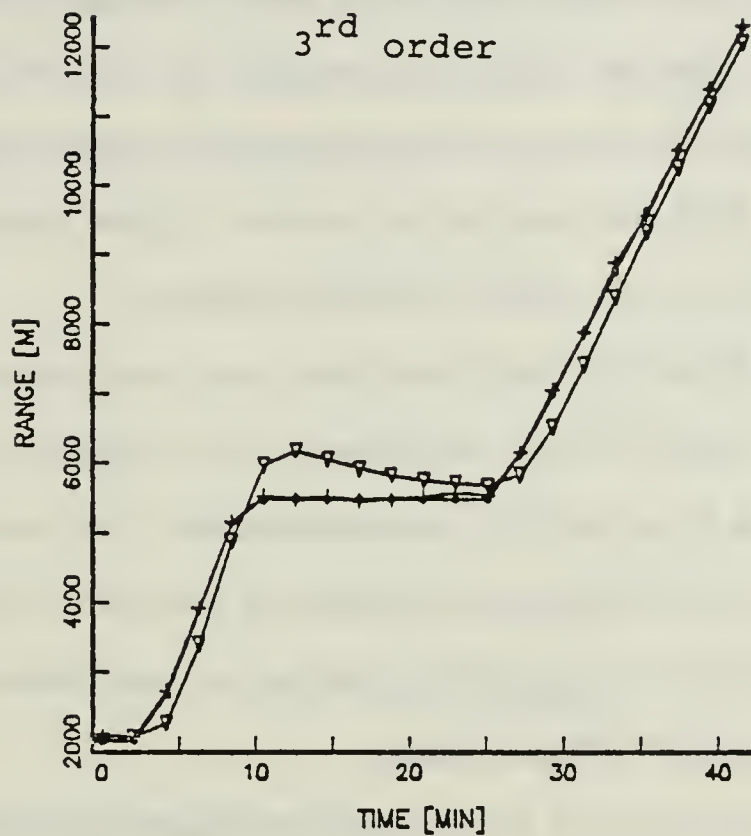
A range dependent, nonnegative noise is used in this simulation in place of the range independent normally distributed noise used in past work.

a. Dependence on SNR

The dependence of the delay estimation noise standard deviation (STD), on the range, via its dependence on the SNR, was modeled here in two ways. In the first model the range dependence is lumped into the following equation.

$$STD_i(R) = STD_{i_0} \cdot R^p \quad (2.96)$$

POSITION:ACTUAL •, MEASURED +, ESTIMATED ▽



POSITION:ACTUAL •, MEASURED +, ESTIMATED ▽

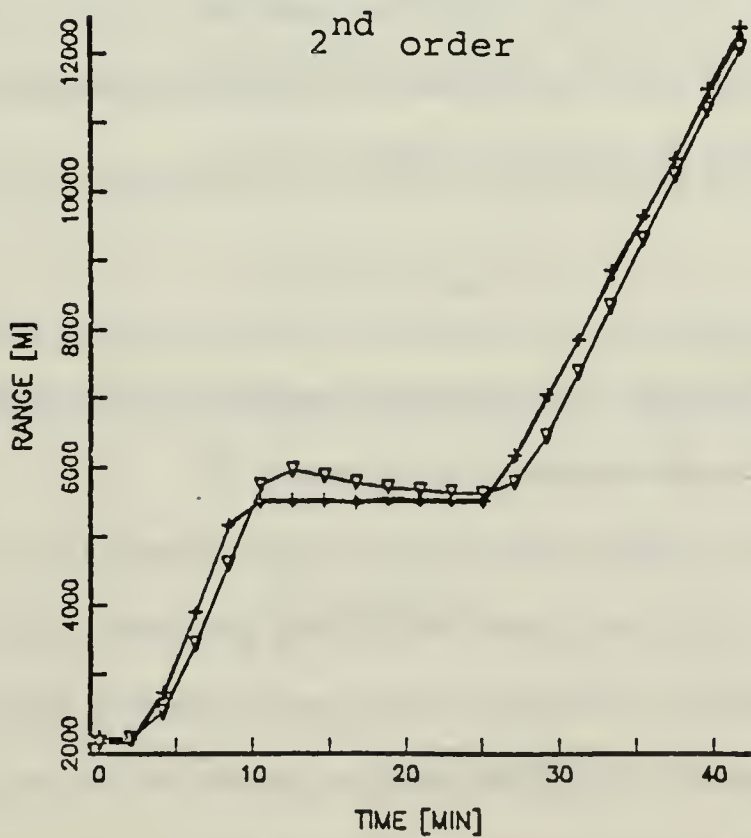


Fig. 2.10. Second order model tracking.

where STD_{i_0} is the i -th TDOA error initial standard deviation at 500 m from the source, and p is the delay noise range power factor which depends on propagation loss. The variable p takes on values in the range of 1 to 3. A low value for p ($p = 1$) corresponds to a high SNR and cylindrical propagation while a higher value ($p = 2$) corresponds to low SNR and spherical propagation. Higher p values corresponding to increased loss due to ray bending were not considered.

In the second model, a more recent and detailed description was used based on Ref. 14. Here the exact dependence of the variance on the bandwidth, the observation time T and the SNR was implemented. The parameters of the first simplified noise model (STD_0 and p) were set to provide an overall similar noise variance which is similar to the results of the second noise model.

b. Nonnegative Time Delay

Another feature of the time delay estimation for a single receiver is the inability to distinguish a leading signal replica from a lagging one. This results from the symmetry of the autocorrelation function (ACF) of real signals. The nonnegative time delay effect was simulated by applying the absolute value operator to the time delay after the noise was added. That is

$$\tau_{i\ m} = |\tau_i + v_i| \quad (2.97)$$

where $v_i \sim N(0, STD_i^2(R))$. This operation produces a bias primarily for $\frac{\tau_i}{STD_i(R)} < 1$, which is also discussed in Appendix D.

After the addition of the noise the simulated TDOA undergoes a non-linear inversion to depth and range which also produces a bias. The bias was studied for the idealized, homogeneous and space invariant delay noise, by Moose in Ref. 11. Investigation of this error and its correction for the IH case, and the means to account for it are discussed in Chapter Four.

c. Depth Range and Bearing Noise

When the filter was evaluated by itself (without the prefilter) noise was added to the depth and range measurement directly. Normally distributed range dependent noise was used such that

$$D_m = D + v_d \quad (2.90)$$

$$R_m = R + v_r \quad (2.99)$$

where

$$v_d \sim N(0, STD_r^2(R)) \quad (2.100(a))$$

$$v_r \sim N(0, STD_d^2(R)) \quad (2.101(b))$$

and the standard deviations given by

$$STD_d(R) = STD_{d_0} \cdot R^{p_b} \quad (2.101(a))$$

$$STD_r(R) = STD_{r_0} \cdot R^{p_b} \quad (2.101(b))$$

with STD_{d_0} STD_{r_0} being the initial STD at 500 m and p_b the range dependence factor.

Range dependent noise was added to the bearing channel as well in order to maintain a consistent uniform simulation. The bearing measurement is thus

$$B_m = B + v_b \quad (2.102)$$

where

$$v_b \sim N(0, STD_b^2). \quad (2.103)$$

The bearing error standard deviation used here is given by:

$$STD(R)_B = STD_{b_0} \cdot R^{p_b} \quad (2.104)$$

where STD_{b_0} is the bearing error standard deviation at 500 m from the source.

E. SIMULATION

1. Model Description

The simulation model was designed to evaluate the overall MP tracker performance, both in the idealized homogeneous case and later in the realistic and *IH* environment (Chapter Four). The following were set as subgoals for the design:

- Support of a multilevel system evaluation starting from the individual algorithm up to the complete integrated system.
- Provide a detailed evaluation of the 3-D maneuvering target tracker performance with emphasis on the 3 axis integration and the tracker modifications.
- Support of a gradual departure from the idealized homogeneous MP configuration towards the more realistic *IH* case. The transition includes both the simulated *IH* measurement and the algorithm designed to deal with this distortion. This again is in support of Chapter Three.

In order to maintain a consistent and unified simulation environment the model was designed to meet all of the above subgoals by optional use of its various components. The model is discussed here in its entirety; however the details of some of its components are addressed in the following chapters.

A block diagram of the simulation model is shown in Fig. 2.11. The simulation proceeds as follows. Depth, range and bearing target position D, R, B is generated by the scenario generator. The depth and range are converted to TDOA τ_1, τ_2 by the MEDIUM. Noise generated by the NOISE module is added to the TDOA to form the measured τ_{1m}, τ_{2m} which are fed to the PREFILTER. The

prefilter performs a functional inversion to compute the depth and range measurements D_m R_m . Noise is also added to the bearing to simulate a realistic bearing measurement B_m . The TARGET TRACKER uses the three noisy measurements to produce a 3-D target estimate. The estimate includes position R_{op} , B_{op} , rate R_{op} , B_{op} and command $U_{r op}$, $U_{b op}$, for the range and cross range axis, and position D_{op} for the depth axis. The noisy measurements and the tracker estimates are compared to the output of the scenario generator to produce the measurement and estimation errors. Details of each of the blocks are described below.

The SCENARIO GENERATOR contains a model for both the target and its pilot. It includes the target dynamics (Eq. (2.10)) as well as a prescribed target trajectory and it outputs the target position in depth, range, and bearing. Three different types of pilots were programmed.

Pilot 1 describes the target motion by an initial state and a set of discrete and independent sequences of maneuvering commands along each of the three axis.

Pilot 2 is similar to Pilot 1 except it provides a continuous gradual change of the maneuvering command.

Pilot 3 prescribes a target moving along a straight horizontal line with constant speed (Eq. (2.8)). As discussed in Section C this target will be seen as maneuvering by a cylindrical coordinate tracker.

The MEDIUM converts the target depth and range coordinates to time delay differences τ_1, τ_2 (or t_1, t_2). It includes a model for the effects of the medium, the receiver, and the noise. Two groups of models were programmed, namely the homogeneous group and the inhomogeneous group described below.

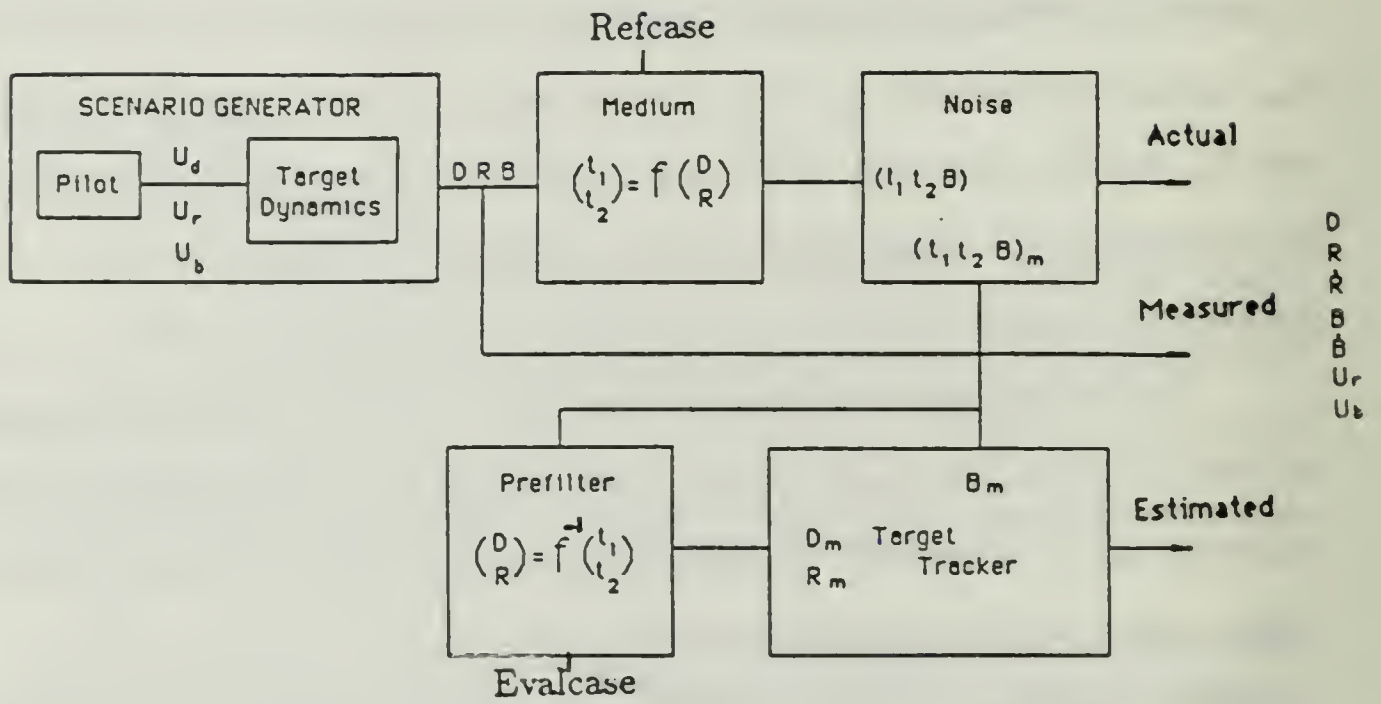


Fig. 2.11. Simulation block diagram.

The homogeneous group.

Medium 1 This is a bypass mode where the depth and range are used directly, without the conversion to time delays and back to depth and range. This mode is used to evaluate the MM tracker by itself.

Medium 2 The approximate formulas valid for $R \gg D$, [Ref. 9]

$$\tau_1 = \frac{2D_0(D_0 - D)}{RC} \quad (2.105a)$$

$$\tau_2 = \frac{2(D_w - D_0)(D_w - D_0 + D)}{RC} \quad (2.105b)$$

were used for the direct function.

Medium 3 The exact closed form analytical expression of time delays as function of depth and range derived by Hassab (Eq. (1.1)) were used here. The implied assumptions here, besides straight line propagation, are that the delays are perfectly resolvable and can be associated with their corresponding paths.

The inhomogeneous group.

Medium 4 This is the only medium that was implemented in the group. Here the three assumptions implied above were removed and an IH medium with finite resolution and non-associable time delays is generated. The theory and implementation of Medium-4 are the subject of Chapter Three. TDOAs for the realistic IH medium are noted as t_1, t_2 .

The NOISE models were used for the TDOA measurements. They were noise type (NT) one and two. NT 1 used Eqs. (2.96) and (2.97). NT 2 used Eq. (2.96) and the more elaborate noise model which provides the STD_i as a function of range and the target signal to noise ratio at range of 1 m (SNR₀). The model and the parameters it uses are described in Appendix D.

When no medium and prefilters were used, noise was added directly to depth and range using Eq. (2.98) and (2.99). Noise was also added to the bearing according to Eq. (2.102).

The PREFILTER converts the noisy TDOA estimates transforming them to depth and range. This is done by inverting the nonlinear direct function. Six different prefilters were designed and grouped into two groups: homogeneous and inhomogeneous prefilters.

Homogeneous prefilters.

Pre-filter - 1 This is the bypass case where no functional inversion is done since the inputs are depth and range, corresponding to medium 1.

Pre-filter - 2 This uses the following approximated relation

$$D = D_0 - \frac{\tau_1 D_w}{\tau_1 + \frac{D_0}{D_w - D_0} \tau_2} \quad (2.106a)$$

$$R = \frac{2D_0 D_w}{C \left(\tau_1 + \frac{D_0}{D_w - D_0} \tau_2 \right)} \quad (2.106b)$$

valid for $R \gg D$ corresponding to medium-2 [Ref. 9].

Pre-filter - 3 This is the exact analytic closed form relation of Eq. (1.2) corresponding to Medium 3.

Inhomogeneous prefilters.

Pre-filters - 4,5,6 These correspond to the inhomogeneous medium, with finite TDOA resolution and non associable delays of medium 4. These again are discussed further in Chapter Three.

The TRACKER uses the measured depth, range and bearing as inputs for the 3-D maneuvering MM target tracker. Third and second order target models with first and second order smoothers were realized. The command bank was either fixed or adaptive as discussed in Section D.1.

2. Description of the Output Plots

Three main plots are produced as output for each axis of the cylindrical coordinate system; they are the position, the speed and the command plots. When a combination of plots is presented the plot symbol markings are synchronized in

time on all the plots of a given run to provide a means for cross reference between them.

The values of the simulated Runs were recorded and plotted only every fifth sample time to avoid cluttering of the picture. An example of a full sample rate plot (with a point plotted for every sample time period) versus a reduced sample rate (point plotted every fifth sample time) is shown on Fig. 2.12.

The position plots (depth, range, bearing, and X, Y as functions of time) include the true, measured, and estimated positions. The true position is the scenario generator output D, R, B ; the measured position is the prefilter depth and range outputs D_m, R_m and noisy bearing B_m ; and the estimated position is the tracker output D_{op}, R_{op}, B_{op} . Position error plots show the difference between the measured or estimated positions and the true position.

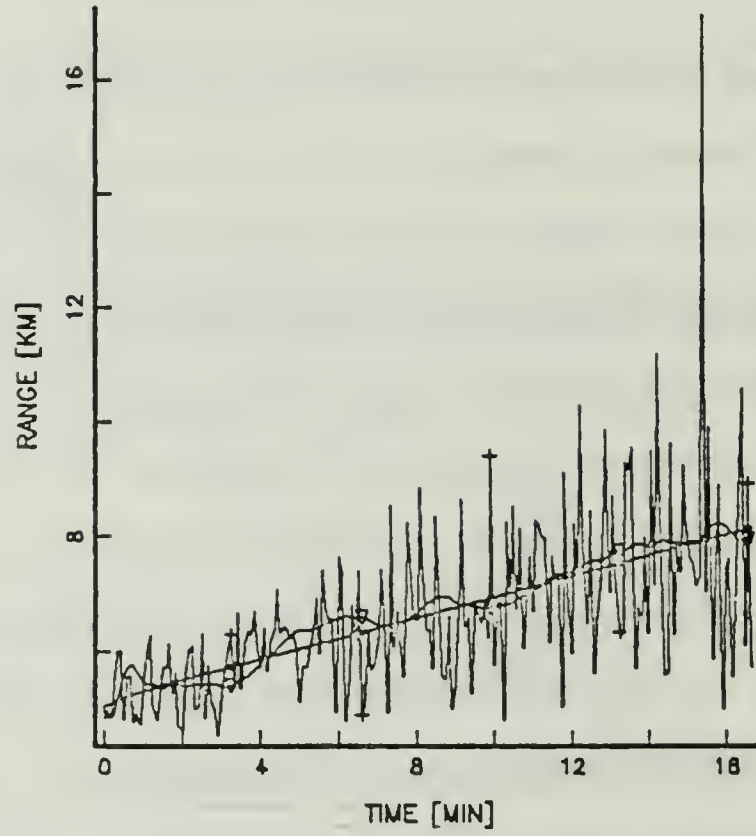
The speed plots present range or cross range speed as a function of time. Various combinations of the actual and estimated speed and speed command are included. The center of the command bank is also shown. Note that when Pilot-3 was used, constant U_x and U_y are applied (Eq. (2.8)). The commands U_r and U_b are not used. The model however does estimate U_r and U_b , which are presented on the plots.

Command weights of the recursive Bayesian estimator are plotted in 3-D plots of the weight vector as a function of time. These plots provide a good measure of the MM adjustments and tracking quality.

3. Parameters Selection

The large number of parameters required for each run dictated a strict and well controlled mechanism of parameter selection. This was especially required for the realistic IH case where there was a large amount of ocean and acoustic data and parameters. The data was divided into the following three categories: target

RANGE:ACTUAL •, MEASURED +, ESTIMATED ▽



RANGE:ACTUAL •, MEASURED +, ESTIMATED ▽

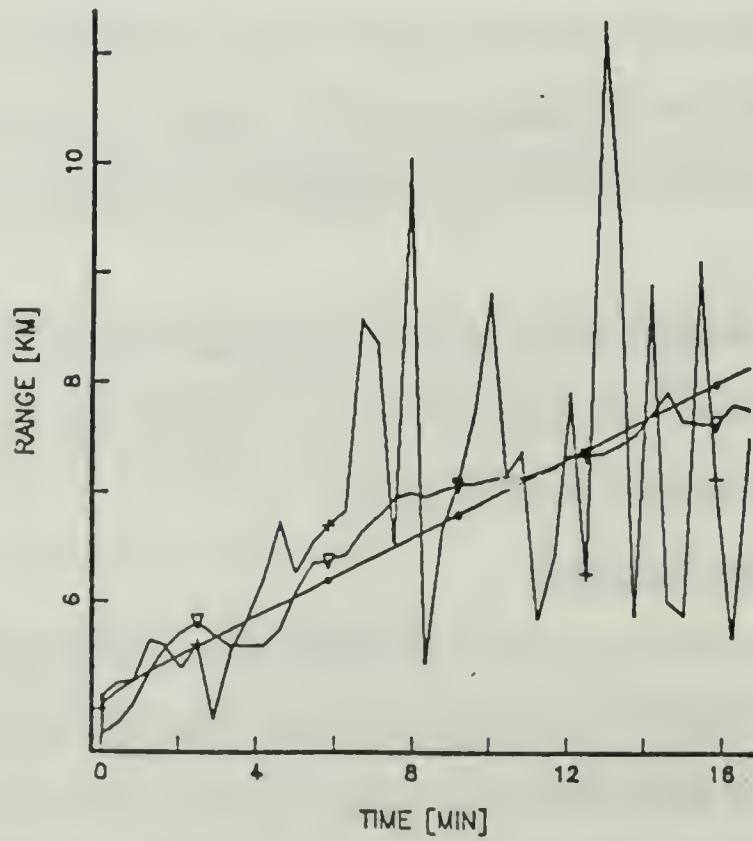


Fig. 2.12. Plot sampling rate.

and scenario; medium and prefilter; MM parameters. The detailed definition of the parameters and their values in the simulation is presented in Appendix D.

F. SIMULATION RESULTS

Five straight line trajectories are presented differing mainly in the noise used.

Run 1 used range dependent depth and range noise without the multipath measurement ($Mdn = 1, Pfn = 1$). The range dependence p was set at 1 and the depth and range error STD at 500 m were set to 1 and 50 respectively.

Runs 2 - 5 used range dependent TDOA noise based on the improved noise model ($NT = 2$) with SNR and p set according to Table 2.3.

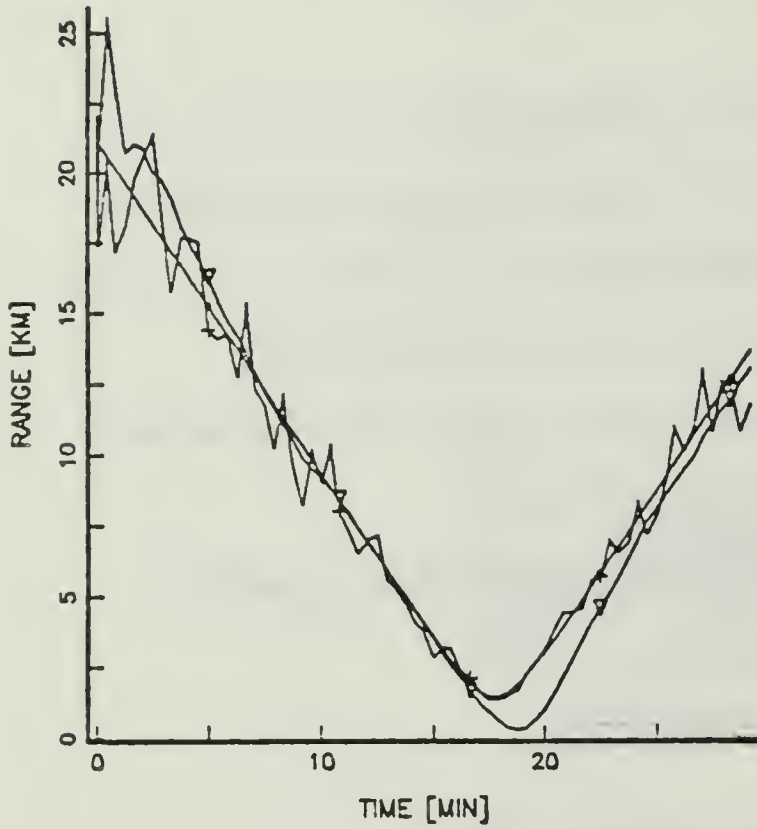
A detailed list of the other parameter settings is included in Appendix E.

TABLE 2.3
NOISE PARAMETERS

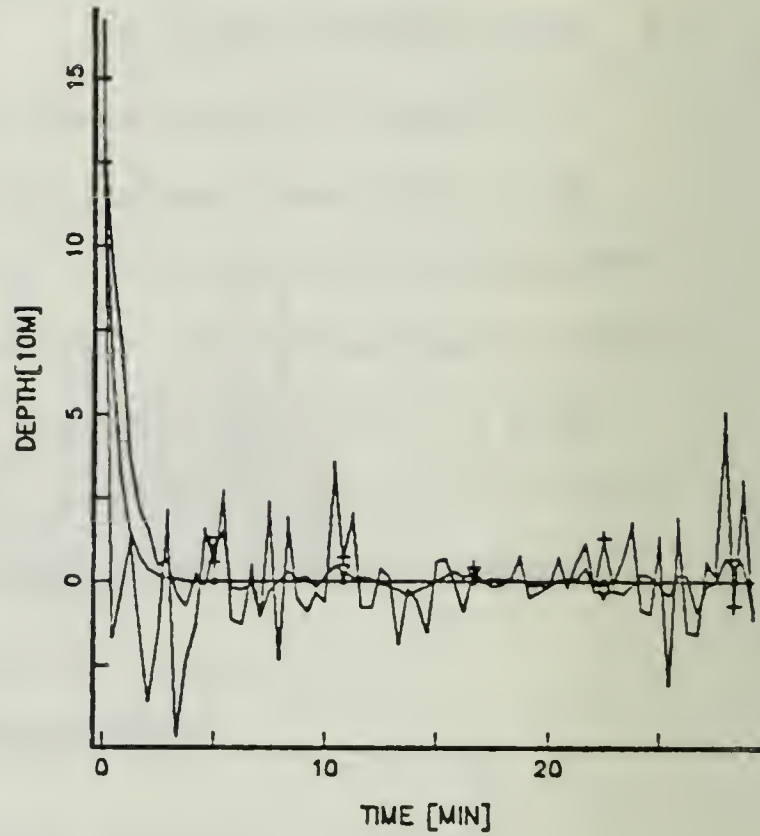
Run	SNR ₀ [dB]	p
2	50	1
3	70	2
4	60	2
5	50	2

Results of Run 1 are shown in Fig. 2.13. Range (a) depth (b) and range error (c) are shown. The increase of measurement and tracking errors with increasing range is seen on all three plots. The very effective noise filtration of the filter is demonstrated in Fig. 2.13c after the completion of the initial transient (around the 12th min and on). The range measurement noise STD which was 1000 m at 10 km was reduced to less than 100 m. Range error reaching 17km develops around the CPA which occurs at the 17th minute at a range of 3 km. The results of this

a. RANGE:ACTUAL •, MEASURED +, ESTIMATED ▽



b. DEPTH:ACTUAL •, MEASURED +, ESTIMATED ▽



c. RANGE ERROR:MEASURED + ESTIMATED ▽

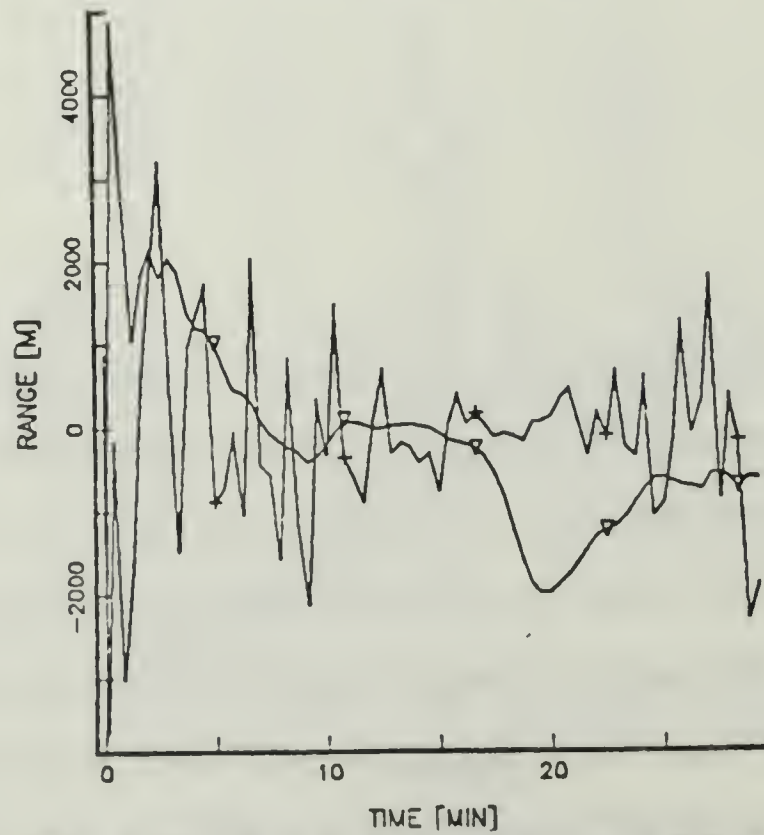


Fig. 2.13. Run-1: Range dependent DR noise.

Run set a reference performance for the MM maneuvering target tracker by itself (without the prefilter).

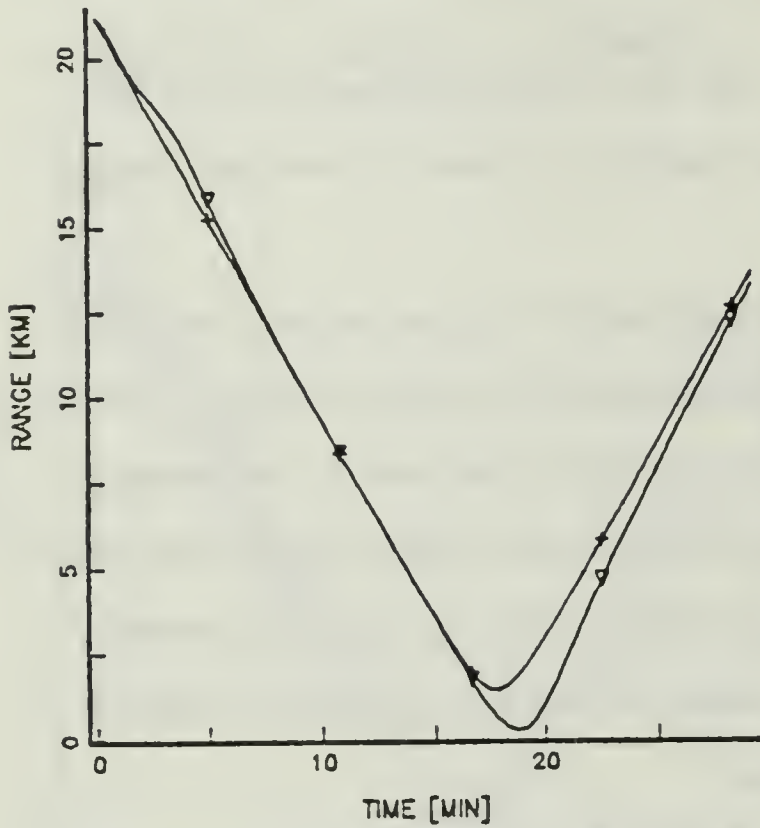
Results of Run 2 are shown in Fig. 2.14. The performance of the MM tracker and the homogeneous medium and prefilter are demonstrated with range dependent TDOA noise.

As can be seen, the cylindrical propagation ($p = 1$) provides very favorable conditions even when the initial SNR_0 is relatively low (50 dB at 1 m range). Note the four model update cycles the MM goes through in response to the changing range rate. Also note the vanishing range tracking error which results from the use of the advancing smoother (25th minute in Fig. 2.14a). Good bearing tracking and the combined horizontal tracking are shown for this run in Fig. 2.15. The XY tracking error at the CPA is clearly evident.

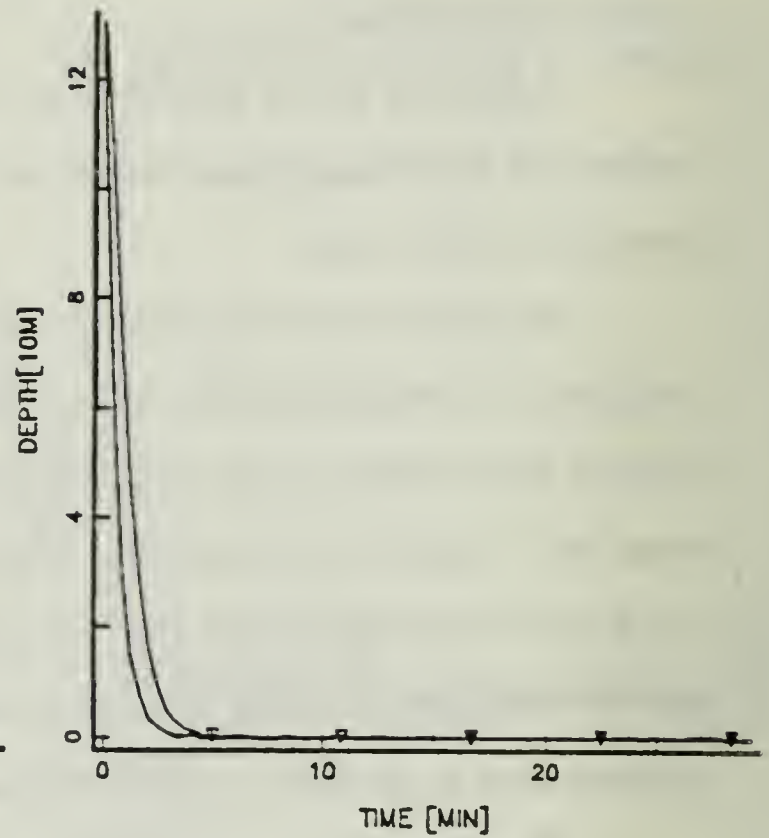
The effect of increasing TDOA noise as a result of decreasing target signal strength (Run-3, 4) is shown in Figures 2.16 and 2.17. The failure of the tracker in Run 4 past the range of 15Km at the 27th minute of this run is also evident in the command estimation plot shown in Fig. 2.17c.

Very noisy TDOA measurements resulting from low SNR_0 and spherical spreading (Run-5) is shown on Fig. 2.18. Large estimation bias which results from the nonnegative effect is clearly seen at ranges larger than 12 km. The depth is also underestimated at these ranges.

a. RANGE: ACTUAL \bullet , MEASURED $+$, ESTIMATED ∇

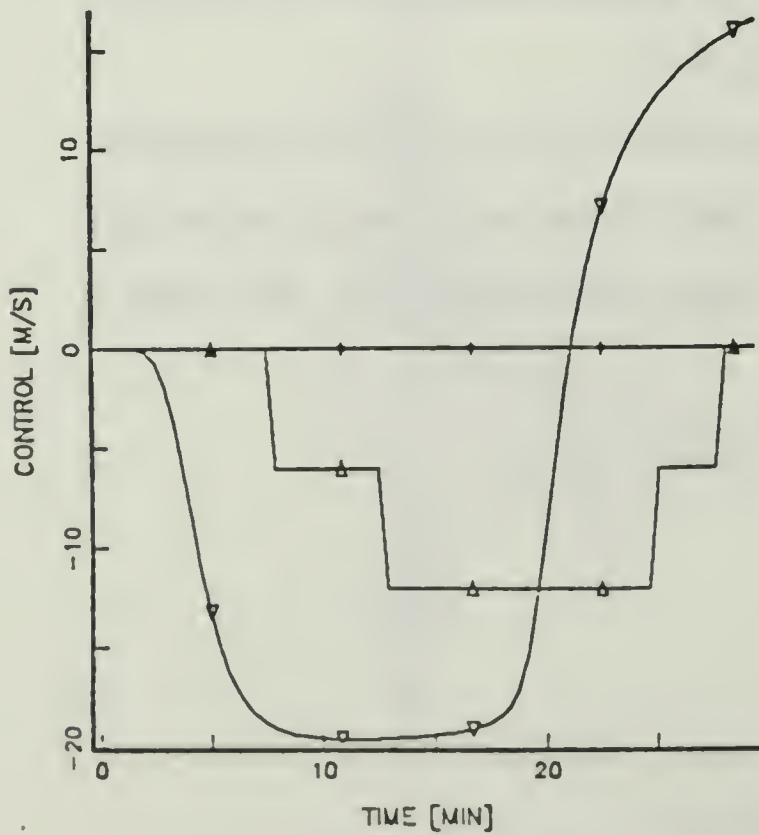


b. DEPTH: ACTUAL \bullet , MEASURED $+$, ESTIMATED ∇



c. ACTUAL: CONTROL \bullet

ESTIMATED CONTROL ∇ CENTER Δ



d. ADAPTIVE WEIGHTS

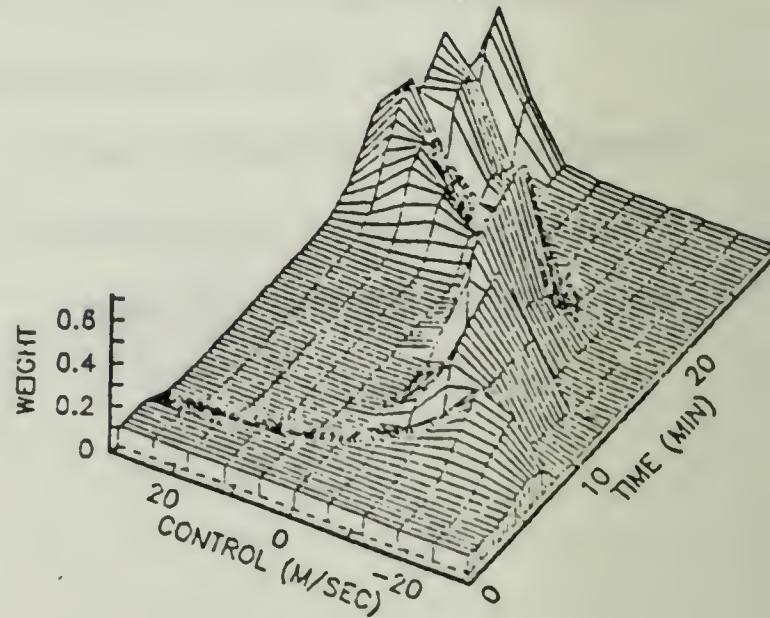
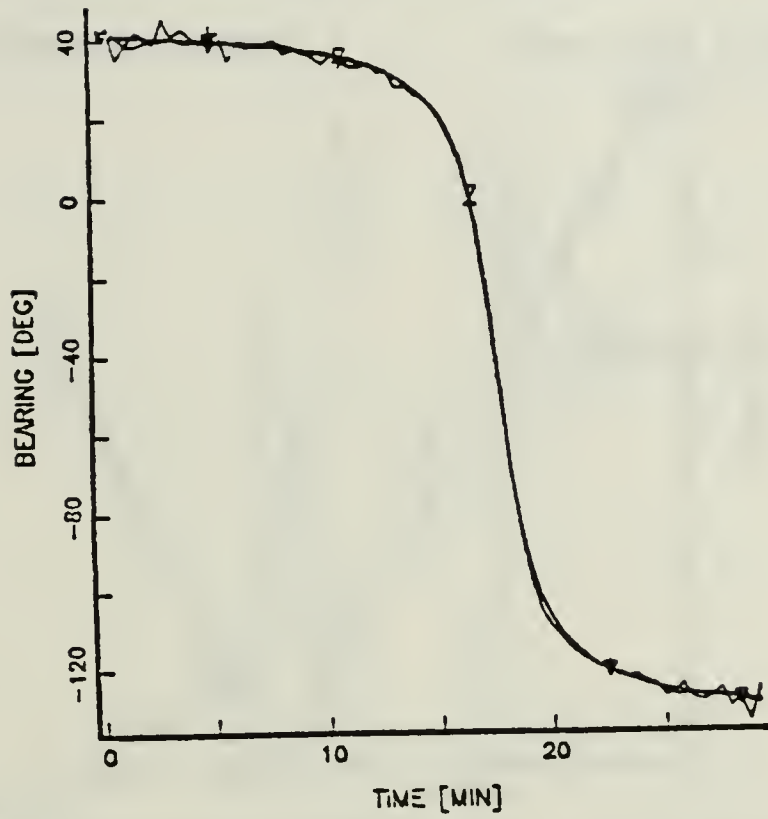


Fig. 2.14. Run-2: Low TDOA noise ($p = 1$).

BEARING: • ACTUAL + MEASURED ▽ ESTIMATE



X-Y: OBSERVER X ACTUAL • MEASURED + ESTIMATED ▽

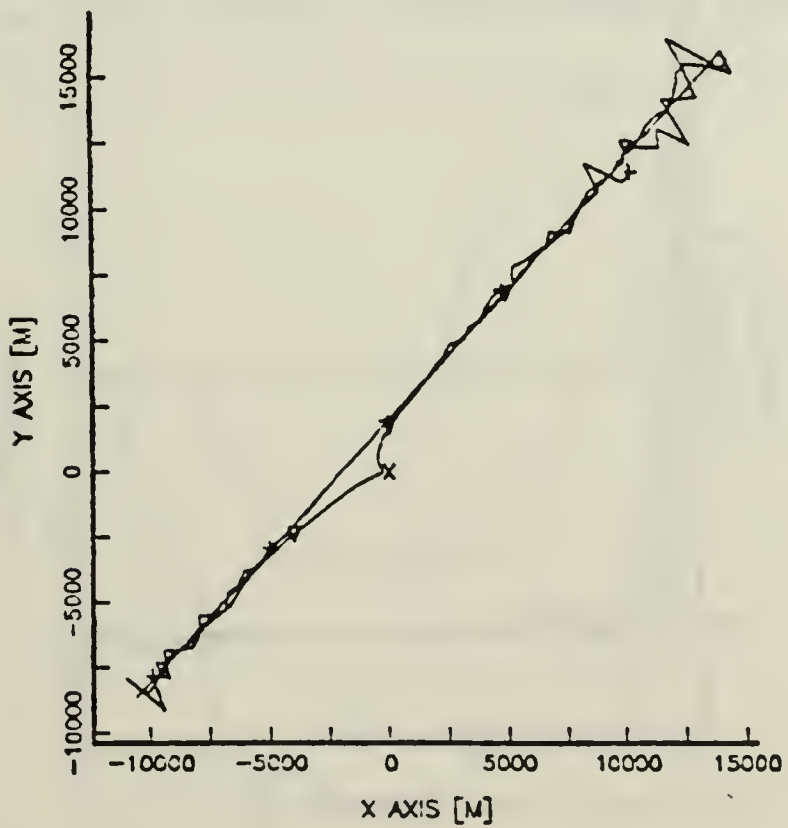
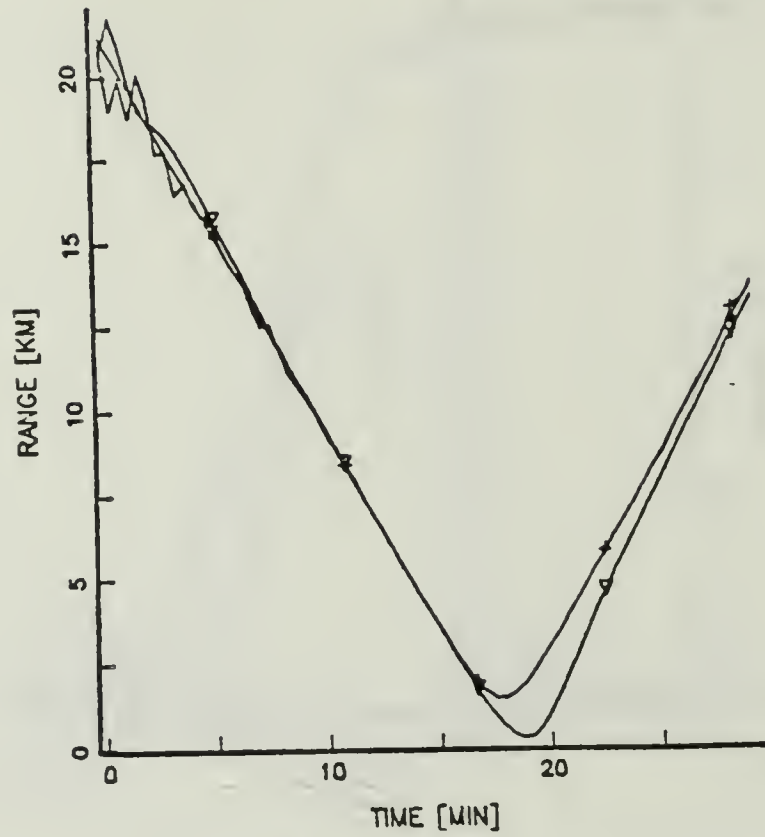


Fig. 2.15. Run-2: Bearing and XY plot.

RANGE:ACTUAL •, MEASURED +, ESTIMATED ▽



DEPTH:ACTUAL •, MEASURED +, ESTIMATED ▽

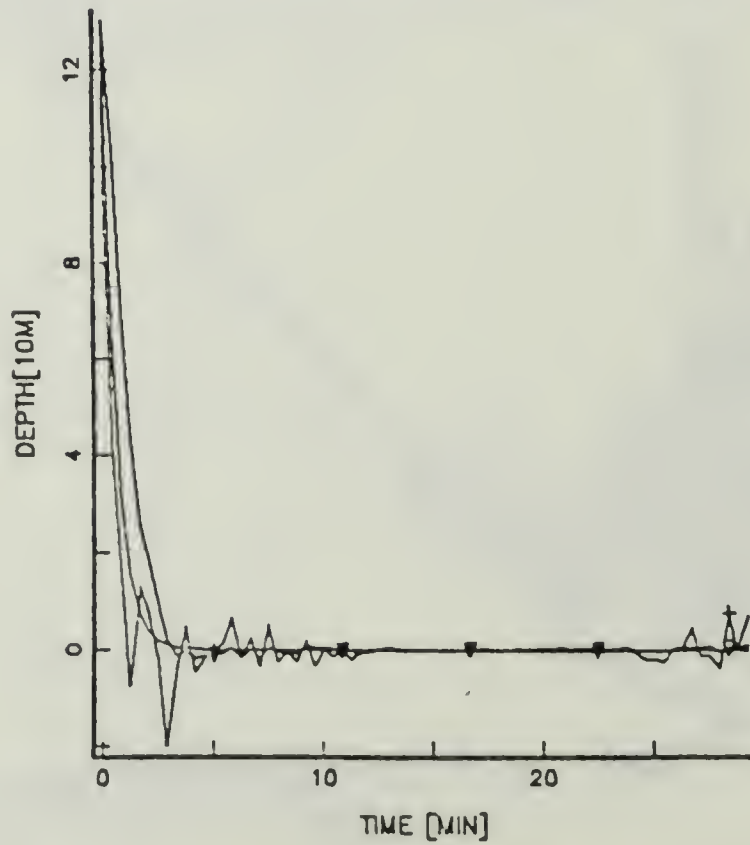
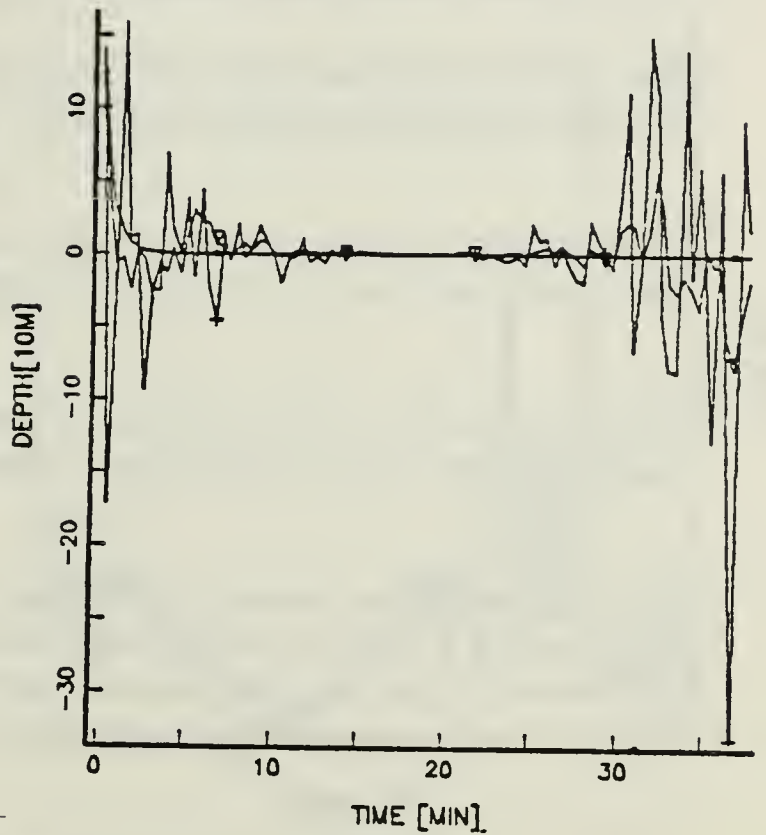
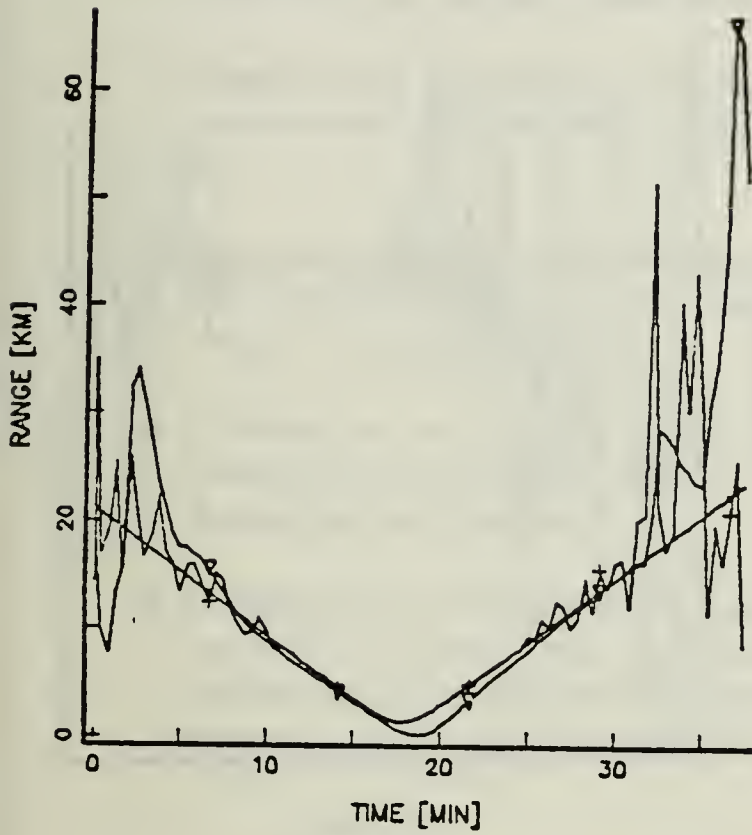


Fig. 2.16. Run-3: Range dependent noise SNR_0 of 70 dB.

RANGE:ACTUAL •, MEASURED +, ESTIMATED ▽

DEPTH:ACTUAL •, MEASURED +, ESTIMATED ▽



ACTUAL: CONTROL • SPEED +; ESTIMATED CONTROL ▽ CENTER Δ

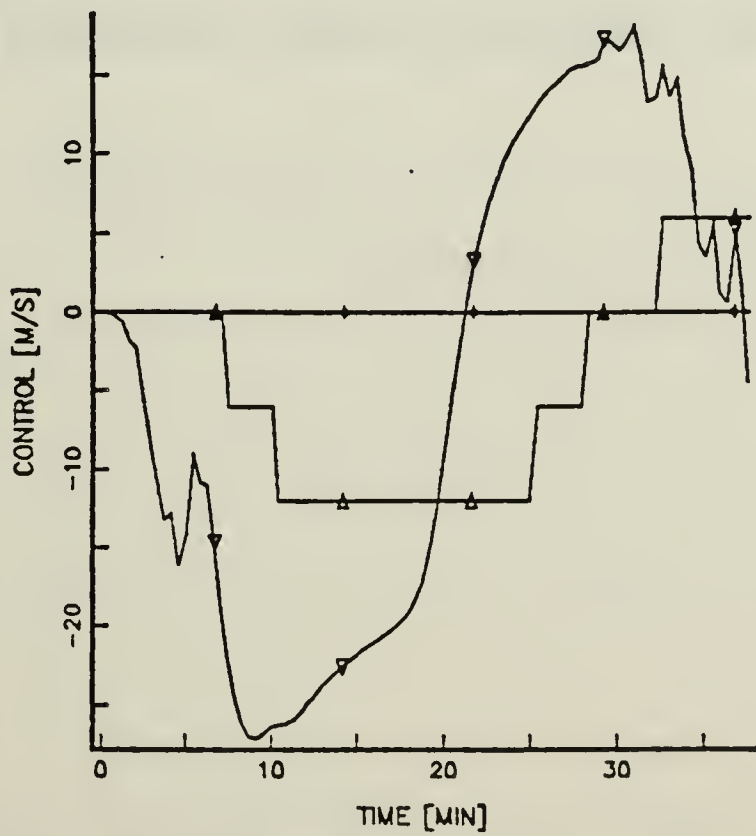


Fig. 2.17. Run-4: Range dependent noise SNR_0 of 60 dB.

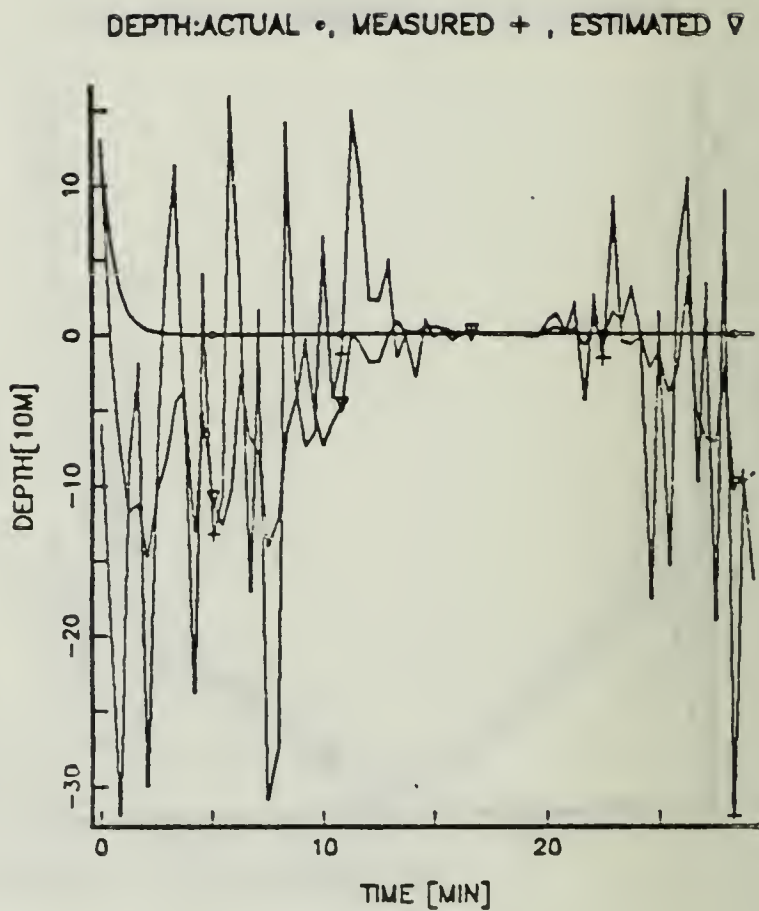
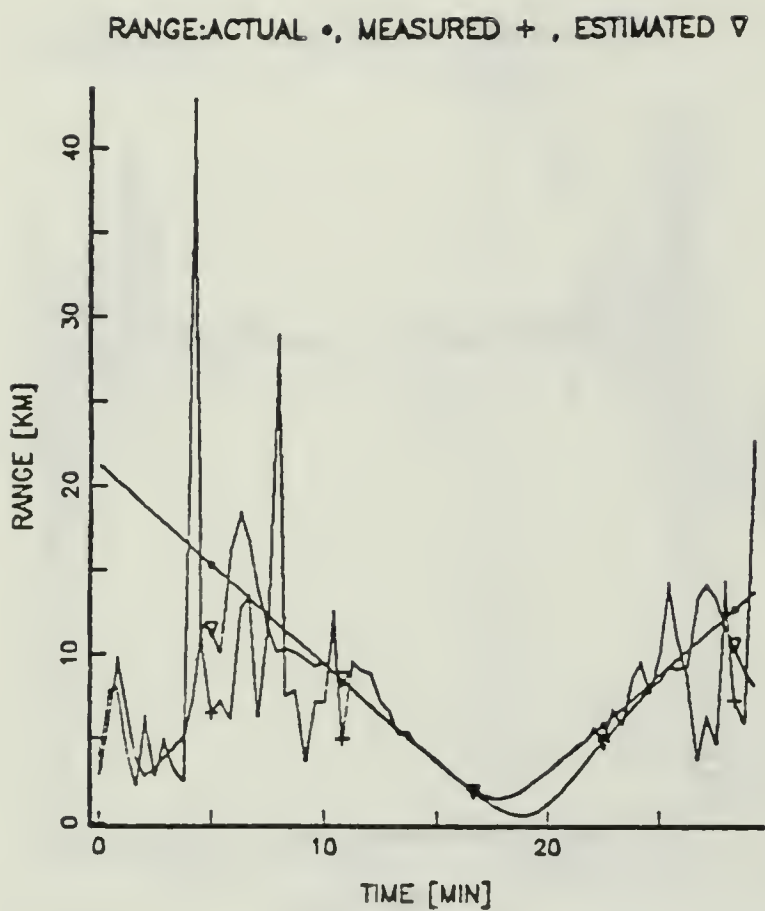


Fig. 2.18. Run-5: High range dependent noise SNR_0 of 50 dB.

G. SUMMARY OF TRACKER EVALUATION

The performance of the modified target tracker is summarized below.

- Generally the tracker is well suited for 3-D maneuvering target tracking.
- Measurement noise variance is significantly reduced by the tracker. The range measurement STD of 1000 m can be easily handled and reduced to around 50 m.
- The performance depends strongly on range, especially when range dependent MP measurements are used. However up to 15-17 km the filter tracks well without readjustments.
- Tracking errors that can reach 2 km in range develop at short ranges for nonmaneuvering targets moving along straight lines due to the coordinate decoupling and linearization.
- Recentering of the command bank around the average actual command is required in order to remove the inherent MM estimation bias. The new model update technique devised here effectively accomplishes this task by recentering the command bank around the estimated command value.

III. INHOMOGENEOUS REALISTIC MULTIPATH DEPTH AND RANGE MEASUREMENTS

A. INTRODUCTION

The following idealizing assumptions mentioned in Chapter One and used in previous broadband MP tracking studies are removed in this chapter:

- Homogeneous straight line propagation.
- No propagation and reflection loss.
- Infinitely resolvable TDOA.
- Ability to associate delays with acoustical path.

The impact of these effects on the tracker is investigated in Section B. Section C presents the improved prefilter which provides the functional inversion of time to depth and range measurement for the IH realistic medium. Chapter Four analyzes the performance of the new inversion algorithm as a component in the overall MP tracking system.

B. REALISTIC MEDIUM AND RECEIVER EFFECTS

1. Propagation Loss and Reflections

The most dominant effect the medium has on the propagating acoustic wave is the transmission loss. Three contributors to the loss are discussed: the spreading, the absorption, and the imperfect reflections from the boundaries. Special attention is given to the effect that the reflection from the non-ideal boundaries has on the multipaths.

a. Spreading Loss

The spreading loss, as the name implies, is the result of the spreading of the acoustic energy over a growing area, as the distance from the source increases. In spherical spreading, the energy spreads evenly over the surface of a sphere. This makes the intensity, the power per unit area, inversely proportional to the squared range. The relation is

$$I(R) = I_0 \cdot R^{-2} \quad (3.1)$$

where I_0 is the intensity at a distance of 1 m from the source.

Under other propagation conditions different range dependency results. For example, with cylindrical propagation the intensity is inversely proportional to the range itself, that is

$$I(R) = I_0 \cdot R^{-1} \quad (3.2)$$

In deep water, away from the surface or the bottom, one finds spherical propagation to be a good assumption for short ranges. In shallow water, where MP effects are more dominant, cylindrical propagation is a better representation.

In the IH case the wavefront is distorted by the variation in the speed of sound. Although the resulting spreading loss is not simple, a dependence on the p -th power of range can still be useful as a first order approximation. The approximation is

$$I(R) = I_0 \cdot R^{-p} \quad (3.3)$$

where the empirical constant p , which we call the range propagation power, is not limited to integers.

b. Absorption Loss

Part of the energy of the propagating acoustic wave is absorbed by the water and eventually is turned into heat. The absorption loss depends on the salinity of the water, the frequency, and the distance traveled. In short to medium ranges (below 15 km), and at sufficiently low frequency (below 10 KHz) this is not a dominant phenomenon and will therefore not be considered here.

c. Reflections From the Boundaries

The laws of pressure and velocity continuity across the boundary govern the reflections from the surface and the bottom [Ref. 23]. A wave propagating in medium 1 impinging on a boundary at an angle β_1 is both reflected back at an angle β_1 and refracted into medium 2 at an angle β_2 as shown in Fig. 3.1.

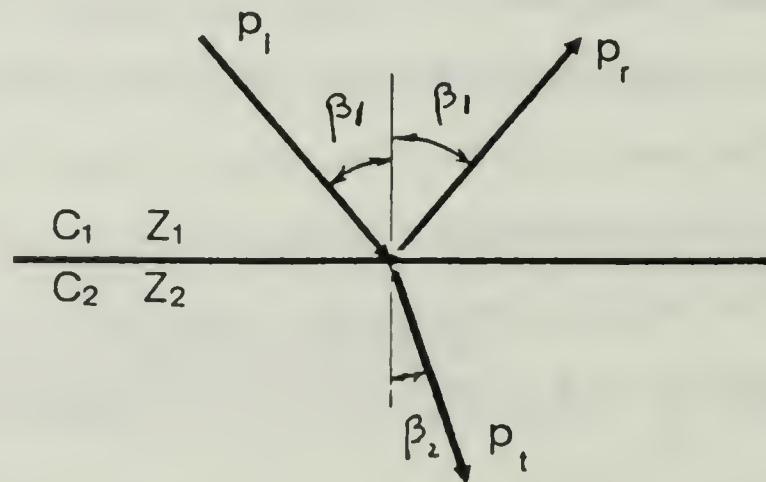


Fig. 3.1. Reflection from a boundary.

The acoustic pressure reflection coefficient defined as

$$\Gamma = \frac{p_r}{p_i} \quad (3.4)$$

where p_i, p_r are the acoustic pressures of the incident and reflected waves in medium 1. The reflection coefficient is given by

$$\Gamma = \frac{Z_2 \cos \beta_1 - Z_1 \cos \theta_2}{Z_2 \cos \beta_1 + Z_1 \cos \theta_2} \quad (3.5)$$

where Z_1 and Z_2 are the specific acoustic impedances in media 1 and 2, respectively. The specific acoustic impedance is defined as the ratio between the complex amplitude of the acoustic pressure p and that of the magnitude of the particle velocity U . The angle β_2 is given by $\beta_2 = \sin^{-1} \left(\frac{C_2}{C_1} \sin \beta_1 \right)$ where C_1 and C_2 are the speeds of sound in the two media.

The specific acoustic impedance for a plane wave can be expressed in terms of the speed of sound C and the equilibrium density ρ_0 of the medium as

$$Z = \rho_0 \cdot C \quad (3.6)$$

which is known as the characteristic impedance.

Since the characteristic impedance of air is much smaller than that of water, the surface boundary has a reflection coefficient close to -1 (see Eq. (3.5)). Further, since the characteristic impedance of the bottom is generally larger than that of the water, the resultant reflection coefficient of the bottom is positive.

The reflections from the water air boundary becomes somewhat more involved when the layer of air bubbles formed near the surface by the wind and the ocean waves is considered. But unlike the air (which is isotropic) the bottom may be lossy and anisotropic. In particular, shear waves excited by the impinging

acoustic wave travel in the bottom with different characteristics than the refracted longitudinal waves. These effects give rise to less predictable and complex acoustic impedance and complex reflection coefficients which strongly depend on the bottom type. For a boundary with frequency dependent characteristic impedance $Z_2 = r_2 + jx_2$, the pressure reflection coefficient will vary both with frequency and angle of incidence, and will depend on the bottom type and sea state (for surface reflection). Exact prediction of the phase of a reflected wave is made difficult by the large variation in pressure reflection coefficients. This phenomena has a marked influence on MP tracking. The intensity, which is related to the square of the pressure, has the reflection coefficient Γ_I given by

$$\Gamma_I = |\Gamma|^2 \quad (3.7)$$

which also depends on the above ocean and acoustic wave parameters. In a very simple practical analysis, the energy loss due to the various boundary effects is lumped into a single number called the reflection loss. The reflection loss depends mostly on the sea state, the bottom type, and the frequency band. Loss values in the range of 3 to 30 dB per bounce are commonly found. The sensitivity of the reflection phase to frequency and angle of incidence has a marked influence on MP measurements.

2. Inhomogeneous Medium

a. Speed of Sound Variations

The speed of sound in the water is given by the formula [23]

$$C = 1449.2 + 4.6T - 0.055T^2 + 0.00029T^3 + (1.34 - 0.01T)(S - 35) + 0.016D \quad (3.8)$$

where T is temperature in degrees centigrade S is the salinity in parts per thousand, and D is the depth in meters.

The sound speed is obviously not constant in the vertical water column, due to change of the pressure and the temperature with depth. The variation of sound velocity with depth, referred to as the sound velocity profile (SVP) is the main source of inhomogeneity in the acoustic ocean medium. Waves propagating in such a medium are refracted in a complicated manner, and obey the second order linear partial differential scalar wave equation [20]

$$\nabla^2 \varphi(t, \mathbf{r}) - \frac{1}{C^2(\mathbf{r})} \cdot \frac{\partial^2}{\partial t^2} \varphi(t, \mathbf{r}) = \chi_m(t, \mathbf{r}) \quad (3.9)$$

where $\varphi(t, r)$ is the velocity potential at time t and position r . $C(\mathbf{r})$ is the speed of sound at position r , and $\chi_m(t, \mathbf{r})$ is the source distribution (volume flow rate per unit volume). The acoustic particle velocity vector $\mathbf{U}(t, \mathbf{r})$ and pressure $p(t, \mathbf{r})$ are given by

$$p(t, \mathbf{r}) = -\rho_0 \frac{\partial}{\partial t} \varphi(t, \mathbf{r}) \quad (3.10)$$

$$\mathbf{U}(t, \mathbf{r}) = \nabla \varphi(t, \mathbf{r}). \quad (3.11)$$

Solution of the wave equation for the general case is very difficult. However, when the speed of sound is a linear function of depth the approximate ray acoustic solution yields simple closed-form equations. The detailed development of the ray acoustics approximation is based on the WKB approximation and is presented, for example, in Ref. 20. The resulting ray tracing equations are presented below.

b. Ray Tracing

The parameters and geometry of a typical ray-trace are shown in Fig. 3.2. Note that the rate of change of sound speed with depth is a constant known

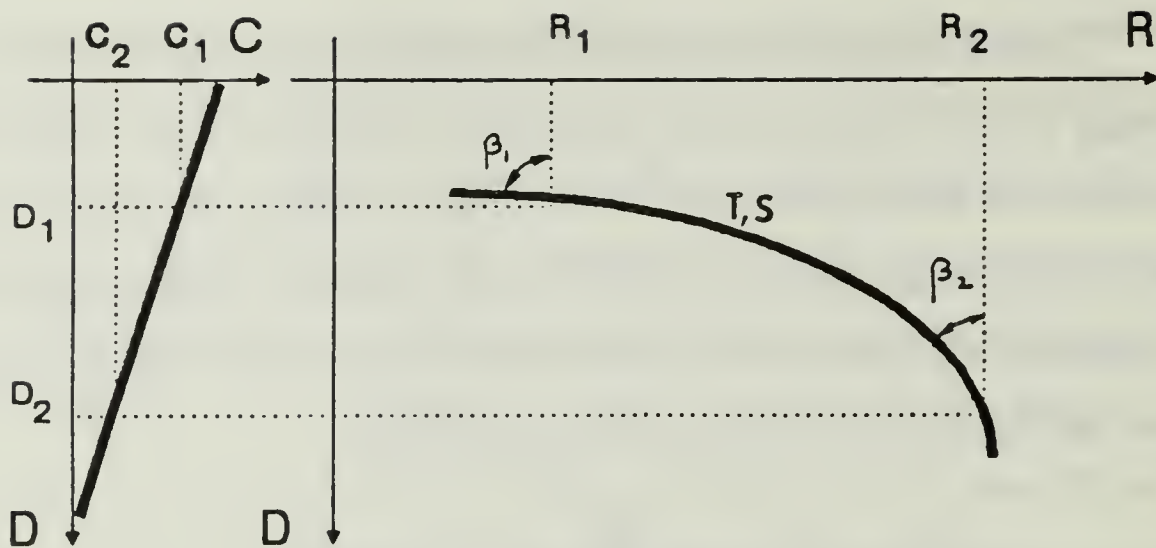


Fig. 3.2. Acoustic ray path.

as the sound speed gradient g , which has units of $[\text{sec}^{-1}]$, and the speed of sound C is given by

$$C(D) = C_0 + gD \quad (3.12)$$

where C_0 is the speed of sound at the surface.

In transition from depth D_1 where the sound speed is C_1 to depth D_2 with sound speed of C_2 , the ray angles β_1 and β_2 obey Snell's law

$$\frac{\sin \beta_1}{\sin \beta_2} = \frac{C_1}{C_2} \quad (3.13)$$

Thus a ray emanating from a source at D_1, R_1 , at an angle β_1 , reaches depth D_2 at an angle β_2 given by

$$\beta_2 = \sin^{-1} \left(\frac{C_2}{C_1} \sin \beta_1 \right) = \sin^{-1} \left[\frac{C_0 + gD_2}{C_0 + gD_1} \sin \beta_1 \right] \quad (3.14)$$

and at a range R_2 given by

$$R_2 = R_1 + \frac{C_1}{g \sin \beta_1} (\cos \beta_1 - \cos \beta_2) \quad (3.15)$$

which can be evaluated by solving Eq. (3.14) for β_2 and substituting into eq. (3.15). The travel time T and the arc length S of the path are given by

$$T = \frac{1}{g} \ln \frac{\tan(\beta_2/2)}{\tan(\beta_1/2)} \quad (3.16)$$

and

$$S = \frac{C_0}{g \sin \beta_1} (\beta_2 - \beta_1). \quad (3.17)$$

The ray traverses the depth range (DR) plane along of a circle with radius R_{ray} given by

$$R_{ray} = \frac{C_0}{g} = \frac{C_1 \cos \beta_1}{g} \quad (3.18)$$

centered at the initial range and the conceptual depth D_{center} . This is the point where the speed of sound would have become zero if the gradient had been constant to that point; it's value measured from the surface is therefore given by

$$D_{center} = -\frac{C_0}{g}. \quad (3.19)$$

Tracing the ray intensity is based on conservation of energy. A hypothetical amount of radiated power trapped in a ray tube produces intensity which is inversely proportional to the cross sectional area of the tube. Tracing the cross sectional area along the tube, using the ray tracing equations, provides the required intensity computation.

$$\frac{I_{(D_1, R_1)}}{I_{(D_2, R_2)}} = \frac{S_{(D_2, R_2)}}{S_{(D_1, R_1)}} \quad (3.20)$$

A singular case arises when the cross sectional area of the ray tube reduces to zero and drives the intensity to infinity. This is called a focal point. Focal points in which the intensity is very high are actually encountered in the ocean and the acoustic intensities measured there are very high. Ray acoustic intensity computations are obviously not valid under such conditions. A ray going through

a focal point is phase shifted by 90 deg. This phenomenon which is experimentally measurable, can be explained analytically although not in a trivial manner.

Ray equations allow tracing a ray in a medium of constant SVP gradient, however, a constant SVP gradient is rarely the case in practice. When the SVP is not linear, it can be represented by a piecewise linear function which has constant gradients within depth layers. Eq. (3.14) through (3.17) are then used to trace a ray inside a given layer. The continuity of the linearized SVP and Snell's law ensure ray angle continuity in the transition between layers. Consecutive tracing of the ray inside the constant gradient layers can thus construct the complete ray path throughout the entire medium.

c. Effect on MP

(1) **Time Delay.** An example will help demonstrate the effect of the IH propagation on MP depth and range measurement. A set of time delays for an IH case is computed for a given target and set of ocean conditions using Eq. (3.16). These time delays are then used as independent variables of the homogeneous inverse function Eq. (1.2). The erroneous inverted depth and range are compared to the original values.

A constant gradient of $g = 0.05 \text{ sec}^{-1}$ in the 100 m near the surface,*in water depth of 513 m and a target at depth of 100 m and range of 7 km,** produce TDOAs to a receiver at depth of 162 m of $\tau_1 = 5.48 \text{ ms}$ and $\tau_2 = 28.92 \text{ ms}$. When substituted into Eq. (1.2), which is based on straight line propagation, a depth of 19 m and range of 5.64 km are produced. This represents a percent error of 20% in range relative to the true 7 km range.

* See case C2251 in Appendix E

** Measured relative to the receiver, see Fig. 2.1

(2) Lack of Closed Form Solution - The Eigenray Problem.

Of significant importance is the fact that in all the tracing equations the initial transmission angle at the source (β_1) is assumed to be known. This angle, which can alternatively be replaced by the reception angle (β_2), actually 'selects' the ray to be traced.

The reverse problem of finding the terminal angles of a ray passing through two given end points is called the eigenray problem. The eigenray problem does not have a closed form solution in the IH case, especially not in the multilayered SVP case. This is part of the difficulty which prevented compensation for the medium inhomogeneity in previous work and thus became a key challenge of our work.

(3) **Loss of Direct Ray.** Another outcome of the IH propagation is the possible loss of direct path between the source and receiver due to the ray bending. Fig. 1.3a, which was computed by a Fortran program [26] using the ray tracing equations, shows an example of a receiver Rx placed in an area not reached by direct rays from source T_x which is referred to as a "shadow zone." The first arrival in this case is the reflection from the bottom. The second arrival is the ray reflected from the surface and then from the bottom. The third arrival is the one reflected from the bottom first and then from the surface. The above mentioned difficulty to predict the exact amplitude and phase of the reflected wave is further enhanced for a case of double reflection such as the one shown. The polarity of the ACF peaks becomes less predictable. Thus, it is obvious, that the IH medium amplifies the problem of path identification.

In Comparing Fig. 1.3a to Fig. 1.1, the difference in the MP structure is mainly that the direct path T_0 of Fig. 1.1 does not exist in Fig. 1.3b. A scalar called the bounce count (BC) was devised here in an attempt to characterize

the MP structure. It is defined as the total number of depth extremes in the set of the first three resolvable arrivals (two TDOAs).

The bounce count of the straight line propagation of Fig. 1.1 is 2 due to the single bounces of both the surface and the bottom paths. The bounce count of the first three arrivals of the MP structure in Fig. 1.3b is 4 due to the single bounces of the first and second arrivals and the two bounces of the third path. The bounce count therefore distinguishes between the two MP structures.

While ambiguous as an absolute descriptor, the bounce count was found to be very useful in practice primarily in identifying a *change* in the MP structure. By plotting the BC over a depth range cross section of the ocean, it became easy to divide the plane into regions of consistent propagation as will be shown later. Care should be exercised, however, in detailed analysis using the bounce count since radically different MP structures could produce identical bounce counts.

3. Ocean Data

The travel time of paths reflected from the bottom is obviously dependent on the ocean depth. Error in the assumed depth will cause errors in the inverted target depth and range. The CRLB for the joint estimation of ocean depth and target depth and range was developed by Hamilton [Ref. 19] as a composite estimation problem, with depth assumed normally distributed. The impact of a constant depth error is demonstrated in Chapter Four.

4. Receiver and Delay Estimator Effects

The effect of the limited delay resolution, and the inability to associate delays with paths are considered here along with an outline of a hypothetical but realistic form of delay estimation instrumentation.

a. Bandwidth and Delay Resolution

The target broadband noise has a limited bandwidth. Further, the high frequency portion of the spectrum tends to attenuate in a shorter distance than the lower frequency portion as the sound travels through the water, due to absorption processes. The receiver, on the other hand is constrained by engineering design compromises arising primarily from the beamformer, and computational load associated with its sampling rates. The result is that the acoustic receiver bandwidth is rarely ever more than a few KHz wide.

The limited bandwidth translates into a limited resolution between adjacent time lags. If one assumes a uniform signal spectral density over the entire frequency band of 0 to B Hz, the main lobe of the autocorrelation function of the original signal $x(t)$ will be of the form

$$ACF_{xx}(\tau) = ACF_{xx}(0) \cdot \text{sinc}(\tau \cdot B) \quad (3.21)$$

and its first zero occurs at $1/B$ sec. Replicas of the original signal which are less than $1/B$ apart will form a nonresolvable combined ACF peak. (In the extremely unlikely event of two opposite sign equal amplitude replicas the ACF peak may even disappear altogether.)

b. Nonidentifiable Path

The combination of the effects discussed earlier render the association of the TDOA with the corresponding path a difficult task indeed which is impractical in many target tracking situations. The polarity of the ACF peaks is strongly affected by the following:

- Potential loss of the direct reference path.
- Complex frequency and angle dependent reflection coefficients.
- Phase shift through a focal point.

An alternative approach taken here is to rely only on the time difference values, and to disregard the ACF polarity and its possible association with a specific path.

The response of the time delay tracker to this nonresolvable nonassociable situation will determine the behavior of the target tracker. For this reason, the specific instrumentation of the time delay estimator assumed here is briefly described below.

5. Instrumentation Outline

A discrete set of ACF values spanning the range of expected lag time, is computed by time or frequency domain methods, using the time sampled acoustic signal. A polynomial is fitted to the sampled ACF lag data and its first two amplitude maxima, are located (excluding $t = 0$). The lags times corresponding to these peaks are the MP time differences of arrival (or delays). The delays are usually further filtered by a simple exponential averager.*

The first two lags are preferred for the inversion since they result from simpler paths and are expected to have higher SNR. But when any two of the first three ACF peaks coincide only one combined and somewhat erroneous peak is formed. An example where this problem is significant and very typical is a source placed near the surface. The direct and surface reflected paths from the source to a distant receiver will have very similar path length and travel time, and their ACF peak will not be resolvable.

* Another technique of similar consequence uses interpolation between adjacent ACF samples to reconstruct the continuous delay, Friedlander [16].

Other lags corresponding to more complex and longer paths, do exist and can be used in such cases. Having longer lag time, these delays will not vanish, due to loss of resolution, incidentally with the first two. The third or higher lags can thus provide an alternative measurement, at least while one of the first two lags is lost.

In the instrumentation model simulated here a third ACF lag is tracked all along, and is substituted as the second lag only when any of the first three arrivals coincide. The two nonresolvable lags are reported as one lag under this situation. Coincidence is defined with some safety margin that ensures substitution of the third lag prior to the actual loss of resolution.

In Fig. 3.3 plot of the first three TDOA as a function of history time k is shown. At time T_{H_2} the ACF peak of τ_1 is not resolvable from the main lobe at $\tau = 0$, and is consequently replaced by τ_2 which in turn is replaced by τ_3 . The third TDOA τ_3 was tracked but not output before T_{H_2} . If τ_1 and τ_2 merge at T_{H_1} , as shown in Fig. 3.4 their combined peak will be reported as τ_1 and τ_3 will replace τ_2 .

In the straight line homogeneous propagation, identification of the measured delays as τ_1 and τ_2 is assumed such that they can be used in Eq. (1.2). In the realistic IH case the delays are identified instead as the first (shorter) and second (longer) lags. A vector of two time delays, the first of which is always the smaller, is output by the estimator and these modified TDOAs are denoted as τ_1 and τ_2 .

6. Resulting Ambiguity

The proposed method of time delay extraction immediately raises the question of ambiguity. There can obviously be more than one position with the same two time delays as demonstrated by the simple following case.

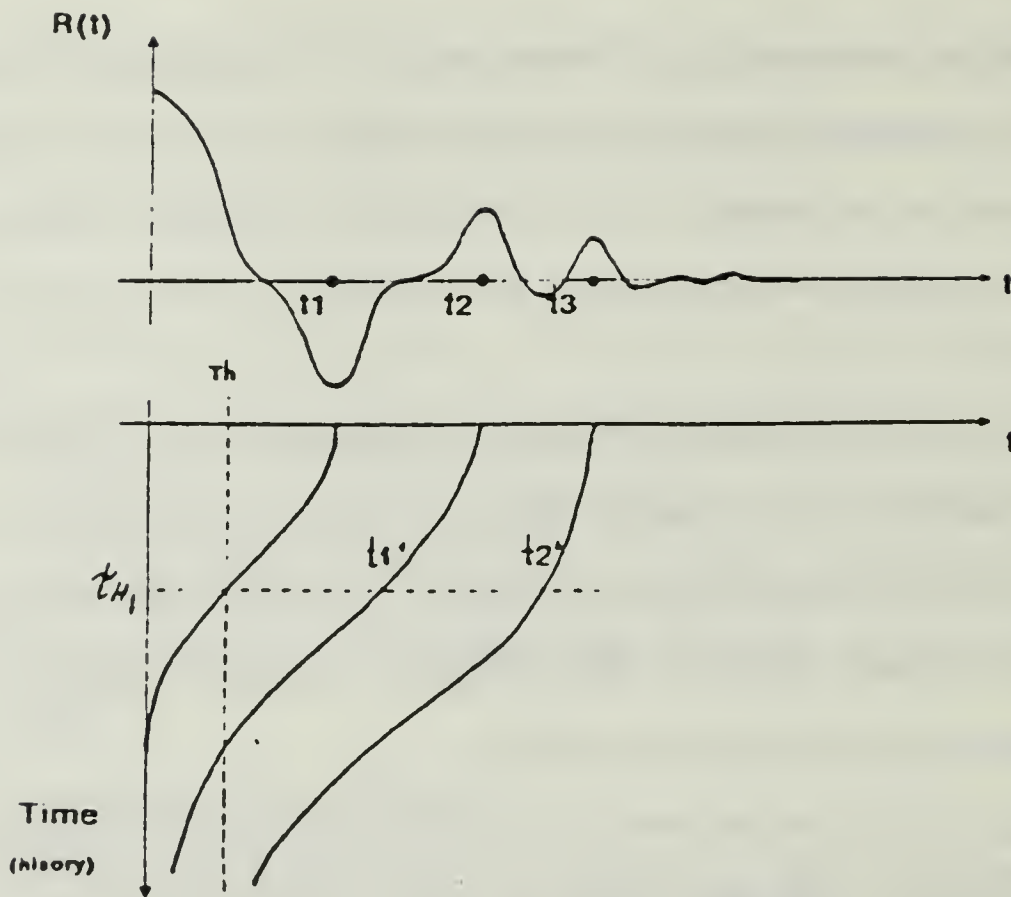


Fig. 3.3. Unresolvable ACF peaks $t_0 t_1$.

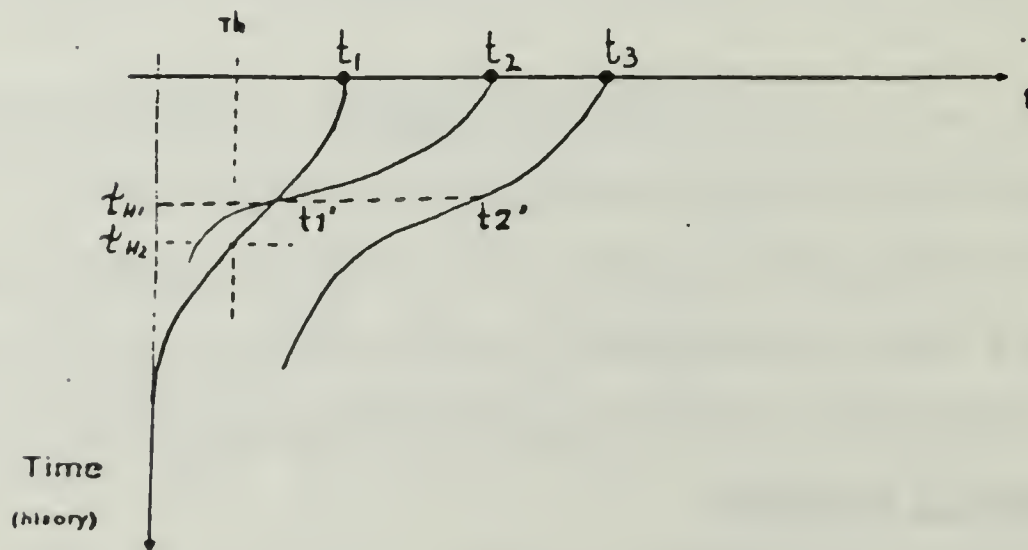


Fig. 3.4. Resolvable ACF peaks $t_1 t_2$.

For an observer at depth 162 m and water depth 503 m the targets:

Position	Target 1	Target 2
Depth m	-100	-242
Range m	6000	4782

produce T_0, T_1, T_2 direct surface and bottom travel time, respectively of

Travel time [sec]	Target 1	Target 2
T_0	4.00055	3.192079
T_1	4.00997	3.210297
T_2	4.01877	3.201499

yielding travel time differences of

TDOA [msec]	Target 1	Target 2
$\tau_1 = T_1 - T_0$	9.41	18.2
$\tau_2 = T_2 - T_0$	18.2	9.41

After sorting these become

Modified TDOA [msec]	Target 1	Target 2
$t_1 = \text{Min}\{\tau_1, \tau_2\}$	9.41	9.91
$t_2 = \text{Max}\{\tau_1, \tau_2\}$	18.2	18.2

Yielding the same $\tau_1 \tau_2$ set for two vastly different depth range positions.

This ambiguity is a direct result of the inability to associate paths and delays. Means to reduce this ambiguity to a manageable proportion are covered in Section C. A more effective use of the high bounce count paths designed to further reduce the ambiguity is discussed in Chapter Six.

7. Graphical Representation of the Medium and Receiver Effects

a. Introduction

The 2-D direct function transformation of source depth and range (DR) position, to MP time delays, (τ_1, τ_2) , can be viewed as surfaces of delays over the 2-D depth-range position plane. These surfaces are the basis of the MP inversion procedure and understanding their nature is important in the development of the inversion process.

The graphical interpretation of the direct function will be presented in this section including the following effects which the medium and receiver have upon this function:

- Lack of path identification.
- Limited resolution.
- IH propagation.

Four types of surfaces are presented starting with a theoretical case of homogeneous propagation, and resolvable and identifiable multipaths. The above listed effects are then added in three accumulating steps ending with the realistic case of IH propagation, limited resolution and non identifiable paths.

b. Case Definition

The number of parameters determining the MP structure is very large and attempting to investigate all of their various combinations is an impossible and not a valuable effort. A number of representative cases were selected and the parameters involved were coded into cases. A case name is composed of one letter and four digits, e.g., C1123, which has the following meaning. The leading character defines the type of assumptions and instrumentation used. The first

digit defines the SVP and the second digit defines the ocean and observer depth. The last two digits define a grid of depth range points for which the TDOAs are computed. A detailed description and settings of the various parameters is given in Appendix E.

To demonstrate the nature of the direct function surfaces three cases were used. The first case for an ocean depth around 500 m and receiver depth of 162 m (U1111) represents homogeneous propagation and infinitely resolvable TDOAs which are associable with the paths for bottom depth of 503 m and receiver depth of 162 m. The second case (S1111) represents the same case but without the associability of TDOA with the multipath. The third case (C1111) represents the same case with both the TDOA-path associability and the perfect resolution assumptions removed. Three dimensional (3-D) surface and contour plots of TDOA τ_1, τ_2 or t_1, t_2 over the DR plane are plotted for each case. Regions of consistent MP structure are indicated by contours of bounce count over the DR plane. A short description points to the issues of interest in the plots.

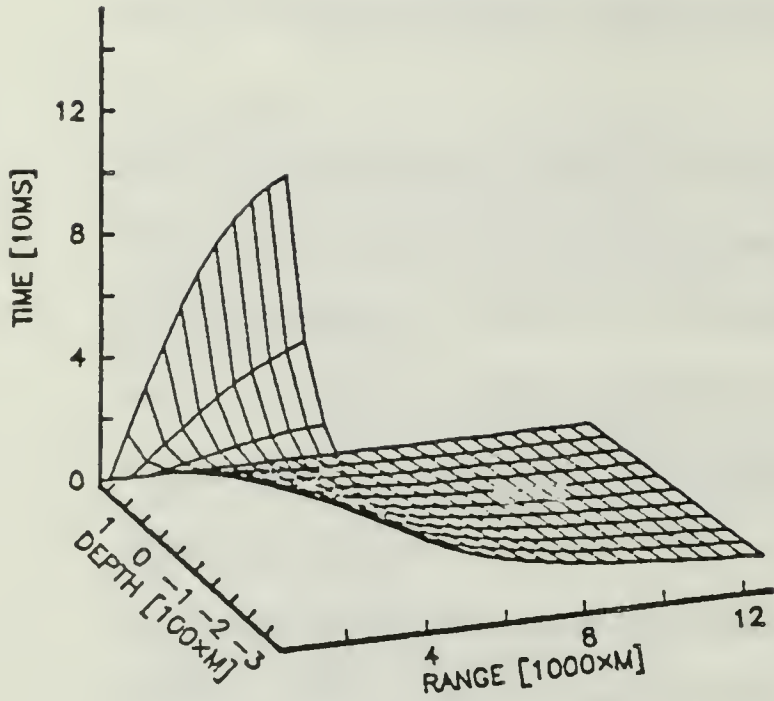
c. TDOA Surfaces

Homogeneous, perfectly resolvable and identifiable U1111.

TDOA surfaces and contour lines for this ideal case are shown in Fig. 3.5.

Both surfaces are monotonic and τ_1 can be either smaller or larger than τ_2 . Both delays decrease with range but opposite changes in τ_1, τ_2 result when depth is changing along a fixed range. Note that τ_1 is small and τ_2 is large close to the surface, and the reverse is true near the bottom. No bounce count plots are presented since the count is 2 all over the plane. Note the vanishing τ_1 and τ_2 near the surface and the bottom respectively which causes the merging of the corresponding ACF peaks with the main ACF lobe at $\tau = 0$. These lags are substituted by those from multiple reflection paths in the limited resolution case. Also note that the TDOA

Surface bounce τ_1



Bottom bounce τ_2

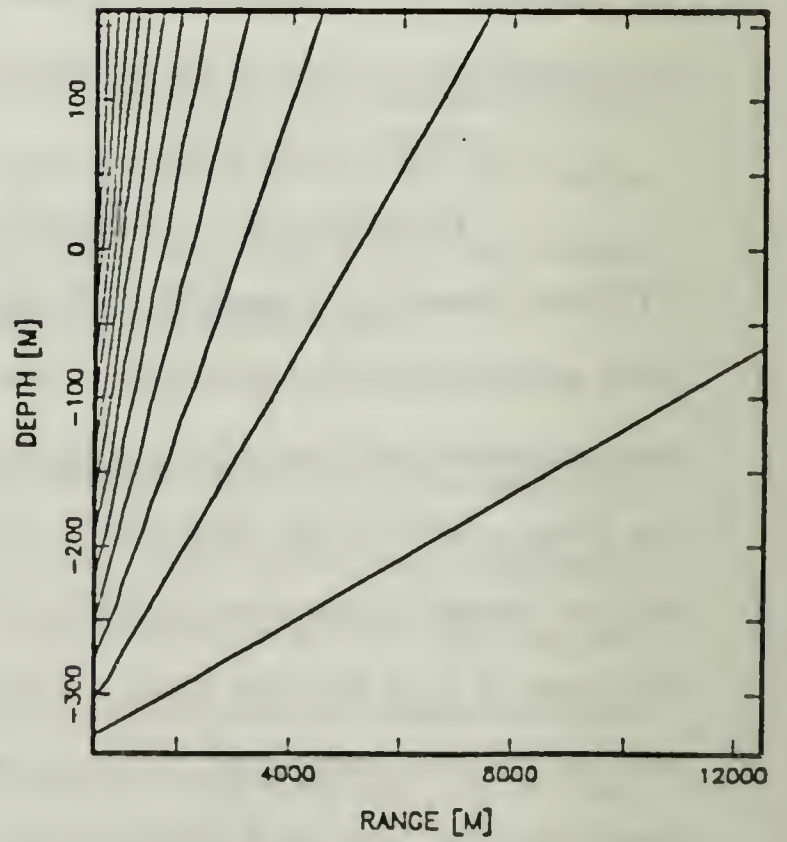
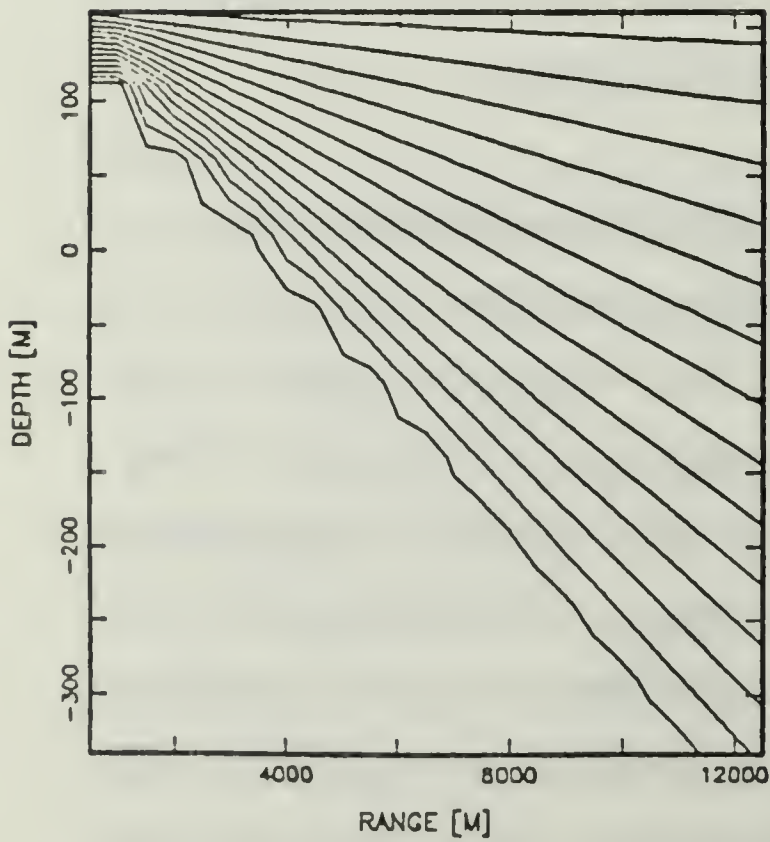
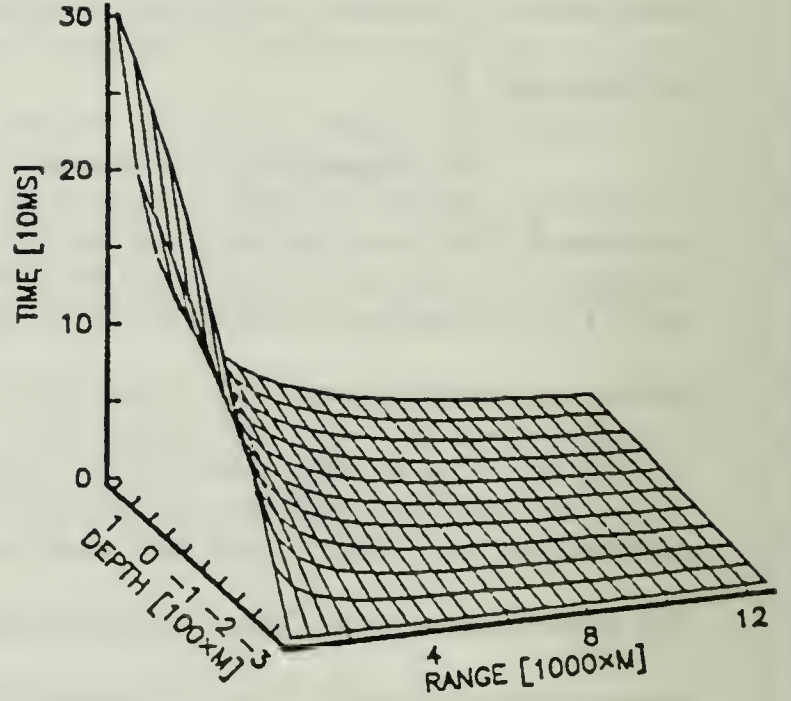


Fig. 3.5. Ideal TDOA surface (U1111)

vanishes with range, this tends to make the effect of delay estimation noise more significant at longer ranges. Since in addition the TDOA estimation noise increases with range, the MP method becomes inherently limited to short ranges.

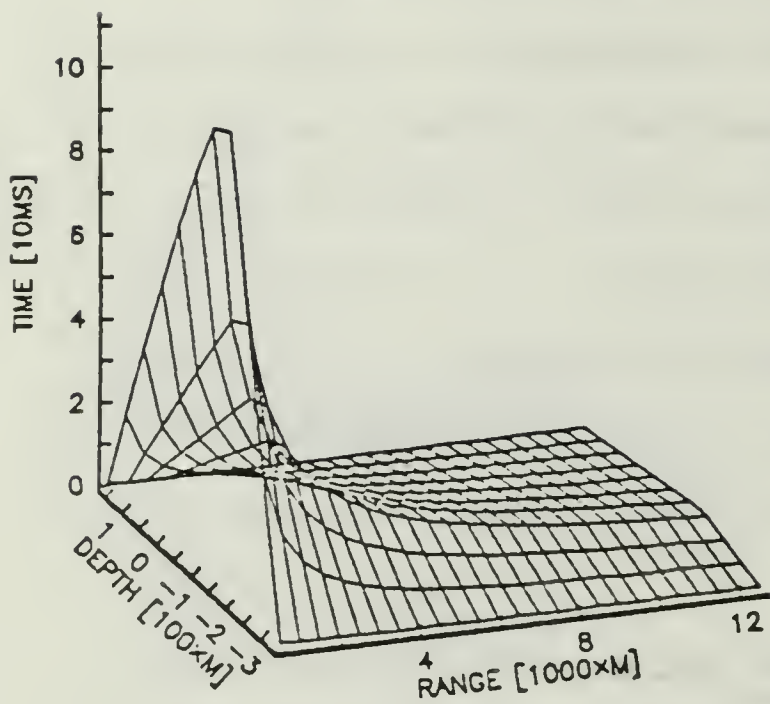
Homogeneous sorted perfect resolution S1111 modified TDOA τ_1, τ_2 surfaces and contours for this ideal case where association of the path and delays is not assumed are shown in Fig. 3.6. When the TDOAs are sorted to produce t_1 and t_2 as described earlier the result is $t_1 < t_2$ by definition. The monotonicity of the surfaces is lost along the DR loci where $t_1 = t_2$. The trend of reduced delays τ_1, τ_2 at long ranges has not changed. The depth still determines the relation between τ_1 and τ_2 but not in the simple unambiguous manner as in the unsorted case.

It is only τ_1 now that vanishes near the surface, when it becomes smaller than the delay estimation resolution it will be replaced by what is here plotted as τ_2 . The τ_2 will then be replaced by the arrival lag of the next multipath, the one bouncing from both the surface and the bottom. Since this will only happen for the realistic receiver, the bounce count here (perfect resolution) is still 2 all over the DR plane and is therefore not plotted. Contours of TDOA in the first 100 m near the surface are shown in Fig. 3.7 as a reference for the later comparison to an IH case.

Homogeneous realistic finite resolution C1111. Fig. 3.8 shows the resulting surfaces when the TDOA are not associable with the multipath (sorted) and a finite delay resolution (0.5 ms) is assumed.

The main difference between this and S1111 case is the substitution of a high order reflection time delay when time delays from simpler reflections are not resolvable. This comes about near the surface where τ_1 is small and at depth of around -176 m relative to the receiver where τ_1 and τ_2 are similar causing the

SECOND TO FIRST ARRIVAL



THIRD TO FIRST ARRIVAL

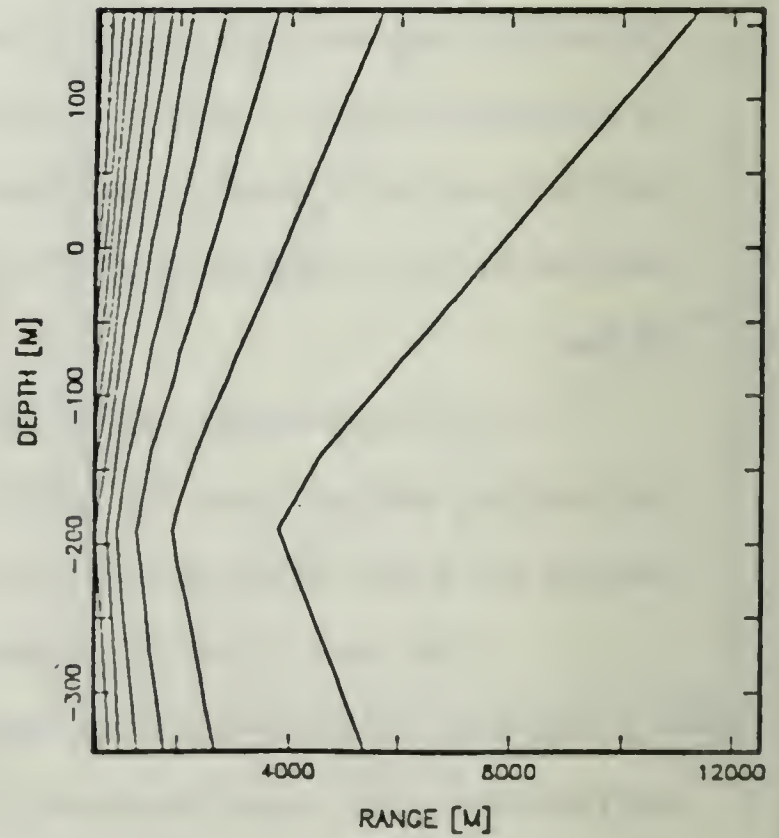
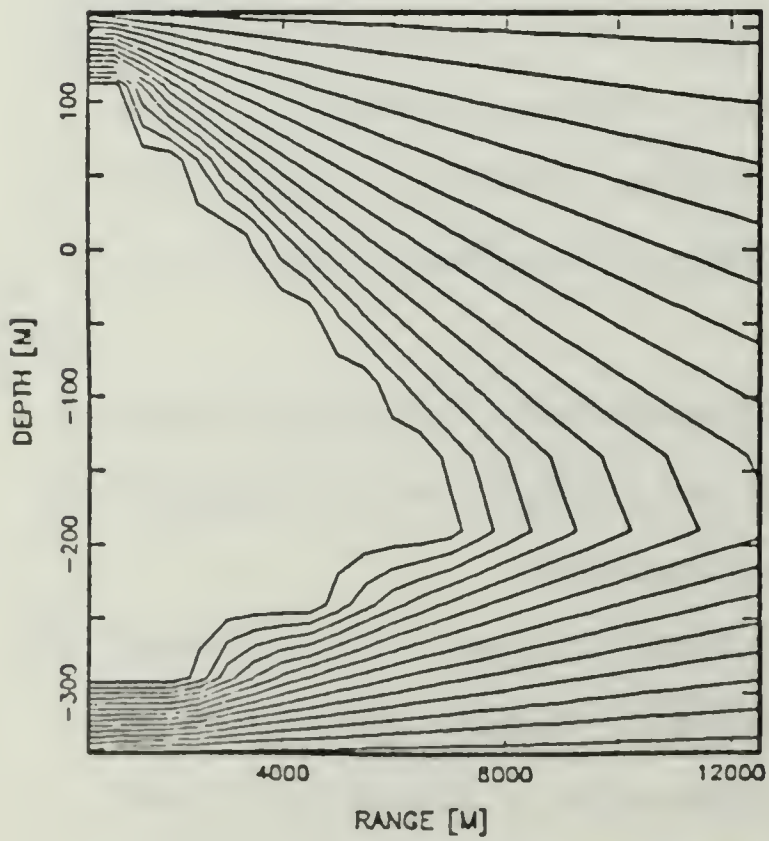
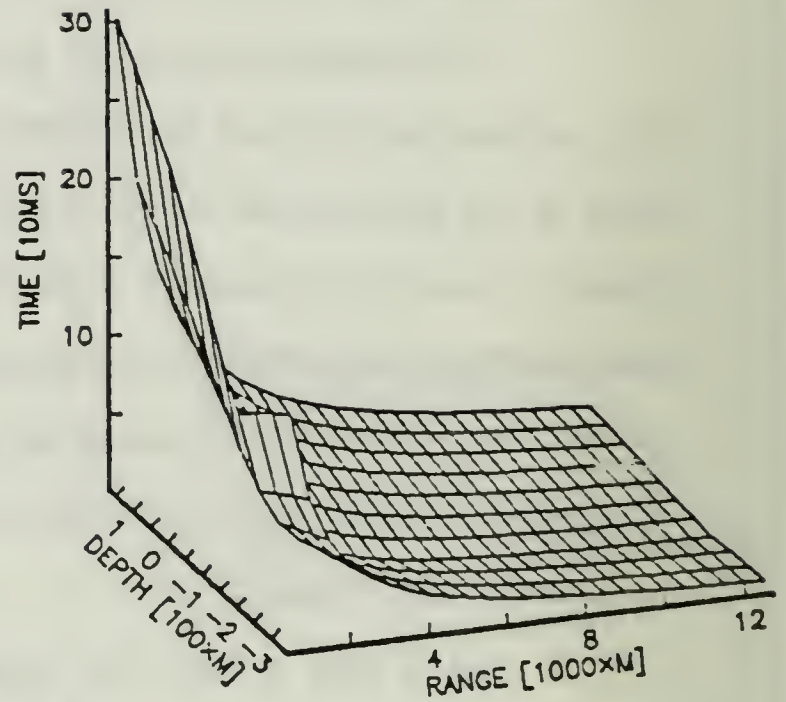
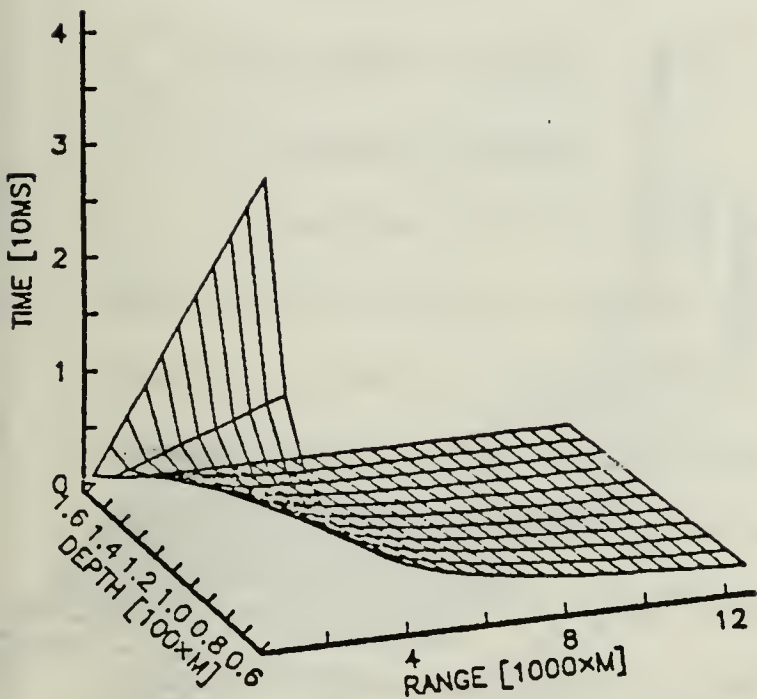


Fig. 3.6. Modified TDOA surface, homogeneous medium (S1111).

SECOND TO FIRST ARRIVAL



THIRD TO FIRST ARRIVAL

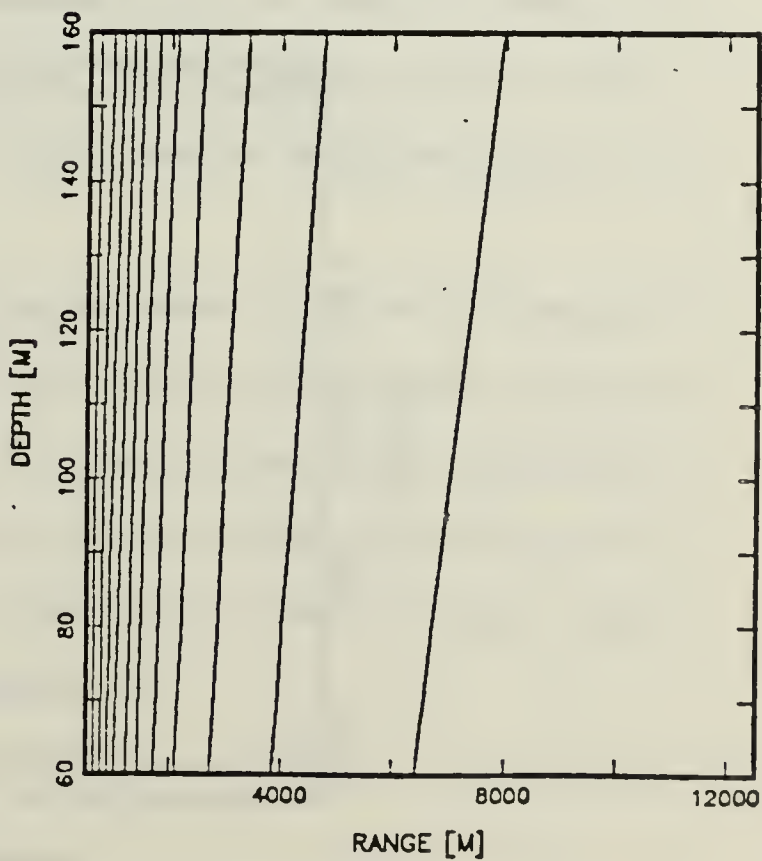
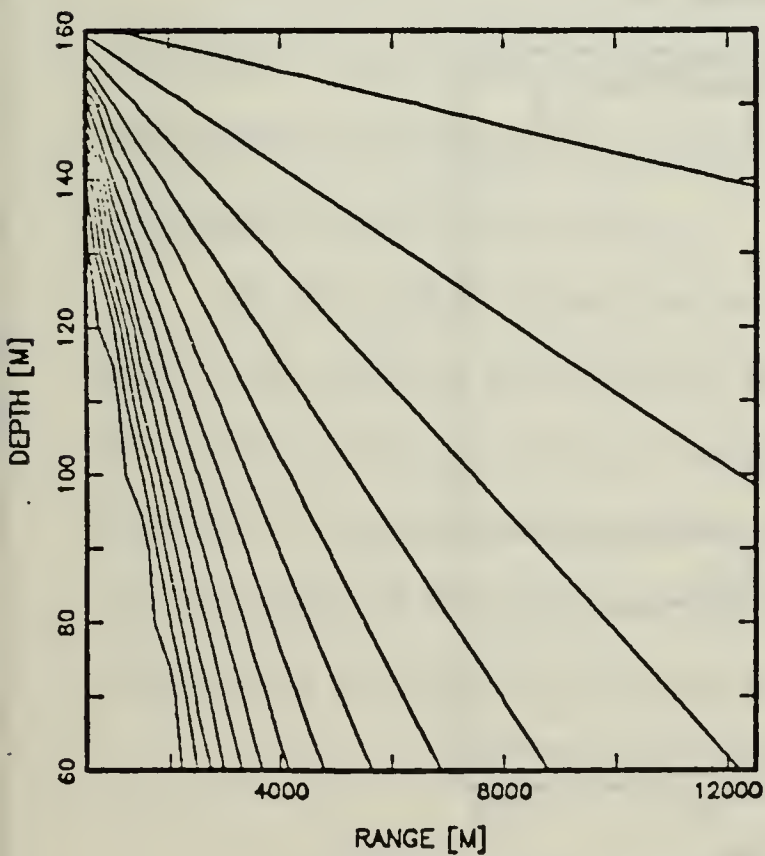
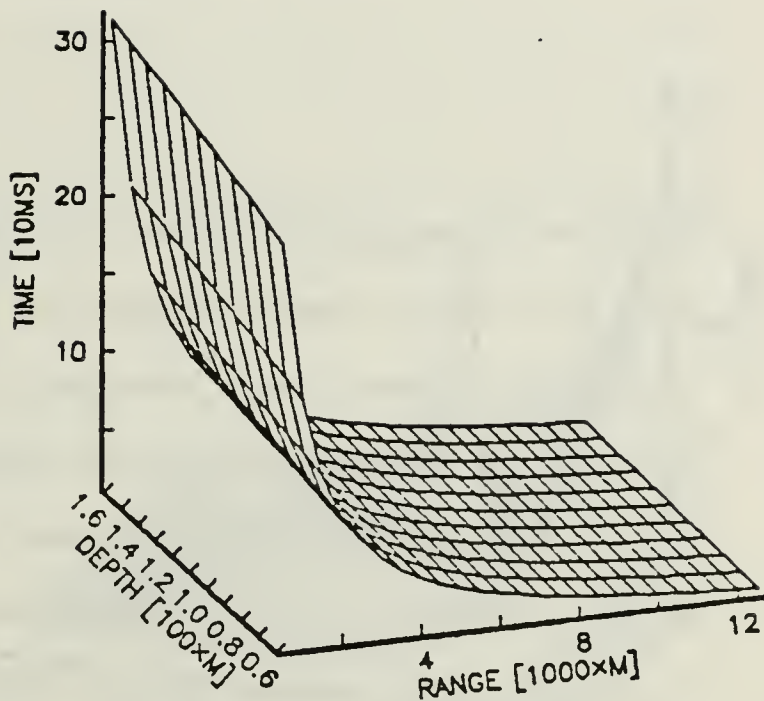
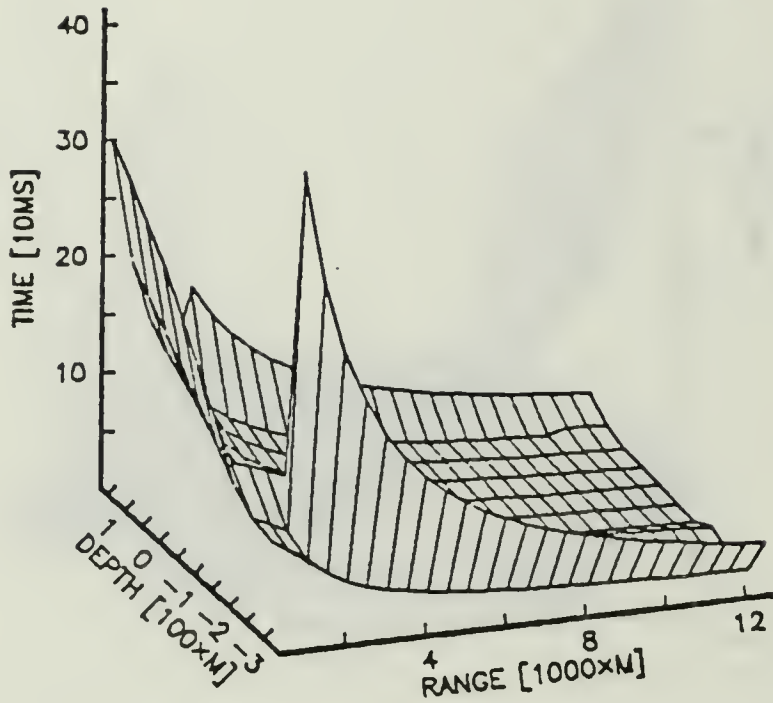
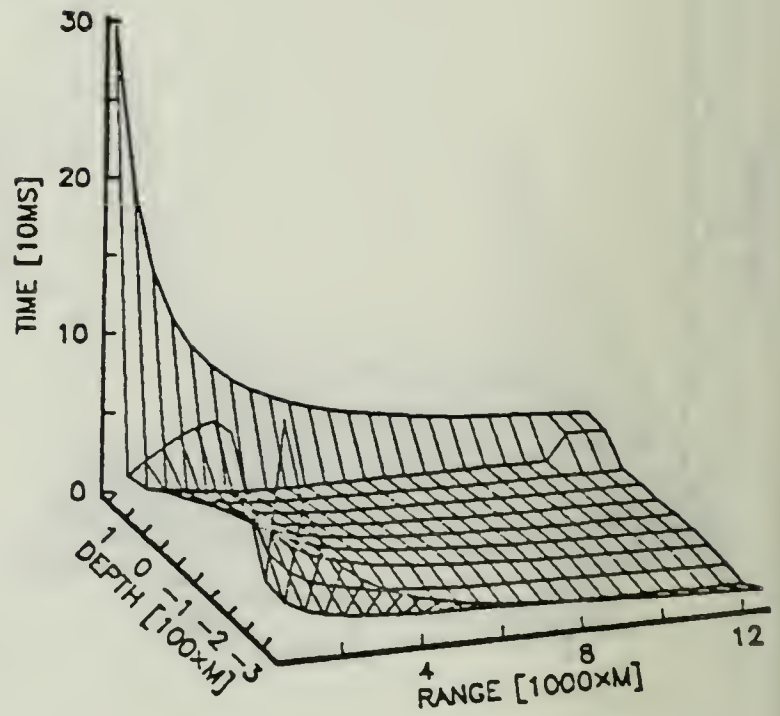


Fig. 3.7. Modified TDOA near the surface (S2251).

THIRD TO FIRST ARRIVAL



SECOND TO FIRST ARRIVAL



BOUNCE COUNT

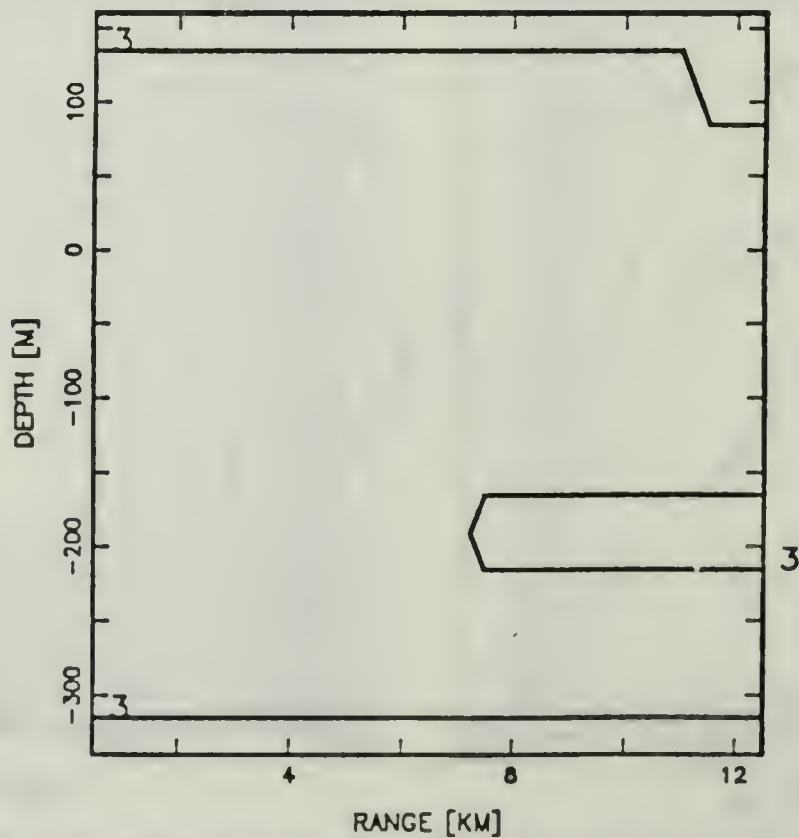


Fig. 3.8. Finite resolution TDOA and bounce count (C1111).

replacement of τ_2 by the lag corresponding to the higher bounce count path (t_3). The bounce count plot is helpful in recognizing this effect which of course is also obvious on the TDOA surface and contours as well.

C. IMPROVED FILTER

1. Concept Overview

The subject of this section is inversion of realistic IH multipath time difference of arrivals (TDOA) to source depth and range coordinates. Since there is no closed form solution for either the direct or the inverse relation between time delays and position, a two-step numerical solution is developed. As before the function that computes depth and range from time delays is referred to simply as the direct function, and the procedure that computes depth and range from time delays is referred to as the inverse function. The latter may at times be multivalued and so may not be a one-to-one function in the mathematical sense.

First, the direct function values of the TDOA are computed over a discrete grid of target depth and range positions. This computation is done off-line. Measured time delays are then inverted to obtain position (depth and range). This computation must be done on-line.

In the off line computation an eigenray model is used to find the travel times of the multiple paths between the receiver and a given depth and range point. The travel time produced is further processed to simulate the realistic delay estimation. Generation and processing of the TDOA is repeated for every point in the entire DR grid. The processed TDOA data thus produced, is stored as a table of time delay as a function of the depth and range.

In the on line step, a set of two measured time delays is inverted to produce depth (and range) using 2-D linear interpolation. Depth (and range) values of three points in the direct function table, which have time delay values closest to the measured set, are used as a basis for the interpolation. To locate these points a unique search algorithm is developed. The algorithm takes advantage of a priori information available in the form of the predicted target position. The prediction, in turn, is derived from past depth and range measurements processed by the target tracker.

The use of the eigenray model and the delay estimation simulation to generate the direct function is described in Section C.2. The inversion process is described in Section C.4.

2. Direct Function

The precomputed tabulated direct function of the modified TDOA over the DR grid is computed by means of an eigenray model which is repetitively exercised over the DR grid points. This process is described next.

a. The Eigenray Model

An eigenray model is a program that finds the multiple rays which path between two given end points, providing their angles, path length and travel time. Computing the TDOA of the MP structure requires very accurate computation of the path travel time. This results from the TDOA being a difference of a few milliseconds between travel times which are of the order of a few seconds.

In the search for an eigenray model only compact programs requiring small computation time on readily available microcomputers were considered. This was done in order to maintain compatibility both with the computational resources available to this research and those available in onboard systems. Since no closed form solution for the eigenray problem is available (recall discussion in Section

III.B.2.c) the eigenray models are iterative in nature. The conflicting requirements for high accuracy, limited word length and short run times are met by only a few existing models.

Appendix F discusses the SMART (SMall Acoustic Ray Trace, Ref. 22) selected as the eigenray model for this thesis*. The program computes the dependence of range on initial angle and uses this relation in its iterative search for the eigenray.

b. Generation of Direct Function Table

The SMART model produces the sound travel times for an eigenray set pertaining to one receiver and one source. The generation of the complete direct function table requires the following five additional steps.

1. Repeatedly exercising the model for all the source points on the discrete grid of target depth and range (DR) positions.
2. Selecting the shortest travel time as the first arrival and subtracting it from the travel time of the other paths. The resulting differences correspond to the time lags of the ACF.
3. Sorting the paths in ascending travel time order. This corresponds to the estimator logic which assumes that it is not possible to directly associate the TDOAs with the paths.
4. Applying the resolution limitation by eliminating delays which are less than the resolvable difference away from their preceding delay.
5. Selecting the shortest two delays and storing them as the tabulated direct function.

The last step is in need of further elaboration. The data structure used for the purpose of storing the direct function table is a 3-D array \mathbf{Q} of dimension $2 \times N_d \times N_r$ indexed by ℓ, i, j . The first array index ℓ , selects the first and second

* The proprietary model was made available to this research courtesy of Mission Sciences Corp., Commack, N.Y.

delays $t_1; t_2 (\ell = 1, 2)$. The second and third indices i and j select a point on the depth and range grid respectively. The variables N_d and N_r are the number of depth and range steps in the grid. Each point $[i j]$ in the grid thus conceptually corresponds to a four element vector called a quad (q) which has the following four values:

$$q_{ij} = D_g[i], R_g[j], t_1[i, j], t_2[i, j] \quad (3.22)$$

where $D_g[i]$ is the depth implied by the depth grid index i . $R_g[j]$ is the range implied by the range grid index j . t_1, t_2 are the two modified TDOAs given by $t_1 = T_1 - T_0$, and $t_2 = T_2 - T_0$, and stored in positions $\mathbf{Q}[1, i, j]$ and $\mathbf{Q}[2, i, j]$ respectively, where T_0, T_1, T_2 are the ordered travel times of the first three resolvable paths such that $T_0 < T_1 < T_2$. Namely

$$t_2 > t_1. \quad (3.23)$$

The vectors D_g and R_g are the depth and range grid scale vectors

$$D_g = D_{g0} + \Delta D \cdot (0, 1, 2, \dots, N_d - 1) \quad (3.24a)$$

$$R_g = R_{g0} + \Delta R \cdot (0, 1, 2, \dots, N_R - 1) \quad (3.24b)$$

with D_{g0}, R_{g0} the initial grid points at shallow depth and short range, and $\Delta D, \Delta R$ are the grid step sizes.

c. Interpolation

Linear interpolation of the TDOA values for points of the DR grid is used to provide a continuous TDOA function of the DR position. The values of the $t_1(t_2)$ depth and range of the three quads

$$q_{i_1 j_1}, q_{i_2 j_2}, q_{i_3 j_3}$$

which form the closest triangle that surrounds an input point $D_{in}R_{in}$ on the DR plane, are used to linearly interpolate the $t_1(t_2)$ values at that point. Two linear planes of the form

$$\tau_\ell = A_\ell D + B_\ell R + C_\ell \quad (3.25)$$

are formed in the $t_1 DR$ and $t_2 DR$ subspaces as follows.

$$\tau_\ell[i_1 j_1] = A_\ell \cdot D_1 + B_\ell R_1 + C_\ell \quad (3.26a)$$

$$\tau_\ell[i_2 j_2] = A_\ell D_2 + B_\ell R_2 + C_\ell \quad (3.26b)$$

$$\tau_\ell[i_3 j_3] = A_\ell D_3 + B_\ell R_3 + C_\ell. \quad (3.26c)$$

If one defines the vector τ_ℓ as

$$\tau_\ell = \tau_\ell[i_1 j_1], \tau_\ell[i_2 j_2], \tau_\ell[i_3 j_3] \quad (3.27)$$

where $\ell = 1, 2$, then Eq. (3.26) can be written in matrix form as

$$\tau_\ell = \begin{bmatrix} D_1 & R_1 & 1 \\ D_2 & R_2 & 1 \\ D_3 & R_3 & 1 \end{bmatrix} \begin{bmatrix} A_\ell \\ B_\ell \\ C_\ell \end{bmatrix}. \quad (3.28)$$

Solving for the parameters one obtains

$$\begin{bmatrix} A_\ell \\ B_\ell \\ C_\ell \end{bmatrix} = \begin{bmatrix} D_1 & R_1 & 1 \\ D_2 & R_2 & 1 \\ D_3 & R_3 & 1 \end{bmatrix}^{-1} \tau_\ell. \quad (3.29)$$

The plane parameters the $t_1 t_2$ at any specific point $D_{in}R_{in}$ can be interpolated with the formula

$$t_1 = [A_1 \ B_1 \ C_1] \cdot [D_{in} \ R_{in} \ 1]^T \quad (3.30a)$$

and

$$t_2 = [A_2 \ B_2 \ C_2] \cdot [D_{in} \ R_{in} \ 1]^T \quad (3.30b)$$

as shown graphically in Fig. 3.9.

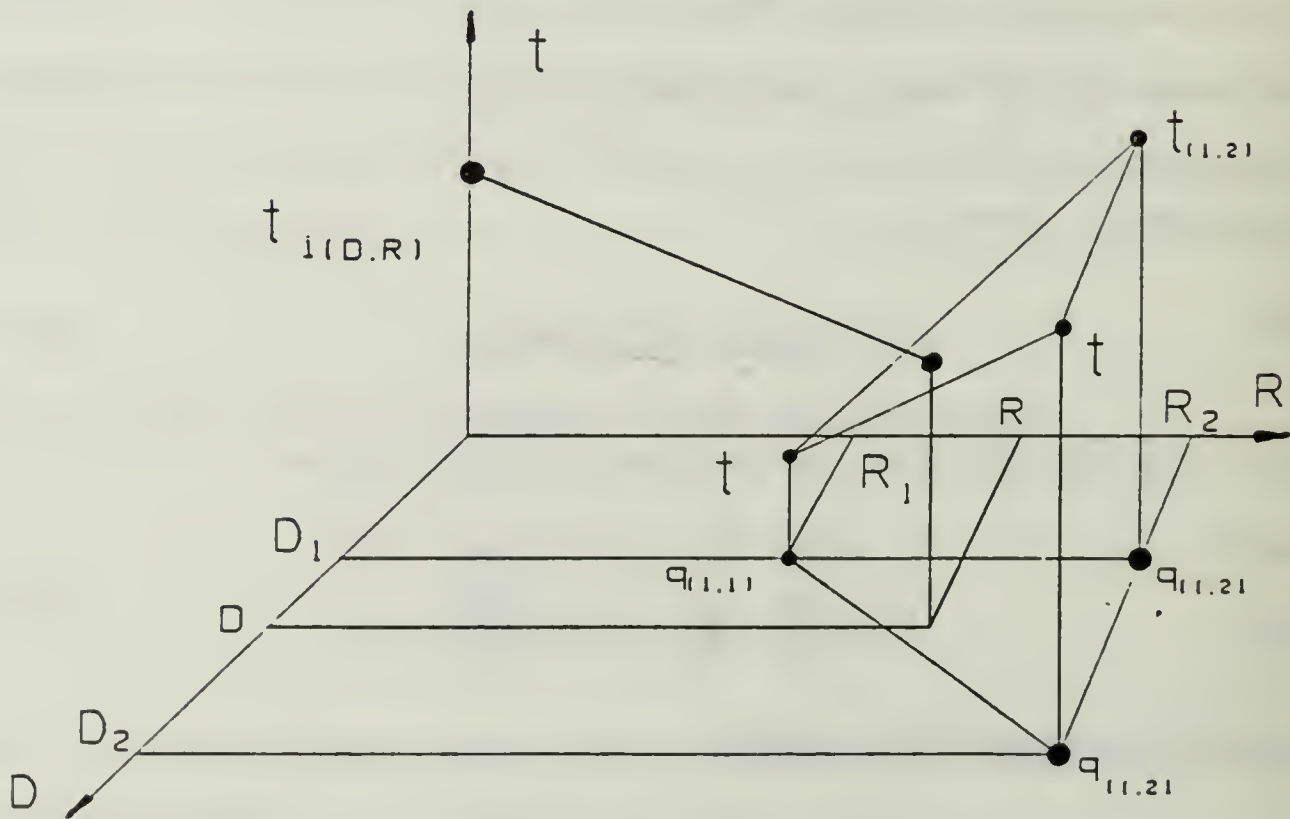


Fig. 3.9. Linear interpolation.

The ordering of the tabulated discrete direct function according to depth and range enables finding the triangle of closest quads by rounding the input $D_{in}R_{in}$ to the closest DR grid values.

d. Implementation

SMART is a proprietary product which was obtained for this research in a form executable on an IBM personal computer. The travel time data generated by this program was transferred to a large mainframe computer (IBM). Here, the rest of the processing in steps 2 through 5 and the target tracking simulations were performed. The mainframe was selected primarily because of its good APL interpreter and the excellent engineering graphics support provided by GRAFSTAT [Ref. 27].

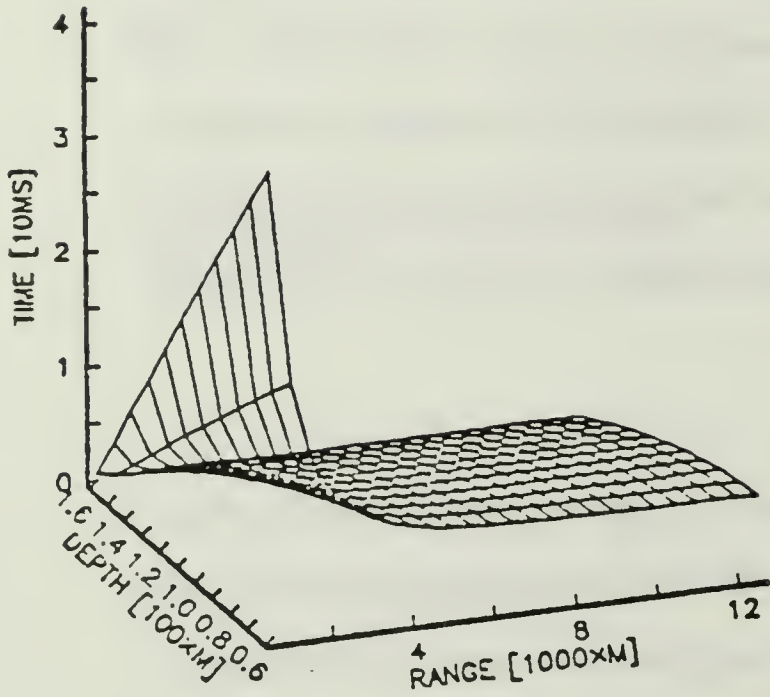
3. TDOA of IH Surfaces

Two examples of the resulting interpolated discrete direct function surfaces are presented here. The form is the same as that used for the homogeneous cases presented in Section B. The cases are coded using the casename code described in Appendix E.

An inhomogeneous finite resolution nonassociable case (A2251) is presented first. The TDOA surfaces of SVP with a positive surface gradient of 0.05 sec^{-1} and very high delay resolution (0.05 ms) are shown in Fig. 3.10. Note that the DR grid only covers the first 100 m of the 500 m water column. The contour plot of the t_1 surface for the homogeneous case (case S2251) was shown in Fig. 3.7.

While the basic trends of the $t_1 t_2$ surfaces are similar for homogeneous and IH cases, the specific TDOA values differ. This can be seen most distinctively on the contour plot for t_1 which here happens to be the delay between the surface bounce and the direct path, and is in general longer than the t_1 produced by straight line propagation. The difference results from the fact that the average speed of sound is smaller along the IH surface bounce path than along the homogeneous surface bounce. The bottom bounce lag t_2 is less affected since the most of its path is in the region below the observer where the speed of sound is constant and identical

SECOND TO FIRST ARRIVAL



THIRD TO FIRST ARRIVAL

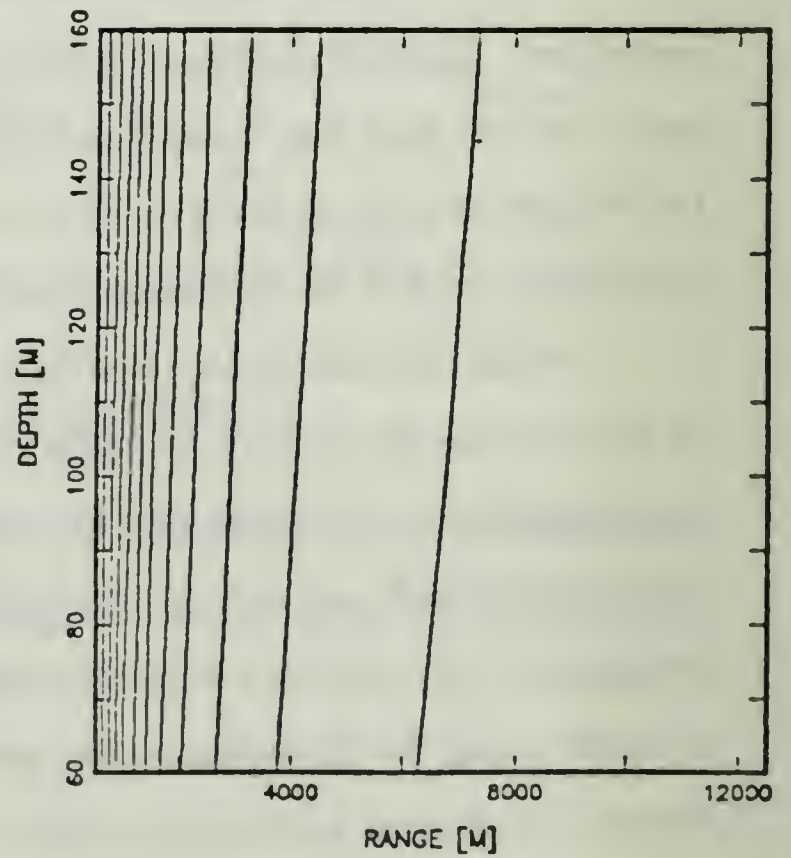
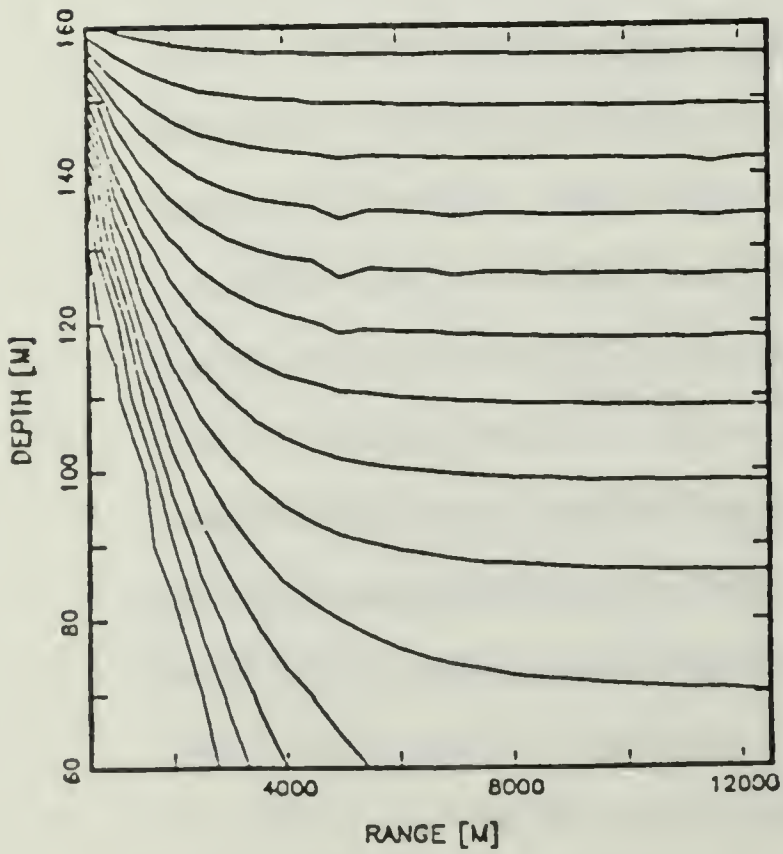
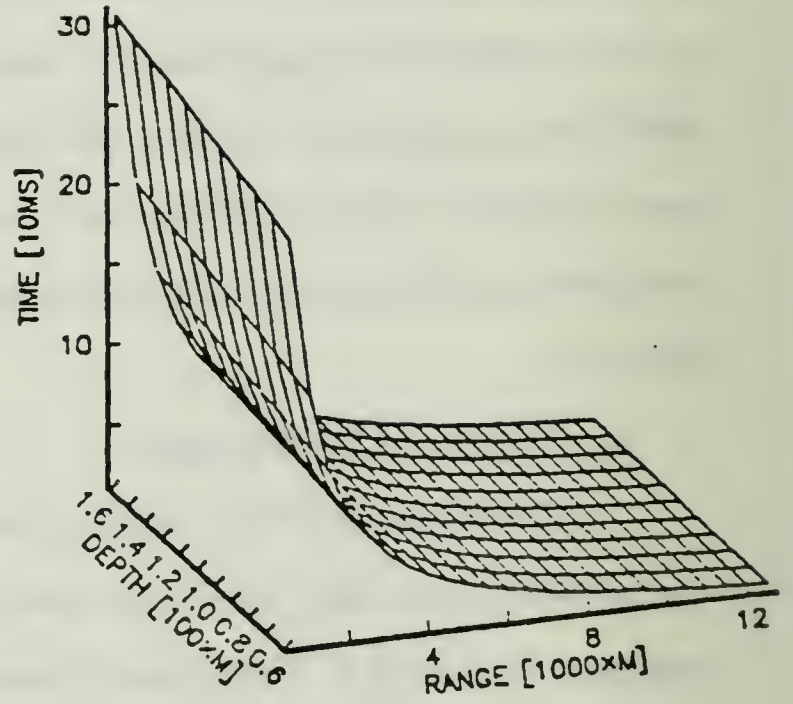


Fig. 3.10. Inhomogeneous TDOA surface (A2251).

in both cases. The TDOA surfaces for the same medium conditions, but with a finite delay resolution of 0.5 ms (Case 2251), are shown in Fig. 3.11. The inability to resolve the surface bounce is clearly seen along the first depth grid line of both TDOA plots.

4. 2-D Function Inversion

a. Overview

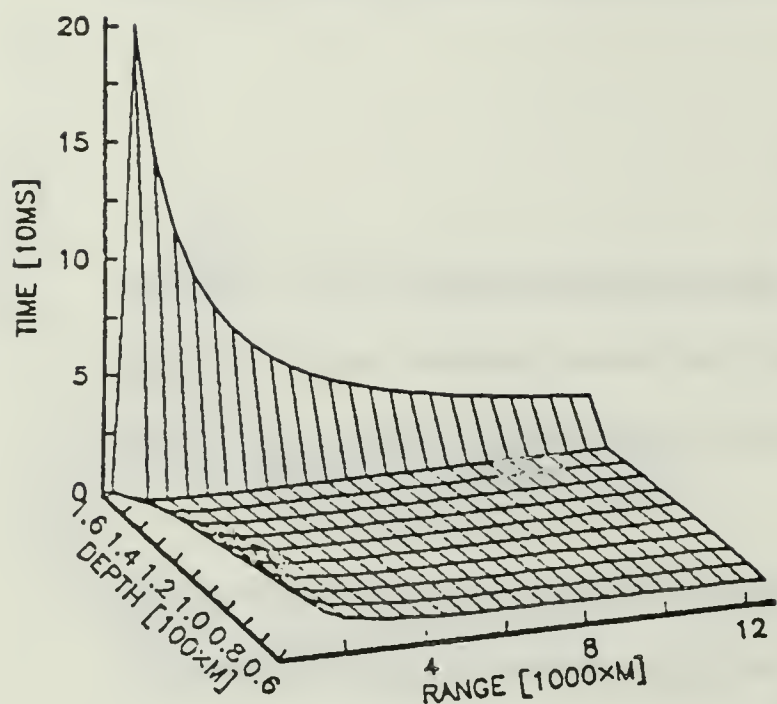
The inversion algorithm is an on-line transformation of a 2-D TDOA input measurement vector into a 2-D depth and range position vector DR. The time delays need not, and in most cases *do not*, coincide with points on the direct function generating grid.

The task can be stated graphically when the 2-D transformations are viewed as mappings between the position and delay planes. The direct function maps constant depth and range lines (DR grid) into curved contours on the $t_1 t_2$ plane; the inverse function maps a $t_1 t_2$ grid into curved contours on the depth range plane. The inversion task is thus defined as finding the intersection of the inverse mapping $t_1 t_2$ contours and reading its DR coordinates.

Typical inverse mappings of constant $t_1 t_2$ on the DR plane were shown in Fig. 3.12 graphically demonstrating the inversion process. Two contours corresponding to t_1 value of 7.5 ms and t_2 values of 30 and 50 ms are shown on Fig. 3.12. One intersection of the 7.5 and 30 ms contours is shown (a). Four intersection points of the contours corresponding to $t_1 t_2$ values of 7.5 ms and 50 ms are shown (b through e). The multiple intersections indicate the inherent ambiguity of the realistic case which was discussed in Sec B.

Typical direct mappings of constant depth and range (DR grid) into the $t_1 t_2$ plane are shown in Fig. 3.13a. These contours are computed using ideal straight line propagation. From Eq. (2.106) it is clear that the depth is

SECOND TO FIRST ARRIVAL



THIRD TO FIRST ARRIVAL

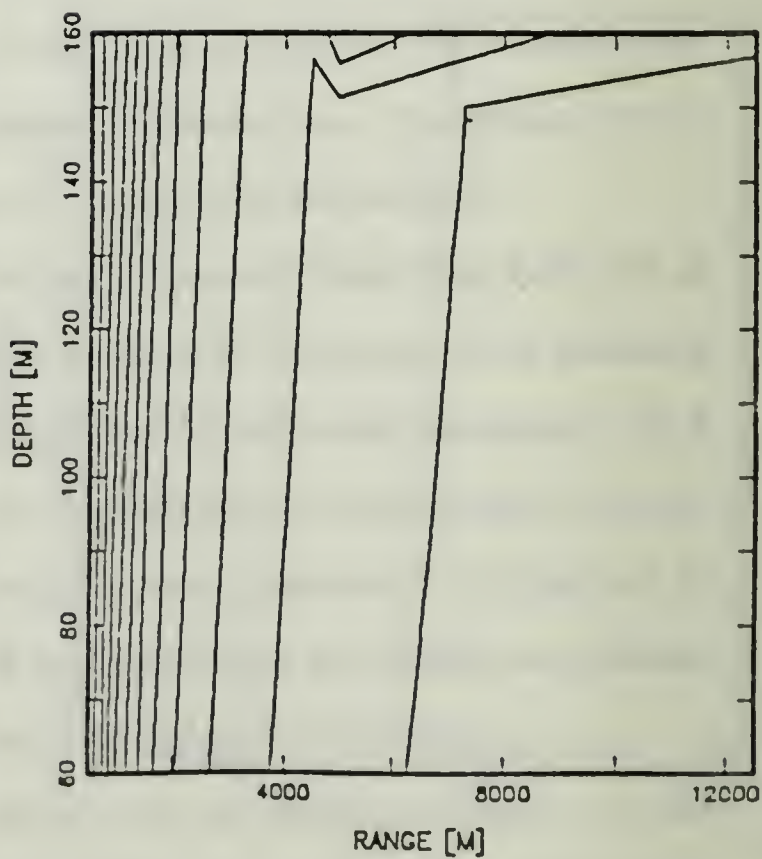
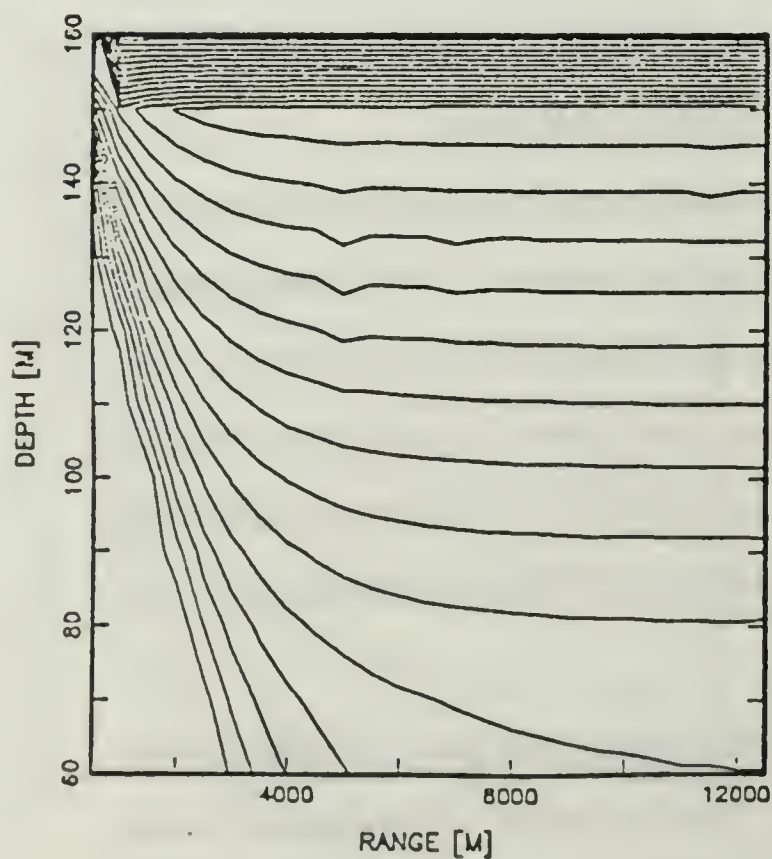
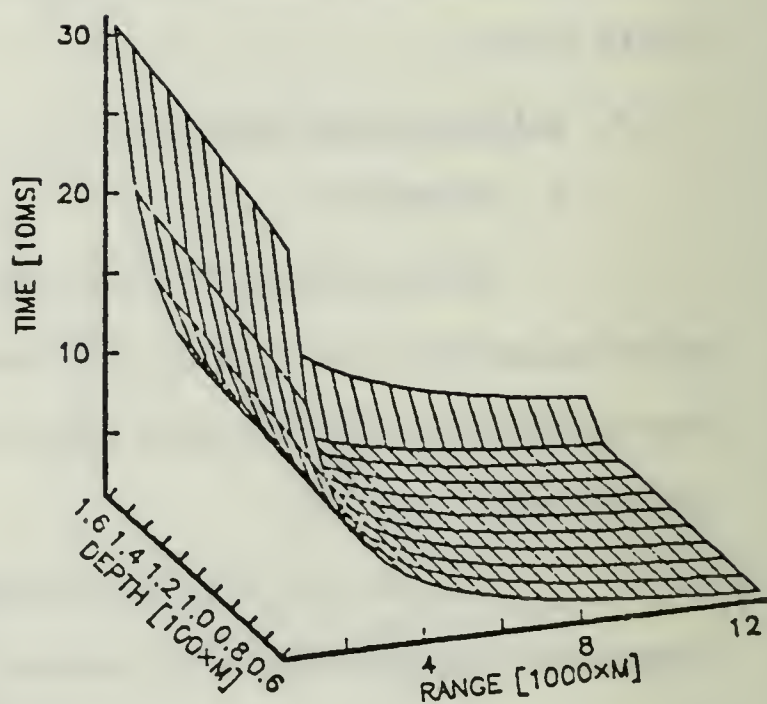


Fig. 3.11. Inhomogeneous and unresolvable TDOA (C2251).

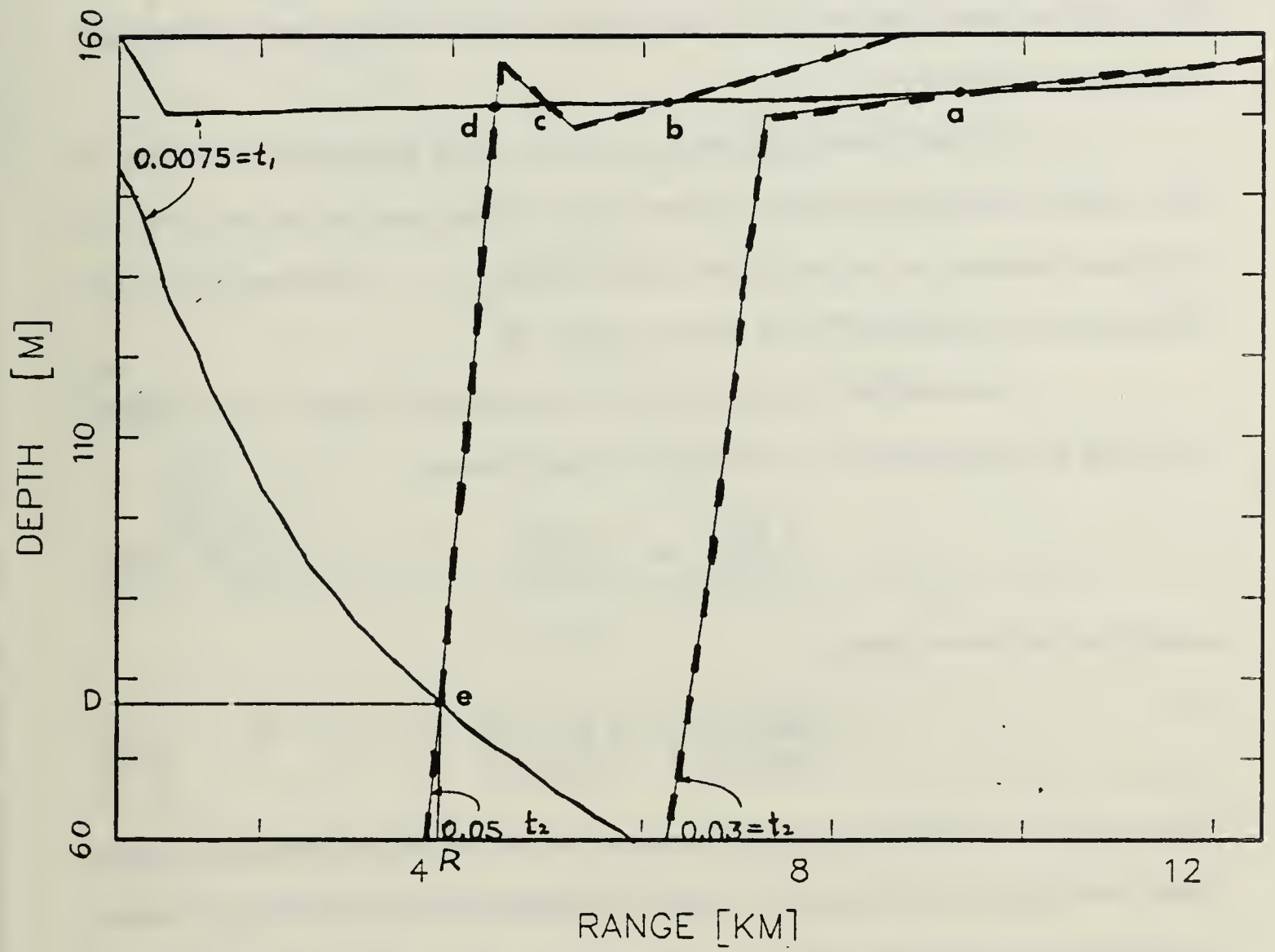


Fig. 3.12. Graphical inversion.

dependent on the ratio τ_1/τ_2 while the range is dependent on the weighted sum $(D_w - D_o)\tau_1 + D_o\tau_2$. This dependence explains the straight line nature of the inverse direct mapping. The dots along the contours of Fig. 3.13 represent quads. The depth and range are defined by the contours and the TDOAs are the Cartesian coordinates of the dots.

A typical direct mapping of quads for an IH realistic case is shown in Fig. 3.13b. Note that the order of the points on the plane is lost and that the points are restricted to the half plane defined by the $t_2 > t_1$. This results from the definition of the modified TDOA (Recall Section B).

A cornerstone of the inversion is the fact that a quad q_{ij} is in itself invertible in the sense that it provides the transformation

$$\begin{pmatrix} t_1 \\ t_2 \end{pmatrix}_{[ij]} = f \begin{pmatrix} D[i] \\ R[j] \end{pmatrix} \quad (3.31)$$

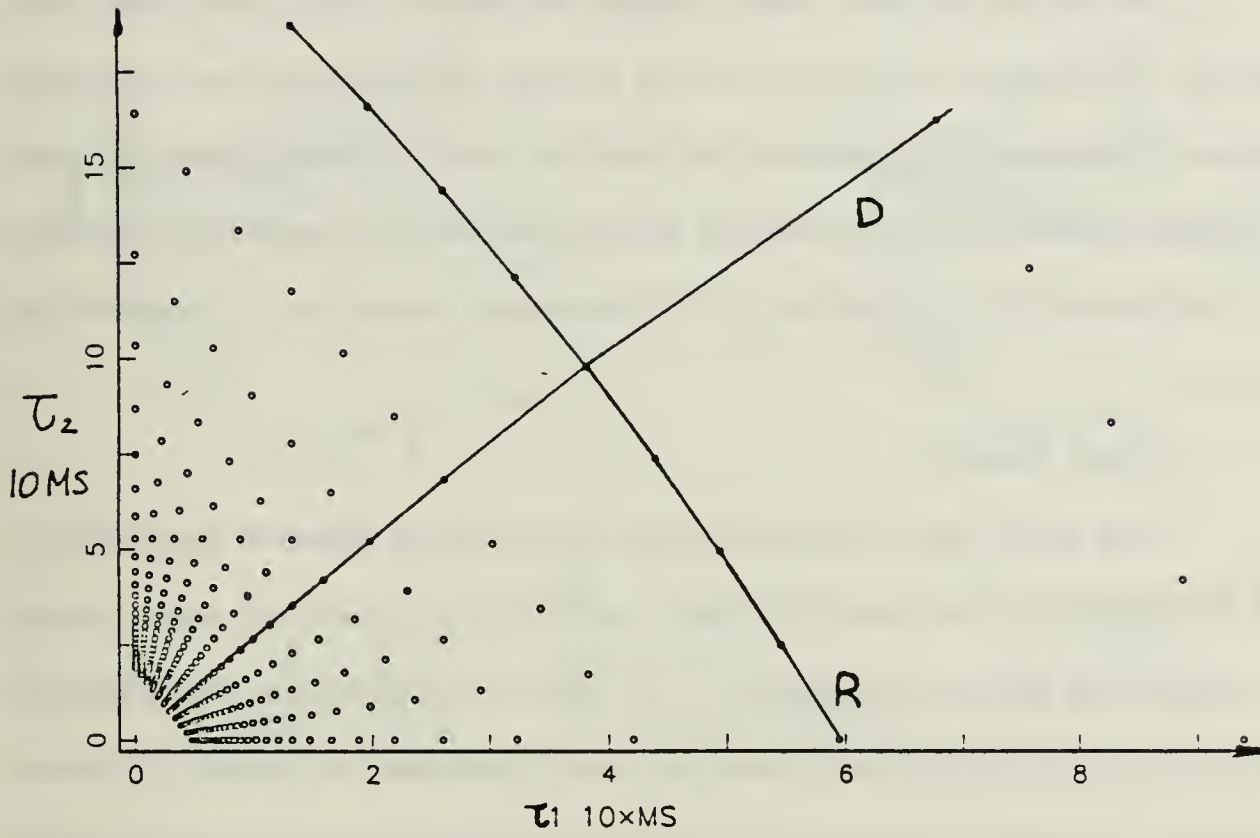
as well as the inverse relation

$$\begin{pmatrix} D[i] \\ R[j] \end{pmatrix} = f^{-1} \begin{pmatrix} t_1[i, j] \\ t_2[i, j] \end{pmatrix}. \quad (3.32)$$

The quads can therefore be viewed in reverse, namely as defining depth and range values over the $t_1 t_2$ delay plane. Linear interpolation can be called upon again to compute depth and range values at $t_1 t_2$ points which do not coincide with any quad.

Although the inversion procedure seems theoretically quite simple, its practical implementation is complicated by the following fact: the quads in the \mathbf{Q} array are not ordered on the $t_1 t_2$ plane as they are on the DR plane grid. This is especially true for the realistic IH case as shown in Fig. 3.13b. The search for the three interpolation quads is therefore much more elaborate than the simple rounding procedure used for the direct interpolation. The retrieval of the quads

a. MAPPING DR GRID INTO T_1T_2 PLANE (U1111)



b. MAPPING DR GRID INTO T_1T_2 PLANE (S1111)

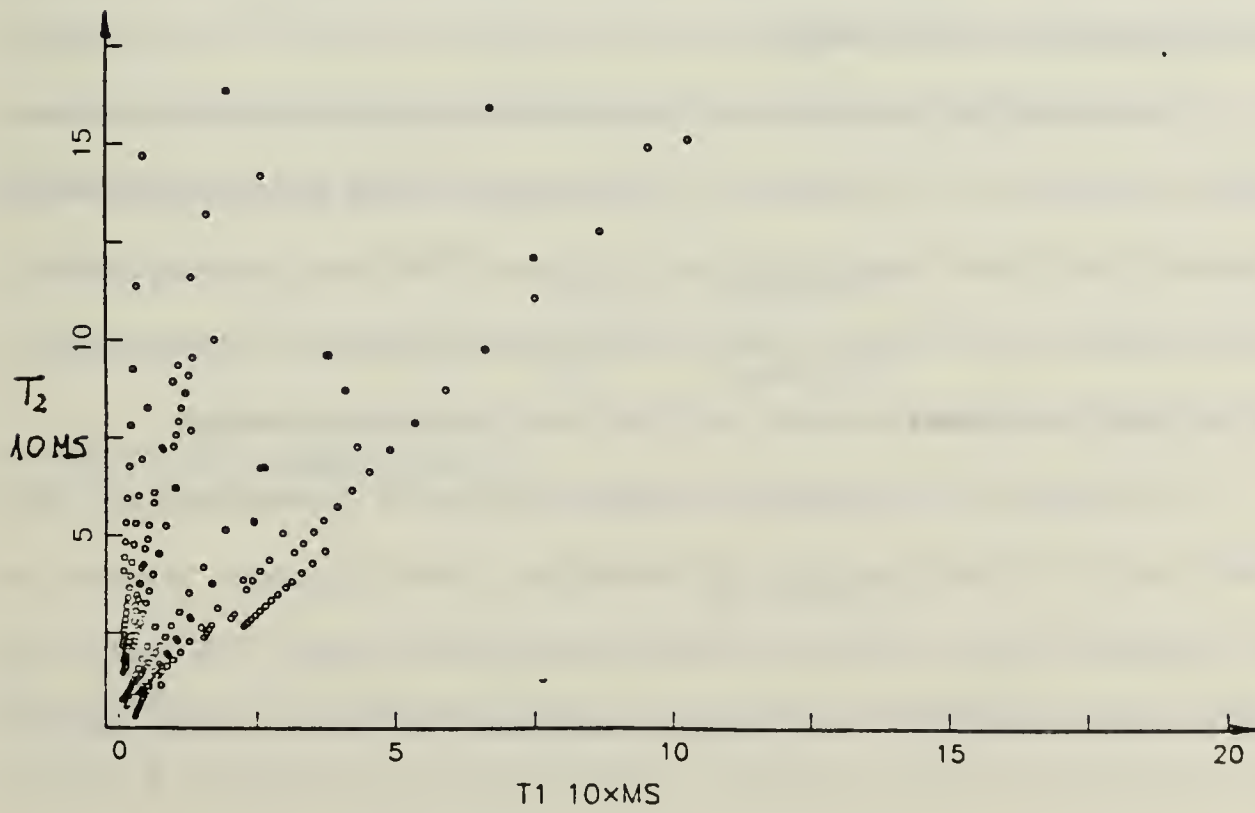


Fig. 3.13. Depth range mappings.

here involves a search which is drastically effected by the ambiguity of the surfaces. The search is described in the next section.

Once an appropriate quad triangle is located, depth and range are interpolated. If multiple solutions are found one has to be chosen and reported as an output. The complete procedure includes the search, the interpolation, and the ambiguity resolution. The inversion is defined here as the *inversion* procedure (which is performed by the prefilter). The inversion procedure is described in Section C.4.

b. TDOA Search

Every three direct function quads, each relating values of depth D (or range R) to delays $t_1 t_2$ can specify a plane in the $D t_1 t_2$ (or $R t_1 t_2$) space which can be used for the inverse interpolation. In order to improve the interpolation accuracy, only quads forming small triangles which surround the input $t_1 t_2$ point are considered. The total number of combinations of three quads out of the total $(ND \times NR)$ quads is $\frac{(ND \times NR)!}{3!}$. This makes exhaustive search for the smallest surrounding triangle an impossibility.

Since different triangles produce different interpolation results, successive prefilter iterations for the same $t_1 t_2$ point, may produce different depth and range values if the selected triangles are not the same. This is an undesirable situation. For example, a static target could produce changing position measurements, causing the target tracker to respond as if the target were maneuvering.

The impact of a nonunique triangle selection is demonstrated in Fig. 3.14. Part c and e of the figure show the same four quads ($q_1 q_2 q_3 q_4$) grouped in different triangles together with the resulting interpolated range. The quads are placed on a cartesian grid for clarity purposes only and the values marked near the

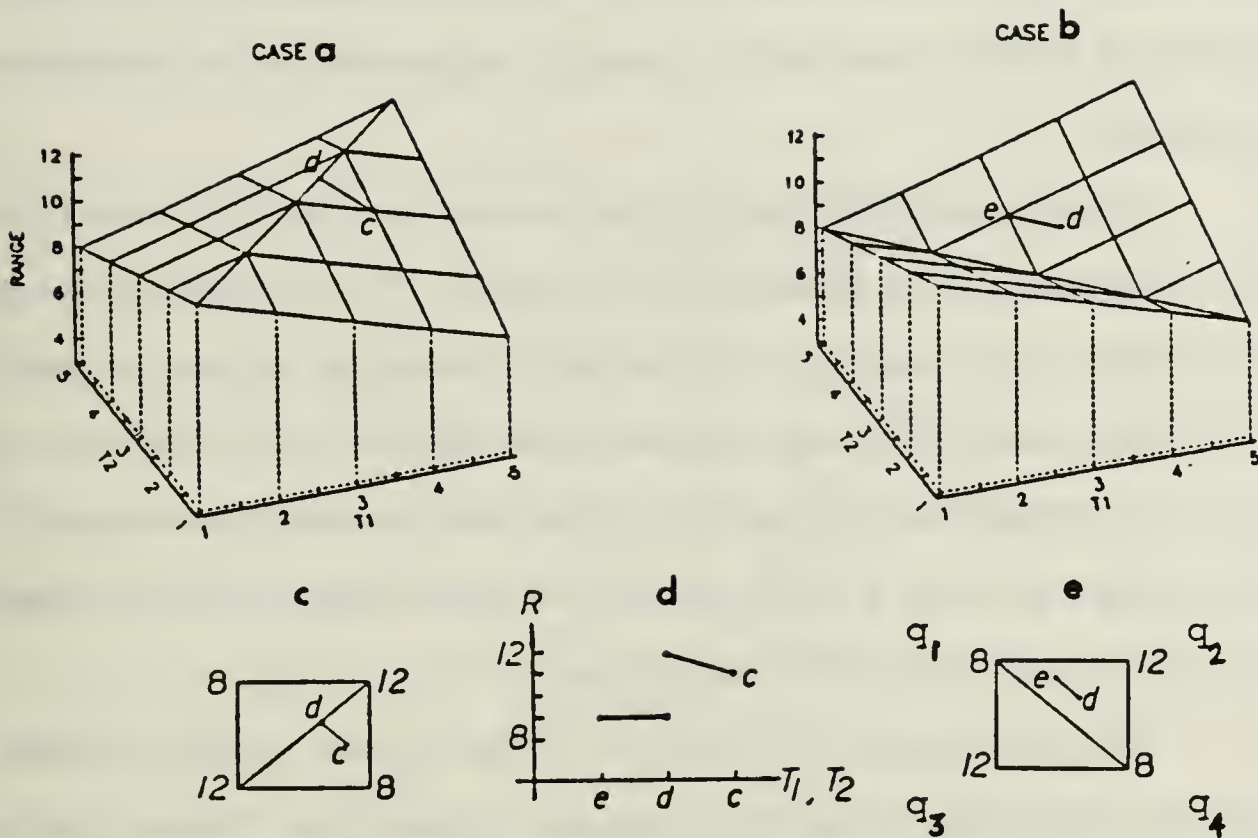


Fig. 3.14. Non-unique triangle selection.

quads (8 and 12) are the range values of the quads. Three interpolation triangles can be selected for range interpolation for a target moving from point e to point c. These triangles are the set (case A)

$$Tri1 : (q_3, q_2, q_4)$$

$$Tri2 : (q_1, q_3, q_2)$$

or the single triangle (case B)

$$Tri3 (q_1, q_3, q_4) .$$

Selecting $Tri1$ for target position e to d and $tri2$ for position d to c (case A) will provide a continuous range interpolation. Selecting $tri3$ for the complete trajectory

a to c will also yield continuous interpolation (a constant). Selecting *Tri3* for positions e to d followed by *tri2* for d to c will result in the discontinuous interpolated range shown in d. This discontinuity in range is troublesome for the maneuvering target tracker.

The uniqueness problem has two aspects. One part of it results from the unordered nature of the points on the t_1t_2 plane. This part can be overcome by constructing unique triangles either for the whole grid at one time or locally, when and where needed using some algorithm. An example of this problem is the fact that every triangle that surrounds the input point can itself be surrounded by another yet larger triangle. A simple rule of choosing the smallest possible triangles (for example by area) could solve this problem.

The other aspect of the problem, is the inherent ambiguity resulting from the non-monotonicity of the direct function. This ambiguity, discussed earlier, is demonstrated here again with an emphasis on its relation to the triangle selection. Six quads marked q_1 through q_6 are shown mapped on the t_1t_2 plane in Fig. 3.15a with the corresponding depth values as the vertical axis. The folding surfaces formed by the quads helps one understand the name Manifold by which they are called. As expected, the non-monotonicity of the direct function results in two possible interpolation triangles *tri1*: (q_1, q_2, q_3) and *tri2*: (q_4, q_5, q_6) for an input point-p. The problem arises because both triangles are "valid." Any attempt to resolve the dilemma by constructing a "unique" triangular grid like the sample in Fig. 3.15b may create wrong interpolating triangles by mixing delay values from two separate areas of the non-monotonic function (e.g. q_2, q_4, q_3).

The two triangles represent two separate areas on the DR plane for which the particular MP structure generates similar delay values t_1t_2 . This is caused by the following combined effects: the IH propagation; the limited resolution

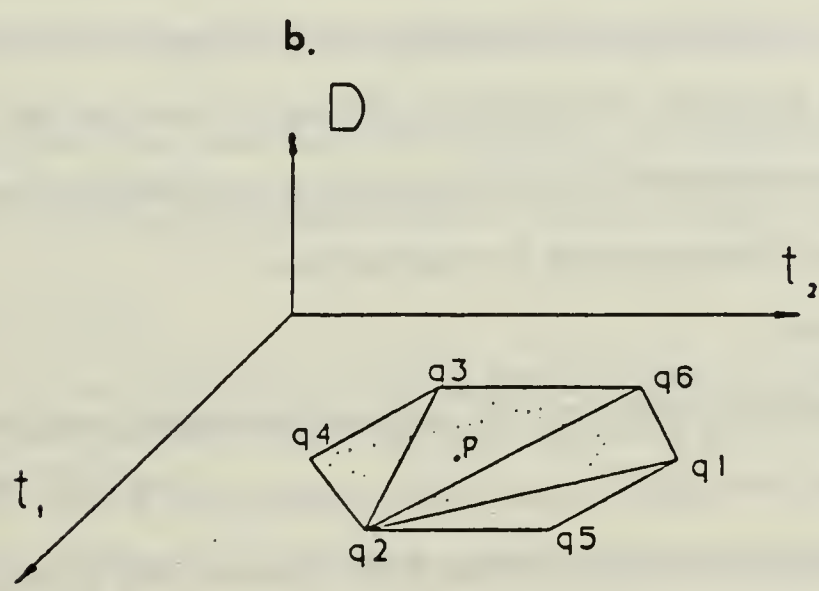
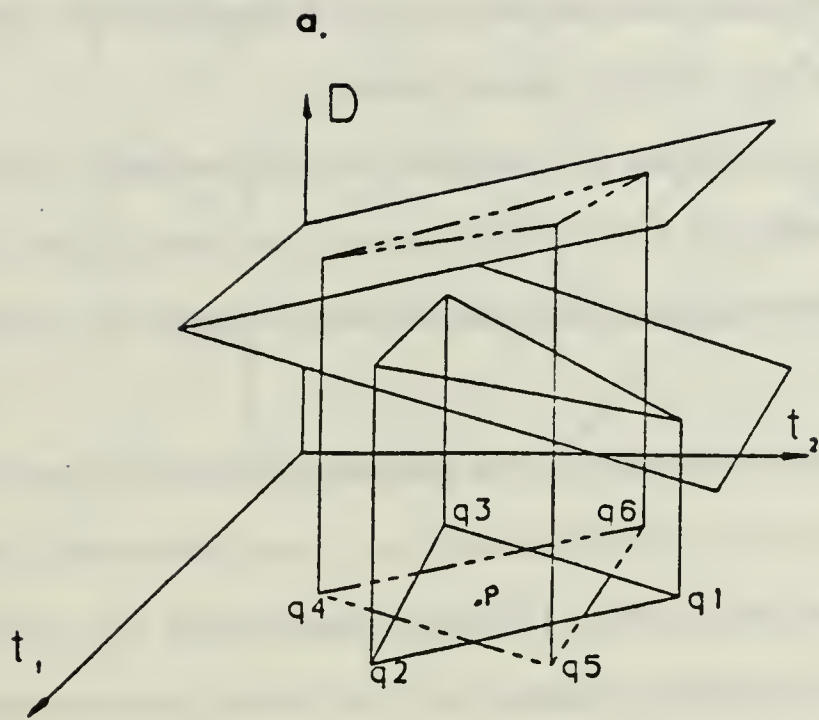


Fig. 3.15. Ambiguous triangle selection.

receiver; and primarily the lack of path delay association and the corresponding assumed instrumentation logic (described in Section B). The triangles selection mechanism that is used, has to retain the option of selecting both triangles *tri1* and *tri2* since they are both valid for interpolation.

Attention is directed at this point to the fact that while *tri1* and *tri2* are partially overlapping in the TDOA plane, they are disjoint in the DR plane. This difference is significant and is used later to assist in the selection of the triangles.

An algorithmic solution to the general problem of uniquely selecting a triangular grid over a set of unordered points in a plane does exist. Surprisingly enough, it was developed only recently (1975) by Shamos [Ref. 28]. The solution is elaborate and involves a geometric construction but it does guarantee unique triangles. However it does not solve the above mentioned problems of eliminating valid and creating nonvalid triangles. The Shamos solution is therefore not applicable for the problem of non-monotonic function inversion and a different new approach had to be devised here. This approach is described next.

c. DR Search

The difficulties encountered in selecting triangles resulted from the unordered scattering of the quads in the TDOA plane (Fig. 3.13b). On the DR plane the quads are ordered on the Cartesian grid. Constructing a unique disjoint set of triangles which exhaustively covers the depth range plane is trivial and can be done by splitting each rectangle of the DR grid into two triangles using parallel diagonal lines as shown on Fig. 3.16. The set of triangles thus formed is defined as the DR triangles space. A key idea in the search is to consider only triangles

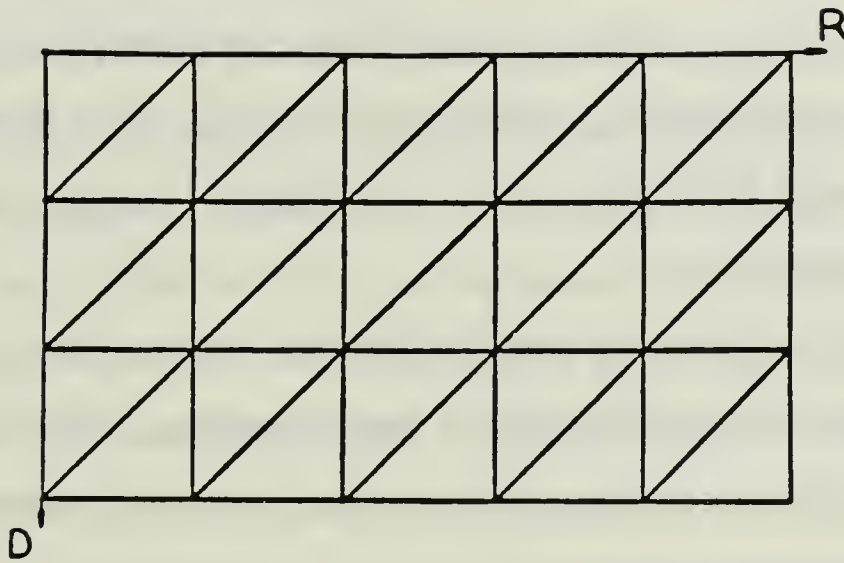


Fig. 3.16. Unique valid DR triangle set.

in the delay plane that arise from the mapping of triangles from the DR triangles space. This delay triangles space has the following distinct advantages:

1. The set is unique.
2. The set is completely valid. That is, the triangles are locally the smallest and will not be constructed by erroneously grouping quads from disjoint areas of the direct function.
3. The set is sufficient. That is, the option of choosing all valid TDOA triangles is maintained.
4. The search space size is significantly reduced. The number of possible triangles is reduced from $\frac{(N_d \cdot N_r)!}{3!}$ to $2 \cdot N_d \cdot N_r$. This is a reduction from order $O(n!)$ to order $O(n)$.
5. Construction of the set is trivial and does not require computation.
6. The set facilitates an efficient structured search. The search for the surrounding TDOA triangle can utilize the structure of the underlying DR grid in an effective binary type search.

Viewed in the context of the graphical statement of the inversion problem (Fig. 3.12) the search now is for the DR triangle that surrounds the intersection point of the t_1, t_2 contours of the inverse function on the DR plane. The existence of a solution is conditioned by the monotonicity of the direct function over the region of the triangle which dictates that the DR grid be made smaller than the minimum monotonic region.

Since the DR grid of quads is Cartesian, searching for a minimum rectangle that contains the desired triangle is more convenient. After the surrounding rectangle is found the specific triangle(s) can then be located by examining the two triangles that make up the rectangle.

d. Localized Search

Finding the particular triangle in the total set of $2 \cdot N_d \cdot N_r$ grid points that surround the $t_1 t_2$ input measurement point requires further searching. The test to see if the point is within a triangle,* involves some computation and the search space, though reduced can be still very large. Hence the possibility of exhaustively considering all the triangles is not desirable. A binary-type search made possible by the DR ordered grid structure can reduce the average computation load. In addition it can focus the attention on the area where the solution is most likely to be found.

A place at which to start the search (a root) is provided by the target tracker predicted position. If a target state vector has already been established, then the next target measurement is most likely to be found in the vicinity of the predicted DR position. Starting the search with the rectangle that surrounds the predicted position is only the natural choice.

* The test, referred to as the inversion test is described later.

The Q array indexes required to retrieve the quads associated with this rectangle are produced, as they were for the direct function interpolation, by rounding to the closest DR grid values. If the rectangle that surrounds the predicted point also surrounds the $t_1 t_2$ point the search has produced the required triangle and it terminates. Upon failure, however, the search has to continue over a growing and more distant set of DR rectangles until a surrounding one is located. This *local* search ensures that the solution closest to the target will be found first. This significantly reduces the ambiguity inherent in the MP inversion.

Two different search strategies were designed and implemented for this purpose. The first, titled MEA (means ends analysis) is a directed search strategy common in artificial intelligence applications. The second method referred to as local search algorithm (LSA) is a breadth first type search performed in tiers of growing distance from the predicted point.

The MEA method performed very effectively for monotonic direct functions but failed in non-monotonic cases. The LSA algorithm performed very well for all cases and the computational load, usually associated with breadth first search, was reduced by an innovative dual phase evaluation algorithm. A brief description of the local search algorithm is presented next and a more detailed explanation of its components is presented in Appendix G. The system block diagram is shown in Fig. 3.17. Note the feedback of the predicted position as a root for the prefilter's local search.

e. The Local Search Algorithm (LSA)

Given the TDOA measurement point the goal of the LSA is to produce an interpolation triangle that surrounds the intersection of the inverse function $t_1 t_2$ contour lines. The search commences in a DR rectangle where the solution is most likely to be found, namely at the predicted target position. The search progresses

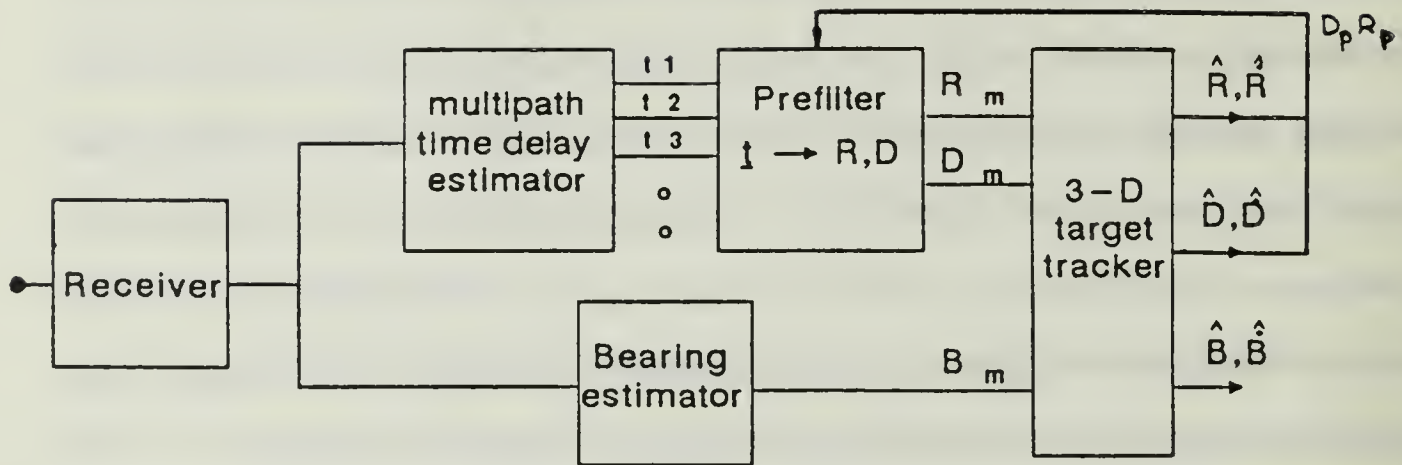


Fig. 3.17. System block diagram.

by increasing the rectangular search area until a solution is found or until the dimensions of the area have reached a specified maximum limit. Upon termination (success or failure) the algorithm reports the number of solutions found, the size of the area actually searched and the triangles found (if any).

The localized search is a part of the overall inversion algorithm. The inversion initiates and uses the outputs of the search to produce the desired measurement depth and range. The interface between the inversion and the search is given in Table 3.1.

A numerical analysis procedure, originally developed for finding zeros of complex functions (Hamming [29]) was modified to apply to the search. One test and two recursive procedures are used in the LSA, they are the inversion test the outward and the inward searches. The inversion test examines a given rectangular on the DR grid to find out if a solution may exist in it. The outward search

TABLE 3.1

LSA INTERFACE VARIABLES

LSA input:

$t_1 t_2$	Delay measurements (input point).
DR prd.	Target predicted position, depth range.
Max size	Maximum search area size ,depth range.

LSA output:

Num	The number of triangles found.
Area size	The size of area searched before the solution was found.
Solution	The quad triangles.

examines the current (input) rectangle using the inversion test. As long as the test fails (no solution in the current area) and as long as the maximum search area has not been reached, the search area grows outward. If the maximum area is reached and a solution was not found a failure is reported.

The inward search attempts to locate a solution inside a given rectangular area. It starts by performing the conditional inversion test on the entire area. If the test succeeds the area is divided to four quadrants and a solution is searched for in each quadrant by means of a recursive call to the inward search. The recursion terminates either when a 1×1 rectangle is reached, or when the test indicates that a quadrant does not contain a solution. If a 1×1 rectangle is formed, an additional surrounding test is performed on the two DR grid triangles that comprise that rectangle to determine which if any of them contains a solution. All the triangles thus found are reported as outputs to the inversion procedure for further processing.

The search as a whole is thus completed. The surrounding triangles closest to the predicted target position are reported to the inversion procedure

for the further processing which is discussed next. The local search algorithm is demonstrated in Fig. 3.18. Fig. 3.18(a) shows two iterations of the outward search initiated at point p . Fig. 3.18(b) shows three iterations of the inward which produce two solutions corresponding to the two intersections of the $t_1 t_2$ contour lines. A more detailed description of the LSA is presented in Appendix G including a detailed pseudo code description.

f. The Inversion

The inversion procedure performs the prefilter operation of transforming the input measurements TDOAs to depth and range measurements. It uses the direct function table and the local search algorithm described earlier. The inversion performs the following five tasks.

- Initialization of the search
- Interpolation
- Ambiguity resolution
- Failure handling
- Performance monitoring.

Each of these is described in more detail below.

(1) **Initiation of the Search Process.** The process is initiated by setting up the first 1×1 search rectangle and starting the outward search. The initial rectangle is set by quantizing the target predicted position to the closest DR grid position.

(2) **Interpolation.** Once the appropriate three quads are located, the depth and range need to be interpolated. Linear and bilinear interpolations were used.

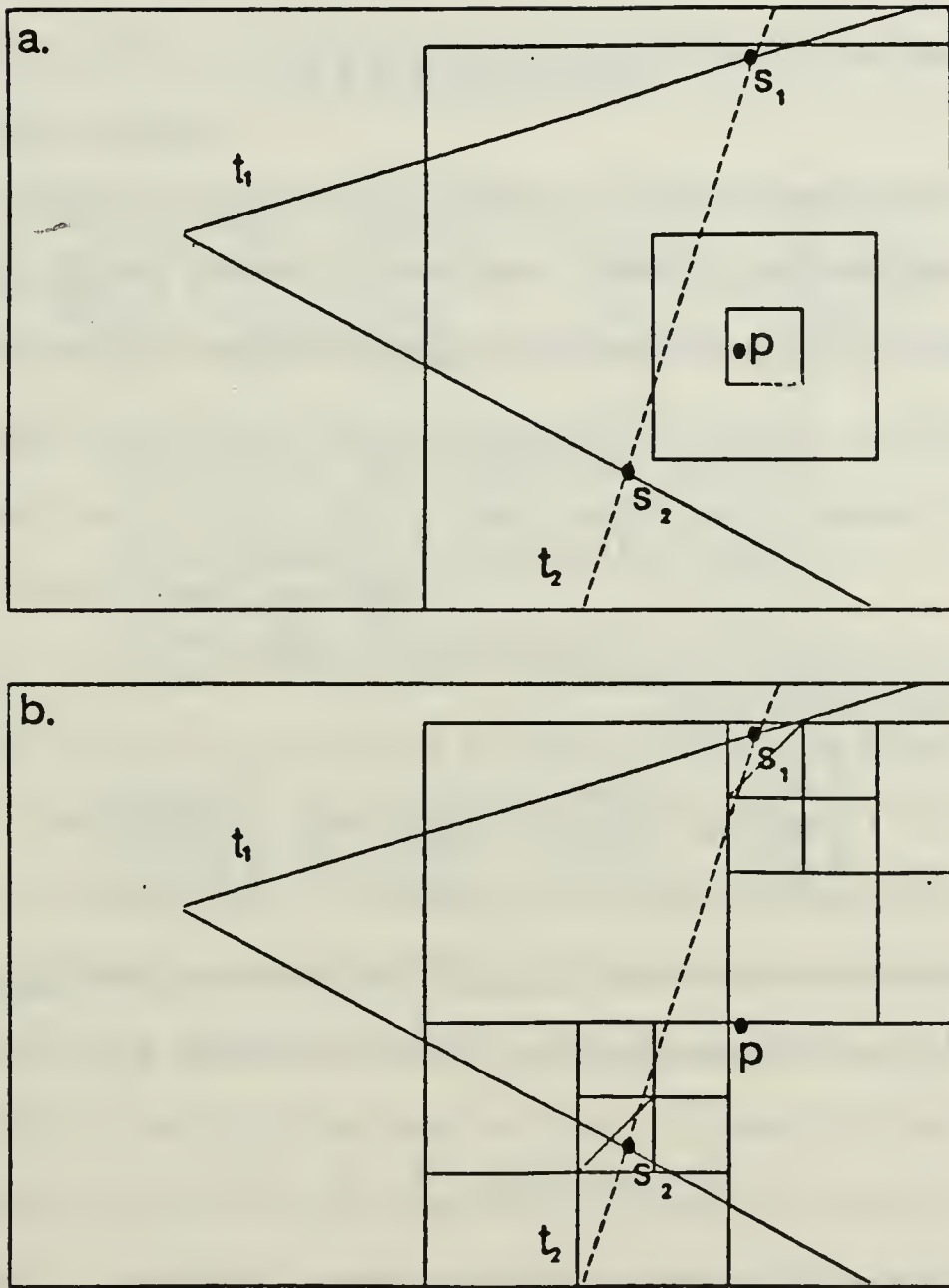


Fig. 3.18. Outward and inward search.

Linear interpolation is done in much the same way as the time delay interpolation is done. The interpolation equations are similar to those described earlier for the direct function interpolation. (See Section C.2.c.)

A linear plane in the depth (range) t_1, t_2 space of the form

$$D = A_d t_1 + B_d t_2 + C_d \quad (3.33)$$

is defined by the three quads $q_{i_1, j_1}; q_{i_2, j_2}; q_{i_3, j_3}$ where $q_{i,j}$ is defined in Eq. (3.22) and the subscripts index the three points of the selected triangle on the original depth range grid. The equations for the plane coefficients in the depth $t_1 t_2$ space are

$$\begin{aligned} D[i_1 j_1] &= A_d \cdot t_1[i_1 j_1] + B_d \cdot t_2[i_1 j_1] + C_d \\ D[i_2 j_2] &= A_d \cdot t_1[i_2 j_2] + B_d \cdot t_2[i_2 j_2] + C_d \end{aligned} \quad (3.34)$$

$$D[i_3 j_3] = A_d \cdot t_1[i_3 j_3] + B_d \cdot t_2[i_3 j_3] + C_d$$

which takes the matrix form

$$\begin{bmatrix} A_d \\ B_d \\ C_d \end{bmatrix} = \begin{bmatrix} t_1[i_1 j_1] & t_2[i_1 j_1] & 1 \\ t_1[i_2 j_2] & t_2[i_2 j_2] & 1 \\ t_1[i_3 j_3] & t_2[i_3 j_3] & 1 \end{bmatrix} \cdot \begin{bmatrix} D[i_1 j_1] \\ D[i_2 j_2] \\ D[i_3 j_3] \end{bmatrix} \quad (3.35)$$

from which the parameter vector $(A_d B_d C_d)^T$ can be solved. The depth (range) at the specific $t_{1_m} t_{2_m}$ measurement point can be interpolated as

$$D = (A_d B_d C_d) \cdot (t_1 \quad t_2 \quad 1)^T. \quad (3.36a)$$

And similarly for range

$$R = (A_r \quad B_r \quad C_r) \cdot (t_{1_m} \quad t_{2_m} \quad 1)^T \quad (3.36b)$$

with $A_r B_r C_r$ solved by an equation like Eq. (3.35) with $R[i, j]$ substituted for $D[i, j]$.

Bilinear interpolation was tested as well. The bilinear interpolating surface [Ref. 30] applied to depth interpolation takes the form

$$D = A_d \cdot t_1 + B_d \cdot t_2 + C_d \cdot t_1 \cdot t_2 + D_d. \quad (3.37)$$

The coefficients A_d, B_d, C_d, D_d of the bilinear interpolation can be determined by solving the matrix equation

$$\begin{bmatrix} t_1[i_1 j_1] & t_2[i_1 j_1] & t_1[i_1 j_1] \cdot t_2[i_1 j_1] & 1 \\ t_1[i_2 j_2] & t_2[i_2 j_2] & t_1[i_2 j_2] \cdot t_2[i_2 j_2] & 1 \\ t_1[i_3 j_3] & t_2[i_3 j_3] & t_1[i_3 j_3] \cdot t_2[i_3 j_3] & 1 \\ t_1[i_4 j_4] & t_2[i_4 j_4] & t_1[i_4 j_4] \cdot t_2[i_4 j_4] & 1 \end{bmatrix} \cdot \begin{bmatrix} A_d \\ B_d \\ C_d \\ D_d \end{bmatrix} = \begin{bmatrix} D[i_1 j_1] \\ D[i_2 j_2] \\ D[i_3 j_3] \\ D[i_4 j_4] \end{bmatrix}. \quad (3.38)$$

While linear interpolation uses a triangle formed by three quads, the bilinear interpolation requires a square of four quads. The closest square, however, is naturally produced by the local search algorithm.

(3) Ambiguity Resolution of Multiple Solutions. When multiple solutions exist in the search rectangle a choice is made among them by interpolating all of the candidate solutions and selecting the one closest to the predicted position (point S2 in Fig. 3.18). For a single linear measurement and a normally distributed measurement noise and prediction error, this solution will be the more likely one. Realistically the measurement is nonlinear, and the two measurements (depth and range) do not have the same variance. An alternative more rigorous choice would imply extensive computations that are expected to produce practically the same results. A potentially more rigorous approach to the overall ambiguity problem is discussed in Chapter Six.

(4) Failure Handling. A search can terminate without a solution for one of the following two reasons:

1. The measurement noise resulted in placing the t_1 t_2 input point outside of the maximum search area or even outside the complete DR grid.

2. The search area reached the maximum size without covering the actual measured source position.

When an inversion triangle is not found, the predicted target position is returned by the inversion procedure as an output. This can be thought of as a lack of innovation in the current measurement, and effectively reduces the sampling rate of the system. The tracker performance degrades as a result. When the search failure occurs infrequently (low failure rate) only the response to fast target maneuvers is hampered. Frequent failures (high failure rate) can lower the effective sampling rate of the observer below the Nyquist rate required to sample the target's dynamics. This drastically reduces the quality of the tracking. Frequent failures are unfortunately fed back in the form of search areas centered around the wrong target position. This in turn increases the chances of failure and eventually leads to a complete loss of tracking. A large maximum search area limit will reduce this effect, but requires increased on-line computation. The maximum search area limit is thus a key system parameter which needs to be optimized for the prevailing noise conditions and the available computational resources.

In experimental simulation of the MP tracking system the overall effect of the inversion failure was surprisingly gradual and meaningful tracking of maneuvering targets was demonstrated with up to a 50% failure rate. The robust performance can probably be attributed to a more-or-less symmetric delay error distribution. In such cases the elimination of the extreme measurement errors at either ends of the distribution caused by the failure does not affect the mean depth and range values. Therefore, as long as the tracking errors are not large and the search area is centered properly around the predicted position, the impact of eliminating extreme delay measurements is mild.

(5) **Prefilter Performance Monitoring.** The inversion procedure also monitors the performance of the search by averaging the number of solutions and the search area size. The averaging is done by means of an autoregressive lowpass filter. The average solution count should ideally be one, a lower value indicates search failures, while a higher count indicates ambiguity. The search area average helps optimize the maximum search area and is a measure of the load associated with the search. It also provides a good indication of the effects that delay measurement noise has on the search. The solution count and the area size proved to be very useful in the overall system performance evaluation.

g. 2-D Function Inversion Summary

A 2-D function inversion algorithm was devised, capable of translating realistically estimated MP TDOA generated by an IH medium to source depth and range position. An eigenray acoustic model identifies and precomputes the travel time of rays to the receiver from hypothetical targets placed at the coordinates on a depth range grid. The travel time is transformed to TDOA using an assumed, ACF based, realistic receiver and delay estimation instrumentation and stored in a tabulated direct function. The inversion is performed by inverse interpolation over three or four relevant points in the grid located by means of a special local search algorithm (LSA). A total of three prefilters were programmed. They were numbered with prefilter numbers (PFN) 4 through 6 (see Chapter Two, Section E). Prefilters PFN-4 used linear interpolation and the MEA search; PFN-5 used linear interpolation and the LSA. PFN-6 used bilinear interpolation and the LSA.

The procedure was carefully evaluated and the detailed evaluation scheme and results are presented in the next chapter. In general the performance

was good indicating that the procedure is suitable for incorporation into a multi-path tracking scheme.

IV. IMPROVED PREFILTER PERFORMANCE

An intensive evaluation of the prefilter was performed and the results are presented in this chapter. Section A discusses the motivation for the evaluation and some of the expected results. Section B presents the evaluation scheme. Section C contains a detailed presentation and analysis of the results.

A. MOTIVATION

The prefilter forms a central part of the overall MP target tracking system. Examining its performance is a necessary prerequisite to analysis of the overall system. The simulation has to provide all the realistic conditions under which the prefilter is expected to operate as a part of the MP tracker. In addition, the simulation conditions have to be separately controlled in order to isolate their impact on the prefilter. The effects of the following issues on the prefilter performance are investigated:

- Medium effects.
 - IH propagation.
 - Propagation loss.
 - Bottom depth errors.
- Delay estimation.
 - Delay noise bias.
 - Noise range dependence.
- Prefilter design
 - Grid size.
 - Interpolation errors.

The overall performance of the prefilter is expected to vary over the depth and range grid. This is due to the range dependence of the noise and the nonlinearity of both the inversion and the time delay estimation algorithms. To separate the effects the evaluation is performed over the entire 2-D grid in two steps. In the first step a range independent TDOA noise is assumed; in the second step the noise is range dependent.

The above nonlinearities give rise to two range bias errors. The first is a range underestimation bias which results from the overestimated TDOAs produced by the nonnegative effect (see Appendix D.) The other is caused by the delay to position transformation, which is inherently nonlinear. This second bias tends to overestimate the range, and is discussed next. The effect of both biases on depth is dependent on the particular MP structure.

An example of the effect of the nonlinear TDOA to range inverse transformation, is shown in Fig. 4.1. A section of the range dependence on t_1 for a constant value of t_2 is shown in Fig. 4.1a. A zero mean normal input noise distribution (Fig. 4.1c) is transformed to an asymmetric and non zero mean range distribution (Fig. 4.1b). The typically negative value of $\frac{\partial^2 R}{\partial t_1^2}$ leads to an overestimated range. This can be seen in Fig. 4.1b where the actual range is 1855 m and the mean is 2050 m.

Circles representing contours of a joint distribution of $t_1 t_2$ measurements* were transformed to the DR grid. The results, shown in Fig. 4.1d demonstrate the asymmetry of the DR measurement noise.

The inversion bias was studied by Moose [11] for the idealized homogeneous case. The combined opposing effect of the inversion and the nonnegative delay are

* $\sigma_{t_1} = \sigma_{t_2}$; t_1 and t_2 independent.

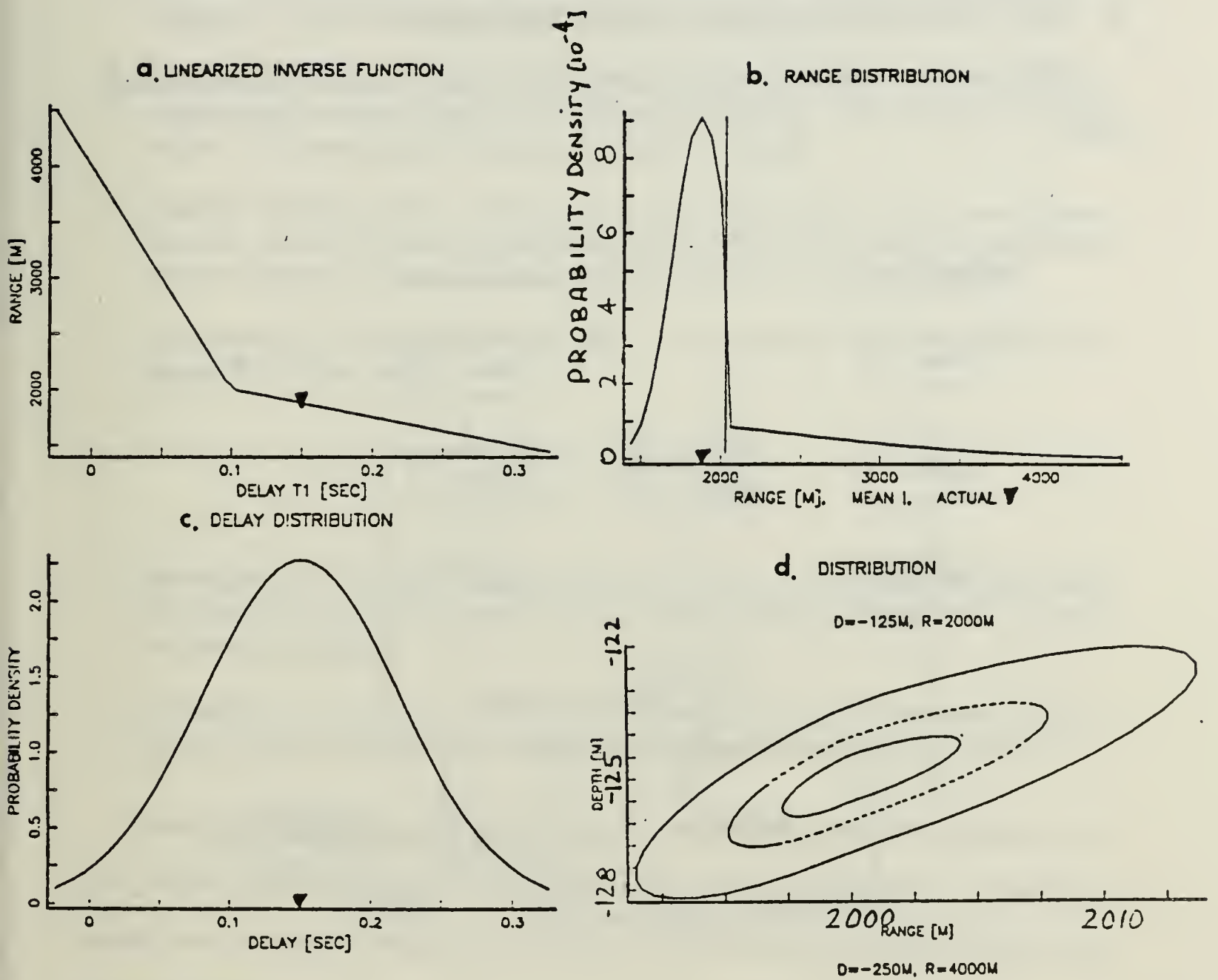


Fig. 4.1. Nonlinear inversion bias.

examined here for the IH case. Means to compensate for these biases are discussed as well.

B. THE PREFILTER EVALUATION SCHEME

The evaluation scheme shown schematically in Fig. 4.2 involved the following steps.

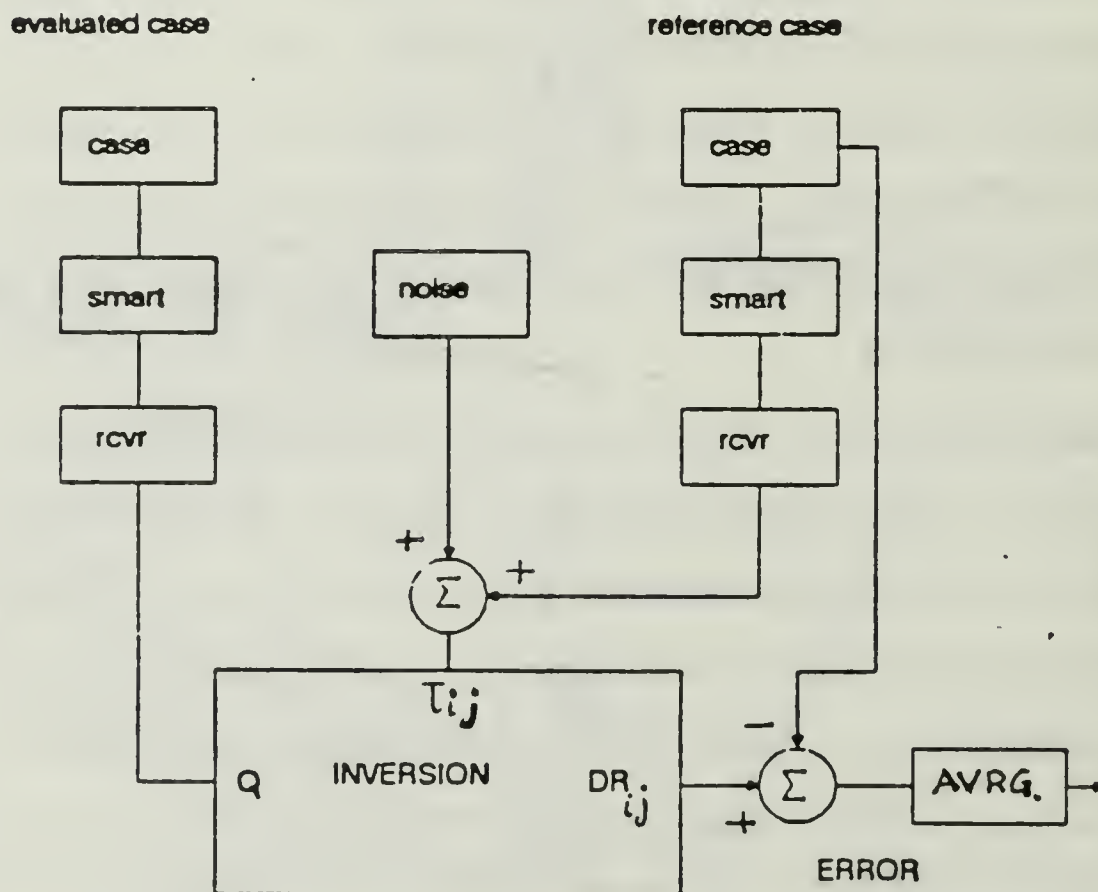


Fig. 4.2. Inversion performance evaluation.

1. Generation of the reference and evaluated direct function tables using the SMART program and the instrumentation model (see Chapter Three.). Two separate sets of conditions are used: the "actual" (the reference case or Re-case) and the "assumed" (the evaluated case or Evalcase). The conditions

such as SVP bottom depth grid size etc. may be different for the Refcase and the Evalcase. It is the effect of these differences that is being evaluated.

2. Generation of the delay measurement noise for every point in the grid and adding it to the delays t_1, t_2 , of the (reference) TDOAs.
3. Simulation of the noisy target predicted position D_p, R_p by adding depth and range noise to every point on the grid values $D_{[i]}, R_{[j]}$. This supports investigation of the search algorithm in an open loop mode.
4. Transformation of the measured t_1, t_2 into depth and range measurement D_m, R_m via the inversion procedure (prefilters 5 or 6) using the evaluated direct function (i.e., the assumed ocean) and the noisy reference point.
5. Comparison of the measured D_m, R_m to the reference $D_{[i]}, R_{[j]}$ values and generation of the errors

$$D_{error} = D_m - D[i]$$

$$R_{error} = R_m - R[j]$$

6. Repeating the above for all the points in the DR grid. Recording for each point the errors along with the search performance measures (number of solutions and search area size).
7. Averaging the output over small local 2-D windows to provide an estimate of the local mean and variance and a local prefilter performance measure.

Recall that a failed search will return the reference point as the inverted output. When noise is not added to the reference point this will produce a zero error which is not a precise account for the event. This will become evident from some of the results.

C. EVALUATION RESULTS

The evaluation was performed about 150 times for a variety of conditions. The results of eight summary cases are presented next. The cases investigate the effects of the following issues:

- Depth range grid size.
- Linear versus bilinear interpolation.
- TDOA bias error.
- Acoustic medium inhomogeneity.
- Range independent TDOA noise.
- Range dependent TDOA noise.
- Range dependent prediction point reference.
- Bottom depth error.

Each of the next eight subsections describes one evaluation. Each subsection describes the purpose of the simulation experiment and the expected results, the actual experimental results and analysis of the evaluation, and conclusions. The output plots include:

- Local average of depth and range errors.
- Local average of inversion error STD.
- Local average of the solution count (this monitors the performance of the search algorithm.)
- Average error as function of range (range error profile). This is generated by taking error averages over all of the depth points for a given range. The error profile is normalized as marked on the plots.

1. Effects of Grid Size

The purpose of this Run was to examine the effect of grid size on interpolation error and optimize the grid for the intended use. The key parameters used are given in Table 4.1.

The depth and range results of the inversion with linear interpolation over the medium density DR Evalcase grid (S1111), are compared to the exact depth

TABLE 4.1
INTERPOLATION EVALUATION GRIDS

Grid density	High	Medium	Low
Casename	S1155	S1111	S1144
Initial depth [m]	160	160	160
Depth Step size [m]	10	50	100
Number of steps	11	11	6
Initial range [m]	500	500	1000
Range step size [m]	250	500	1000
number of steps	99	25	13

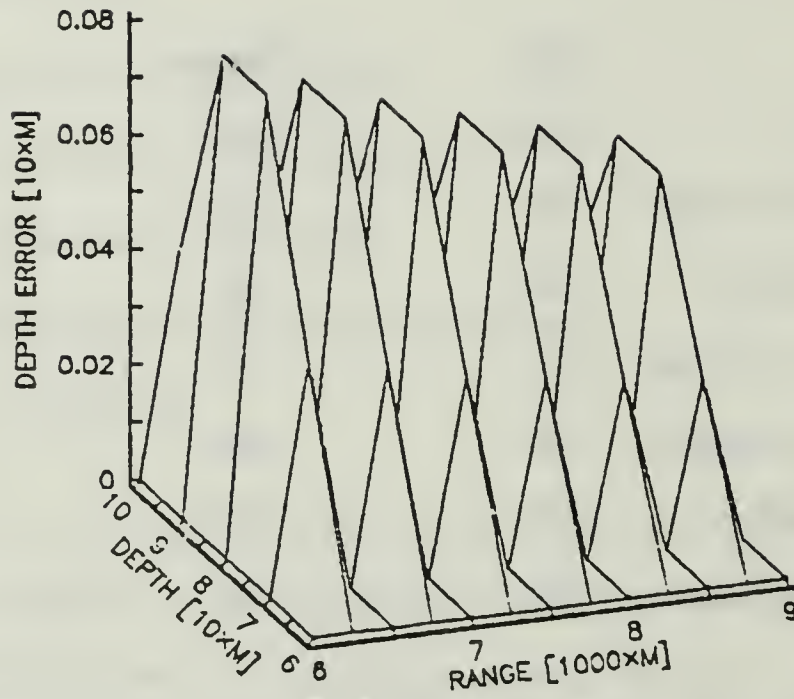
and range values of the high density DR Refcase (S1155) grid. The results are shown in Fig. 4.3. The maximum errors were 16 m in depth and 100 m in range.

An interesting point was revealed by these plots. The interpolation errors depend on the degree of curvature in the direct and inverse functions. The curvature is very small at long ranges making the interpolation error inversely proportional to the range. This is clearly seen in Fig. 4.3. The significance of the interpolation errors is greater at short ranges than at long ranges since the other inherent MP tracking errors are reduced at short range. The grid size should therefore be optimized for the short range performance.

A more coarse grid (Evalcase S1144) was evaluated using the medium density grid as the reference (Refcase S111). The results shown in Fig. 4.4 reach a maximum depth error of 20 m and a maximum range error of 200 m.

Conclusion: The grid size depends primarily on the direct function. A more curved and more rapidly changing function will require a finer grid to maintain

DEPTH ERROR



RANGE ERROR

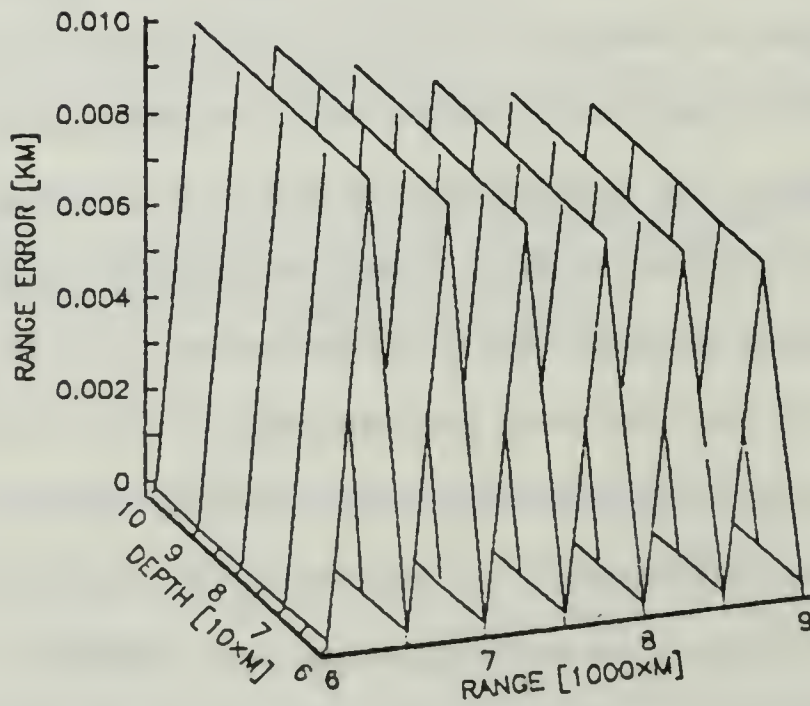
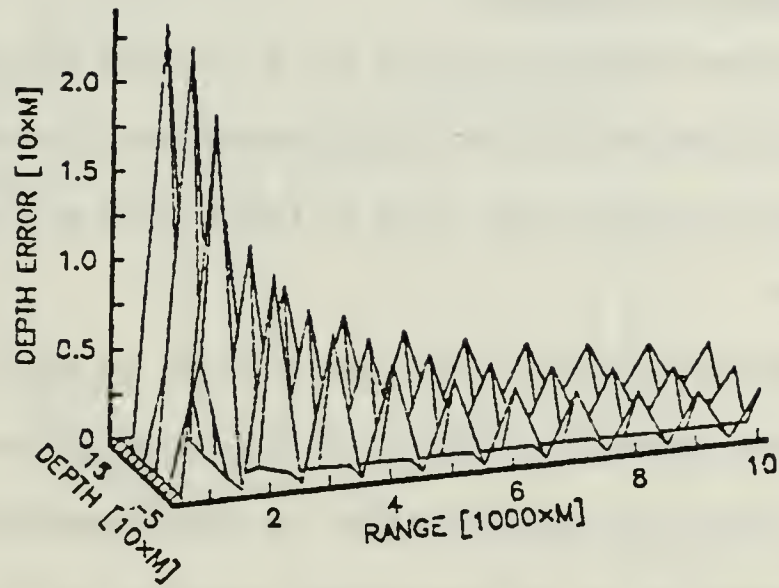


Fig. 4.3. A 50×500 m DR grid interpolation error.

DEPTH ERROR



RANGE ERROR

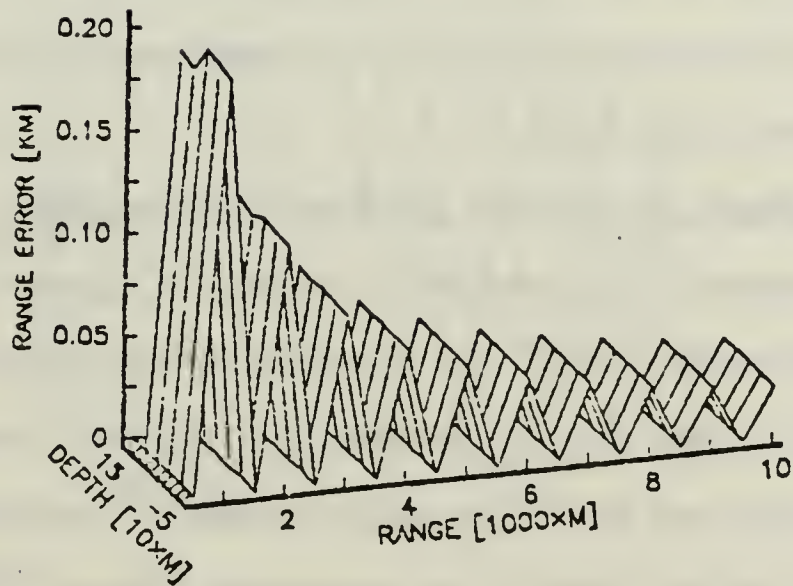


Fig. 4.4. A 100×1000 m DR grid interpolation error.

low errors. For the nominal homogeneous case, in water depth on the order of 500 m and ranges up to about 20 km a direct function Q grid size of $2 \times 20 \times 40$ will be required. This is a very reasonable size which is easily within the capability of current onboard microcomputers.

2. Bilinear Interpolation

The purpose of this evaluation was to compare the performance of linear and bilinear interpolation. The key parameters used are the same as those used for the medium grid evaluation (See Table 4.1) with S1155 as the Refcase and S1111 as the Evalcase.

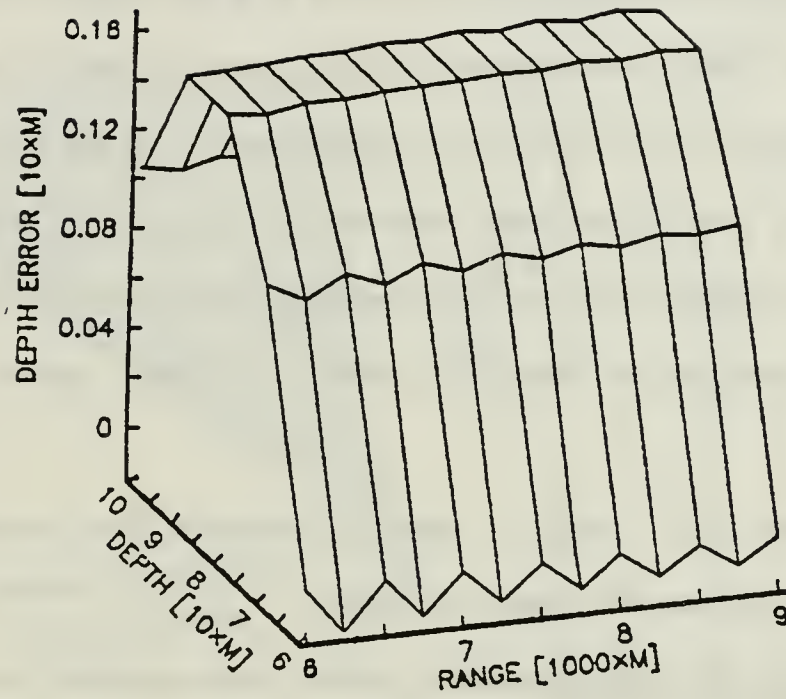
Error surface for the bilinear interpolation are plotted in Fig. 4.5. The difference between the results of the two interpolation methods is small (compare to Fig. 4.3). The smaller depth errors in the linear interpolation result from the fact that the triangular area of interpolation is smaller than that of the rectangular area used by the bilinear method. The bilinear interpolation provides a smoother interpolation but has a larger absolute error.

Conclusion: Both linear and bilinear interpolation produce satisfactory results. The error of the linear method is slightly smaller. The choice of which method to use can be based on implementation considerations. Linear interpolation was used for most of this study.

3. The Effects of Acoustic Medium Inhomogeneity

The purpose of this evaluation run was to examine the effects of the medium inhomogeneity. A SVP with a positive surface gradient of steepness that is characteristic of many practical problems ($g = 0.05 \text{ sec}^{-1}$.) was used as the reference case (A2251) and the TDOAs were converted to depth and range assuming a homogeneous medium (straight line propagation, Evalcase S2251).

DEPTH ERROR



RANGE ERROR

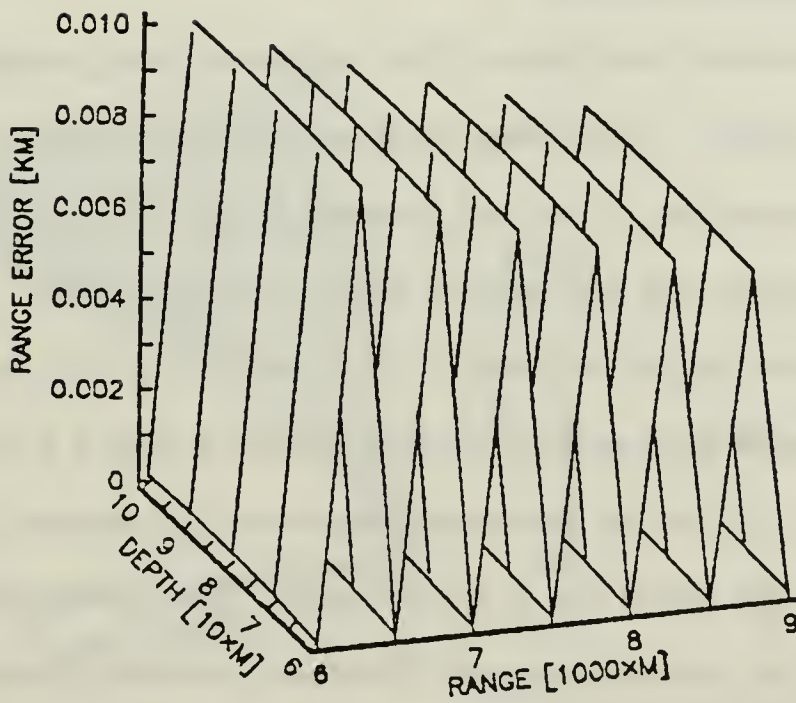


Fig. 4.5. Bilinear interpolation error.

Depth and range inversion errors are shown in Fig. 4.6 as surfaces and as contour plots. Very large errors are developed especially at long ranges. Observe that at a range of 12 km the range error is 4 km and the depth error is 150 m.

The trend of the error is expected and is caused primarily by the change in the surface bounce path. Fig. 4.7 shows a comparison of an IH and a straight line propagation where t_1 and t_2 for both cases are the same. The path T_1 is longer (curved instead of straight) and includes portions with average speed of sound lower than in the homogeneous case. The resultant delay t_1 given by $T_1 - T_0$, is longer.

When interpreted as if it were the result of straight line propagation it gives rise to deeper depth and shorter range estimates.

Conclusion: The inhomogeneity of the ocean medium has a gross effect on MP propagation and position measurement. Compensating for this effect is mandatory in order to achieve meaningful depth and range measurements.

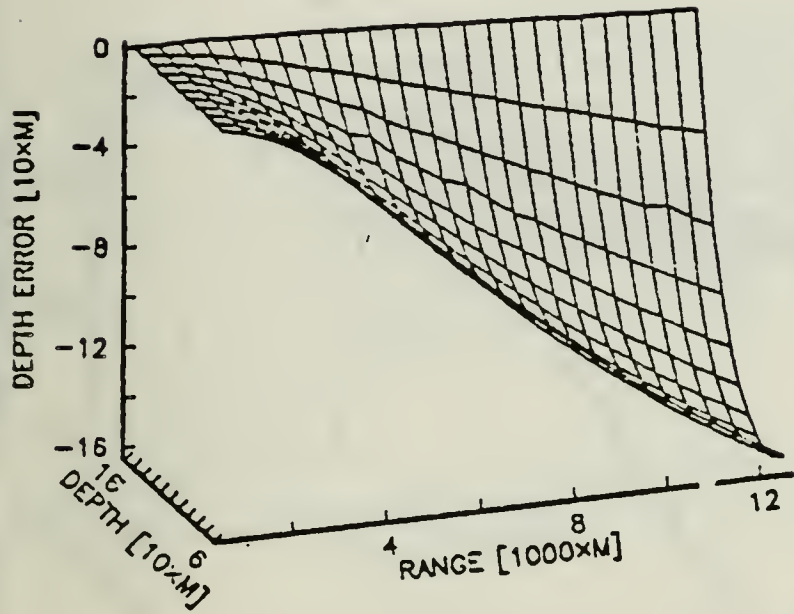
4. Finite Delay Resolution

This case examined the effect of finite delay resolution combined with the effect of the inhomogeneity. The cases used were Refcase C4261 for which the assumed delay resolution is 0.5 ms and Evalcase S4261 for which the assumed delay resolution is perfect and the assumed SVP is homogeneous.

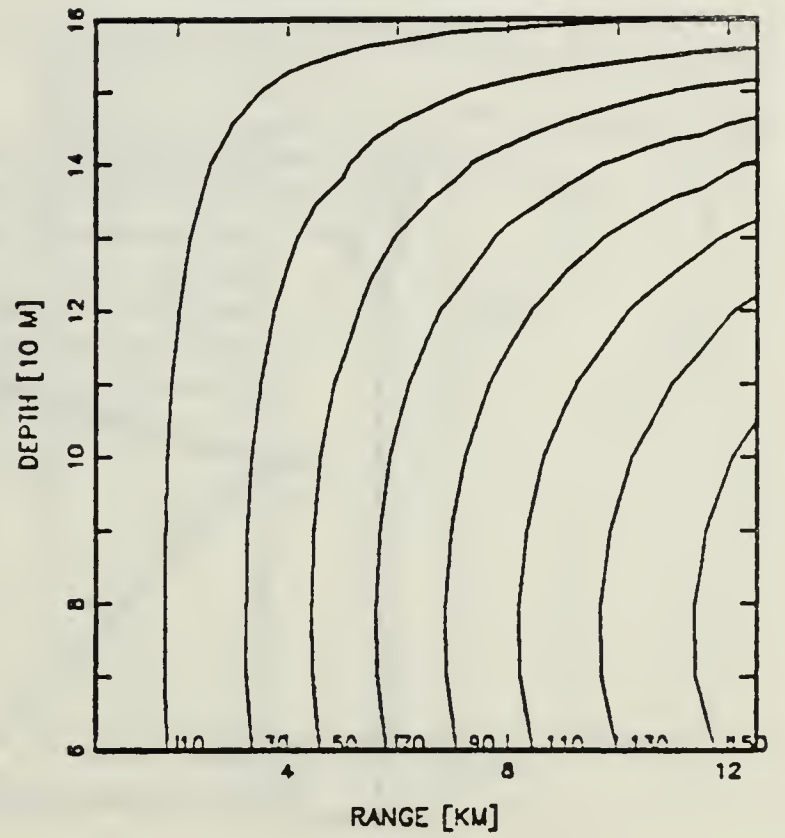
The errors are similar in nature to the errors produced by the previous run. The main difference is along the surface as shown on Fig. 4.8. This difference results from the fact that in the finite resolution case the surface bounce is not resolvable along the first depth line of the DR grid. The first depth grid point is located at a depth of 2m from the surface*. The delay between the direct path and

* The observer depth is 162 m and the grid initial depth is +160 m relative to the observer.

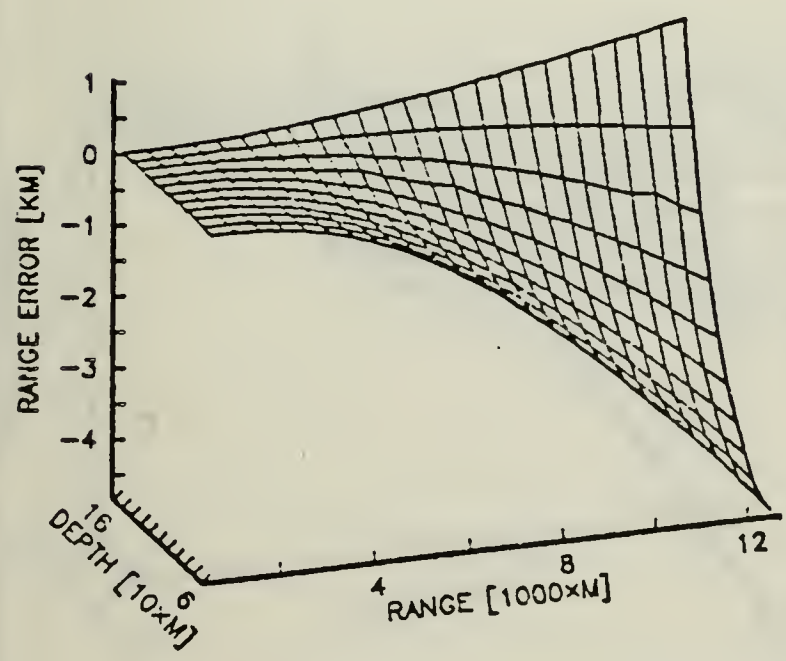
DEPTH ERROR



DEPTH STD CONTOURS[M]



RANGE ERROR



RANGE STD CONTOURS[KM]

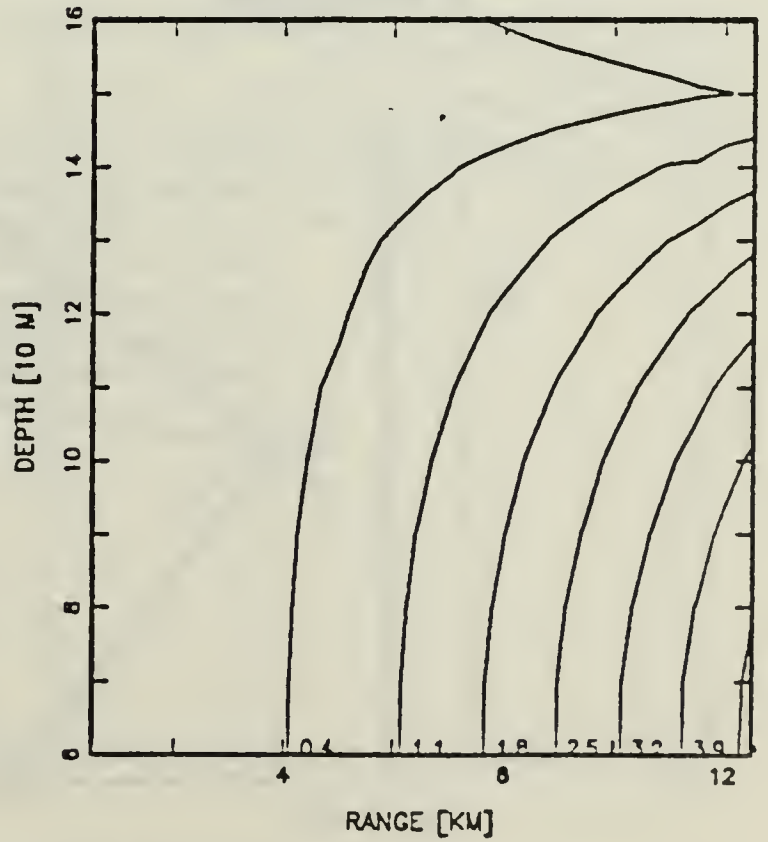
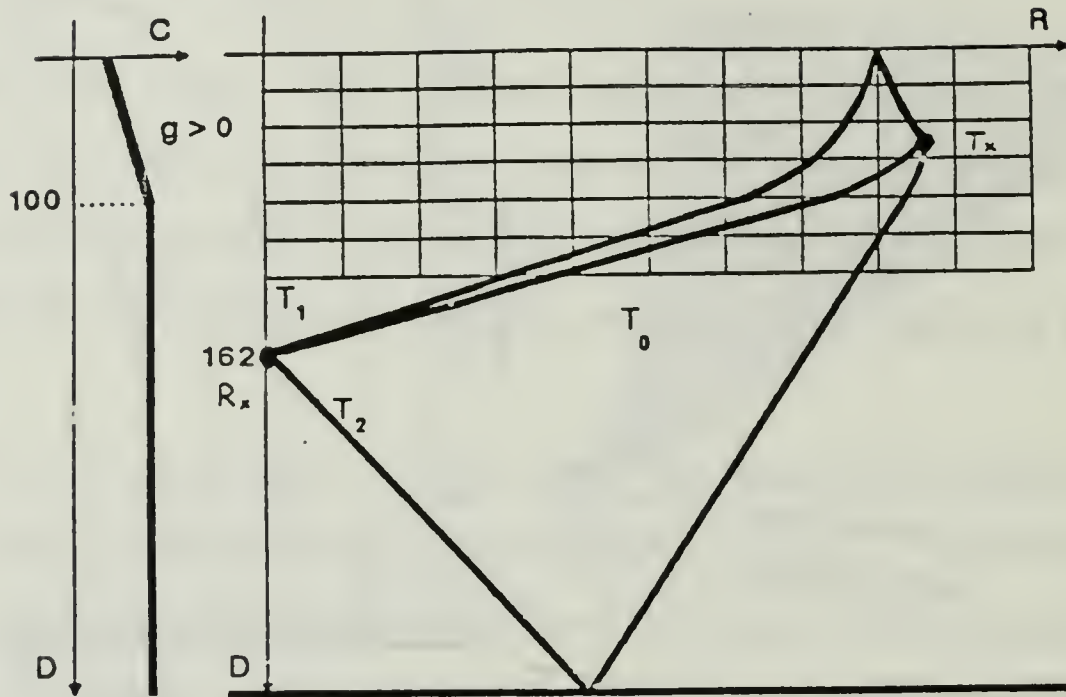


Fig. 4.6. Effect of medium inhomogeneity (A2251).

a. Inhomogeneous



b. Homogeneous

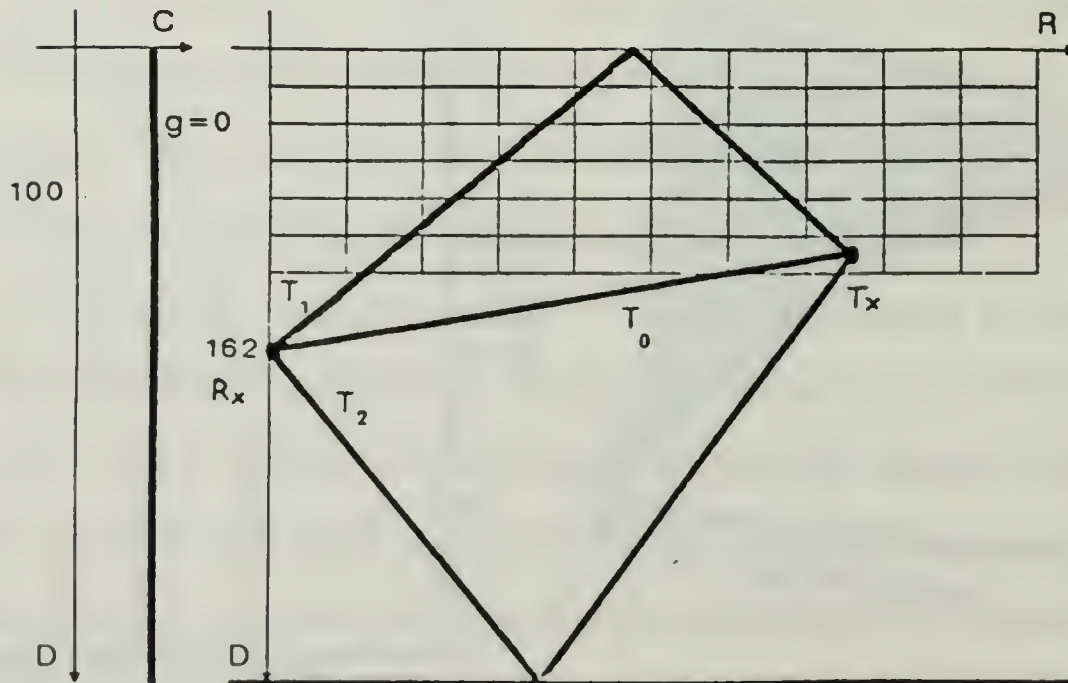


Fig. 4.7. Inhomogeneity error.

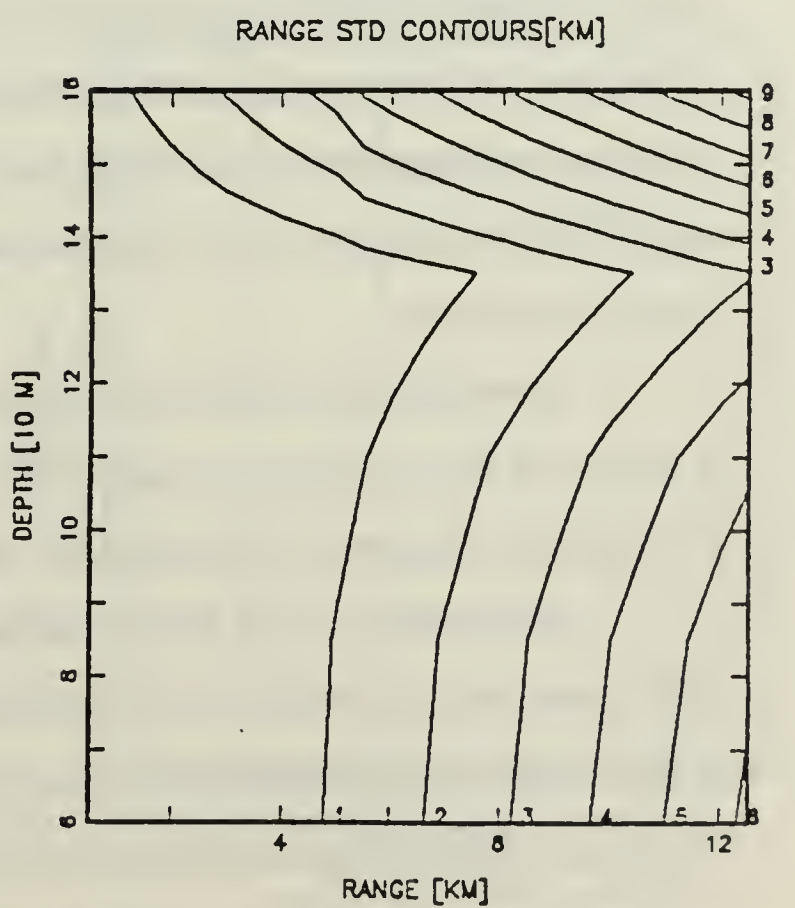
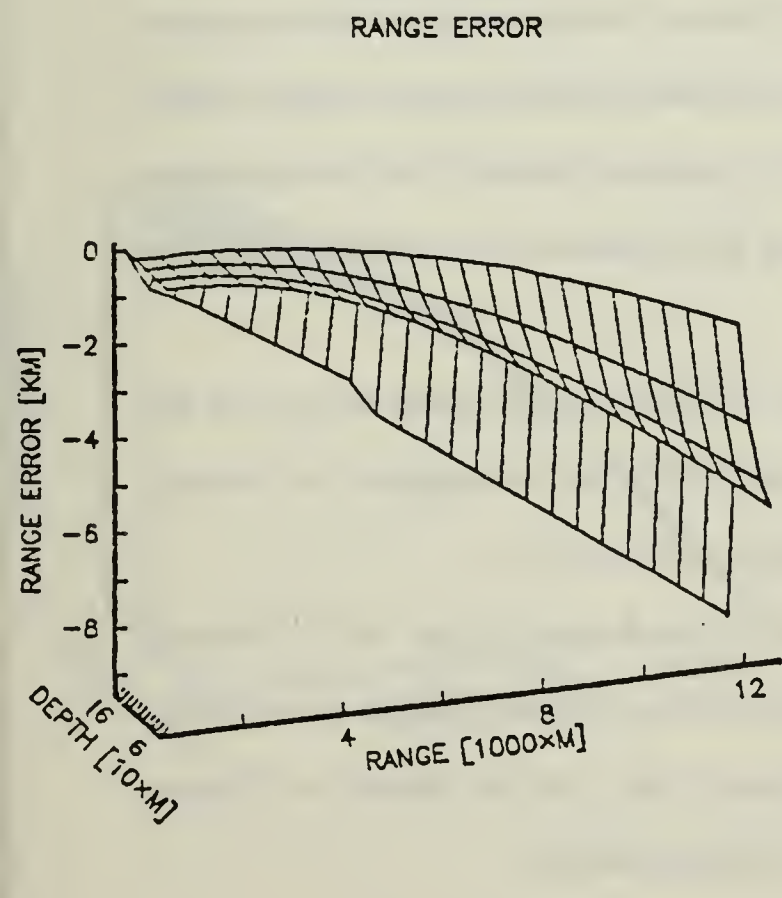
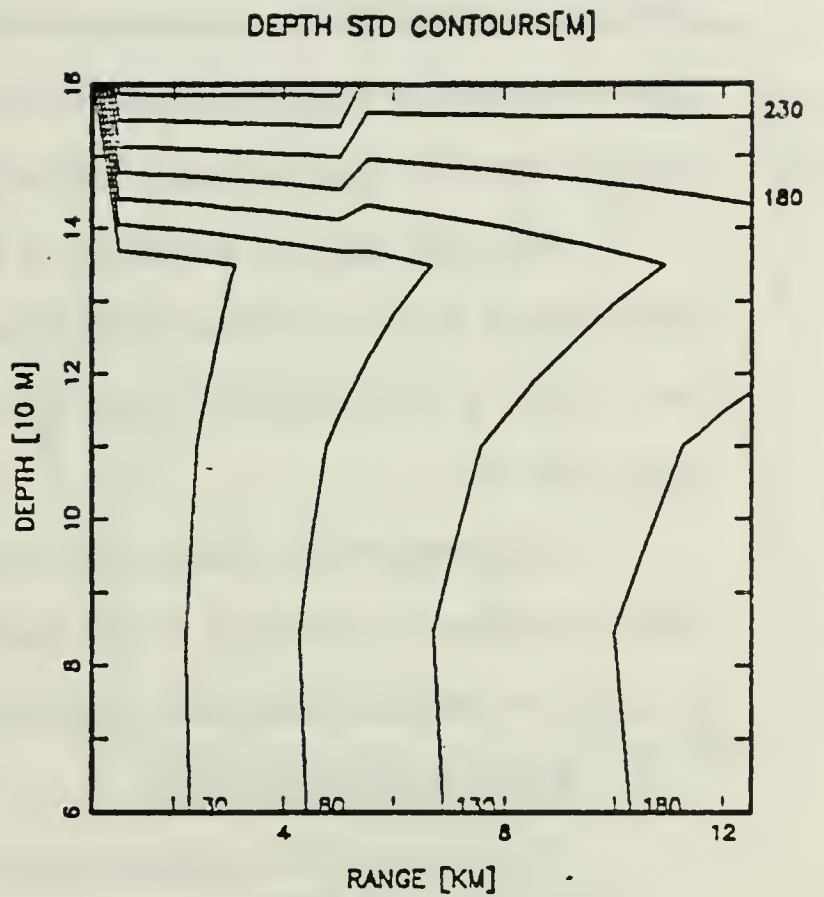
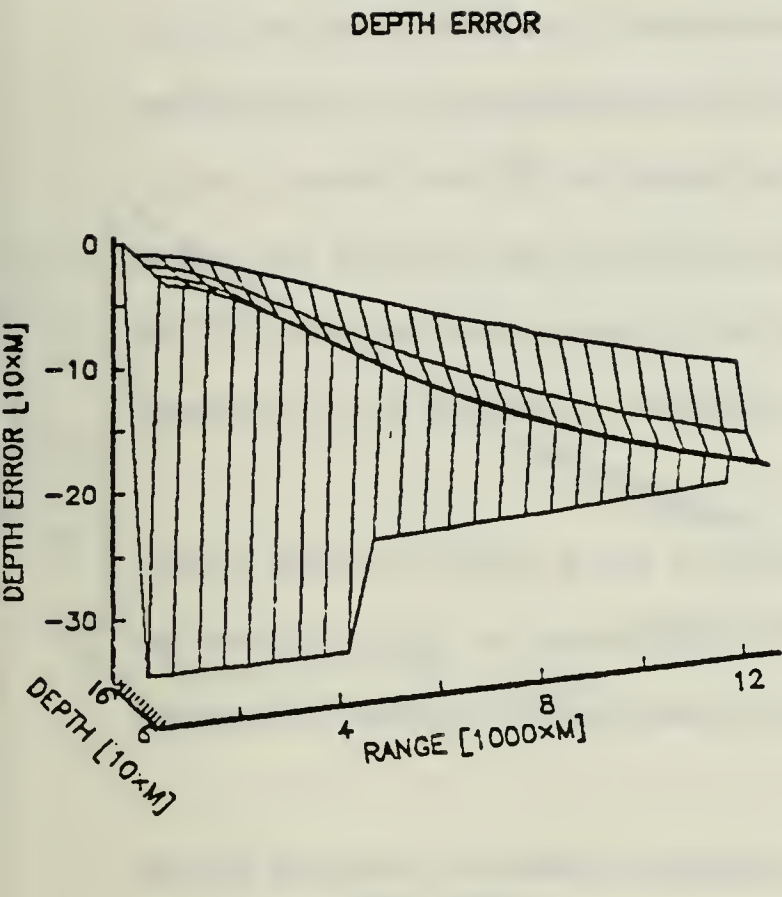


Fig. 4.8. Effect inhomogeneity and of finite delay resolution.

the first surface bounce is smaller than 0.5 ms and therefore is not resolvable. As a result the modified TDOA vector t_1, t_2 is comprised of τ_1, τ_3 here (instead of τ_1, τ_2). This corresponds to a physically different multipath configuration*. Similar effects were demonstrated near the ocean bottom and along the DR loci where $t_1 = t_2$.

Note also that the magnitude of the error over the complete DR grid is larger than in Fig. 4.6. This results from the steeper surface gradient of 0.105 [sec^{-1}] (SVP 4 in Appendix-E) used here compared to the 0.05 [sec^{-1}] gradient used in Fig. 4.6.

Conclusion: The finite delay resolution has a significant effect on the TDOA structure. Accounting for the specific response of the delay estimator to the loss of resolution is mandatory, especially for targets near the ocean boundaries.

5. Delay Estimation Bias

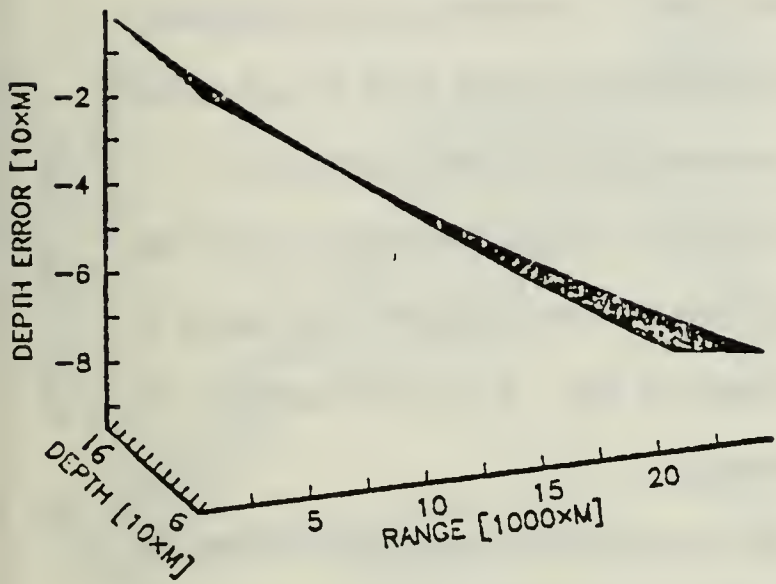
The purpose of this evaluation is to examine the effect of a constant TDOA offset. This was done as a scaling run and supported the independent evaluation of the tracker. It allowed nominal transformation of the predicted delay noise to depth and range measurement errors. Since this is a nominal scaling, the homogeneous case (S3252) is used both as the Refcase and the Evalcase. A τ_1 offset of 1 ms is used as TDOA bias.

The resulting error is shown on Fig. 4.9 and reaches levels of up to 4 km in range and 80 m in depth at range of 25 km. With actual range in the vicinity of 12 km the range error is 1 km and the depth error is 40 m.

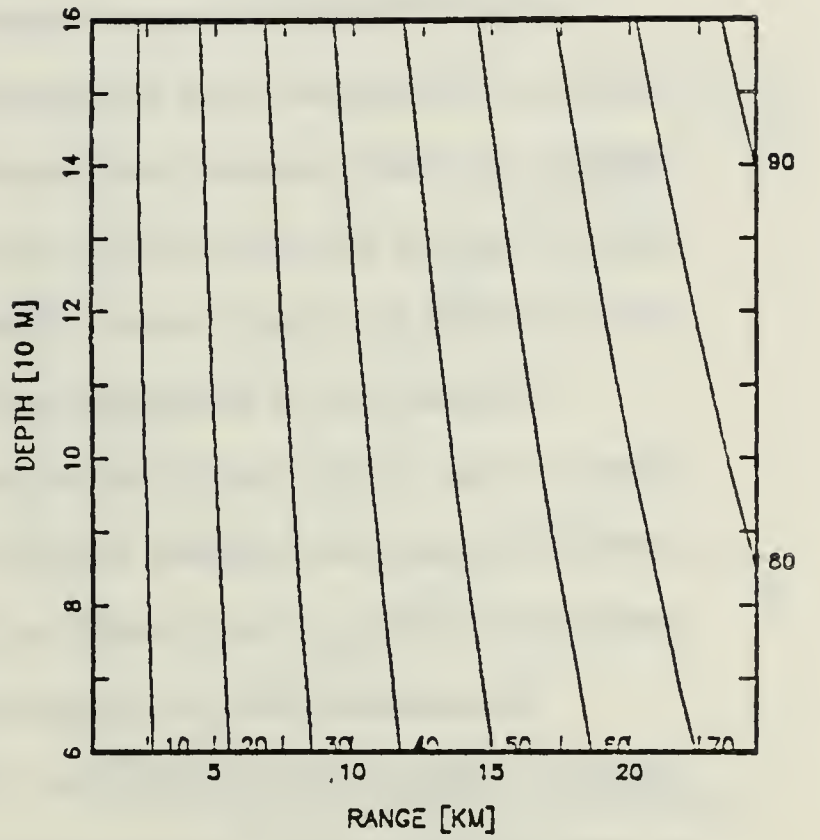
Conclusion: If the tracker operates over a range of up to 12 km and TDOA noise of the order of 1 ms is assumed, the range error STD can be expected to lie between a few hundred meters and about 1 km. As was shown in Chapter Two, such errors can be handled by the MM target tracker.

* See Chapter Three, Section III.B.5.

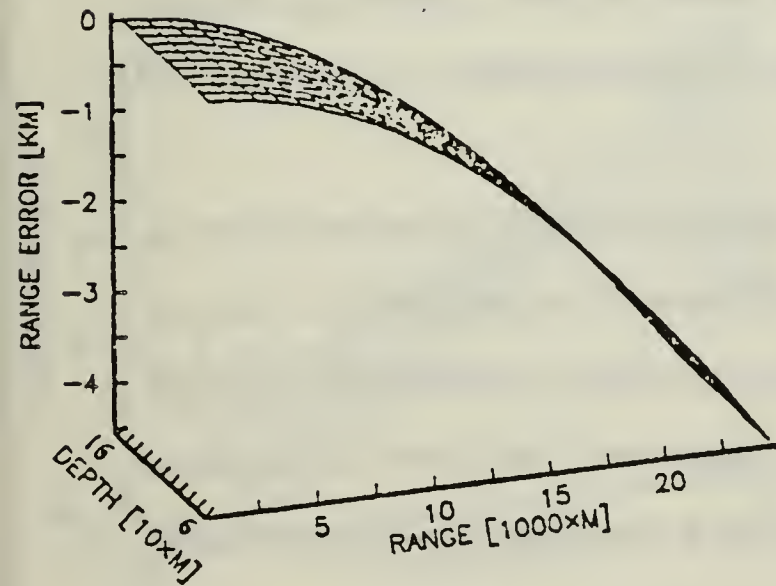
DEPTH ERROR



DEPTH STD CONTOURS[M]



RANGE ERROR



RANGE STD CONTOURS[KM]

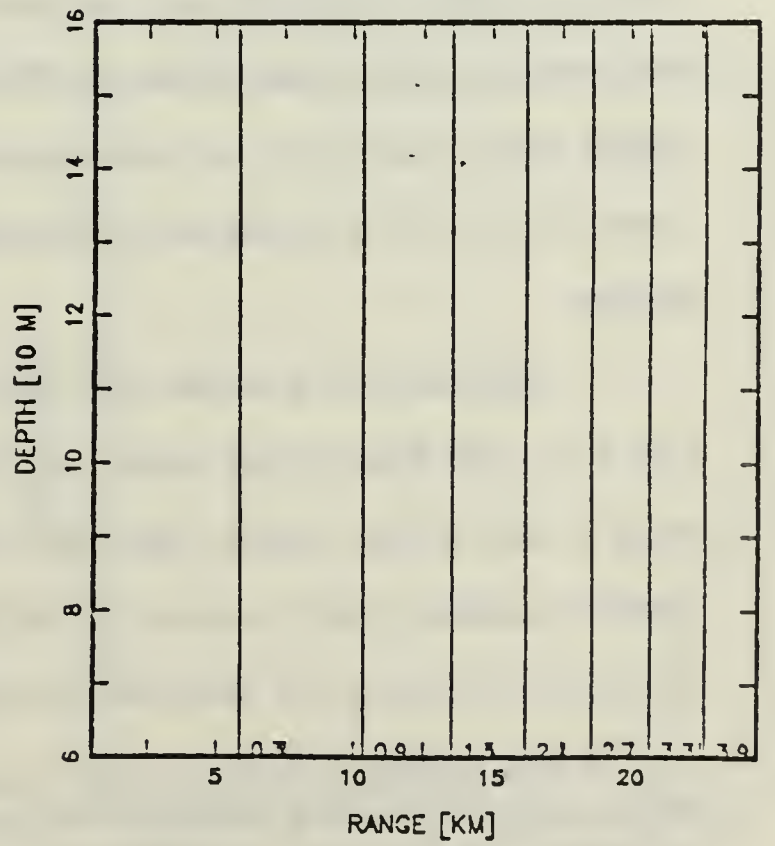


Fig. 4.9. TDOA constant bias error ($\tau_1 + 1ms$).

6. Effects of Range Independent Noise

The effect of a stationary (range independent) random noise on both the variance and the mean of the DR measurement was examined. The Refcase and Evalcase were both taken as the homogeneous S4261. A stationary, range independent ($p = 0$), see Eq. (3.3)) TDOA noise with STD of 1 ms for both t_1 and t_2 was used. The local averaging window for the plots was 3×7 in grid step units.

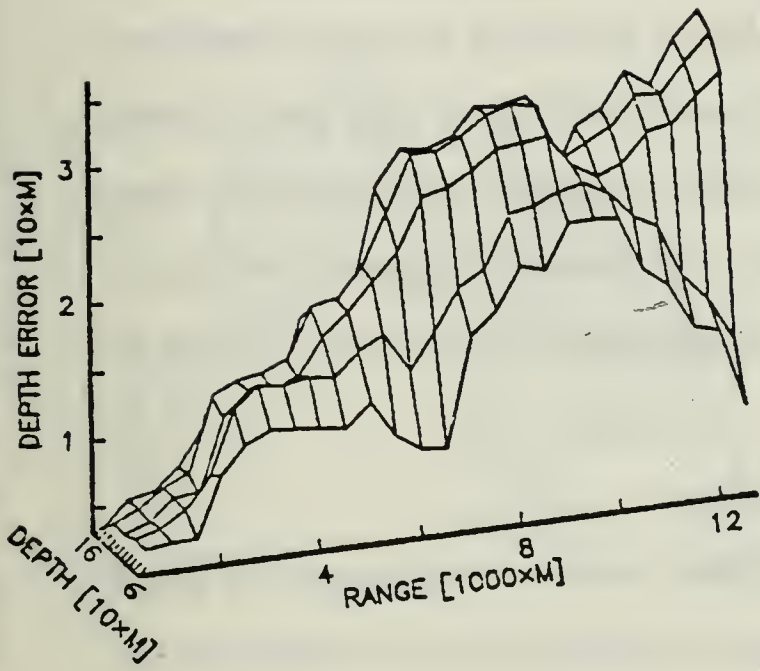
Surface plots of locally averaged STD of the depth and range errors are shown on Fig. 4.10a. The depth and range errors were averaged over depth to provide the range error profile which is shown on Fig. 4.10. The profiles are normalized to 100 m in depth and 1 km in range.

The maximum error is consistent with the earlier scaling results performed using the constant TDOA offset (Fig. 4.9). Contours of locally averaged number of solutions (Fig. 4.10d) indicate frequent failure of the inversion near the deep end of the grid*. This is caused by the TDOA values produced from the noisy measurements. The noise drives the TDOA measurements out of the interval of TDOA values covered by the precomputed direct function. Increasing the area covered by the DR grid will solve part of the problem and reduce the frequency of failures.

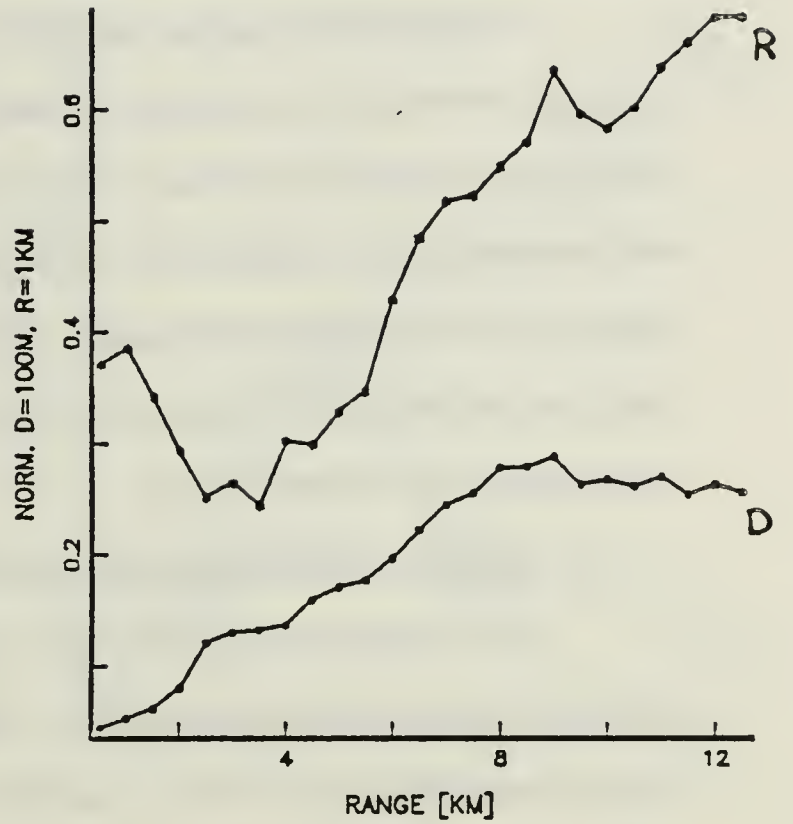
The results of a similar case with TDOA error STD of 5 ms are shown in Fig. 4.11. This figure shows larger errors and failure of the algorithm at a shorter range (7 km in Fig. 4.11d). Note that the term failure indicates only that the effective sampling rate is reduced by half at ranges over 7 km (recall the comment at the end of Section B). More frequent failure is the reason for the superficially

* The frequency of failure is 50 % along the 0 solution contour line since the line separates the regions between 0 and 1 average solutions. The contour line does *not* imply that there are no solutions at ranges longer than those indicated by the contour.

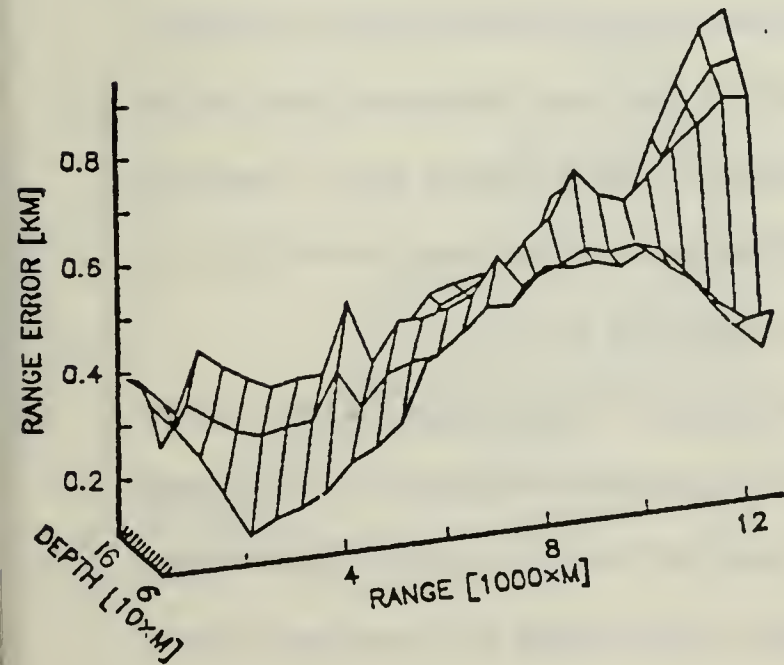
a. DEPTH STD DEV



b. OUTPUT STD $\cdot D \cdot R$



c. RANGE STD DEV



d. NUMBER OF SOLUTIONS

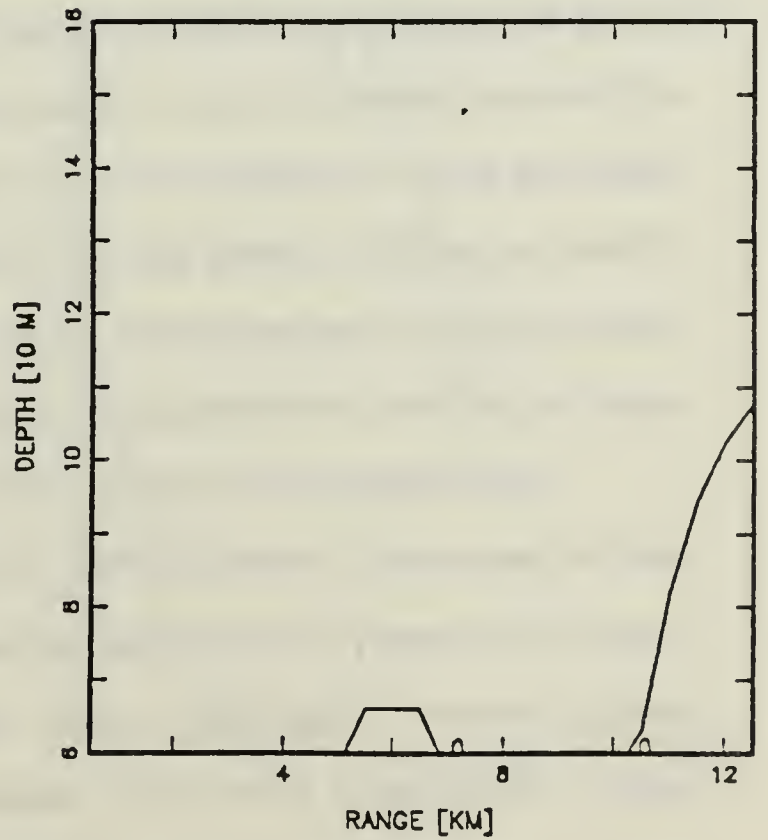


Fig. 4.10. Range independent TDOA and DR noise (1 ms).

lower error values at the long range. The effect of the reduced sampling rate on the overall system is investigated in Chapter Five.

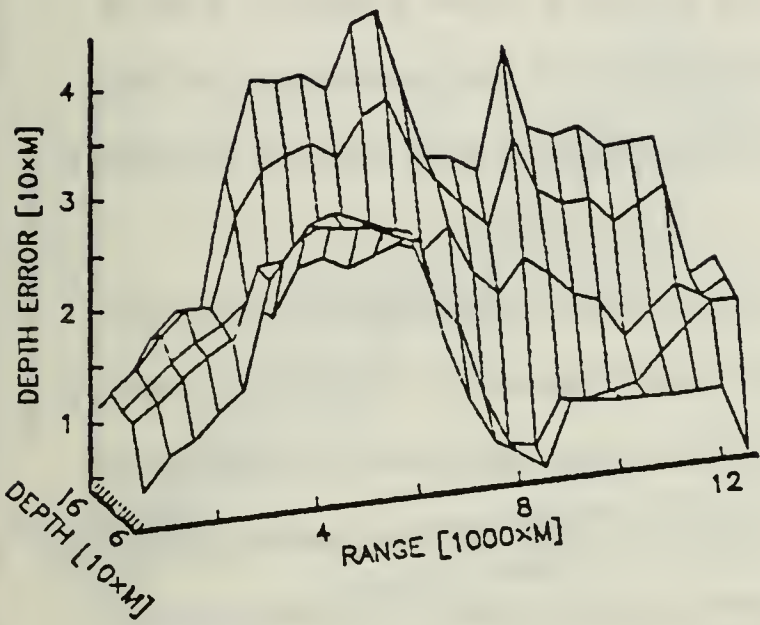
Conclusions: Errors with STD on the order of 30 m in depth and 0.5 km in range are expected at ranges around 10 km as a result of a range independent TDOA noise with STD of 1 ms. For TDOA noise with STD of 5 ms similar depth and range errors are expected at a range of 5 km. As shown in Chapter Two these errors can be handled by the target tracker. The inversion algorithm does fail at long ranges if the noisy delay measurements fall outside of the interval covered by the precomputed direct function.

7. Effects of Range Dependent Noise

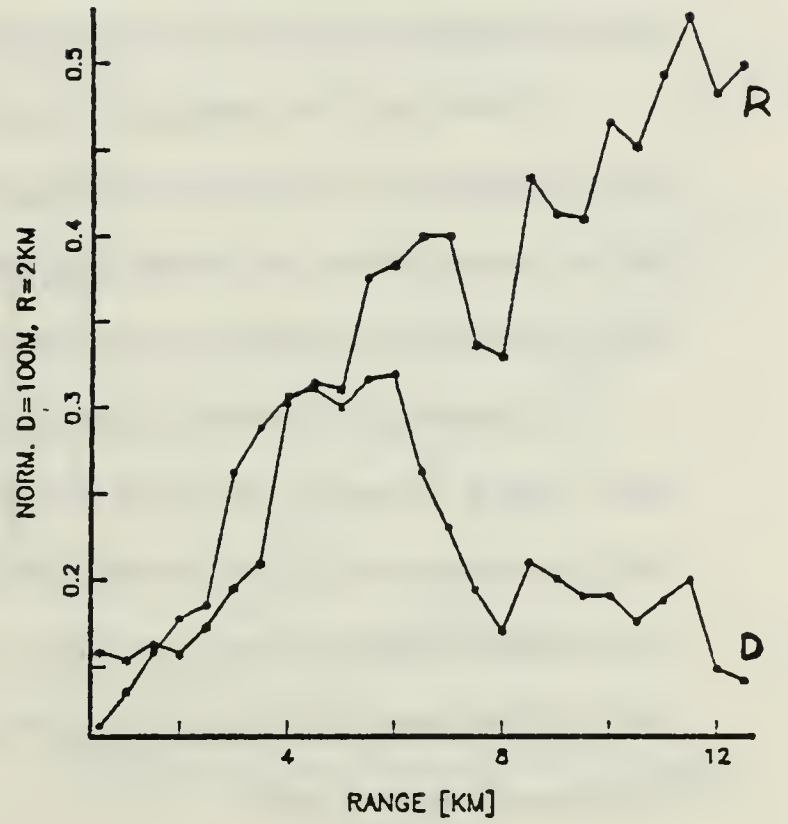
The response of the inversion of TDOA which is contaminated by range dependent noise was examined here. Range dependent noise was added to the target predicted point as well. Case S4261 was used both as the Refcase and the Evalcase. Range dependent noise (Eq. (2.96) $NT = 1, P = 1$), with t_1, t_2 STD of 0.2 ms at initial range of 500m, was used. The TDOA noise STD varied linearly with ranges between 0.2 ms to 4.8 ms over the range interval of 0.5 to 12.5 km. This noise level resembles the one produced by the more elaborate noise model ($NT=2$) for a SNR of 60dB and $p = 2$ which is a fairly typical case. Predicted position DR noise was varied from 0.4 to 250 m in depth and from 10 to 6.25 m in range proportional to the second power of range ($p_b = 2$).

The resulting error profile is shown on Fig. 4.12 along with the contour line for the number of solutions. Note the sharp range dependence of the inversion error STD on range. Also note that for the practical case used here a sharp "knee" develops around 12 km (Fig. 4.12c). Beyond this range the error grows very rapidly. This close to second order dependence of the DR measurement noise on range is what motivated setting the parameter p_b to 2. The maximum area size

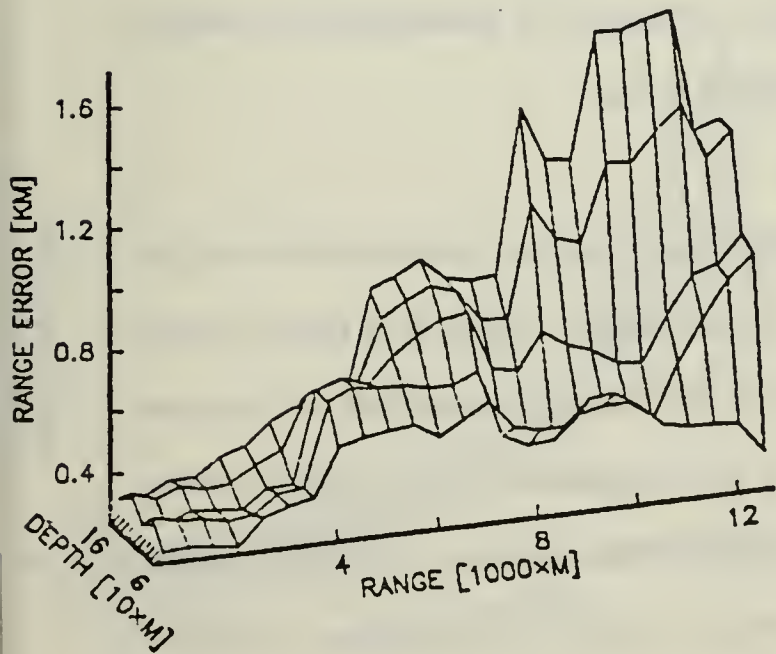
a. DEPTH STD DEV



b. OUTPUT STD $\cdot D \cdot R$



c. RANGE STD DEV



d. NUMBER OF SOLUTIONS

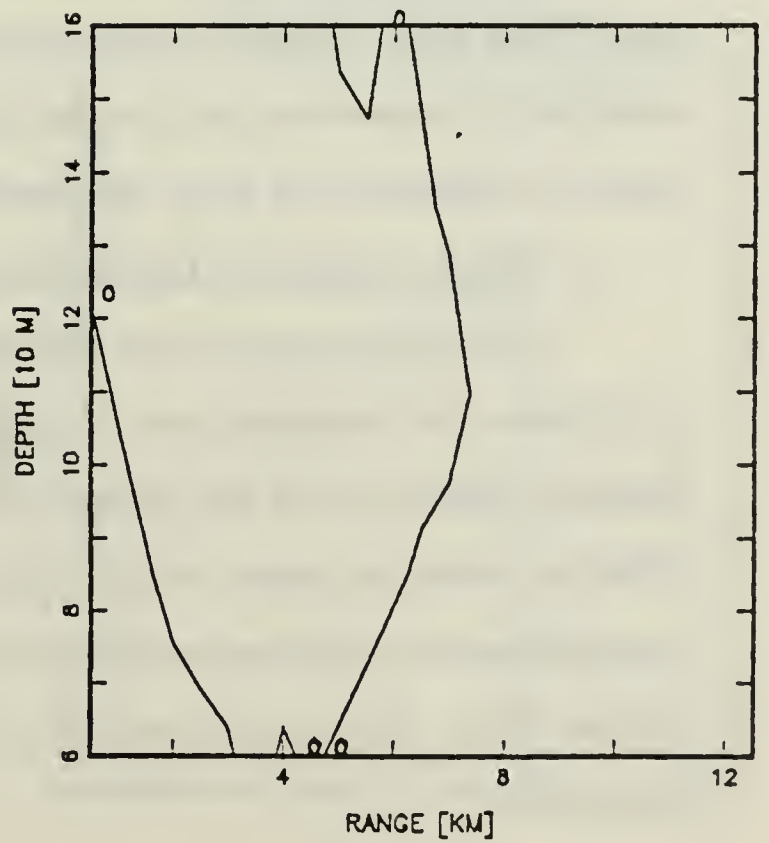


Fig. 4.11. Range independent TDOA noise (5 ms).

was set to 20×25 grid points. This explains why the addition of the DR noise did not degrade the performance significantly. Performance degradation as a result of smaller maximum area size is demonstrated in Chapter Five.

Note that the normalized range STD in Fig. 4.12b at a range of 9 km is approximately 0.3. This implies a range error STD of 3.6 km (considering the 50% failure rate and the 6 km normalizing factor). This value will be useful in Chapter Five in setting the maximum area size.

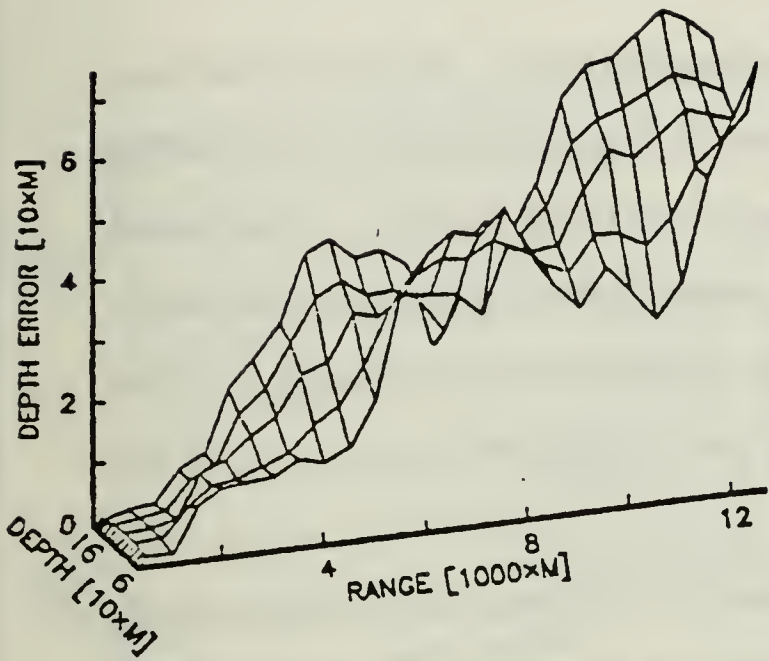
A second interesting observation is the failure along the first range grid line. This is caused by the noise which drives the "measured" TDOA outside of the interval covered by the precomputed direct function. Recall however that the 0 contour line in the number of solutions plot indicates only that the average failure rate is larger than 50%. Similar phenomena were noticed in most simulations along the edges of the DR grid.

Conclusions: The inversion varies with range even for a range independent TDOA noise. The error becomes even more range dependent when the TDOA noise itself is range dependent. Beyond 15 km very large DR measurements develop even for moderate initial range delay estimation noises.

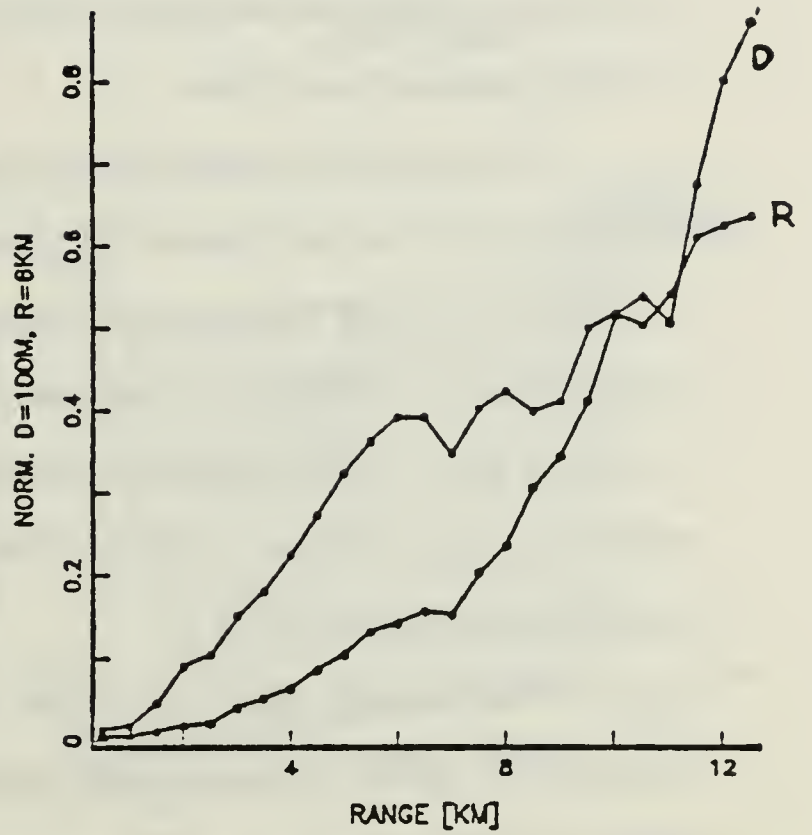
8. Effect of Bottom Depth Error

The purpose of this last inversion evaluation was to quantitatively examine the effects of an erroneous bottom depth on the target depth and range errors. Refcase S1256 for which the bottom depth is 513 m was compared to Evalcase S1556 for which the bottom depth is 550 m. A homogeneous ocean, perfect delay resolution and no noise were used here in order to isolate the effects of the erroneous bottom depth. The inversion was done, however, using the numerical algorithm (prefilter-5).

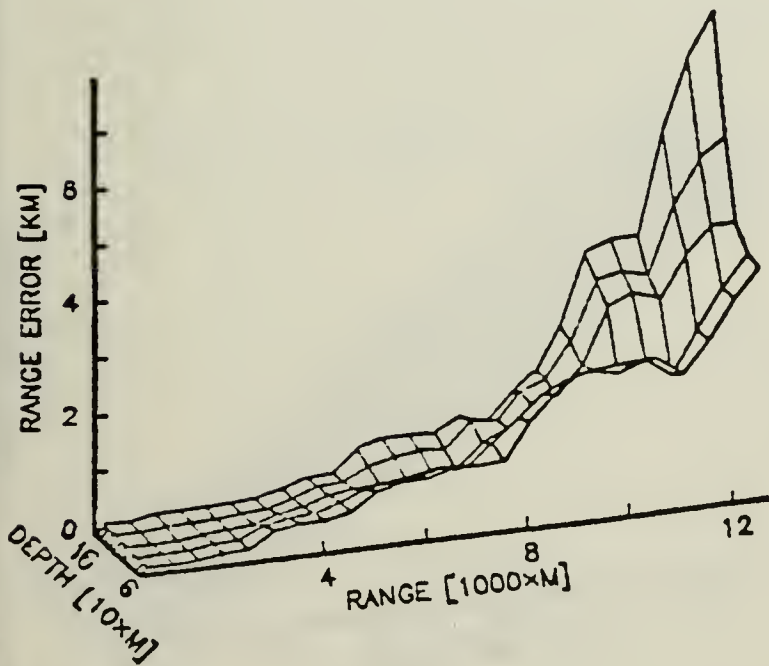
a. DEPTH STD DEV



b. OUTPUT STD • D • R



c. RANGE STD DEV



d. NUMBER OF SOLUTIONS

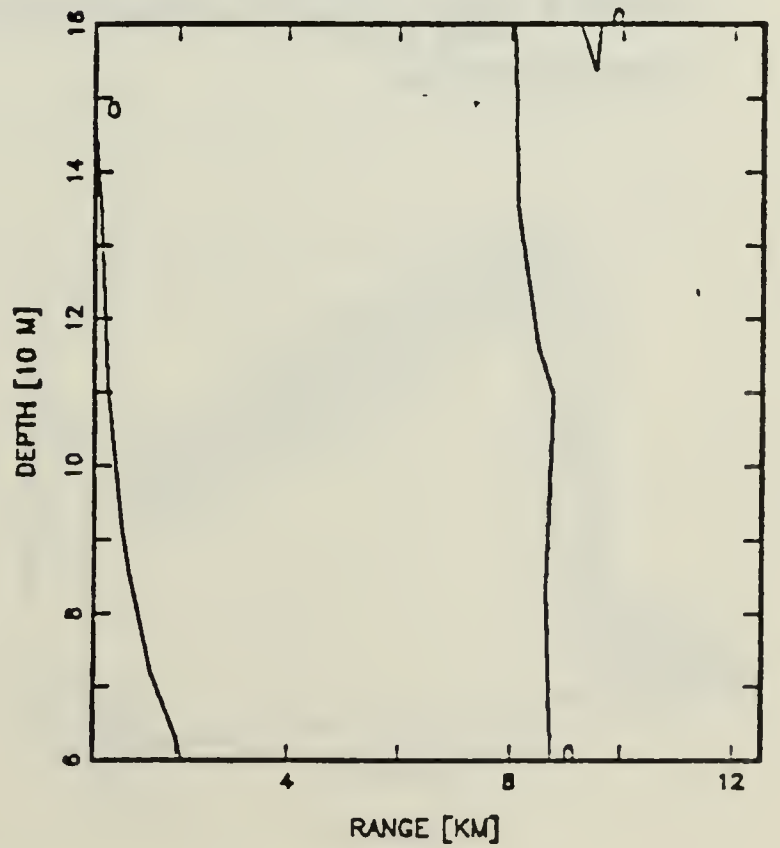


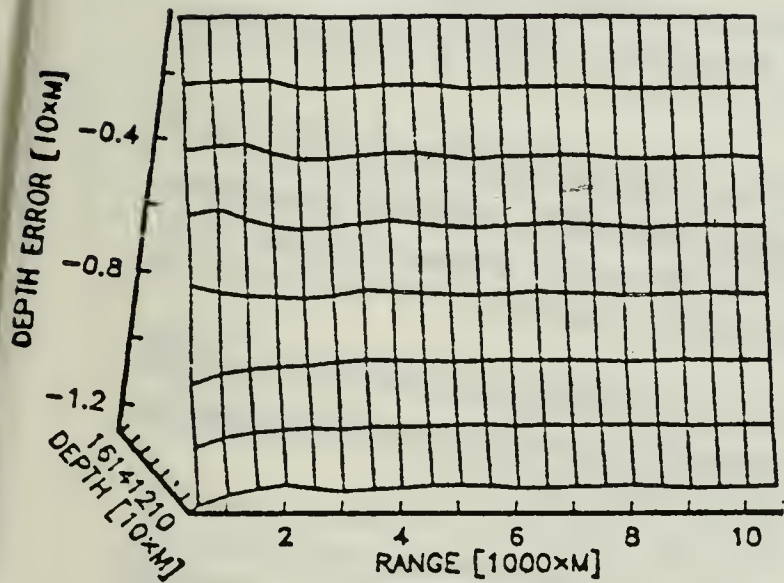
Fig. 4.12. Range dependent TDOA noise.

The effect of this relatively large bottom depth error (37 m which is 7.2% of the total ocean depth) is shown on Fig. 4.13 for short and long ranges. While the resulting range error reached a level of 3 km at 18km, it was limited to 1.5 km for ranges smaller than 10 km.

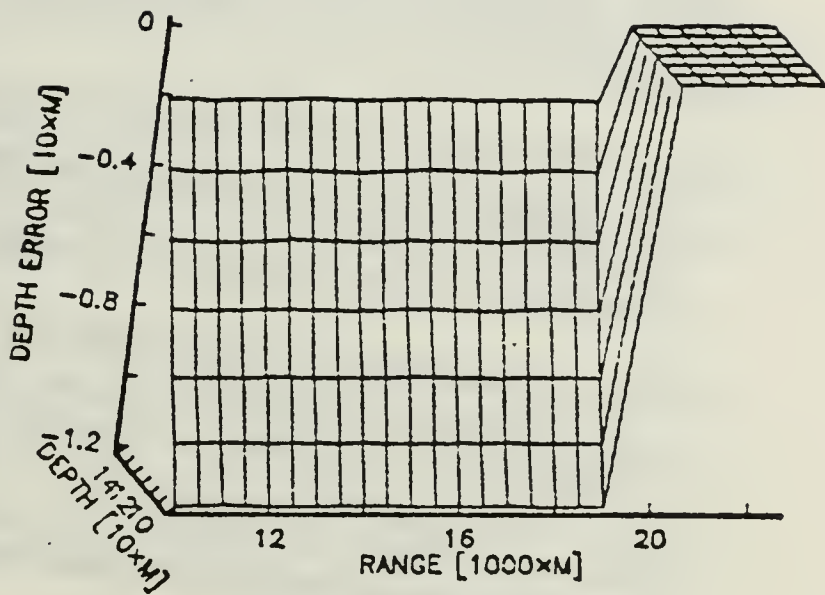
The trend of the error surfaces is explained as follows. The actual (Refcase) ocean produces a bottom bounce TDOA which is shorter than the one produced for the same DR point by the assumed (Evalcase) ocean. This smaller t_2 is interpreted by the inversion (which is done using the Evalcase) as the TDOA of a deeper target at a longer range. The region of no inversion solution at ranges in excess of 18 km resulted from the Refcase t_2 TDOA being smaller than the minimum t_2 in the precomputed Evalcase Table.

Conclusions: Incorrect bottom depth assumptions can give rise to large errors in MP position measurements, primarily at long range. The trend of the error is consistent with other MP tracking error sources in that it increases with increasing range. This error tends to limit practical tracking in shallow water to ranges below 20km.

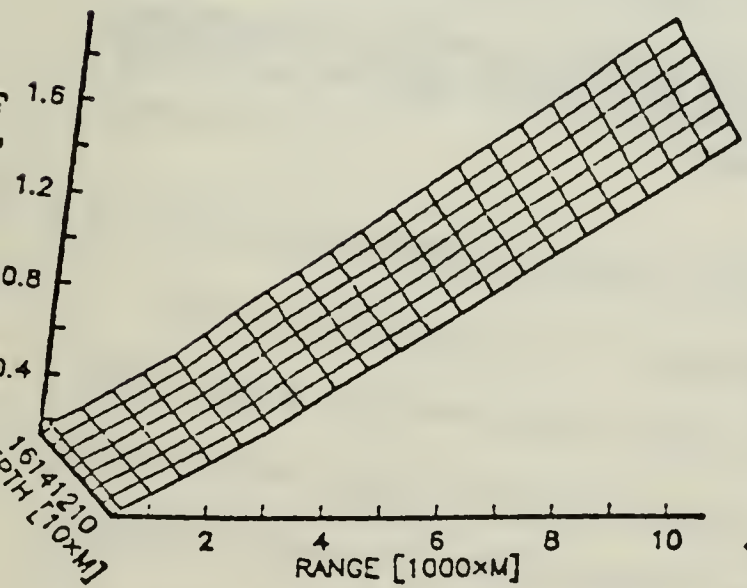
DEPTH ERROR



DEPTH ERROR



RANGE ERROR



RANGE ERROR

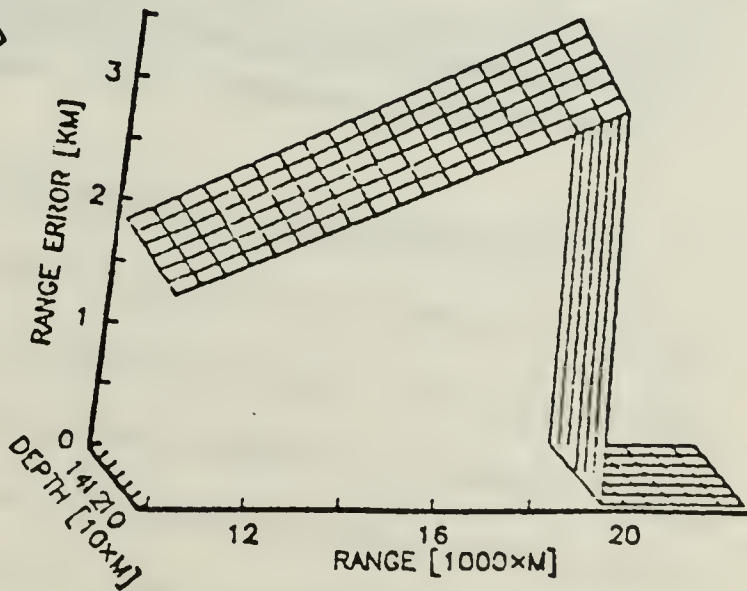


Fig. 4.13. Effect of bottom depth error.

D. SUMMARY OF PREFILTER EVALUATION

The results of these experiments can be summarized as follows.

1. The effect of the inhomogeneity on the MP position measurement is severe and was clearly demonstrated.
2. The depth and range measurement errors are strongly dependent on range (proportional to 2^{nd} to 4^{th} power of range depending on SNR and propagation loss).
3. Errors with STD of up to 40 m in depth and 1 km in range can be expected for ranges of about 7 km and typical targets with $SNR_0 = 60$ dB if spherical spreading is assumed ($p = 2$). Above 12 km the errors increase sharply with range for the typical shallow water case studied here.
4. The inversion algorithm fails under very noisy conditions and around the edges of the DR grid. The failures in these cases are legitimate since the TDOA input values are not representative of points in the DR grid.
5. Errors will result if account is not taken for the loss of delay resolution. In particular one needs to model the response that is expected from the specific type of delay estimator.
6. The algorithm is sensitive to DR grid step size only at short ranges. In general the depth and range step sizes should be tailored to the fluctuation of the specific direct function used and the accuracy desired at short range. Grids of 10 to 50 m in depth and 250 to 500 m in range were used in most of our work.
7. The MP tracking is sensitive to bottom depth errors primarily at long ranges. At ranges below 10 km a low percentage error in bottom depth would produce about twice that percentage error in range.

V. OVERALL PERFORMANCE EVALUATION

A. INTRODUCTION

In this chapter the overall performance of the MP tracking system is evaluated. A total of seven simulation runs which are divided into into three groups are presented. The runs are numbered 6 through 12 following the sequence of the runs begun in Chapter Two. Runs 6 and 7, represented in section B, demonstrate the functional performance and limitations of the integrated prefilter and tracker. Runs 8 through 10, described in Section C, were designed to investigate the effects of medium inhomogeneity and the ability of the new prefilter to compensate for it. Runs 11 and 12, covered in Section D, examine the sensitivity of the IH compensation to the accuracy of SVP measurement. Conclusions are summarized in Section E.

The results are presented in a format similar to the one used for the previous runs and case evaluations in Chapters Two and Four. In each section the goal of the runs and the key parameters used are described first. Then the analysis results are presented. The detailed parameter values for all of the runs is given in Appendix E.

B. INTEGRATED SYSTEM FUNCTIONAL PERFORMANCE

The overall performance of the prefilter integrated in a closed loop with the target tracker was demonstrated using a maneuvering target. The target initially has an outgoing speed (range rate) of 6 m/sec and it makes a sharp maneuver at a range of 9 km turning back towards the receiver at the same speed. Realistic noise (noise type 2, SNR = 50 dB and $p = 2$) is used to investigate the overall

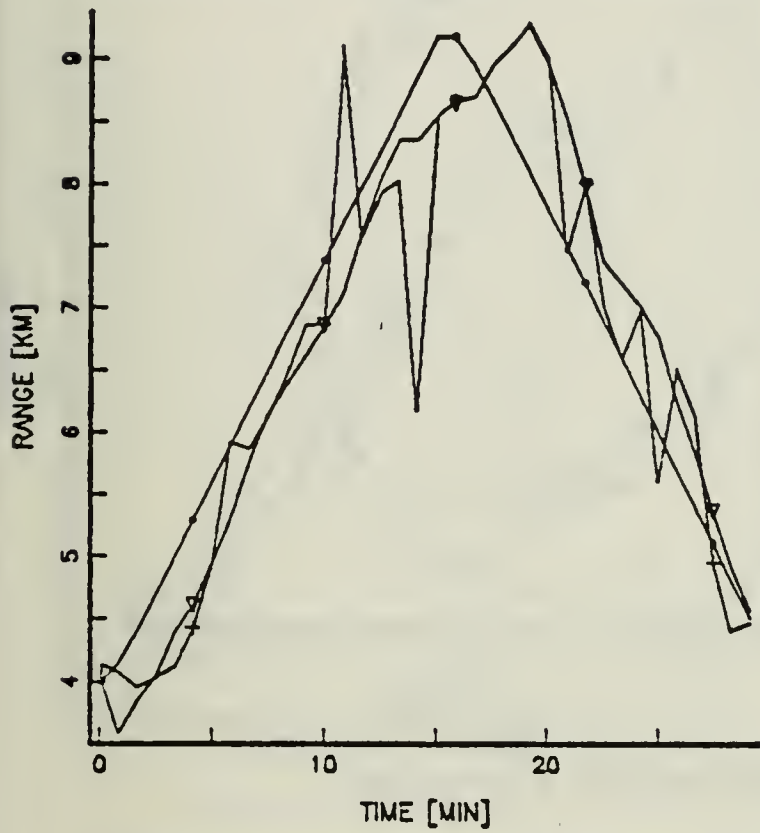
capability of the system through the maneuver. A constant speed of sound is used both as a reference and evaluation medium (case S1111). This is done in order to concentrate on the functional performance of the integrated system when the measurements are noisy.

The key issues investigated here relate to the inversion method. These issues are the ability of the local search algorithm (LSA) to find a valid surrounding triangle and the effects that a reduced effective sampling rate has on the target tracker (recall the discussion of inversion failure in Chapter Three).

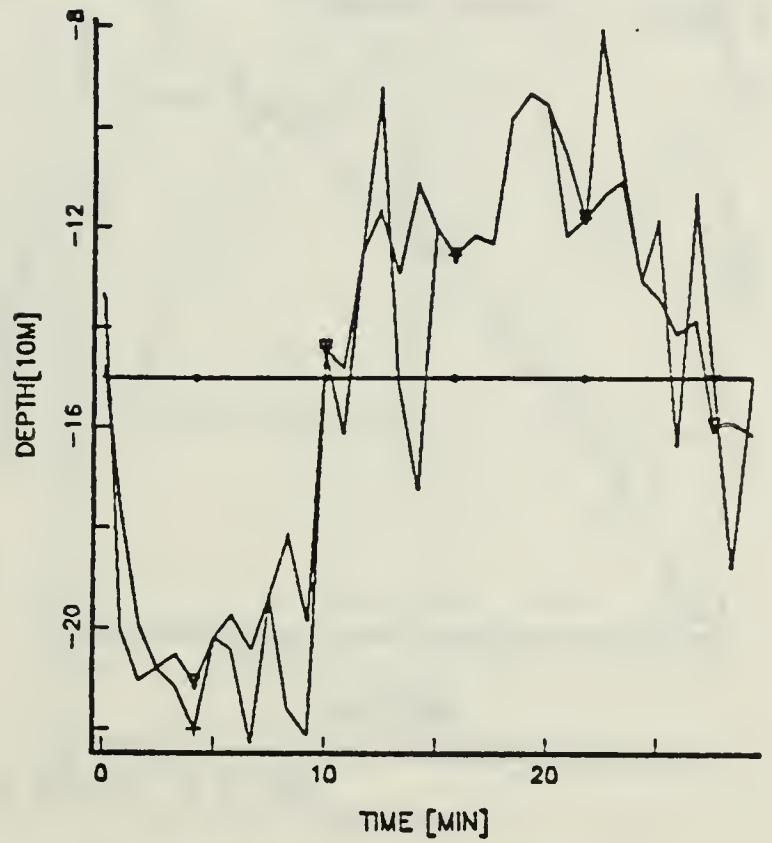
Results of Run 6 are shown in Fig. 5.1. The maximum search area size was ± 200 m in depth and ± 3.75 km in range around the predicted target position (a rectangle of 8×15 DR grid units for case S1111). Fig. 5.1 shows that the overall tracking performance is good. The range tracking error reduces to around 300 m at the 14th minute after initialization is completed. The realistic TDOA noise simulated here increases rapidly with range. This is clearly evident in Fig. 5.1 (note the two resulting range measurements errors around the 13th minute).

The system tracks well through the maneuver with an effective sample rate as low as 40%. This is indicated by the average number of solutions which is close to 0.4 in Fig. 5.1d. Note that the prefilter uses the maximum search area size during the 17th minute as indicated by the normalized size in Fig. 5.1d (actual searched area / maximum area size). Some ambiguity is indicated at shorter ranges where the solution count is larger than 1. This ambiguity affects mostly the depth tracking as can be seen in Fig. 5.1b. This effect is expected when one reviews the TDOA contours of case S1111 which is used here (see Fig. 3.6). The bearing channel tracking and the resultant XY plot of Run 6 are shown for completeness in Fig. 5.2.

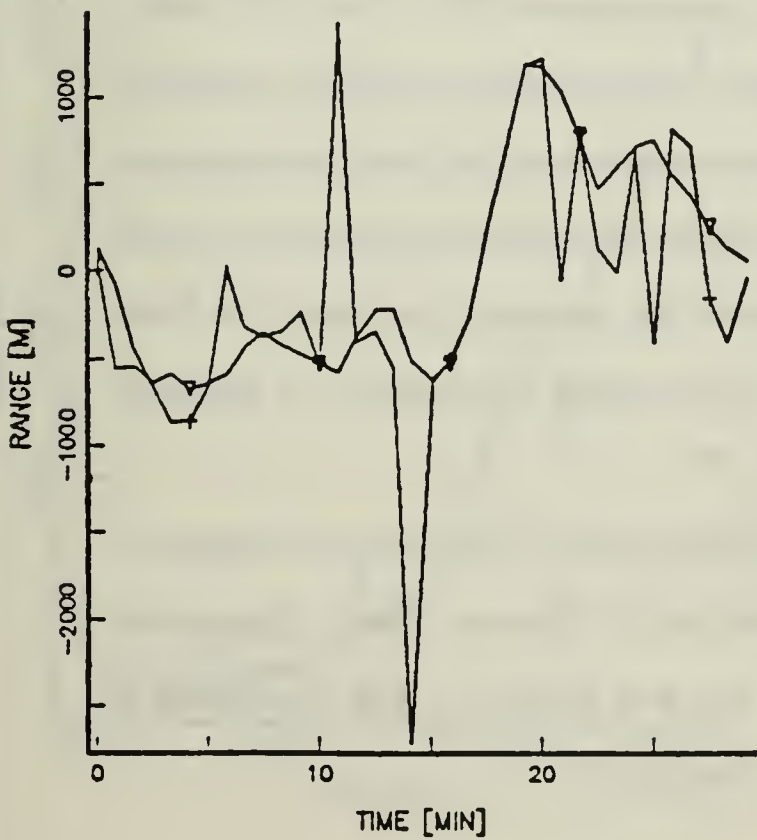
a. RANGE:ACTUAL •, MEASURED +, ESTIMATED ▽



b. DEPTH:ACTUAL •, MEASURED +, ESTIMATED ▽



c. RANGE ERROR:MEASURED + ESTIMATED ▽



d. PREFILTER PERFORMANCE

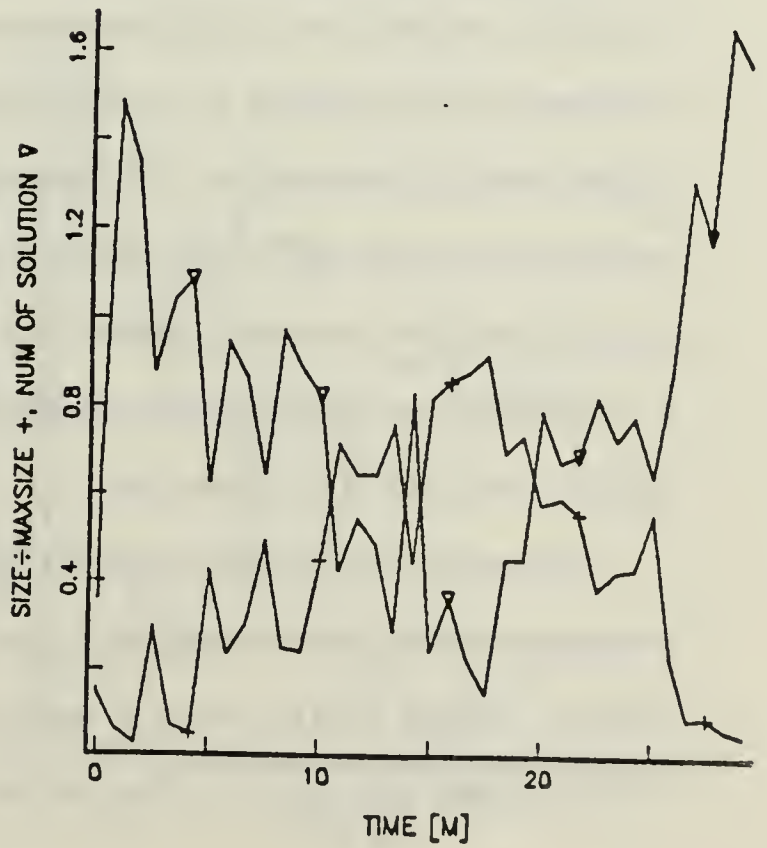


Fig. 5.1. Run-6: IH tracking of a maneuvering target.

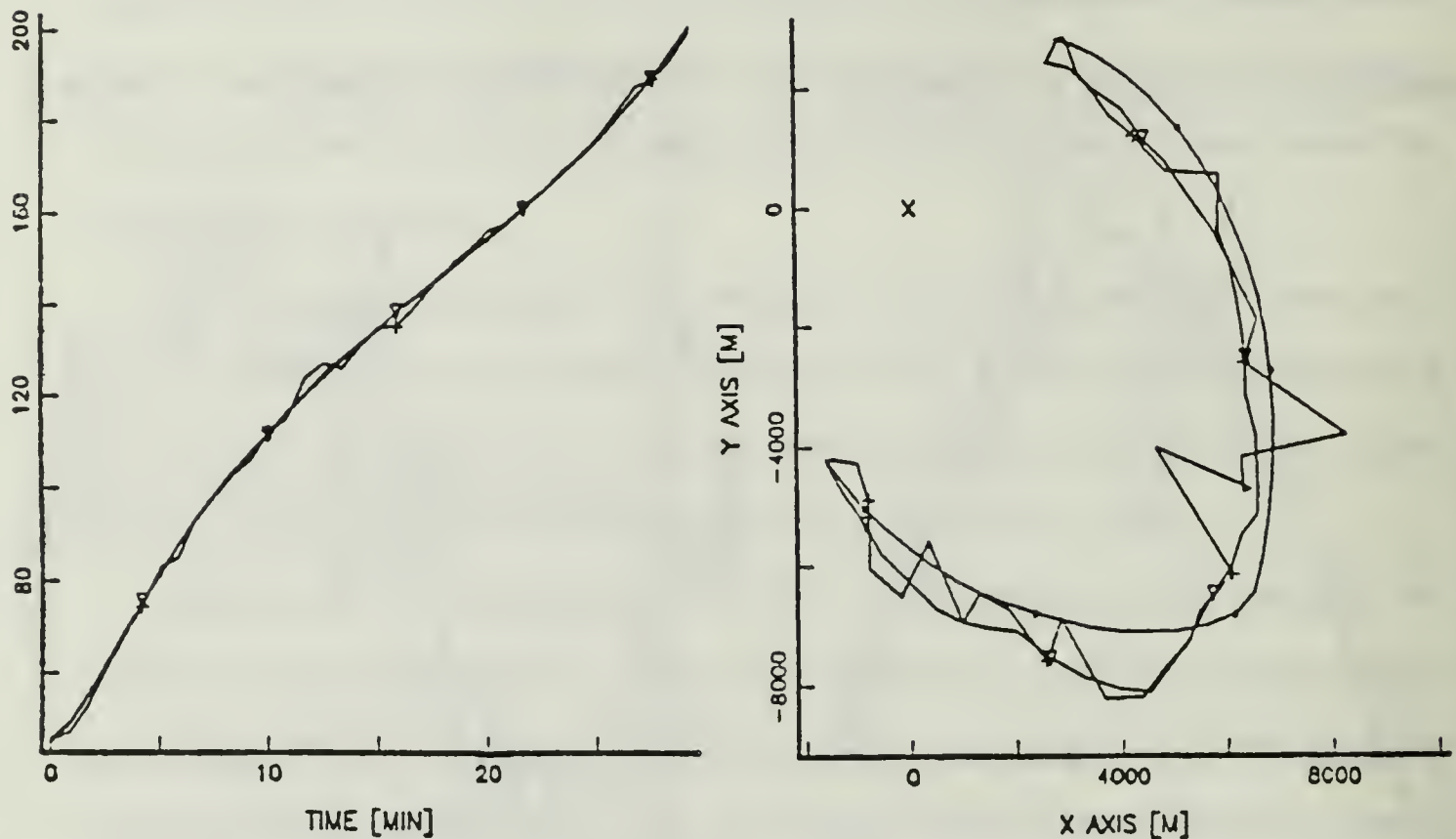


Fig. 5.2. Run-6: Bearing and XY plot.

The same scenario was used in Run 7 with a smaller maximum search area size of ± 125 m in depth and ± 2.25 km in range (a rectangle of 5X9 in the S1111 grid). The results, shown in Fig. 5.3, clearly indicate the failure of the system to track the target through the maneuver. The system loses track when the range tracking error reaches 2 km (in the 20th minute). At this time and range most of the measurements are outside of the maximum search area around the predicted position. This leads to a constant use of the maximum search area size and eventually to a complete failure (over 80% of the iterations).

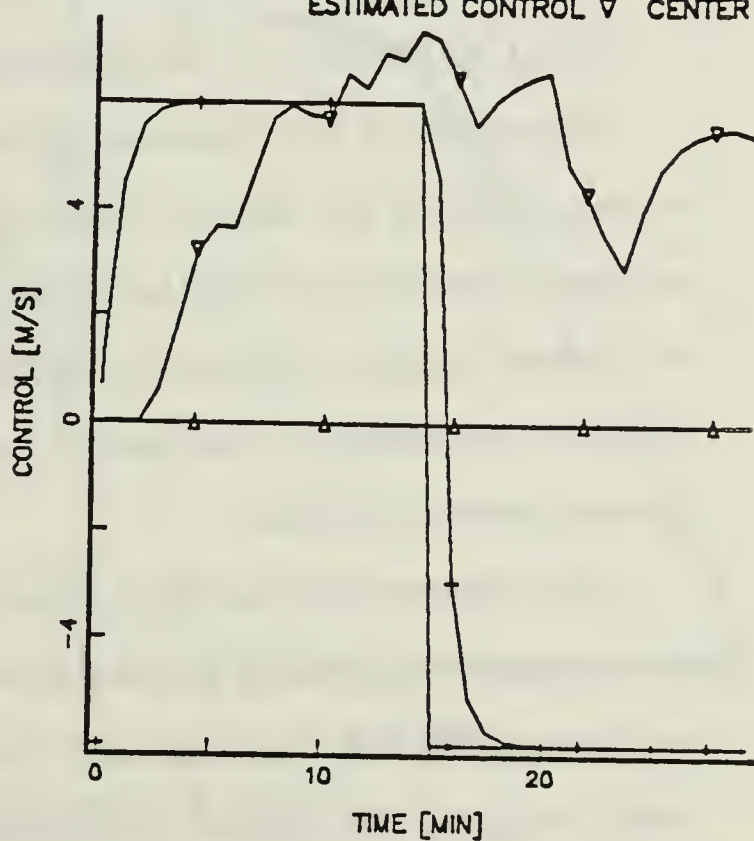
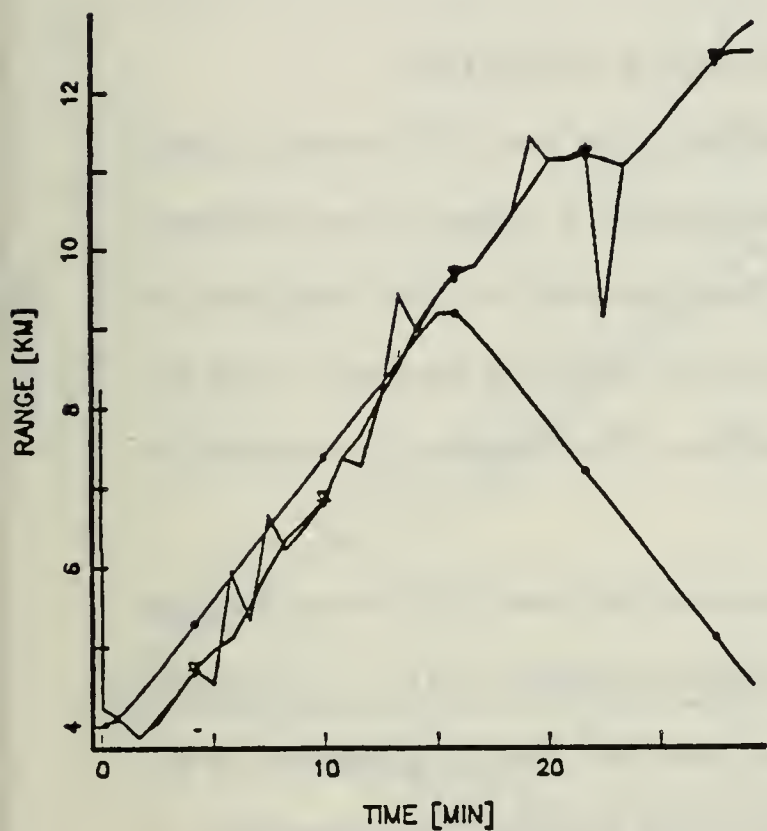
The range measurement error STD for Runs 6 and 7, was estimated using the inversion performance evaluation scheme described in Chapter Three. The typical STD for similar TDOA noise at around 9 km was 3.6 km*. The conclusion is

* Recall the discussion in Chapter Four, Section C.7

RANGE:ACTUAL •, MEASURED +, ESTIMATED ▽

ACTUAL: CONTROL • SPEED +;

ESTIMATED CONTROL ▽ CENTER Δ



RANGE ERROR:MEASURED + ESTIMATED ▽

PREFILTER PERFORMANCE

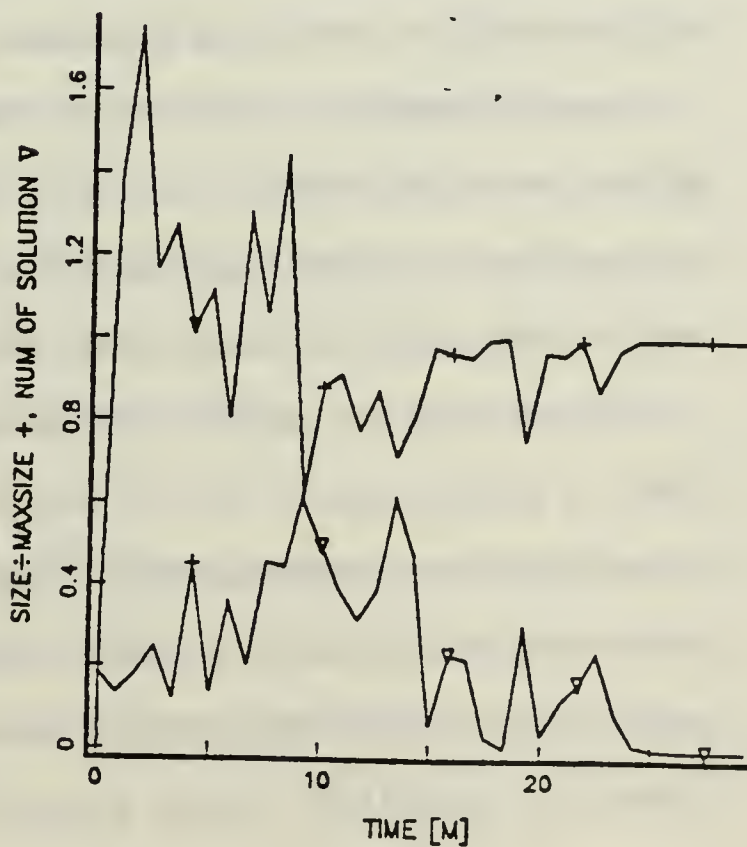
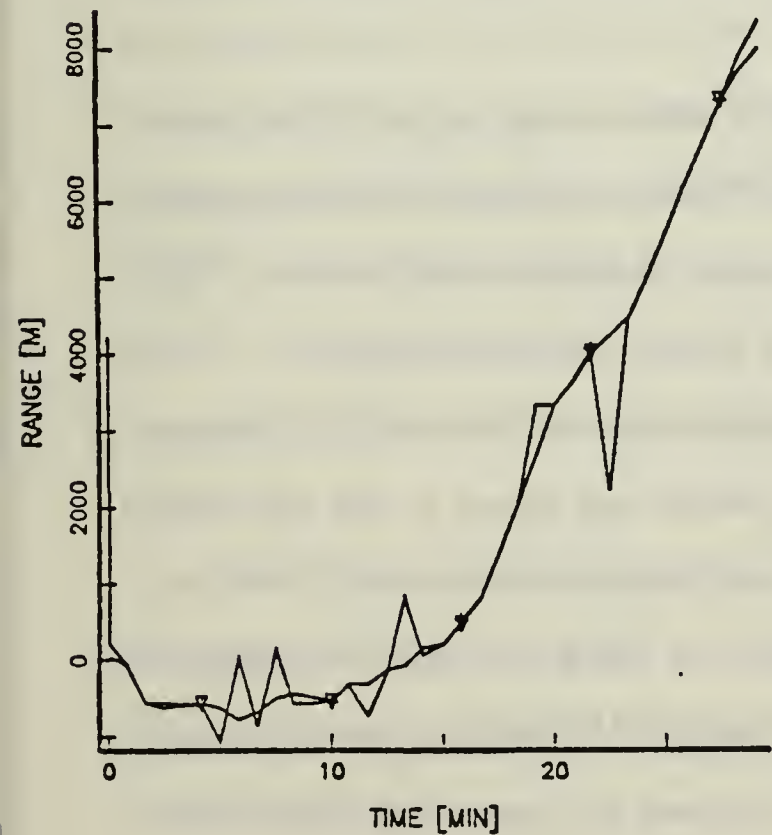


Fig. 5.3. Run-7: Failure due to reduced search area size.

therefore that the search area size should be set to twice the standard deviation of the measurement noise, $((2\sigma_d) \times (2\sigma_r))$.

C. TRACKING IN AN INHOMOGENEOUS MEDIUM

The next three Runs demonstrate the ability of the new MP tracking scheme to compensate for the effects of ocean inhomogeneity. A reference case (Refcase) was used to generate the TDOAs (the direct function table) used for simulation of the “actual” medium. The precomputed direct function table generated using the evaluated case (Evalcase) was used in the prefilter. The Evalcase represented the assumed ocean conditions.

Run 8 demonstrates the effects of an IH medium (Refcase C2251) when straight line propagation is assumed and used in the prefilter (Evalcase S1111) . The results are shown in Fig. 5.4. The large range tracking error of 3.3 km at a range of 10 km clearly indicates the need for compensation for the medium inhomogeneity. A relatively strong target signal (SNR_0 70 dB) was used in order to isolate the IH medium effects from the effects of the noise.

Run 9 examines the same scenario with a weaker target signal ($\text{SNR}_0 = 50$ dB) and its results are shown in Fig. 5.5. The TDOA measurements are noisy now and give rise to a negative range bias which adds to the effect of the IH ocean. The total resulting estimation error for this case is 4 km at the 10 km range.

The use of the new prefilter with the correctly assumed IH medium (Evalcase C2251) is demonstrated in Run 10 and the results are shown in Fig 5.6. The removal of the error associated with the IH medium is clearly evident. The error in the depth channel after the depth maneuver at the 8th minute is caused by the fact that the C2251 grid was limited to a depth of +60m (due to the current limitation of the SMART eigenray program discussed in Appendix F). This error

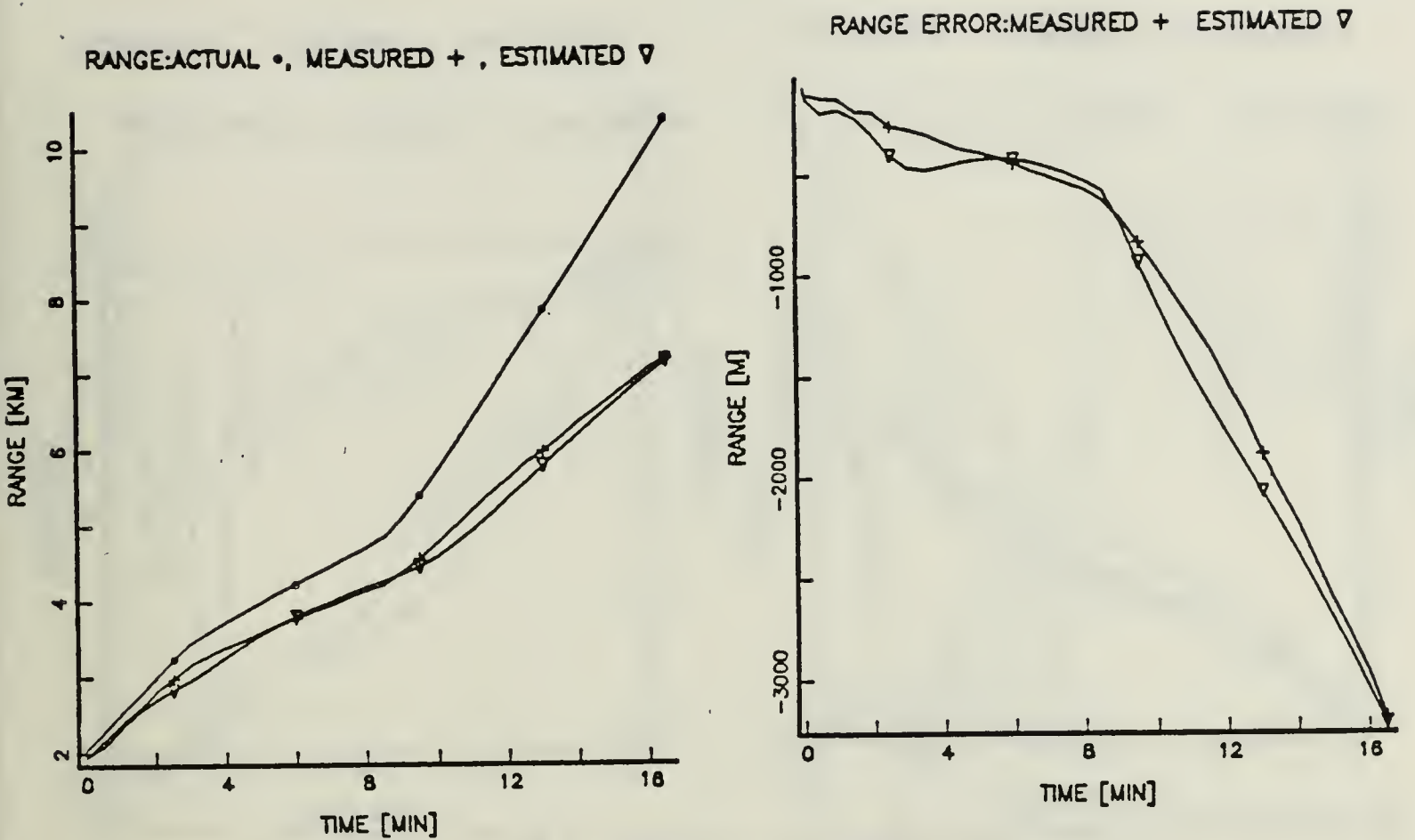
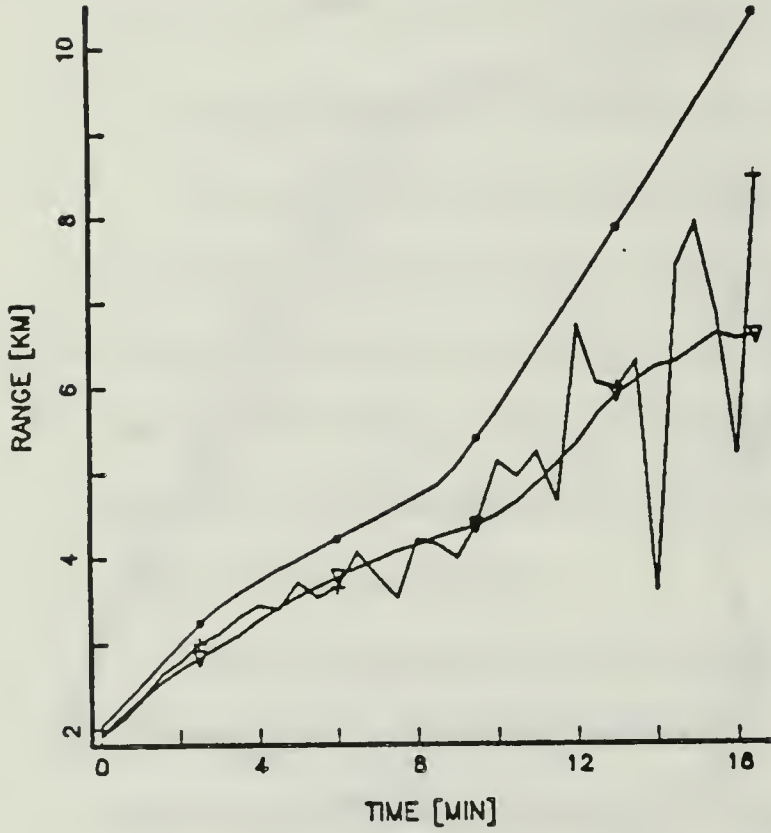


Fig. 5.4. Run-8: Tracking in an IH medium.

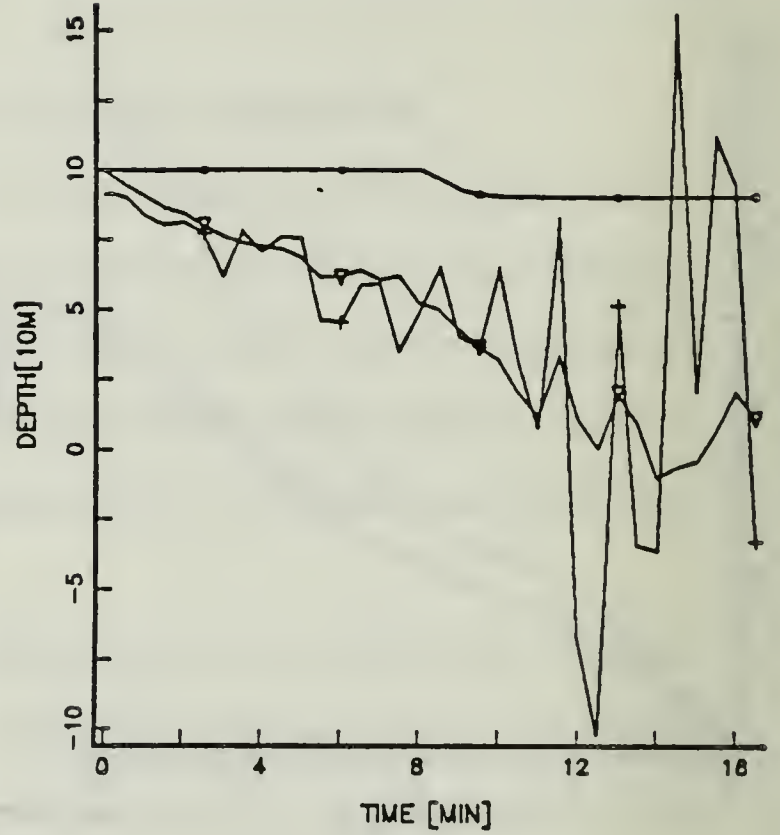
is not present at shallower depths away from the grid edge or if the noise is smaller as demonstrated by the near perfect tracking in Fig. 5.6 where SNR_0 of 70 dB was used. This error can be removed completely if a full grid is employed. The average number of solutions reached 1.8 in some cases since the corresponding TDOA contour lines intersect in four closely located DR positions (see Fig. 3.17 which is taken from typical contours of the same case C2251). The effects of the increased TDOA measurement noise are evident at the long range toward the end of the run.

The overall tracking capability in an IH medium demonstrated by this run is also shown in Fig. 5.6 as an XY plot. The estimated track (heavy line) approaches the actual track (marked with dots) whereas the measurements are very noisy (the fluctuating line).

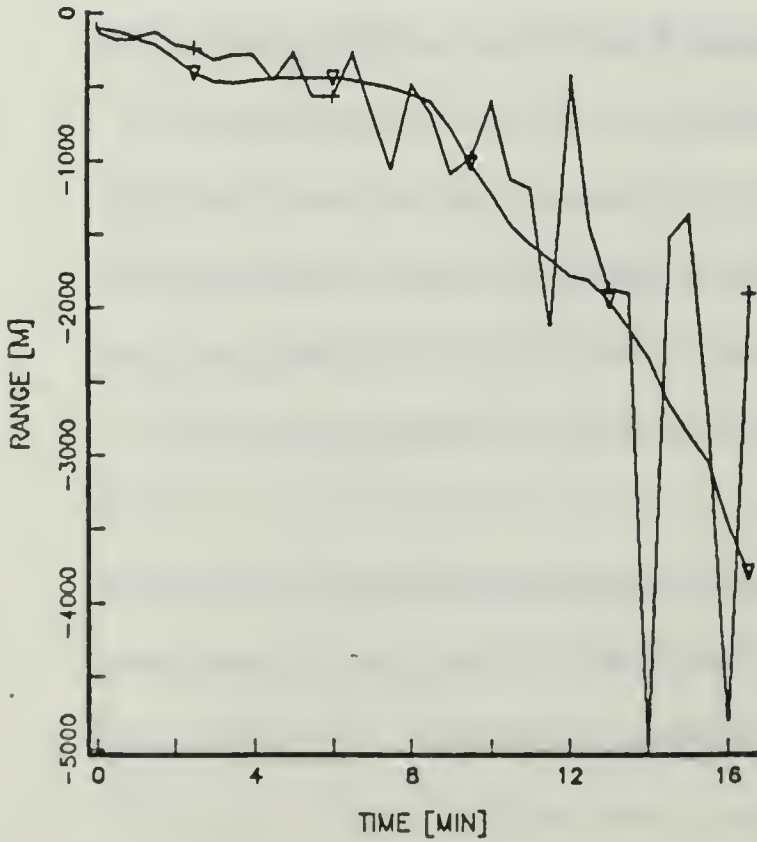
RANGE:ACTUAL •, MEASURED +, ESTIMATED ▽



DEPTH:ACTUAL •, MEASURED +, ESTIMATED ▽



RANGE ERROR:MEASURED + ESTIMATED ▽



PREFILTER PERFORMANCE

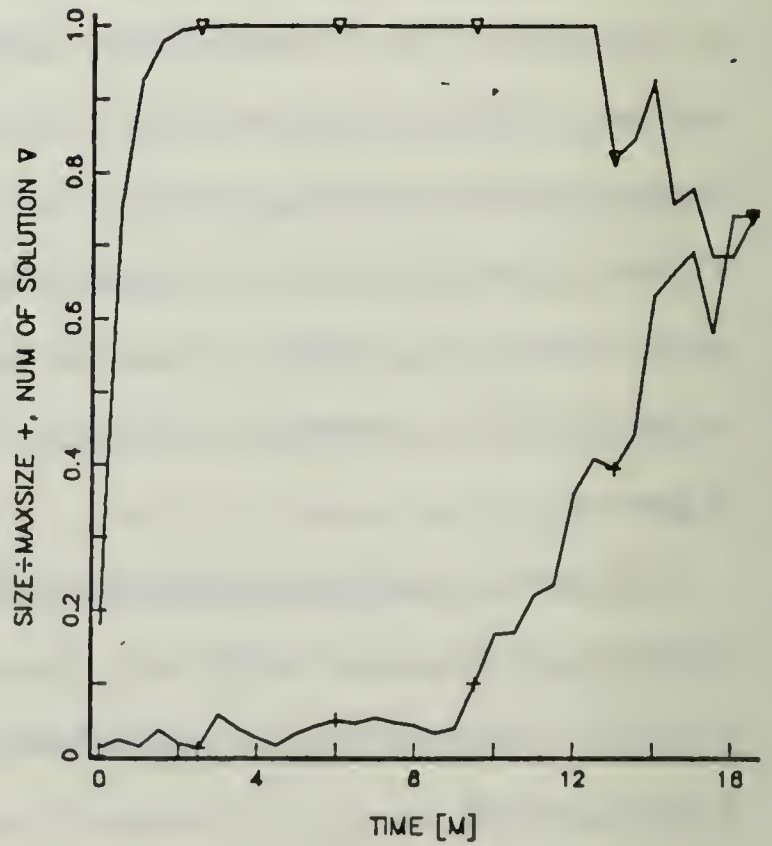
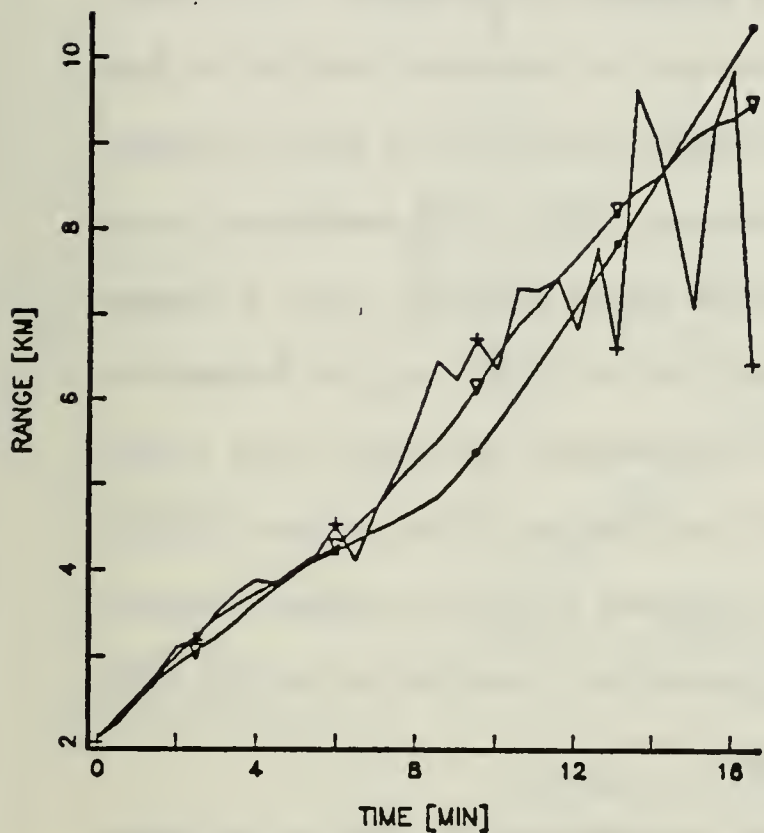
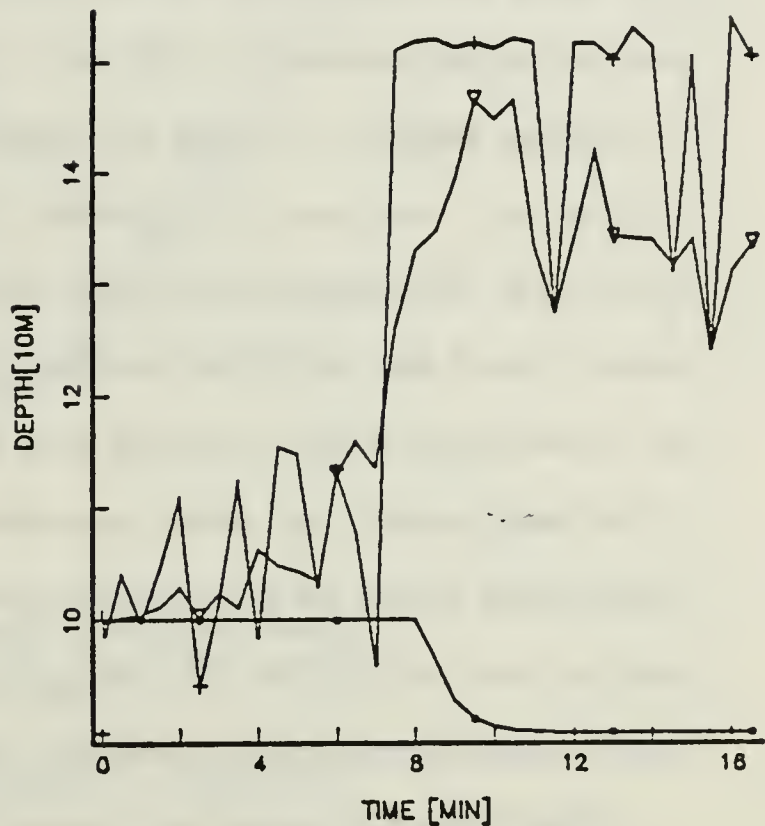


Fig. 5.5. Run-9: Effect of IH and TDOA noise.

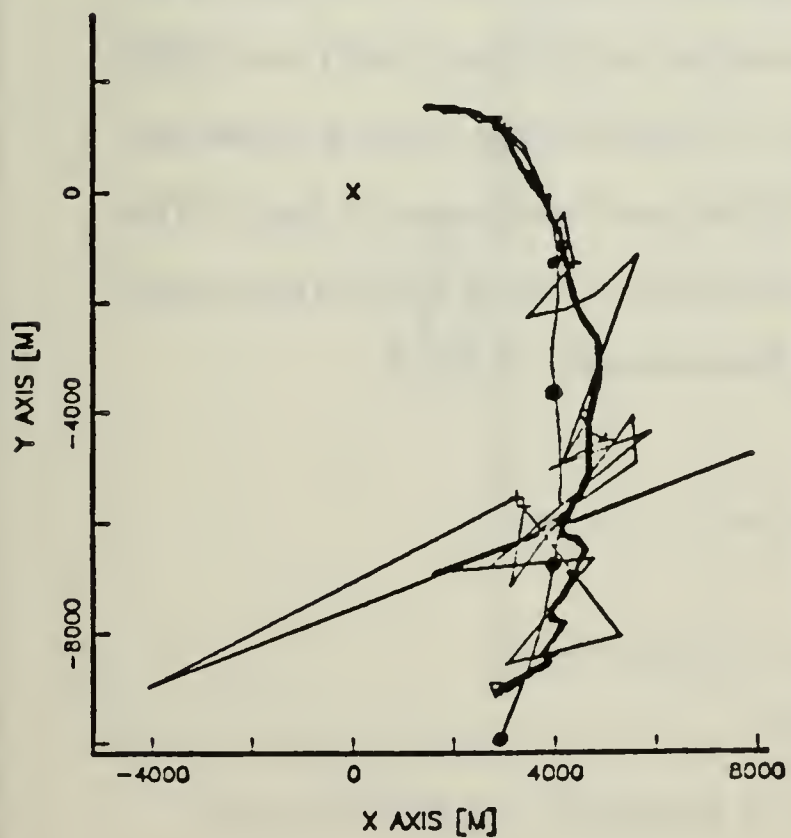
RANGE:ACTUAL •, MEASURED +, ESTIMATED ▽



DEPTH:ACTUAL •, MEASURED +, ESTIMATED ▽



X-Y: OBSERVER X ACTUAL • MEASURED + ESTIMATED ▽



PREFILTER PERFORMANCE

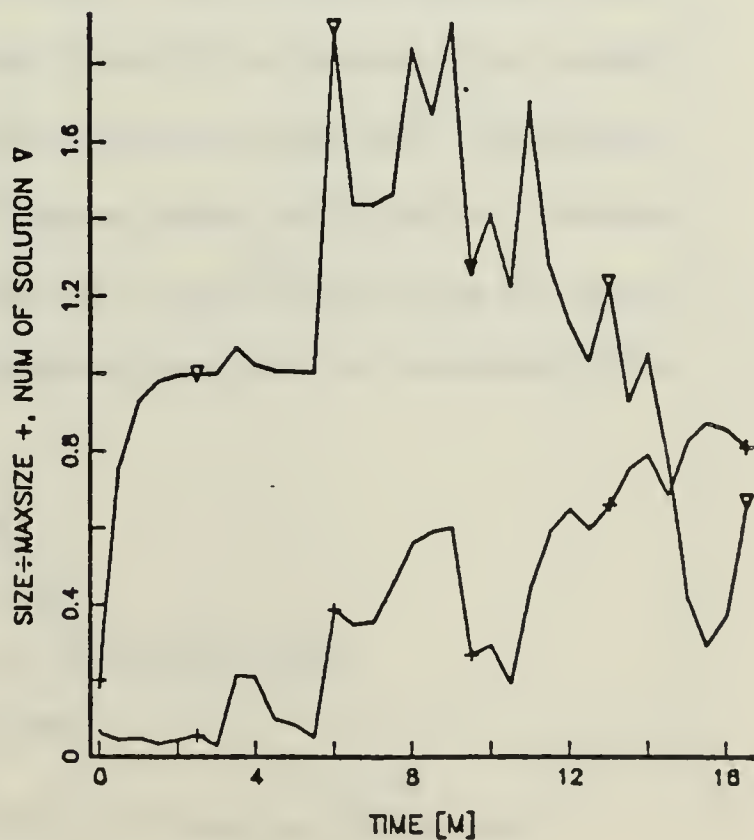


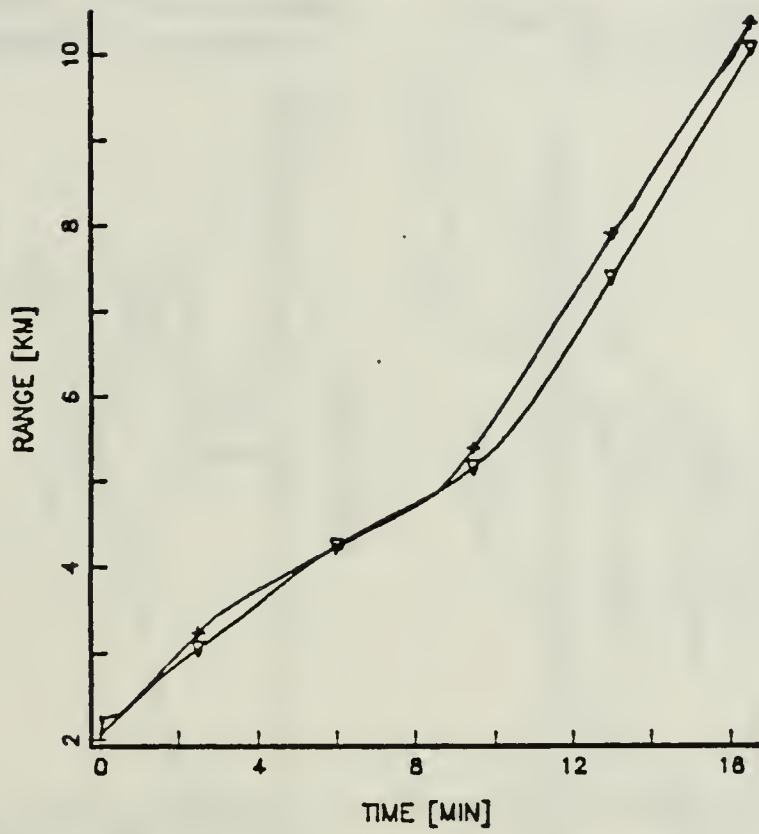
Fig. 5.6. Run-10: Correction for medium inhomogeneity.

D. EFFECTS OF ERRONEOUS SVP

The sensitivity of the IH MP inversion to errors resulting from an assumed SVP which is different from the true SVP is examined in this section. A SVP with positive surface gradient of 0.105 sec^{-1} was used as the actual medium in Run 11 (Refcase A4261). A similar but slightly different SVP with a surface gradient of 0.100 sec^{-1} was used in the prefilter (Evalcase A3253). The results are shown in Fig. 5.8. The range error is quite small for ranges less than 7 km. At ranges greater than 8 km the TDOA resulting from the true SVP using the Refcase are not covered by the direct function used by the prefilter. This again is not a limit of the basic method but rather a result of the limitation of the current SMART model which forced the grid selection (see Appendix F). For the region evaluated here one can conclude that the method is insensitive to small errors in SVP. This trend is expected to extend to longer ranges.

When large SVP errors are present, the resultant tracking error is also large. This is demonstrated by Run 12 where a gradient of 0.105 sec^{-1} was used in the Refcase and a gradient of 0.05 sec^{-1} was used as an Evalcase (C4261 and C2251 respectively). The results, shown on Fig. 5.9, indicate large tracking errors that resemble the effect of the uncompensated IH medium demonstrated in Run 8. This is expected since the SVP error in the assumed SVP in Run 12 is of the same order of magnitude as the total uncompensated inhomogeneity in Run 8.

RANGE:ACTUAL •, MEASURED +, ESTIMATED ▽



DEPTH:ACTUAL •, MEASURED +, ESTIMATED ▽

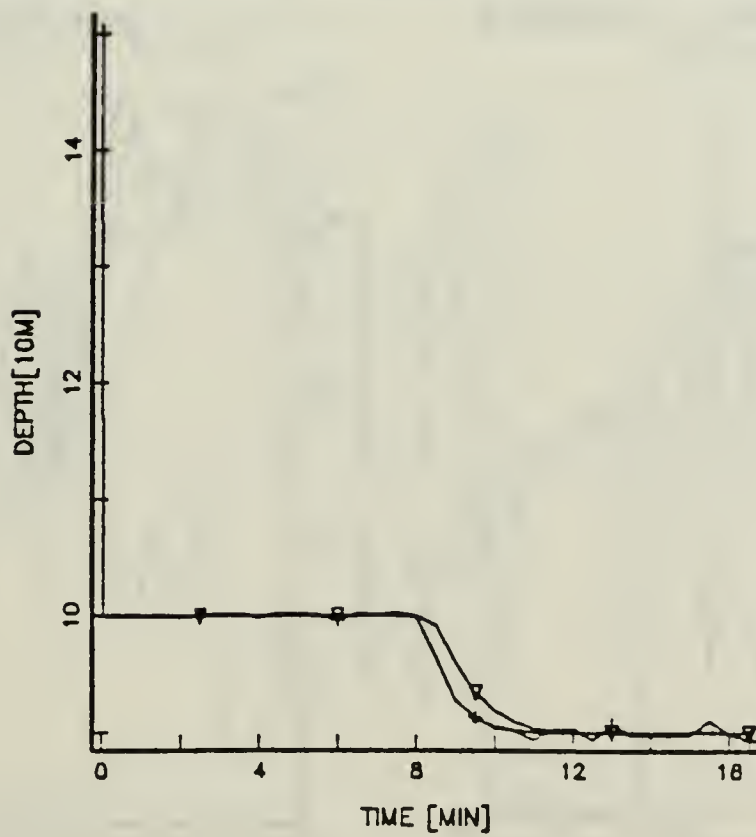


Fig. 5.7. Run 10a: Correction for medium inhomogeneity, low noise.

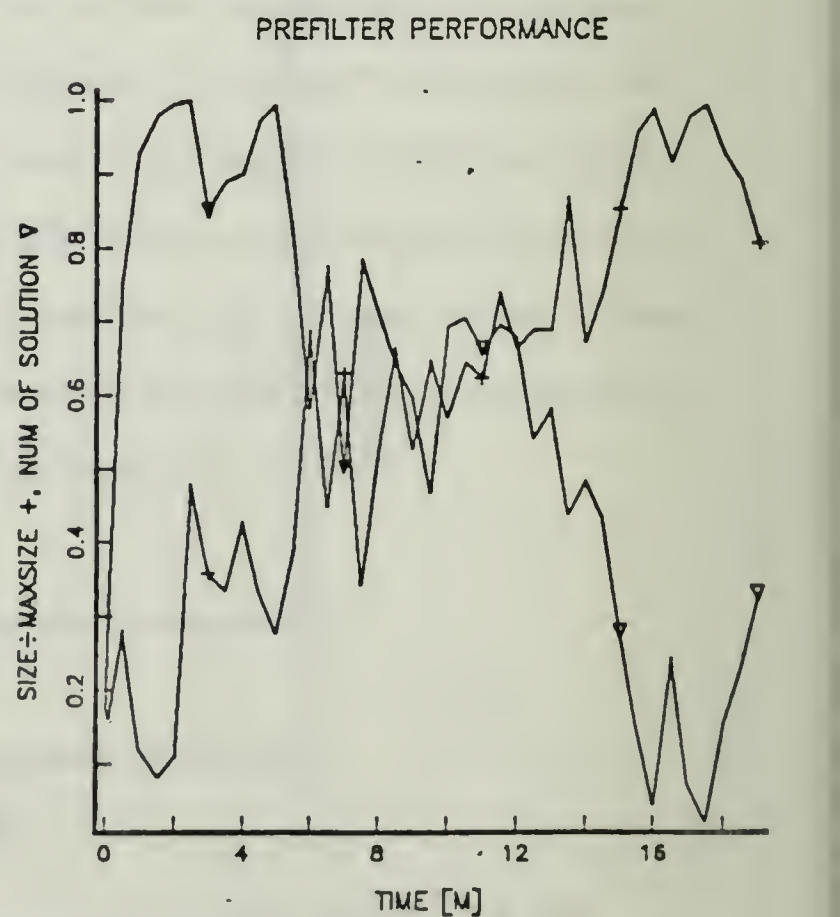
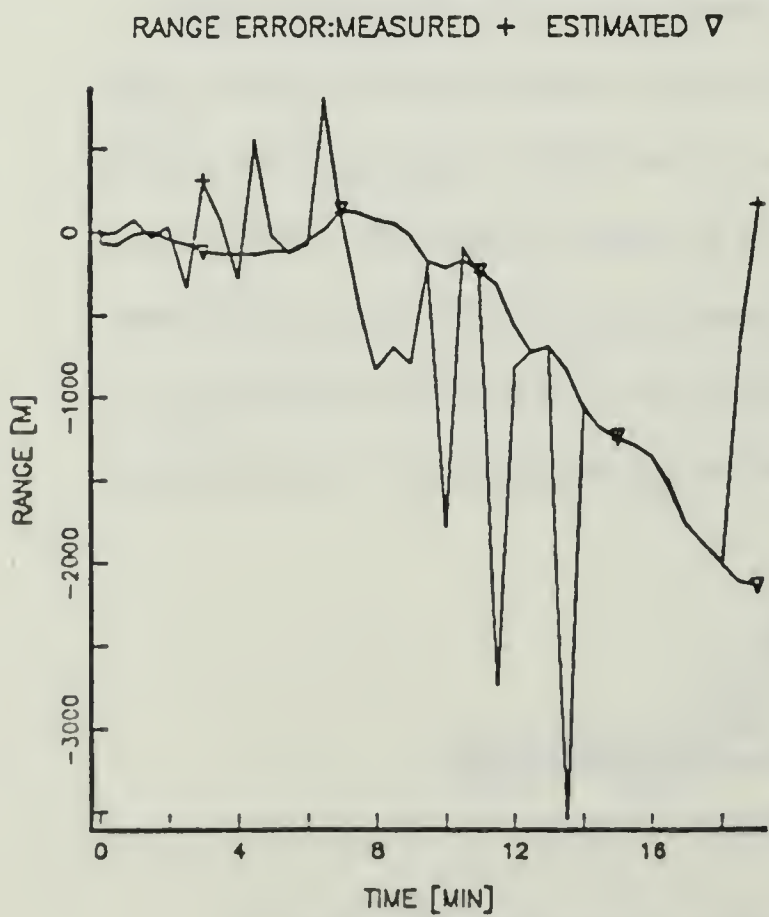
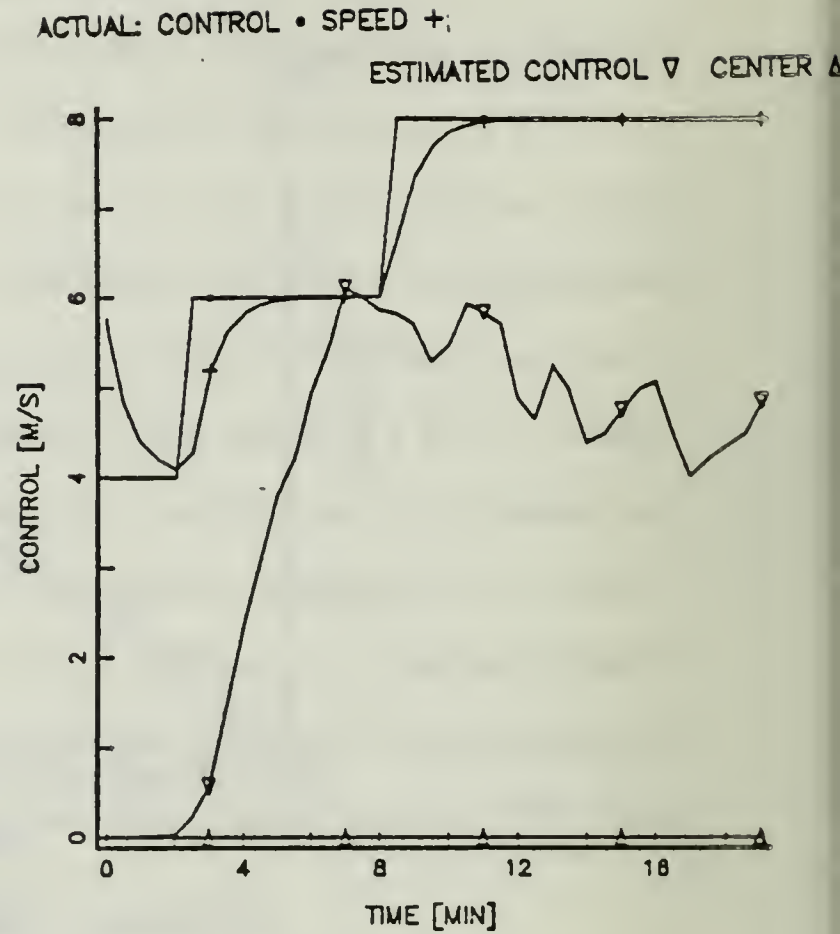
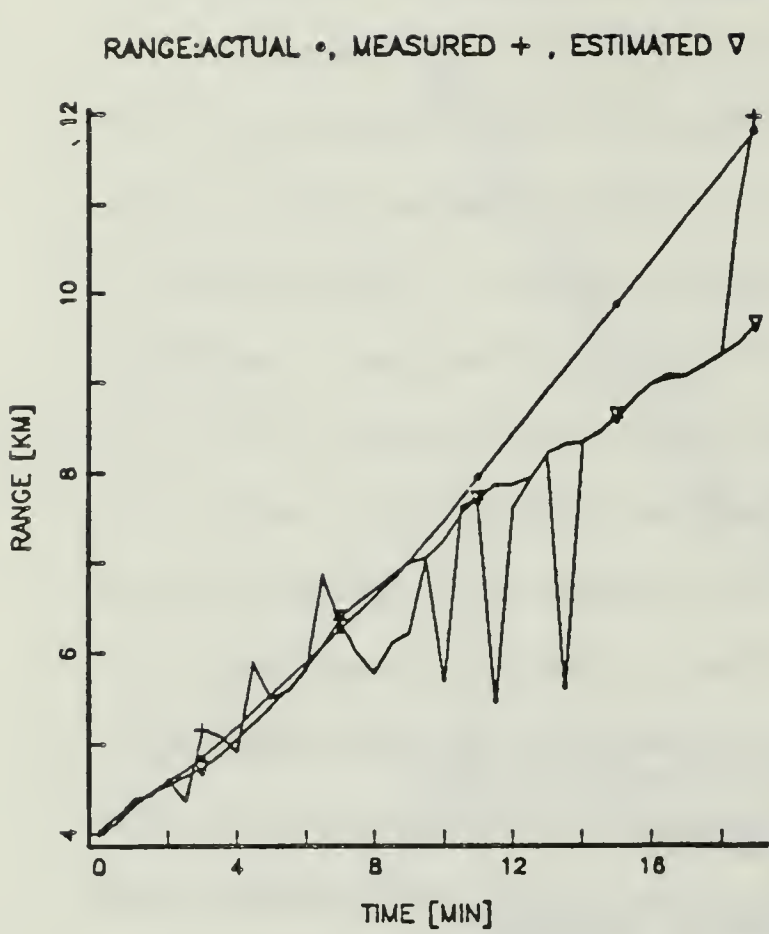
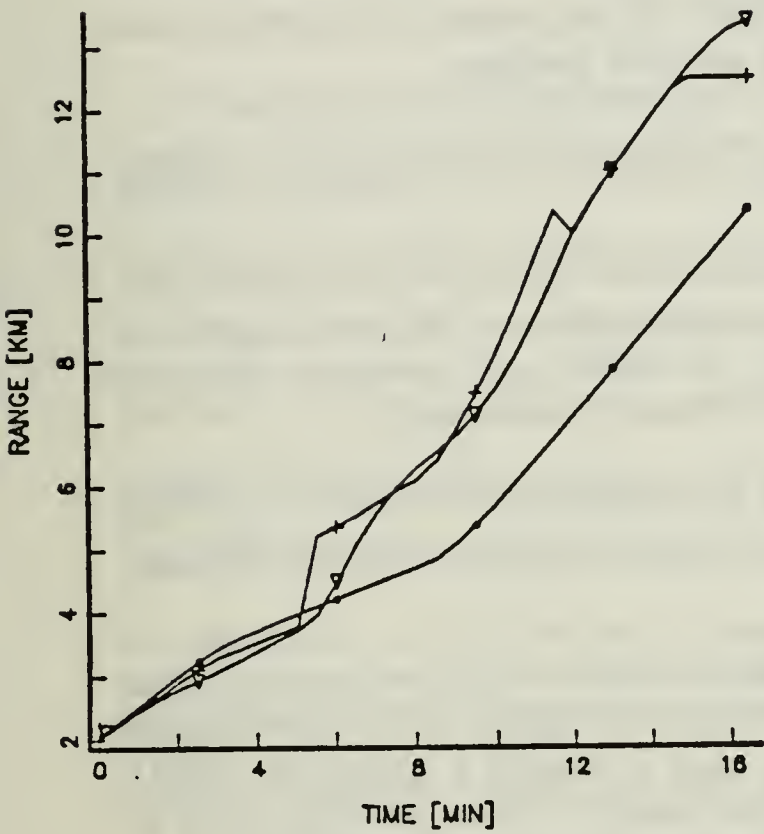
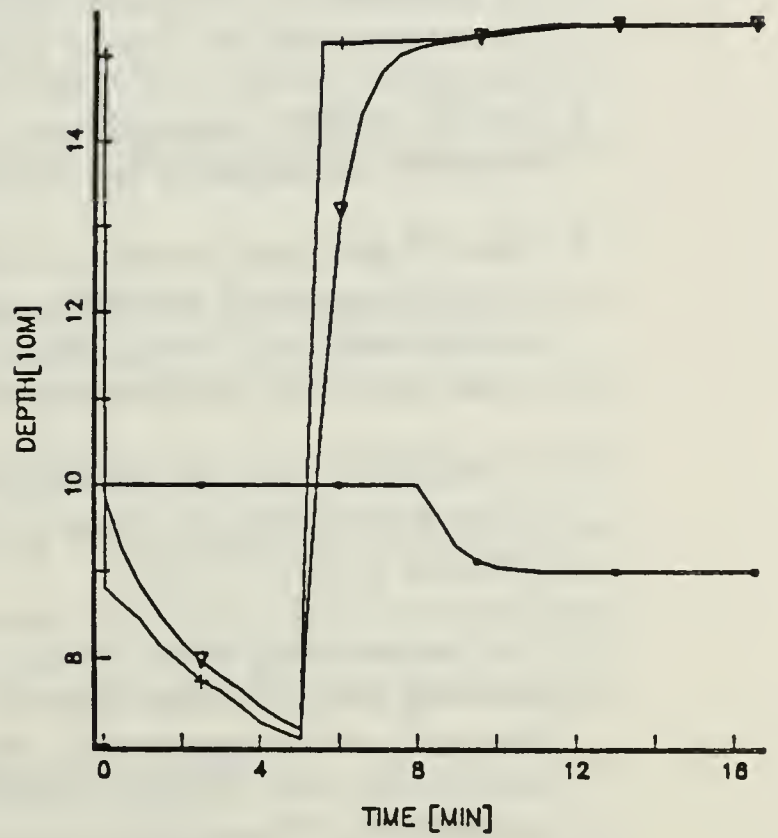


Fig. 5.8. Run-11: Effect of small errors in SVP.

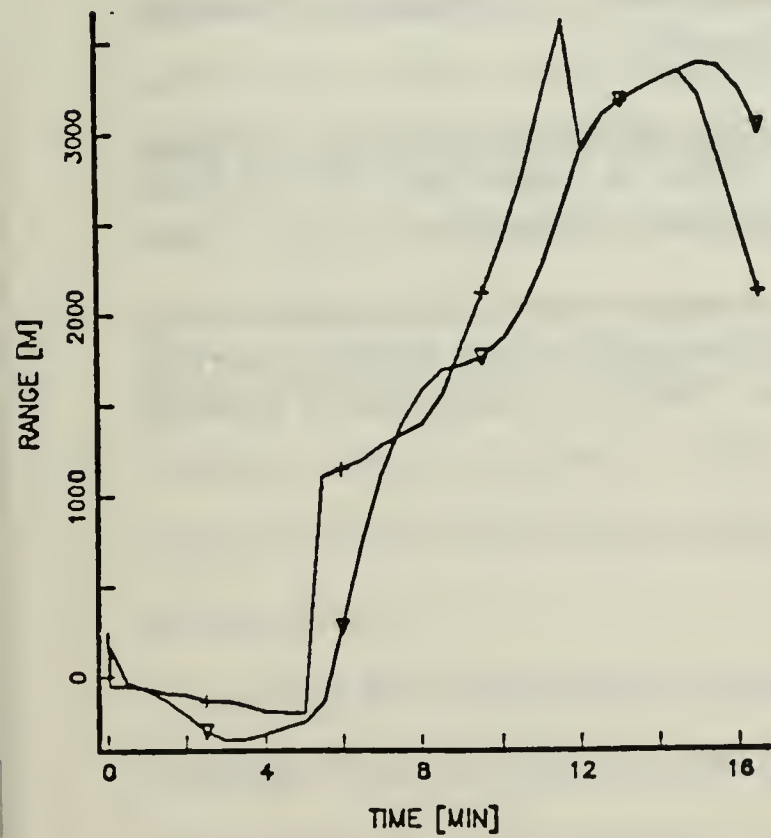
RANGE:ACTUAL •, MEASURED +, ESTIMATED ▽



DEPTH:ACTUAL •, MEASURED +, ESTIMATED ▽



RANGE ERROR:MEASURED + ESTIMATED ▽



PREFILTER PERFORMANCE

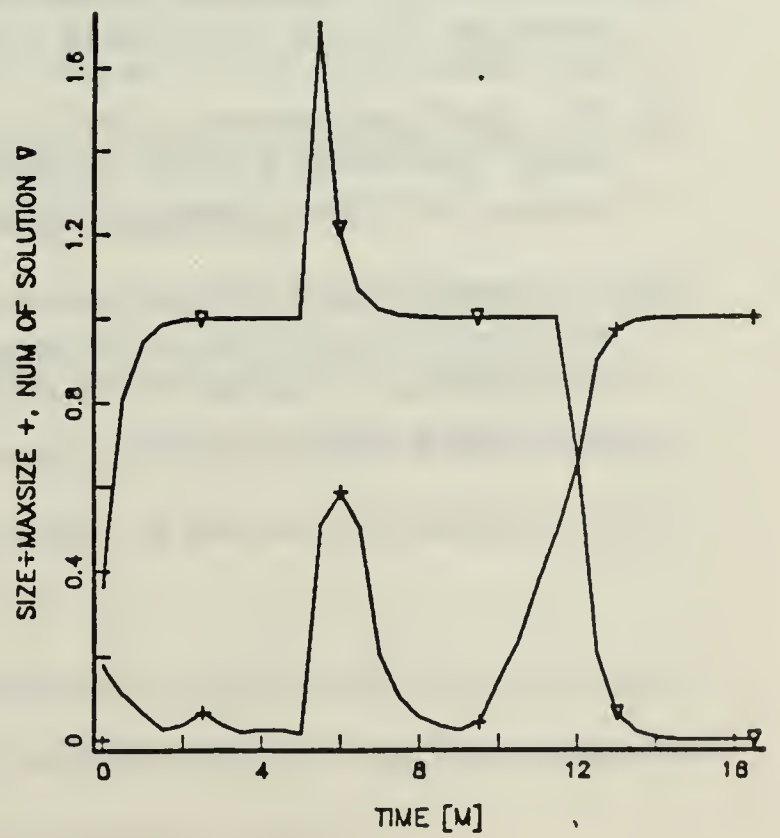


Fig. 5.9. Run-12: Effect of large BT errors.

E. SUMMARY OF SIMULATION RESULTS

The results of the complete system evaluation can be summarized as follows:

1. IH propagation introduces *significant* errors in MP tracking. The effect must be compensated for in order to achieve accurate tracking.
2. The IH prefilter proposed here is functionally sound and can provide compensation for the effects of the IH medium.
3. The DR grid used to compute the direct function should be chosen with care. It should cover all possible target positions, with an additional margin to enable handling of measurement noise. Too wide a grid, primarily along the depth axis, adds ambiguous solutions and should be avoided.
4. As a general rule, the maximum search area size should be made larger than twice the standard deviation of the depth and range measurement noise, i.e., area size $\geq (2\sigma_d) \times (2\sigma_r)$.
5. The maneuvering target tracker can handle reduced effective sampling rates resulting from inversion failures. The original sampling period was selected here as 5 sec to match target dynamics and to provide a reasonable TDOA observation time. Effective sampling rates which at times are reduced to as low as 40% of the original rate can still support reasonable tracking.
6. The inversion is insensitive to small errors between the assumed SVP and the actual one. (5-10% in the sound speed gradient)
7. The overall performance of the MP tracking degrades rapidly with increasing range. This results from the vanishing TDOA at longer range and the rapid increase in TDOA noise due to the attenuated target signal.
8. As a result of the growing noise at longer ranges, measurement biases develop which tend to underestimate the range. Eventually the MP tracking filter fails completely and losses track of the target. Reliable tracking can be expected up to ranges of about 15 km.

VI. CONCLUSION

This chapter concludes the thesis. It includes a brief review of the problem; a short description of the solutions and a summary of the results. It ends with a suggestion for further extension of the work.

Current acoustic broadband MP tracking techniques, which have evolved over the last ten years, are based on straight line propagation. In reality the ocean medium is inhomogeneous and the sound propagates along curved ray paths. MP tracking therefore encounters large errors if the IH propagation is not accounted for. Since there is no closed form relation between the TDOA and source depth and range (DR) for the inhomogeneous case, the compensation for the inhomogeneity is computationally complex and until now had not been done.

Previous MP tracking algorithms have also assumed that the TDOA are always resolvable and associable with the corresponding path. In practical tracking situations the TDOA are not always resolvable due to finite bandwidth of the receiver and association of TDOA with the corresponding path is very difficult. The impact of these assumptions on MP tracking is significant.

In addition TDOA measurements are noisy. The SNR depends on the strength of the received signal which in turn depends on range due to the propagation loss. A realistic overall evaluation of a MP tracking system requires a more accurate model for the noise than those previously used, as well as a simulation of the IH medium effects.

Current MP tracking algorithms employ the multiple model (MM) estimation technique. This technique produces tracking biases since the multiple models are in most cases not centered around a true model of the target.

This work focused on developing a model that accounts for the IH propagation and the effects of realistic TDOA processing. A key contribution of this work is the development of an algorithm to compute depth and range from TDOAs produced by MP in an IH medium. In our approach the TDOAs are assumed to be estimated by realistic instrumentation and thus have limited resolution and are not assumed to be associable with their corresponding path.

The performance of the model is evaluated using a accurate range dependent model for the noise. The depth range calculation is performed with the help of an eigenray program exercised over a DR grid. The realistic TDOAs are numerically computed offline and stored in a direct function table. The measured TDOAs are then used online to produce the corresponding DR using linear interpolation. The method accounts for any multipath structure and is not dependent on the association of the TDOA with the multipath.

The interpolation is performed as follows. The DR and TDOA values of three points in the direct function table that have TDOA values close to the measured set, are used in the interpolation. The triangle of the three closest points in the direct function table is located by means of a unique search algorithm called the local search. The search is limited to a small area centered around the predicted target position in order to improve the efficiency and reduce the ambiguity.

A technique for centering the MM hypotheses bank around the estimated target maneuver command to reduce the tracking bias was also developed. The entire model is shifted in a manner that requires no computation. It is based on an analytically derived linear relation between the command hypothesis bank and the states of the corresponding models. A second order smoother instead of the first order one previously used eliminates the lag error encountered in earlier tracking

designs. An evaluation of the performance of the new MP tracking scheme in shallow waters using a realistic model for the noise shows very good results.

A comprehensive set of test cases were run to evaluate the components of the MP tracker both individually and as a total system. The main results of the simulation show that:

1. Significant errors are introduced in MP tracking by the ocean IH acoustic medium.
2. The new MP inversion method and the tracking technique can compensate for the IH medium effects.
3. The effects of limited delay resolution and lack of TDOA and path associability are also accounted for by the new method.
4. The depth measurement is more affected by the ambiguity resulting from the lack of TDOA path associability than the range measurement.
5. Realistic noise limits the performance of shallow water MP tracking to short ranges (say less than 15 km). The noise initially introduces estimation biases and eventually leads to a complete loss of track.
5. At short ranges the method is insensitive to small errors in SVP. The method is more sensitive to errors in ocean bottom depth. Large errors in SVP or bottom depth introduce large MP measurement errors.
7. Recentering the MM around the estimated maneuver command and the use of the second order smoother significantly reduces tracker estimation bias.
8. The coordinate decoupling technique currently used in MP tracking introduces tracking errors for nonmaneuvering targets around the CPA at short ranges.
9. A second order target model is sufficient for maneuvering target tracking if the Kalman gain is properly trimmed.

There are several directions in which this work can be extended. However the following specific direction is a natural extension of the ideas and offers potential improvement of the results derived here.

Use of more than the first two TDOAs has the potential of reducing the depth and range estimation noise. More importantly use of additional TDOAs will reduce the ambiguity in target position. If, in addition, information on the reflections is available* and the signal spectrum is known then the complete ACF of the received signal can be constructed for every point in the grid. A classification method could then be set up to measure the closeness of the measured ACF to those constructed for the points in the grid. The conditional probabilities of the target position for any of the DR grid points can be generated by the MM tracker and incorporated into the classifier. Interpolation between the closer DR points can then be used to compute the target position.

In summary, this research investigated the influence of realistic conditions on the multipath tracking of maneuvering targets. The inhomogeneity of the acoustic ocean medium; the limitations of TDOA estimation; and the difficulty in association of TDOA with multipath all have a significant effect on the tracking. A new model was devised to counter these effects. A very thorough evaluation of the model was conducted with a special emphasis on the reality of the simulated condition. The results indicate that in general the MP tracking is limited to short ranges. Accurate tracking can only be achieved if the distorting effects of the medium and the delay estimation are compensated for as was successfully done here.

* Such as when operating in a well known and previously measured area of the ocean

APPENDIX A

TRANSITION MATRICES

A separate model of the form

$$X_n = \phi X_{n-1} + \Gamma U_{n-1} + \Psi W_{n-1} \quad (A.1)$$

is used to describe target motion along the X, Y or range R axis. The components of the matrices appearing in this equation are given below.

$$\phi_{11} = 1$$

$$\phi_{21} = \phi_{31} = \phi_{32} = 0$$

$$\phi_{12} = (1 - e^{-\alpha T}) / \alpha$$

$$\phi_{22} = e^{-\alpha T}$$

$$\phi_{13} = [1 + (\alpha_w e^{-\alpha T} - \alpha e^{-\alpha_w T}) / (\alpha - \alpha_w)] \frac{1}{\alpha \alpha_w}$$

$$\phi_{23} = (e^{-\alpha_w T} - e^{-\alpha T}) \cdot \frac{1}{\alpha - \alpha_w}$$

$$\phi_{33} = e^{-\alpha_w T}$$

$$\Gamma_1 = (\alpha T - 1 + e^{-\alpha T}) \cdot \frac{1}{\alpha}$$

$$\Gamma_2 = 1 - e^{-\alpha T}$$

$$\Gamma_3 = 0$$

$$\Psi_1 = \left\{ T + \left[\frac{\alpha_w}{\alpha} (1 - e^{-\alpha T}) - \frac{\alpha}{\alpha_w} \cdot (1 - e^{-\alpha_w T}) \right] \frac{1}{(\alpha - \alpha_w)} \right\}$$

$$\Psi_2 = [\alpha_x (1 - e^{-\alpha_w T}) - \alpha_w (1 - e^{-\alpha T})] \frac{1}{\alpha - \alpha_w}$$

$$\Psi_3 = (1 - e^{-\alpha_w T}) \alpha$$

These parameters are easily derived from Eq. 2.3.3 in Ref. 6 by the change of variables

$$U_n \leftrightarrow \frac{1}{\alpha} U_k \quad (A.2)$$

$$W_n \leftrightarrow \frac{1}{\alpha\alpha_w} W_k \quad (A.3)$$

and

$$\alpha_w = a. \quad (A.4)$$

The advantage of the scaling used here is that both U and W are now in [m/sec], for example a constant process noise W or command U of 1 [m/sec] in the X direction would each yield $\dot{x} = 1$ [m/sec] at the steady state.

For the cross range channel the equation is

$$\dot{B} = \phi_b \cdot B_{n-1} + \Gamma_b U_b + \Psi_b w_{n-1} \quad (A.5)$$

where the components of the matrices are expressed

in terms of the previous models components as

$$\phi_{b11} = \phi_{11}$$

$$\phi_{b21} = \phi_{b31} = \phi_{b32} = 0$$

$$\phi_{b12} = \phi_{12}$$

$$\phi_{b22} = \phi_{22}$$

$$\phi_{b31} = \phi_{31}/R$$

$$\phi_{b32} = \phi_{32}/R$$

$$\phi_{b33} = \phi_{33}$$

$$\Gamma_{b1} = \Gamma_1/R$$

$$\Gamma_{b2} = \Gamma_2/R$$

$$\Gamma_{b3} = 0$$

$$\Psi_{b1} = \Psi_1/R$$

$$\Psi_{b2} = \Psi_2/R$$

$$\Psi_{b3} = \Psi_2/R$$

These results derive from Eq. 2.3.28 in Ref. 6 with the change of variables Eq. (A.2) - (A.4).

APPENDIX B
CONDITIONAL MEAN ESTIMATE

A constant U is to be estimated from the observation $z = U + n$ where $n \sim N(0, \sigma^2)$. The optimal mean square estimate is the conditional mean $\hat{U} = E\{U|z\}$. Two equiprobable hypotheses U_1, U_2 are assumed, which span the range of the expected U . The estimate is thus given by

$$\hat{U} = E\{U|z\} = \sum_{i=1}^2 U_i \cdot P(U_i|z) = \sum_{i=1}^2 U_i \cdot \frac{f(z|U_i) \cdot P(U_i)}{f(z)} \quad (B.1)$$

where $f(z)$ is the density function.

With $P(U_1) = P(U_2) = 1/2$ and the given normal distribution of the noise the estimate \hat{U} is given by:

$$\hat{U} = \frac{U_1 \cdot \frac{1}{\sqrt{2\pi\sigma}} \cdot e^{-(z-U_1)^2/2\sigma^2} + U_2 \cdot \frac{1}{\sqrt{2\pi\sigma}} \cdot e^{-(z-U_2)^2/2\sigma^2}}{\frac{1}{\sqrt{2\pi\sigma}} \cdot e^{-(z-U_1)^2/2\sigma^2} + \frac{1}{\sqrt{2\pi\sigma}} e^{-(z-U_2)^2/2\sigma^2}} \quad (B.2)$$

which after some algebra is:

$$\hat{U} = \frac{X_1}{1 + e^{-[-2z(U_2-U_1)-(U_2-U_1)(U_2-U_1)]/2\sigma^2}} + \frac{X_2}{1 + e^{-e[2z(U_2-U_1)-(U_2-U_1)(U_2+U_1)]}} \quad (B.3)$$

If we let

$$U_s = U_2 - U_1; U_c = (U_1 + U_2)/2; \quad (B.4)$$

and

$$\alpha = \frac{U_s}{\sigma^2}(z - U_c) \quad (B.5)$$

then we obtain

$$\hat{U} = \frac{U_1}{1 + e^\alpha} + \frac{U_2}{1 + e^{-\alpha}} = \frac{U_1 e^{-\alpha/2} (e^{\alpha/2} + e^{-\alpha/2}) + U_2 e^{\alpha/2} (e^{-\alpha/2} + e^{-\alpha/2})}{(e^{\alpha/2} + e^{-\alpha/2})^2} \quad (B.6)$$

which after substitution of Eq. (B.4) becomes

$$\hat{U} = \frac{(U_c - U_s/2)e^{-\alpha/2} + (U_c + U_s/2)e^{\alpha/2}}{(e^{\alpha/2} + e^{-\alpha/2})} = U_c + \frac{U_s}{2} \cdot \frac{e^{\alpha/2} - e^{-\alpha/2}}{e^{\alpha/2} + e^{-\alpha/2}} = U_c + \frac{U_s}{2} \tanh \frac{\alpha}{2}. \quad (B.7)$$

After substitution of Eq. (B.5) the result is

$$\hat{U} = U_c + \frac{U_s}{2} \tanh \frac{U_s}{2\sigma^2} (z - U_c) \quad (B.7)$$

APPENDIX C

COMMAND UPDATE TRANSIENT

In this appendix the transient in command estimate as a result from a command bank update is computed. The transient is defined as

$$\hat{U}_{transient} = \hat{U}_{k+} - \hat{U}_{k-} \quad (C.1)$$

and is given by

$$\hat{U}_{transient} = \mathbf{UI}_{k-} \cdot \mathbf{W}_{k-} - \mathbf{UI}_{k+} \cdot \mathbf{W}_{k+}. \quad (C.2)$$

The transient is the result of the command bank update given by

$$\mathbf{UI}_{k+} = \mathbf{UI}_{k-} + N \cdot \Delta U. \quad (C.3)$$

Examining Fig.2.8 one realizes that for $i = 2$ to n

$$(U_i)_{k-} \cdot (W_i)_{k-} = (U_{i-1})_{k+} \cdot (W_{i-1})_{k+}. \quad (C.4)$$

Applying the above to Eq. (C.2) cancelling terms and recalling that $(W_1)_{k-} = (W_N)_{k+}$ results in

$$\hat{U}_{transient} = (U_N)_{k+} \cdot (W_N)_{k+} - (U_1)_{k-} \cdot (W_1)_{k-}. \quad (C.5)$$

But since

$$(U_N)_{k+} = (U_1)_{k-} + N \cdot \Delta U \quad (C.6)$$

then

$$\hat{U}_{transient} = N \cdot \Delta U \cdot (W_1)_{k-}. \quad (C.7)$$

For an update in the opposite direction one gets with the same arguments

$$\hat{U}_{transient} = -N \cdot \Delta U \cdot (W_N)_{k-} \quad (C.8)$$

APPENDIX D

DELAY ESTIMATION ERRORS

The transformation of the acoustic noise to a biased range dependent delay noise by the time delay estimator is considered here. This noise modeling was done in order to provide a more accurate simulation than previous MP tracking simulations.

A. VARIANCE DEPENDENCE ON SNR

The minimum error variance in estimation of a variable from a measurement with zero mean random noise is given by the Cramer Rao lower bound (CRLB). The bound has been applied to TDOA estimation. Ianniello [Ref 14] gives a current and relevant review of time delay estimation error. The performance of an autocorrelator time delay estimator is evaluated there both analytically and experimentally.

Iannoello shows that if the $x(t)$ signal and the noise $n(t)$ both have uniform spectral density in the band 0 - B Hz and are zero outside of that range, then the variance of the autocorrelation estimate of τ from the single multipath signal

$$y(t) = x(t) + ax(t - \tau) + n(t) \quad (D.1)$$

where a is the relative attenuation (gain) of the path is given by

$$\sigma_{\tau}^2 = \sigma_0^2 \frac{\left[(1 + a^2)^2 + a^2 \right] S_B^2 + 2(1 + a^2) S_B \cdot N_B + N_B^2}{a^2 S^2} \quad (D.2)$$

$$\sigma_0^2 = \frac{1}{BT} \frac{3}{\pi^2 B^2} \quad (D.3)$$

where S and N are the spectral densities of the signal and the noise in the baseband $0 - B$ and T is the observation time. For the special case of $a = 1$ the variance reduces to

$$\sigma_{\tau}^2 = \sigma_0^2 \cdot \frac{3}{\pi^2 B^3 T} \cdot [5 + 4 \text{SNR}^{-1} + \text{SNR}^{-2}] \quad (D.4)$$

which has three dominant regions depending on the signal to noise ratio

$$\text{SNR} = S/N. \quad (D.5)$$

For $\text{SNR} \gg 1$ the variance approaches a constant indicating the performance limit of this type of estimator.

$$\sigma_{\tau}^2 = \frac{15}{\pi^2 B^3 T}. \quad (D.6)$$

For $\text{SNR} \ll 1$ the error variance is inversely proportional to the second squared SNR. In between these two regions there is a transition from constant to dependence on SNR^{-2} .

In his paper Ianniello indicates close agreement of Eq. (D.2) both with simulation results and with the CRLB for the typical case of $\text{SNR} \ll 1$ encountered in practice.

B. VARIANCE DEPENDENCE ON RANGE

For a stationary acoustic noise with bandlimited spectral density NB and signal intensity given by Eq. (3.3) the SNR at the input of the delay estimator becomes range dependent and is given by

$$\text{SNR}(R) = \text{SNR}_o \cdot R^p \quad (D.7)$$

where SNR_o is the SNR at range $R = 1$ [m].

Two models were used here to represent the range dependence of the noise. The first* was a simple dependence on some power p of range within a constant of proportionality σ_0 selected to match realistic noise at ranges $5 < R < 15$ km.

$$\sigma = \sigma_0 \cdot R^p \quad (D.8)$$

This model was used to develop the general trend of the inversion and the tracker when the noise is range dependent. The second noise model* was based on the exact Eq. (D.2) with SNR being the function of range given in Eq. (D.6). Some examples of the STD of TDOA as function of range for typical values of SNR are shown in Fig. D.1 and D.2.

C. DELAY ESTIMATION BIAS

Two of the sources contributing to MP bias errors are associated with the delay estimation. These are the nonnegative character of the delay estimate and the effect of close ACF peaks. These are discussed next.

The symmetry of the autocorrelation function, namely

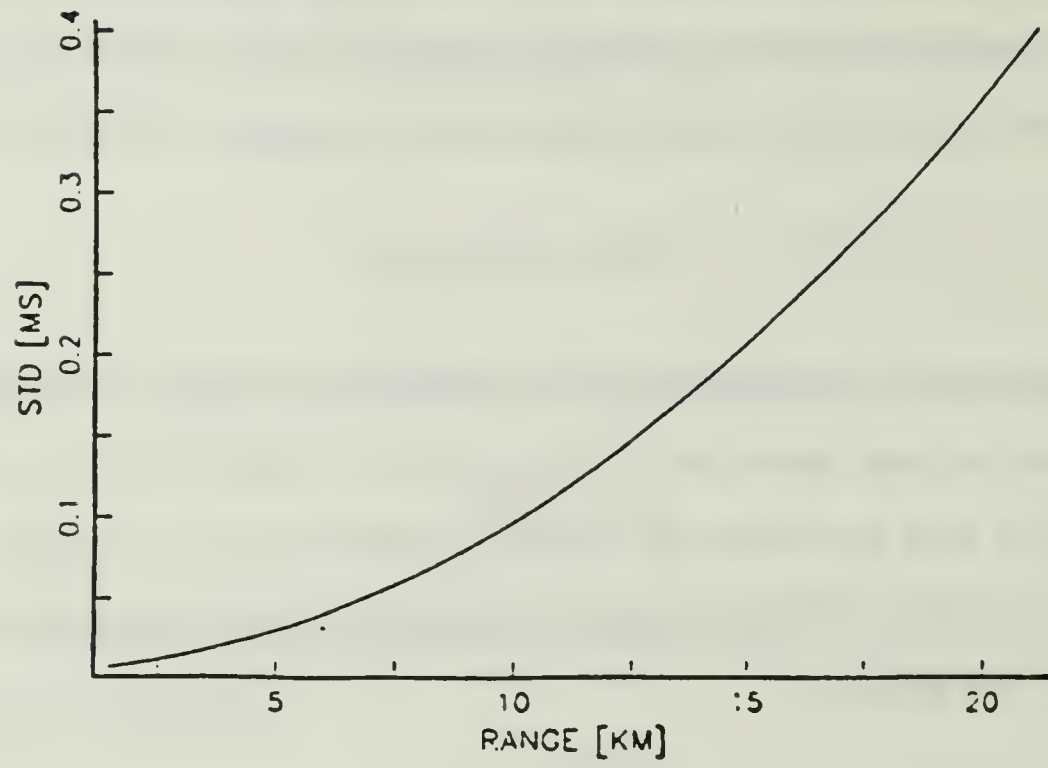
$$ACF(\tau) = ACF(-\tau) \quad (D.9)$$

prevents the discrimination between positive and a negative time delay (a lagging versus a leading replica). Since in the multipath situation, there really is a first arrival followed by lagging replicas, the use of the positive part of the time lag axis is conceptually justified. This however implies that the error in time delay estimation is not a simple gaussian, but rather reflects around the $\tau = 0$. A distribution which is equal to 0 for negative time delays, is used here to describe the estimate τ . An

* Noise type (NT) one.

* NT two

TDOA STD BW=2000, SNRO=70DB, ATN=5DB RPT=2



TDOA STD BW=2000, SNRO=50DB, ATN=5DB RPT=1

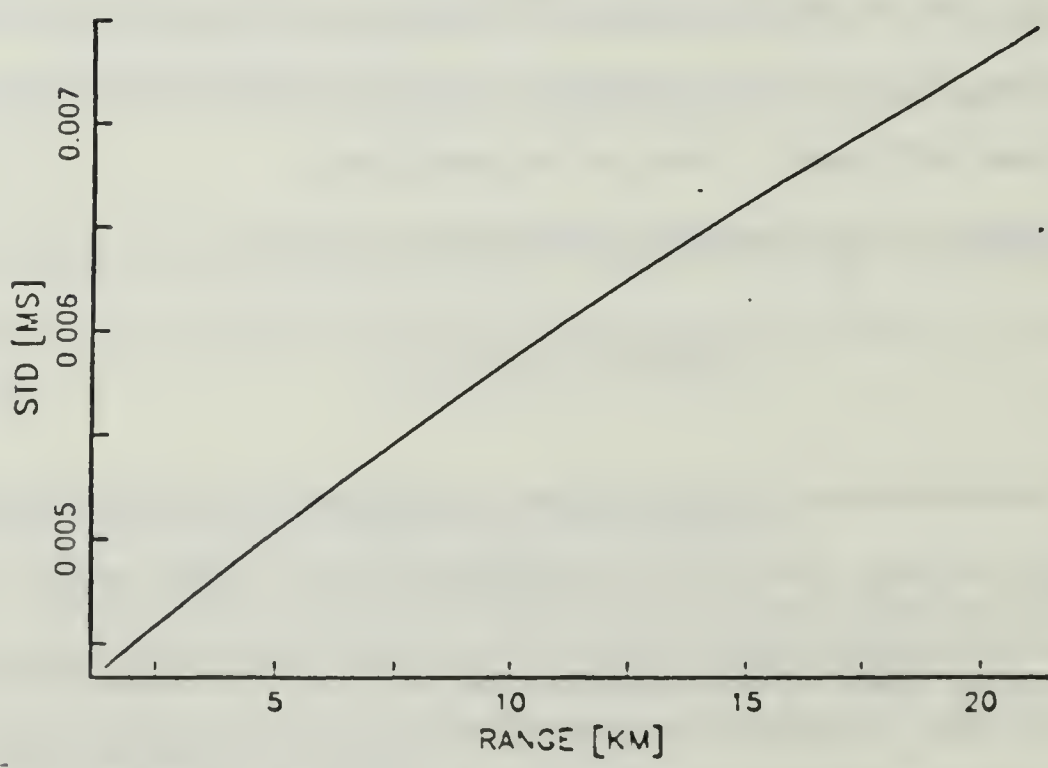
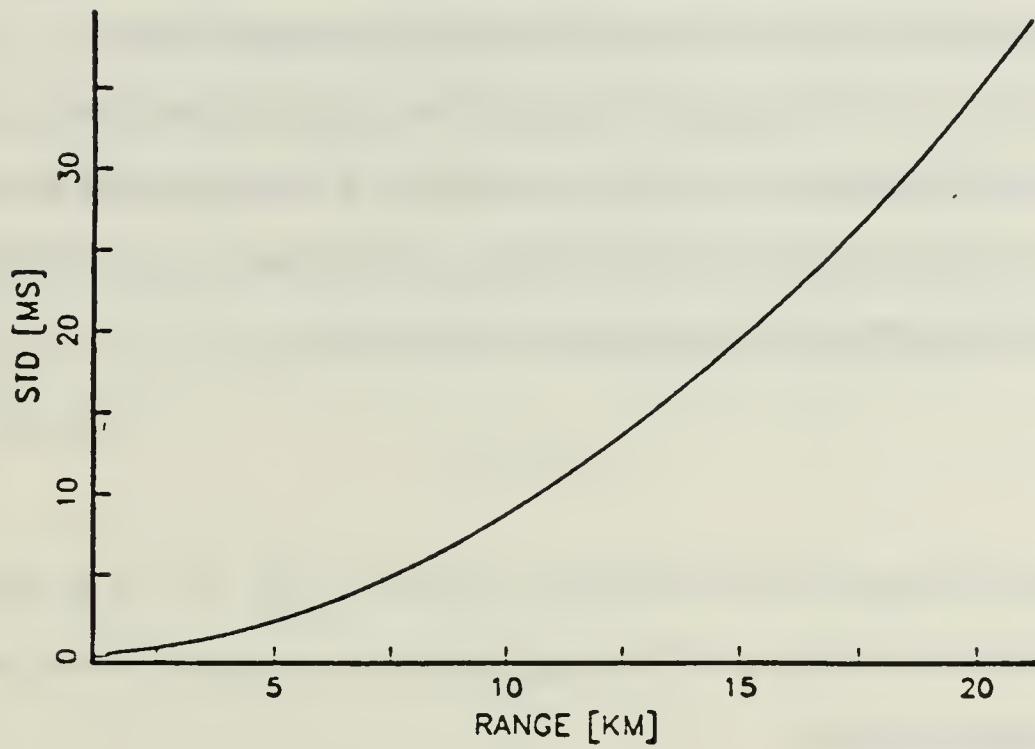


Fig. D.1. Range dependent TDOA noise type 2 (low).

TDOA STD BW=2000, SNRO=50DB, ATN=50B RPT=2



TDOA STD BW=2000, SNRO=60DB, ATN=50B RPT=2

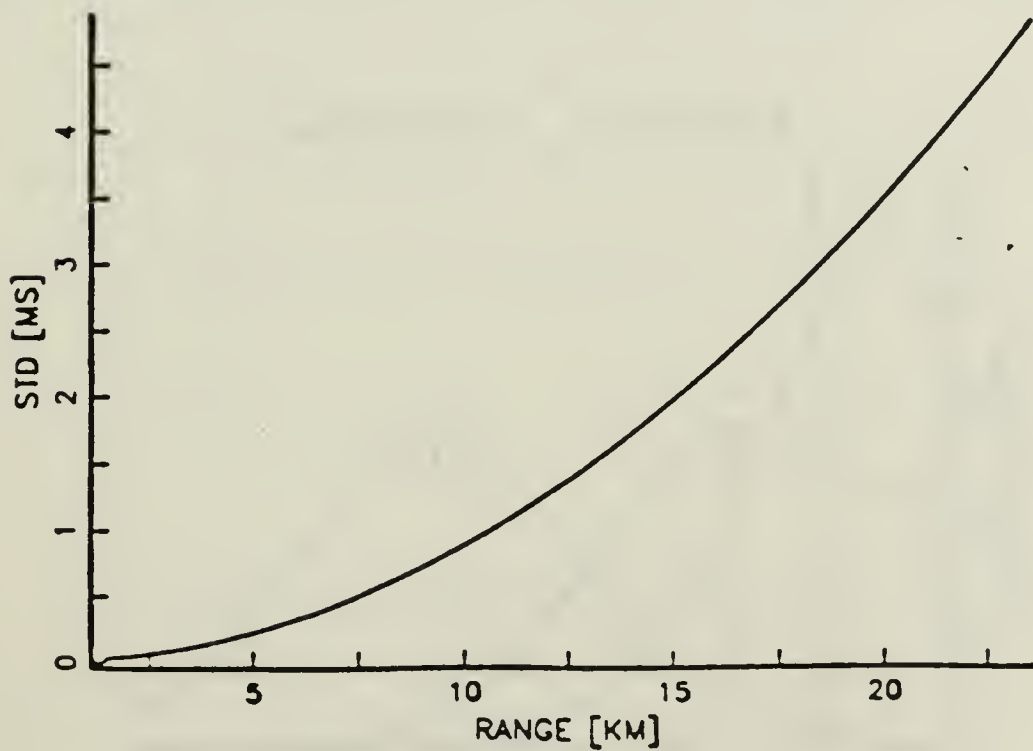


Fig. D.2. Range dependent TDOA noise type 2 (high).

estimate τ . An estimate with this distribution is generated by taking the absolute value of the sum of the time delay and a normal zero mean noise.

When the actual time delay is large relative to the estimation error variance, the effect of reflection around the 0 lag is marginal. When the actual delay is small compared to the error variance the resulting error bias has a stronger effect.

Figure D.3 shows three distributions of the process

$$t = |t + n| \tag{D.10}$$

for t taking the value of $1.8\sigma, 0.85\sigma, 0.22\sigma$ where $n \sim N(0, \sigma^2)$. It is evident that when t is smaller than 0.5σ it will be significantly overestimated which will cause an underestimated range.

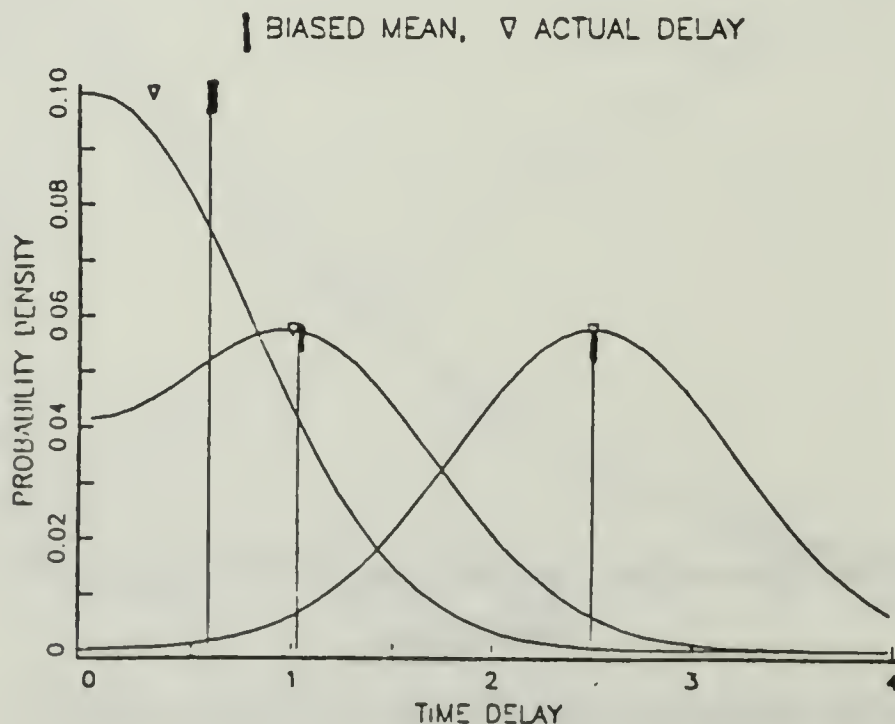


Fig. D.3. Nonnegative bias.

D. CLOSE ACF PEAKS

When the actual delays are short compared to the signal correlation time ($1/B$) the presence of an adjacent peak will shift the location of the estimated peak. This shift can be either positive or negative depending on the specific set of MP and resulting ACF. Since it is analytically predictable it can conceptually be corrected for as is done in the maximum likelihood estimator [14]. This error was therefore not simulated here.

APPENDIX E

DETAILED DATA DEFINITION AND SELECTION

This appendix describes in detail the parameters used in the various simulations and evaluations. Run data parameters are described in Section A. The values selected for the 10 simulation Runs are listed in Section B. Section C describes the case code name.

A. SIMULATION RUN DATA

Target and Scenario Data

- Ad - [sec] The target's depth time constant ($1/\alpha_d$ in Eq. (2.5)).
- Ar - [sec] The target's horizontal time constant ($1/\alpha$ in Eq. (2.2)).
- Pln - The pilot number 1, 2 or 3 per Chapter Two, Section E.

Medium and Prefilter

- Case - A selection of parameters defining the ocean medium and its acoustic modeling.
- Mdn - Medium number 1 through 4.
- Pfn - Prefilter number 1 through 6.
- p - [number] Power of the range dependence of the delay estimation variance (See Chapter Two, Section D.4, Chapter Three, Section A, and Appendix D.)
- p_b - [number] Power of range dependence of bearing estimation noise, (and of DR noise when it is used with medium and prefilter number 1, Eq. (2.101)).

Two cases were used for each Run.

- Refcase - The reference is a set of parameters considered as the "actual" conditions used by the medium program to convert the actual DR position to TDOA.
- Evalcase - The evaluated ocean conditions and used by the prefilter in the inversion of TDOA to DR.
- NT - Noise type 1 = the simplified model Eq. (2.96).
2 = the improved model, Appendix D.
- σ_{t1} - [ms] Standard deviation of TDOA t_1 (or τ_1) estimate at range of 500 m. This parameter is used only by noise model type 1, but is computed for noise model type 2 for reference as well.
- σ_{t2} - Same as above but for $t_2(\tau_2)$.
- σ_d - [m] Depth error standard deviation at range of 500 m, used with medium 1 and prefilter 1.
- σ_r - [m] Range error standard deviation at range of 500 m, used with medium 1 and prefilter 1.
- σ_b - [deg] Bearing standard deviation at range of 500 m.
- Bw - [Hz] Receiver bandwidth.
- Atn - [dB] A vector of surface and bottom bounce losses.
- SNR₀ - [dB] Signal to noise ratio for target at range of 1 m. measured at the input to the delay estimator.

MM Parameters

- T - [sec] System sampling time interval.
- Ord - MM target model order, 2 or 3.
- Aq - [sec] Command noise coloring time constant ($1/\alpha_w$ Eq. (2.7)).

- U_{min} - [m/sec] Lowest speed command in the hypothesis bank.
- U_{max} - [m/sec] Highest speed command in the hypothesis bank.

- N - Number of filters in the MM.

- Pr - Command transition probability 0 to 1.

- An1 - W averaging constant, (iterations to reach 63%) Eq. (2.23b).

- An3 - W_{op}, U_{op} averaging constant, (iterations to reach 63%)
Eq. (2.26) and (2.27)

- An4 - X_{op} averaging constant, (iterations to reach 63%)
Eq. (2.28)

- An - U_c averaging constant, (iterations to reach 63%)
Eq. (2.88)

B. Runs

The specific values of the parameters for each run are given below:

Run - 1

Target and scenario data

Ad - 35 sec.

Ar - 40 sec.

Pln - 3

Mdn - 1

Pfn - 1

p_b - 1

σ_d - 1 [m]

σ_r - 50 [m]

σ_b - 1 [deg]

MM parameters

T - 5 [sec]

ord - 3

A_w	-	25 [sec]
U_{min}	-	-30 [m/sec]
U_{max}	-	+30 [m/sec]
N	-	11
P_r	-	0.9
A_{n1}	-	10
A_{n3}	-	4
A_{n4}	-	5
A_{n9}	-	100
Run	-	2 (All parameters are the same as for Run 1 except the following:)
Pl_n	-	3
Mdn	-	3
Pfn	-	3
$Refcase$	-	S1111
$Evalcase$	-	S1111
NT	-	2
p	-	1
p_b	-	1
σ_{t1}	-	0.005 [m]
σ_{t2}	-	0.004 [m]
σ_b	-	0.08 [deg]
B_w	-	2000 [Hz]
A_{tn}	-	5.5 [dB]
SNR	-	50 [dB]
Run	-	3 (all the parameters are the same as for Run 2 except the following:)
p	-	2
σ_{t1}	-	0.05 [ms]
σ_{t2}	-	0.05 [ms]
SNR	-	70 [dB]
Run	-	4 (All parameters are the same as Run 2 except for the following:)
p	-	2
σ_{t1}	-	0.06 [ms]

σ_{t2} - 0.08 [ms]
 SNR - 60 [dB]

Run - 5 (All parameters are the same as for Run 2 except the following:)

p - 2
 σ_{t1} - 0.018 [ms]
 σ_{t2} - 0.03 [ms]
 Atn - 5.10 [dB]

Run - 6 (All parameters are the same as Run 2 except for the following:)

Pln - 1

Mdn - 4
 Pfn - 5
 p - 2
 p_b - 1
 σ_{t1} - 0.018 [ms]
 σ_{t2} - 0.018 [ms]
 max area size - 8×15
 Atn - 5.5 [dB]
 SNR - 50 [dB]

Run - 7 (All parameters are the same as Run 6 except for the following:)

max area size - 5×9

Run - 8 (All parameters are the same as Run 6 except for the following:)

Refcase - C2251
 Evalcase - S1111
 NT - 2
 p - 2
 p_b - 2
 σ_{t1} - 0.005 [ms]
 σ_{t2} - 0.005 [ms]

Atn	-	55 [dB]
SNR	-	70 [dB]
Run	-	9 (All parameters are the same as in Run 8 except for the following:)
Atn	-	5.10 [dB]
SNR	-	50 [dB]
Run	-	10 (All parameters are the same as in Run 9 except for the following:)
Refcase	-	C2251
Evalcase	-	C2251
Run	-	11 (All parameters are the same as in Run 10 except for the following:)
Refcase	-	A426
Evalcase	-	A3253
Run	-	12 (All parameters are the same as in Run 11 except for the following:)
Refcase	-	C4261
Evalcase	-	C2251
σ_{t1}	-	0.005 [ms]
σ_{t2}	-	0.005 [ms]
Atn	-	5.5 [dB]
SNR	-	70 [dB]

C. Case Definition

A case code is comprised of one character and four digits, (for example C2461). It was used to define the basic MP assumptions. These include homogeneous versus IH propagation, the ocean conditions, the estimation resolution, The DR grid data and some additional parameters. The code is used in the computation of TDOA surfaces over the depth range (DR) grid.

The parameters are defined as follows. The leading character indicates the type of case.

U - Homogeneous propagation, perfectly resolvable and identifiable MP. This is an idealized case where Eq. (1.2) is used to compute the unsorted (hence the U) time delays $\tau_1 \tau_2$. It is used mainly for methodology purposes, demonstrating the differences between the TDOA and modified TDOA.

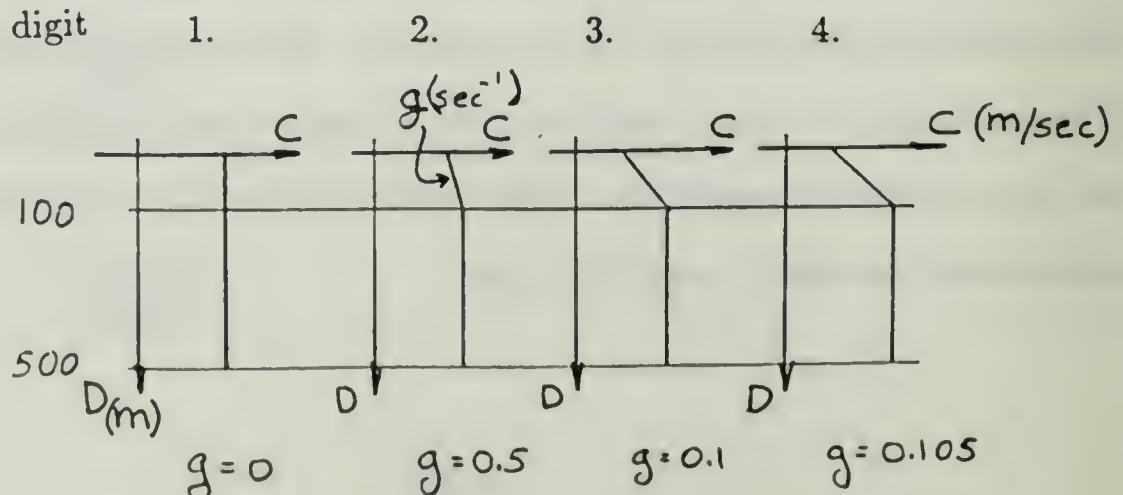
S - Homogeneous propagation, perfectly resolvable but non identifiable paths. Eq. (1.2) is again used to generate the time delays which are then sorted according to delay magnitude (hence the S) at each DR point and denoted by t_1 and t_2 . The variable t_1 is now always the shortest, but it can no longer be associated with surface reflection nor can the longer t_2 be associated with the bottom bounce. This case is useful as an idealized reference for the later IH limited resolution since they are conceptually similar.

A,B,C,D - The realistic IH limited resolution non identifiable cases. The letter indicates the receiver time delay resolution in milliseconds as follows.

A	-	0.05	C	-	0.5
B	-	0.2	D	-	1.0

The four digits define the parameters required for the numerical generation of the TDOA surfaces as follows. The first digit indicates the SVP. Four SVP's of varying inhomogeneity are used throughout this research as shown below:

case 1 st digit



The SVP digit is of course meaningless for the S and U cases where homogeneous propagation (SVP digit = 1) is always assumed.

The second digit details the observer and ocean depth information.

TABLE E.1
DEPTH DATA

case 2nd digit	1	2	3	4	5
Ocean depth m	503	513	-	518	550
Observer depth	162	162	-	162	162

The third and fourth digits describe the discrete depth and range grid used for the direct function table.

TABLE E.2
GRIP DATA

	Grid density	1	2	3	4	5
	Initial depth [m]	160	-	160	160	160
Depth	Step size [m]	-50		25	-100	10
	Number of steps	11		21	6	11
	Initial range [m]	500	500	500	500	500
Range	step size [m]	500	1000	500	1000	250
	number of steps	25	25	49	13	99

APPENDIX F

THE EIGENRAY ACOUSTIC MODEL

This appendix describes the selection of the eigenray model and the evaluation of the SMART model.

A. REQUIREMENTS AND MODEL SELECTION

The general goal of the eigenray model is to find and trace all the rays passing through the two specified receiver and source end points. The following is required from an eigenray model if it is to be used for MP tracking.

1. Correctness and High Accuracy

The total sound travel time from the source to the receiver may be of the order of a few tens of seconds. The milliseconds of travel time difference, while vital for the MP ranging, are a very small percent of the total travel time. This is especially true for the longer ranges where the travel time grows while the differences decrease. The resulting output accuracy requirement is of the order of .001% which dictates even higher precision in the model's internal computations. The issue of correctness relates to the possibilities of not finding an existing path or producing imaginary nonexisting paths; it too is related to the computer word length.

2. Compactness

The eventual use of a MP tracking algorithm in a real time systems application imposes additional constraints on run time, supporting hardware, and size of the model. Research oriented programs requiring extra long computer words or computation time will not fit the smaller data processors usually available for

target tracking in onboard systems. What is required is a program running on a microcomputer that can solve a typical eigenray problem in a matter of seconds.

B. MODEL SELECTION

Some eigenray models were developed in recent years, but the conflicting requirements of accuracy and compactness, narrows the selection to two programs. One model called SMART, for SMAll Acoustic Ray Tracer was developed by Novick of Mission Sciences Corp. [Ref. 22]; the other is a research tool developed by Spiesberger as an application of an earlier model [Ref. 31].

The SMART model was selected because it was better integrated as a working model and provided more detailed output data. The Spiesberger model has the advantage that it can account for a sloped ocean bottom. However this model lacks a reliable transmission loss output and is not well integrated for the intended use here.

The eigenray model is used in a fashion that is separable from the rest of the MP inversion or target tracking algorithm. This provides for easy replacement or upgrading of the model. This also led to our decision to use the more reliable integrated model for this first IH compensation attempt, and maintain the option to upgrade and extend it in the future.

The SMART model was evaluated extensively and the main result of this evaluation is presented in Section D.

C. SMART MODEL - A BRIEF DESCRIPTION

Finding the eigenrays is the first task accomplished by the model. Source and receiver depths are set to the specified input parameters and an iterative search

for the initial angle of the ray which will reach the receiver depth at the specified range, is conducted. The interval of possible ray angles is divided into sectors for which the dependence of range on the angle is a continuous well-behaved monotonic function.

Eigenrays are searched for in every sector that spans the desired range by successive approximation. The procedure terminates when the eigenray reaches a specified range accuracy. Only rays with a total number of bounces less than a specified input value are considered. Forward ray tracing equations similar to those presented in Chapter Three are used to locate the limits of the angle sector, to try out angles in the search process, and to compute the detailed output for every eigenray found.

D. LIMITATION OF THE MODEL

The program does not find eigenrays that are within ± 0.15 deg from the horizontal. This is partially caused by the limitation of intensity computation at these angles (recall discussion in Chapter 3 and Eq. (3.20)). Another cause for the limit is the finite computer word length and the increment used for searching the ray around the horizontal direction. The $\pm 0.15^\circ$ limitation relates to both angle at the source and at the receiver. An example of the problem is shown in Fig F.1. The bounce count (BC) of case C1111* computed using SMART shows a high value along the receiver depth at long range. No loss of a path or loss of resolution should give rise to this phenomena.** The unexpected BC was traced

* See Appendix E for case definition.

** Near the surface and the bottom the corresponding single bounce is not resolvable from the direct path. At depth of -170 m the single surface and

of the eigenray model to detect the direct path. This results from the direct ray being close to horizontal at those ranges. (The vertical separation between the grid depth line at 152 m and receiver at 162 m is 10 m.) These limitations were brought to the attention of the author of the SMART model and are currently being corrected. Since the model is employed in the prefilter in a modular way, these limitations do not effect the generality of the proposed inversion procedure.

The choice of The SVP and geometry selected for use in this work was designed to avoid this problem by limiting the grid to a region were the rays are not horizontal at all. This was done by (1) restricting the DR grid to +60 - +160 m while the receiver was placed at 162 m; (2) limit the maximum range to 25 km; and (3) restricts the SVP gradients to positive surface gradients only. The overall geometry is shown in Fig. F.2.

bottom bounce are not resolvable.

BOUNCE COUNT

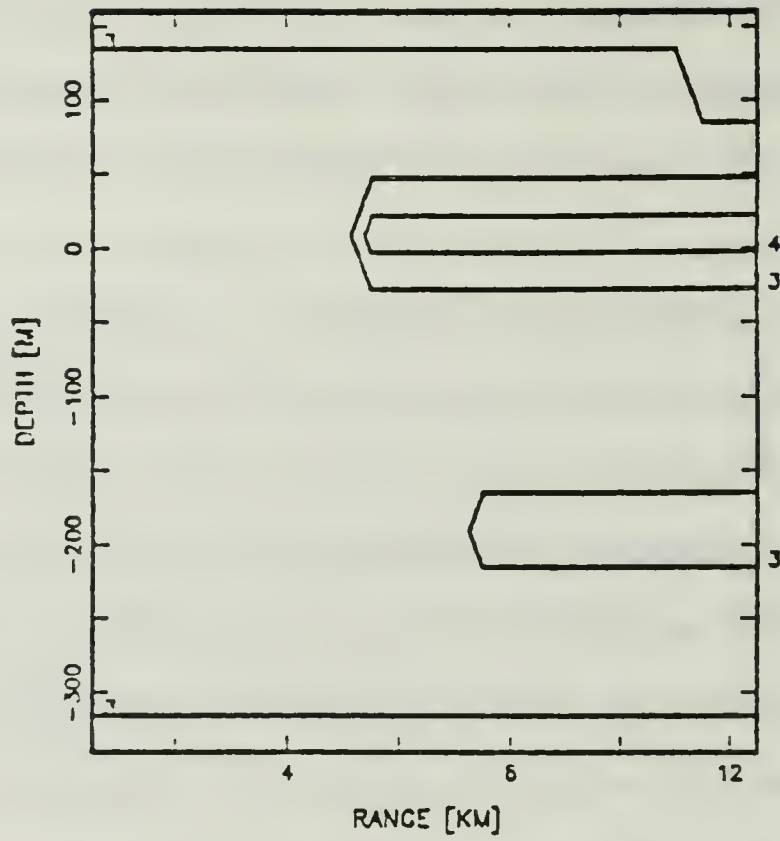


Fig. F.1. Bounce count with missing horizontal rays.

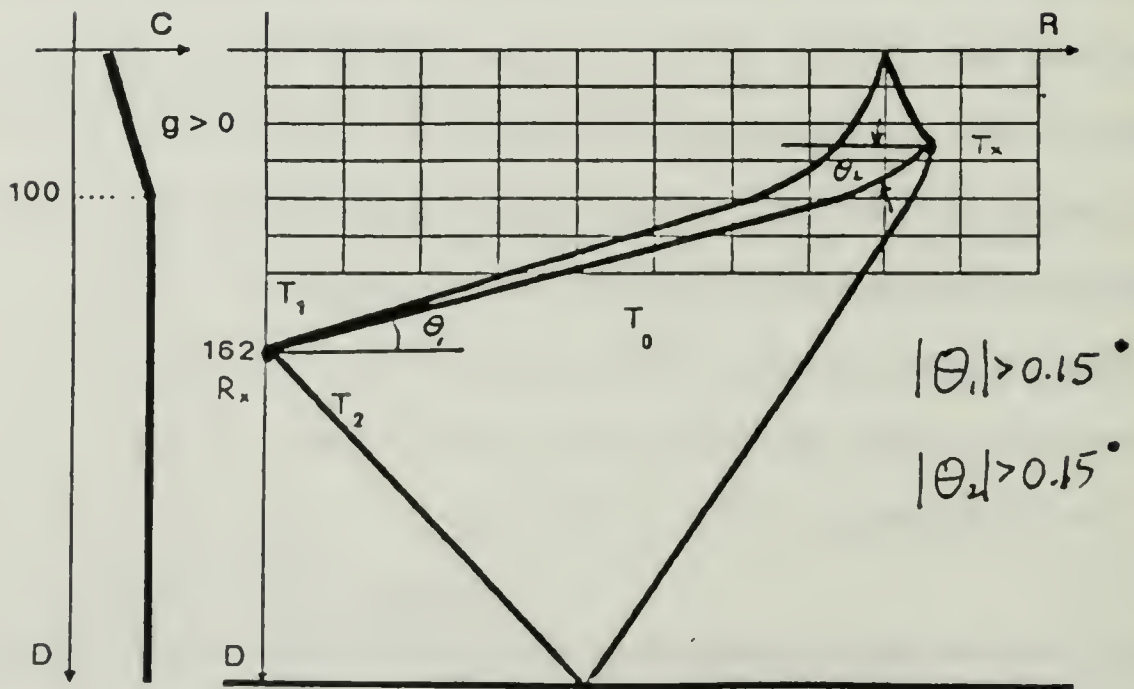


Fig. F.2. Grid without horizontal rays.

APPENDIX G

THE LOCAL SEARCH ALGORITHM

In this Appendix the component of the local search algorithm, the inversion test, the inward search and the outward search, are described. A pseudo code description of the algorithm is also included. The input and output parameters used by the algorithm are defined in Chapter Three.

A Numerical analysis procedure, developed for finding zeros of complex functions [Ref. 29] was modified to apply to the search. For this purpose the search has to be viewed in the context of the graphical statement of the problem as discussed in Chapter Three, that is, as finding the DR coordinates of the point of intersection of the constant t_1 and t_2 contours (see Fig. 3.12). The inversion problem

$$\begin{pmatrix} D \\ R \end{pmatrix} = f^{-1} \begin{pmatrix} t_1 \\ t_2 \end{pmatrix} \quad (G.1)$$

can be rewritten as

$$\begin{pmatrix} D \\ R \end{pmatrix} - f^{-1} \begin{pmatrix} t_1 \\ t_2 \end{pmatrix} = \begin{pmatrix} 0 \\ 0 \end{pmatrix} \quad (G.2)$$

Where the D and R are the unknowns. If the vector function f is written as two separate functions f_1 and f_2 Eq. (G.2) can be written as the two equations

$$D - f_1^{-1} \begin{pmatrix} t_1 \\ t_2 \end{pmatrix} = 0 \quad (G.3a)$$

$$R - f_2^{-1} \begin{pmatrix} t_1 \\ t_2 \end{pmatrix} = 0 \quad (G.3b)$$

The contour lines of Fig. 3.12 represent loci of the DR solution of Eq. (G.3). Every point p on the DR grid with depth D_p and range R_p can be defined in terms

of it's relation to the input t_1 contour by a one digit number C_{p1} given by

$$C_{p1} = \begin{cases} 1 & ; t_{1p} > t_1 \\ 0 & ; t_{1p} = t_1 \\ 1 & ; t_{1p} < t_1 \end{cases} \quad (G.4)$$

and in terms of the it's relation to the second input contour t_2 by another digit C_{p2} given by

$$C_{p2} = \begin{cases} 1 & ; t_{2p} > t_2 \\ 0 & ; t_{2p} = t_2 \\ -1 & ; t_{2p} < t_2 \end{cases} \quad (G.5)$$

C_{p1} and C_{p2} are referred to as *characteristic digits*. An example of the two characteristic digits for some points is shown on Fig. G.1.

A. THE INVERSION TEST

A 1×1 rectangle can contain a solution only if its characteristic digits C_{p1} and C_{p2} are either zero or if they acquire at least two different values in one of the four rectangle corners.

Some examples are shown in Fig. G.1(c). In (a) both C_{p1} and C_{p2} are 1 and -1 at different points. In (b) C_{p1} is 0 and 1, while C_{p2} is 1 and -1 . This rule is a simplified version of a rule analytically derived in Ref [29] from Cauchy's principal value argument.

Note that this simple test is a necessary but not a sufficient condition. Fig. G.1c shows an example of a rectangle which succeeds the test but does not contain a solution. If this simple conditional test succeeds it is followed by a second more rigorous test which checks to see if the two contours actually intersect or just pass through the rectangle. This is done by actually attempting to locate the solution, by means of the inward search described later.

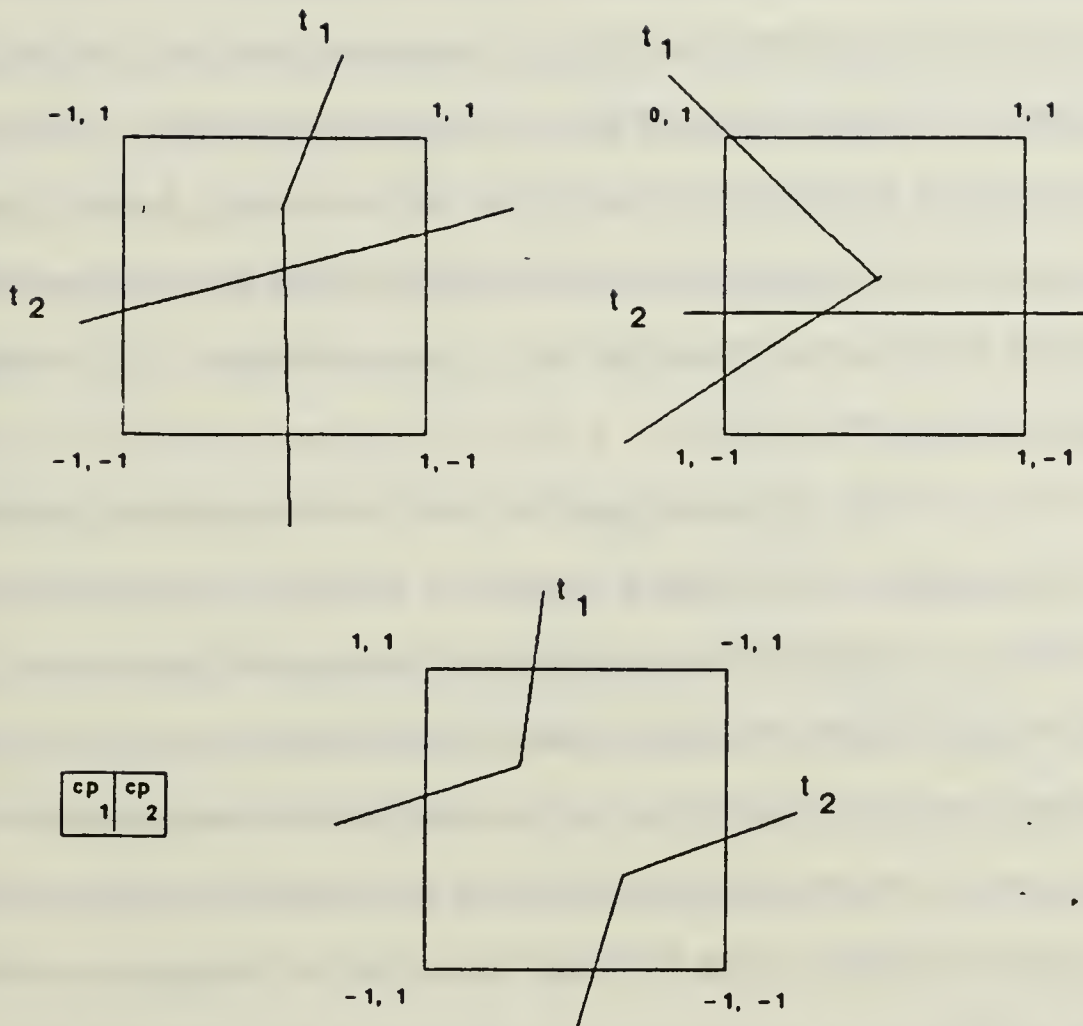


Fig. G.1. Examples of characteristic digits.

B. THE OUTWARD SEARCH

The outward search is a recursive procedure. It performs the inward search over successively growing search rectangles. If a call to the inward search returns in a failure (no solutions in the current rectangle) the search area is increased by tripling the sides of the current rectangle. A new current rectangle is thus formed centered around the previous one with an area nine times larger. The outward search is now called recursively to search the new rectangle. Again it tests for existence of a solution by calling the inward search. Note that in its growth the outward search may in one step include two or more solutions which would then all be located by the inward search.

The search rectangle area is increased by a 9:1 ratio by means of tripling the length of both its sides. This is done in order to minimize the duplicated effort associated with re-examining the original rectangle as part of the recursive search of the new rectangle. However the rectangle is increased only up to the portion of the maximum search area size that still remains within the limits of the grid. If the inward search for the current rectangle is unsuccessful and the search area cannot be further increased in any direction, the procedure terminates in a failure, without any solution.

Upon termination the search procedure outputs the size of the current area, the number of solutions found and the solution quad triangles. If more than one solution is found the calling inversion procedure will select the most likely one, i.e., the one closer to the predicted position after the interpolation is performed. An example of the growing search rectangles is shown on Fig. 3.18 in the dashed line. The search is initiated at point D_p , R_p , and the existence of solution is detected after two iterations.

C. THE INWARD SEARCH

The inward search attempts to locate a solution in a given input rectangular search area. It starts by performing the conditional inversion test on the complete area. If the test succeeds, the region is divided into four (quadrant) rectangles by halving both of its axes. Each quadrant is then searched for solutions by a recursive call to the inward search*. If the possible existence of a solution in the quadrant is indicated by the inversion test the quadrant is subdivided and the process continues recursively. If the test of the quadrant fails, the search in it terminates. The inward recursion thus terminates when either the search area reaches the minimum rectangle (of size 1×1), or if no solution exists in the a specific branch (of the B tree with branching factor 4).

The triangle(s) in the 1×1 rectangle is (are) found by dividing the rectangle into it's two DR grid triangles and performing a test on each to see if it surrounds the point. The surrounding test uses vector product to verify that the input t_1, t_2 point is on the same side of all lines that make the sides of the triangle. The test is as follows: Three vectors S_1, S_2 and S_3 are defined in the $t_1 t_2$ plane as the three sides of the triangle in a cyclic order (see Fig. G.2). Three corresponding vectors V_1, V_2 and V_3 are formed by the input t_1 and t_2 point and the three angles of the triangle A_1, A_2, A_3 respectively. The side of the input point relative to a "side vector" S is given by the sign of the vector product of the corresponding vectors S and V vectors. An input point inside a triangle will be on the same side of all the three side vectors. That is

$$\text{sign} [V_1 \times S_1] = \text{sign} [V_2 \times S_2] = \text{sign} [V_3 \cdot S_3] \quad (G.6)$$

* The search is therefore a B tree search with a branching factor of 4.

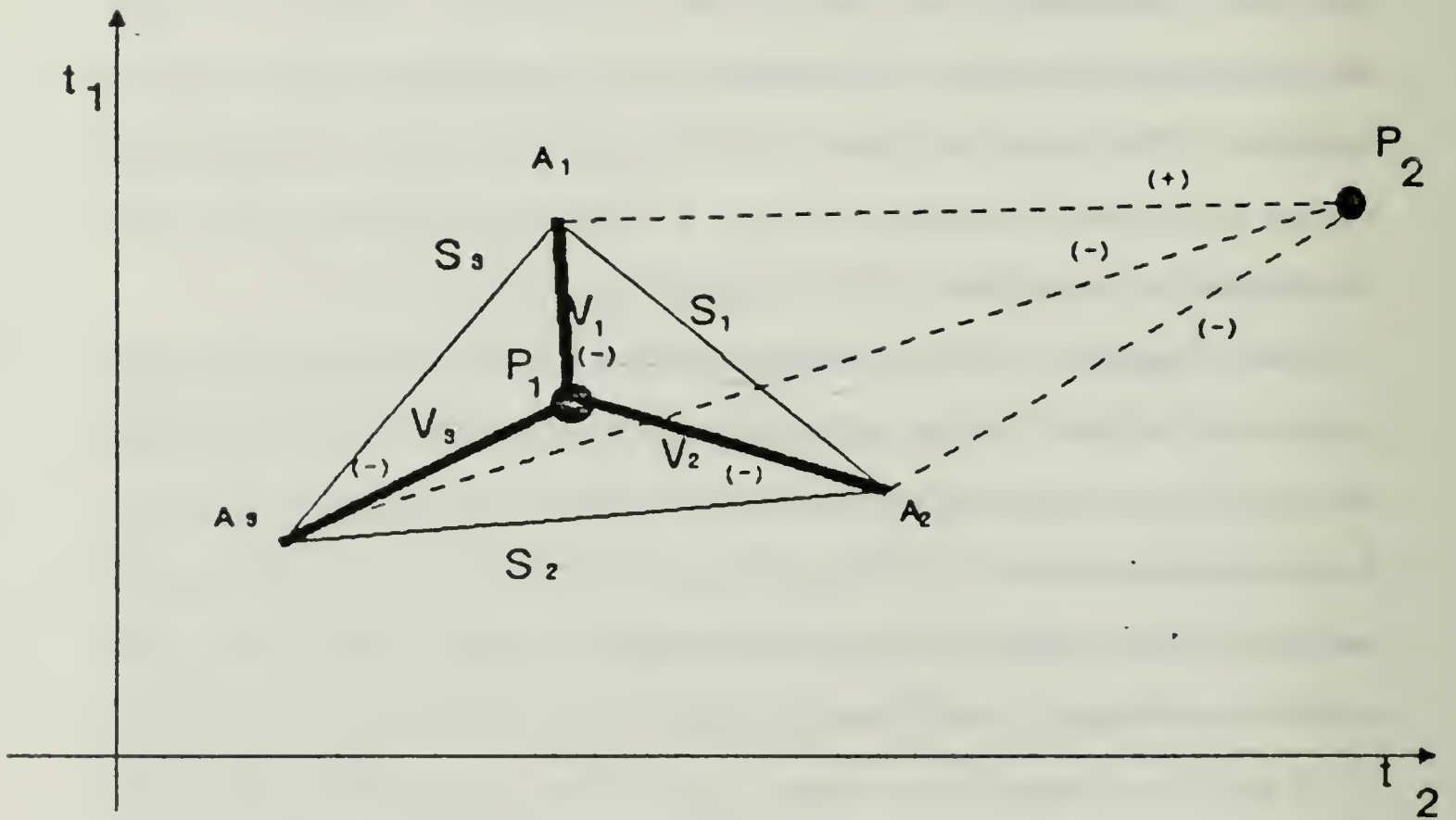


Fig. G.2. Vectors for inside test.

In Fig. G.2 the six vectors are plotted for a point inside (p_1 and full line) and for a point outside (p_2 and dashed lines) a triangle. The signs marked along the V vectors are the signs of the corresponding vector product ($V_i \times S_i$).

The solutions from all the branches of the recursion are reported by the inward search. This ensures that all solutions found in the searched area centered around the reference point are reported for further consideration. In the example shown in Fig. 3.18 three iterations of the inward search are required to locate the actual triangles that surround the point. In this case there were two solutions.

Pseudo code of the local search algorithm follows.

D. PSEUDO CODE FOR THE LSA

TYPE box : a square area in the depth range grid defined by
the DR indexes.

FUNCTION inside (t1, t2 ,tri): boolean;

inside :- 1 if the point t1,t2 is inside the triangle defined
by the three quads of tri on the t1t2 plane;

0 otherwise.

FUNCTION close (INVAR: depth, range): box

close :- the i j (depth range) indexes of the quad box on
the depth range grid surrounding the input
depth range point.

ENDFUNCTION;

PROCEDURE inversion_test (INVAR : t1, t2, current;
OUTVAR : result)

IF

(CP1 equals 0 or changes sign in the current area)

AND (CP2 equals 0 or changes sign in the current area)

THEN result :-1 ELSE result :- 0;

PROCEDURE owtward (INVAR : t1, t2, current , maxsize;

OUTVAR :Qlist, number_of_solutions,areasize)

BEGIN

IF current = previous THEN exit ;reached the size limit.

ELSE

BEGIN

inward (t1, t2,current,qlist, num_of_solutions);

```

IF number_of_solutions /= 0 THEN exit;Solution found.
Else
    BEGIN
        ; Recourse.
        current :- triplized (current).
        outward(t1,t2,current,num_of_solution,areasize)
    END;
ENDIF;
END;
ENDIF;
ENDPROCEDURE.

```

```

PROCEDURE inward (INVAR      : t1,t2,current
                  OUTVAR     : qlist,num_of_solutions);
BEGIN
    IF current = 1 x 1 THEN
        split current box into triangles tri1, tri2;
        FOR tri IN (tri1, tri2) DO
            IF inside (t1,t2,tri) THEN
                add tri to qlist;
                num_of_solutions:- num_of_solutions+1;
            ENDIF;
        ENDFOR;
    ELSE
        qlist :- empty;
        num_of_solution :- 0;
        IF not(inversion_test(t1, t2, current)) THEN exit
        ELSE

```

```

        split current into four quadrants 1 thru 4;
        FOR next IN quadrants 1 through 4 DO
            inward ( t1,t2,next,list,num);
            qlist :- qlist + list;

            num_of_solution :- num_of_solution + 1;
        ENDFOR;

    ENDIF;

ENDIF;

ENDPROCEDURE.

PROCEDURE inversion ( INVAR :t1, t2, DRref,maxsize
                    OUTVAR : depth, range,aver_num,aver_areasize)

var current : box;
solutionlist : list of depth range solutions;
BEGIN
current :- close( DR refpoint);
outward ( t1,t2,current,qlist,num_of_solutions,areasize);
IF num_of_solution = 0 THEN depth, range :- DRref ;a failure
ELSE
    BEGIN
        aver_num :- average_nun x a + num_of_solutions x (1-a);
        aver_areasize :- aver_areasize x a + areasize x (1 - a);
        FOR tri IN qlist DO
            interpolate depth range using tri;
            append solution to solution list;
        ENDFOR;
    ENDIF;
select depth range solution closest to DRref point as depth
range values to output.
ENDPROCEDURE.

```

LIST OF REFERENCES

1. Hassab, J. C., "Passive Tracking of Moving Source by Single Observer in Shallow Water," *Journal of Sound and Vibration*, Vol. 44(1), pp. 127-145, 1976.
2. Hassab, J. C., "Time Delay Processing Near the Ocean Surface," *Journal of Sound and Vibration*, Vol. 35, pp. 489-501, 1974.
3. Singer, R. A., "Estimating Optimal Tracking Filter Performance for Manned Maneuvering Targets," *IEEE Transactions on Aerospace and Electronic Systems*, Vol. AES-6, No. 4, July 1970.
4. Athans, M., Chang, C. B., "Adaptive Estimation and Parameter Identification Using Multiple Model Estimation Algorithm," Technical Note 1976-28, MIT Lincoln Laboratory, Lexington, MA, 23 June 1976.
5. Moose, R. L., "Adaptive Estimator for Passive Range and Depth Determination of a Maneuvering Target," *U. S. Naval J. Underwater Acoustics*, July 1973.
6. McCabe, D. H., "Adaptive Estimation Techniques for Underwater Maneuvering Targets," Ph.D. dissertation, Virginia Polytechnic Institute, 1979.
7. Golson, N.H., Moose, R.L., "Maneuvering Target Tracking Using Adaptive State Estimation," *IEEE Transactions on Aerospace and Electronic Systems*, May 1977.
8. Moose, R. L., Van Landingham, H. F., McCabe, D. H., "Modeling and Estimation for Tracking Maneuvering Targets," *IEEE Transactions on Aerospace and Electronic Systems*, Vol. ASE-15, No. 3, May 1979.
9. Moose, R. L., Dailey, T. E., "Adaptive Underwater Target Tracking Using Passive Multipath Time-Delay Measurements," *IEEE Trans. Acoustic Speech and Signal Processing*, August 1985.
10. Moose, R. L., Caputi, M. J., "A Convergence Analysis of an Adaptive Underwater Passive Tracking System," *Proceedings of the IEEE Conference on Acoustic Speech and Signal Processing*, San Diego, California, 1984.

11. Moose, R. L., Sistanizadeh, M. K., Skagfjord, G., "Adaptive State Estimation for a System with Unknown Input and Measurement Bias," *IEEE Journal of Ocean Engineering*, Vol. OE12, No. 1, January 1987.
12. Moose, R. L., Caputi, M. J., "A Convergence Analysis of a Passive Underwater Tracking System with Nonlinear Feedback," *IEEE Trans. Acoustic Speech and Signal Processing*, Vol. ASSP-34 No. 6, December 1986.
13. Chow, S. K., Schultheiss, P. M., "Delay Estimation Using Narrowband Signals," *IEEE Trans. Acoustic Speech and Signal Processing*, Vol. ASSP-29, pp. 478-484, 1981.
14. Ianniello, J. P., "Large and Small Error Performance Limits for Multipath Time Delay Estimation," *IEEE Trans. Acoustic Speech and Signal Processing*, Vol. ASSP-34. No. 2. April 1986.
15. Weinstein, E., Weiss, A. J., "Fundamental Limitations in Passive Time Delay Estimation, Part 2," *IEEE Trans. on Acoustic Speech and Signal Processing*, Vol. ASSP-32, No. 5, October 1984.
16. Smith, J.O., Friedlander, B., "Adaptive Multipath Delay Estimation," *IEEE Trans. Acoustic Speech and Signal Processing*, Vol. ASSP-33. No. 4. August 1985.
17. Friedlander, B., "On the Cramer-Rao Bound for Time Delay and Doppler Estimation," *IEEE Trans. Information Theory*, Vol. IT- 30, pp. 575-580, May 1984.
18. Schultheiss, P.M., Weinstein, E., "Lower Bounds on the Localization Errors of a Moving Source Observed by a Passive Array," *IEEE Trans. Acoustic Speech and Signal Processing*, Vol. ASSP-29, No. 3, June 1981.
19. Hamilton, M., "Exploitation of Multipath Arrivals in Passive Ranging," Ph. D. dissertation, Yale University, New Haven, Connecticut, September 1986.
20. Ziomek, L. J., Underwater Acoustics, Academic Press, Inc. 1985.
21. Wienberg, H. "Generic Sonar Model," NUSC Tec. Doc. 5971C, Naval Underwater System Center, New London, CT., December 1981.
22. Novick, A., "SMART - Small Acoustic Ray Tracer," Mission Sciences Report No. 1986-1, Mission Sciences Corp., Commack, N.Y., January 1986.

23. Clay, C. S., and Medwin, H., Acoustical Oceanography, John Wiley & Sons, 1977.
24. Saes-Ortiz, R., "Passive Adaptive Tracking Using Multiple Kalman Filters," Master's Thesis, Naval Postgraduate School, Monterey, CA, 1987.
25. Shefi, A., Therrien, C. W., Kirk, D. E., Saez, R., Friedlander, B., "Passive Multipath Target Tracking in an Inhomogeneous Acoustic Medium," *Proceedings of the 1987 IEEE Conference on Acoustic Speech and Signal Processing* Dallas, Texas, April 1987.
26. Fourniol, J. M., "Coupled Acoustic and Ocean Thermodynamic Model," Master's Thesis, Naval Postgraduate School, Monterey, CA, 1987.
27. "GRAFSTAT Introductory Manual," IBM Research, Yorktown Heights, NY, June 1986.
28. Shamos, M. I., Hoey, D., "Closest Point Problems," *Proceedings of the 16th IEEE Symposium of Foundation of Computer Science*, pp. 151-162, October 1975.
29. Hamming, R. W., Numerical Methods for Scientists and Engineers, Dover Publishing, Inc., New York, 1986.
30. Diamessis, J. E., Therrien, C. W., "Modeling Unequally Spaced 2-D Discrete Signals by Polynomials," *Proceedings of the IEEE Asilomar Conference on Signals, Systems, and Computers*, Pacific Grove, CA, November 1986.
31. Jacobs, G., "Multiple Profile Restructuring and Supplemental Plot Program," Task Report Ocean Data Systems, Inc., Rockville, Maryland, Contract No. N000-014-73-C0131, June 1974.

INITIAL DISTRIBUTION LIST

	No. of Copies
1. Professor C. W. Therrien Code 62Ti Naval Postgraduate School Monterey, California 93943-5000	2
2. Professor D. E. Kirk Code 62Ki Naval Postgraduate School Monterey, California 93943-5000	1
3. Professor L. J. Ziomek Code 62Zm Naval Postgraduate School Monterey, California 93943-5000	1
4. Professor R. W. Hamming Code 52Hg Naval Postgraduate School Monterey, California 93943-5000	1
5. Professor S. Garrett Code 61Gx Naval Postgraduate School Monterey, California 93943-5000	1
6. Professor O. B. Wilson Code 61Wl Naval Postgraduate School Monterey, California 93943-5000	1
7. Professor H. Medwin Code 61Me Naval Postgraduate School Monterey, California 93943-5000	1
8. Professor C. R. Dunlap Code 68Du Naval Postgraduate School Monterey, California 93943-5000	1
9. Lt. A. Gal 51 Montsalas Dr. Monterey, California 93943	1

10. CDR M. Marom 1
2101 Etna Place
Monterey, California 93940
11. CAPT S. Horev 1
119 Sea Foam
Monterey, California 93940
12. Mr. A. Novic 1
Mission Sciences Corporation
6090 Jerico Turnpike
Commack, New York 11725
13. Naval Attache 1
Israeli Embassy
3514 N. W. International Drive
Washington, D. C. 20008
14. Professor M. Hamilton 1
Department of Electrical Engineering
Temple University
12th & Norris Streets
Philadelphia, Pennsylvania 12122
15. Dr. I. Ianniello 1
N.O.S.C.
New London, Connecticut 06320
16. Professor I. Dayer 1
Oceanography Department
Massachusetts Institute of Technology
Cambridge, Massachusetts 02139
17. LT M. Shields 1
CR# 590
Naval Postgraduate School
Monterey, California 93943-5000
18. CPT. D. Nitzan 1
c/o Naval Attache
Embassy of Israel
3514 N. W. International Dr.
Washington, D.C. 20008
19. Commodor Y. Haramati 1
c/o Naval Attache
Embassy of Israel
3514 N. W. International Dr.
Washington, D. C. 20008

20. CDR Y. Peery 1
 c/o Naval Attache
 Embassy of Israel
 3514 N. W. International Dr.
 Washington, D.C. 20008
21. Professor L. P. Moose 1
 Virginia Polytechnic Institute
 and State University
 Blacksburg, Virginia 24061
22. G. Jacobs 1
 ODSI
 6110 Executive Blvd., Suite 320
 Rockville, Maryland 20852
23. Mr. E. Carrapezza 1
 Computer Science Department, Code 52
 Naval Postgraduate School
 Monterey, California 93943-5000
24. Professor B. MacLennaa 1
 Department of Computer Science
 University of Tennessee
 Knoxville, Tennessee 37996-1301
25. Library, Code 0142 2
 Naval Postgraduate School
 Monterey, California 93943-5002
26. Professor W. F. Hodjkiss 1
 Marin Physical Lab
 Scrips Institute of Oceanography
 University of California
 San Diego, California 92022
27. J. Schere 1
 EDO Corporation
 111th College
 College Point, New York 11356
28. Professor P. M. Schultheiss 1
 Department of Electrical Engineering
 Yale University
 New Haven, Connecticut 06520
29. CDR A. Shefi 1
 c/o Naval Attache
 Embassy of Israel
 3514 N. W. International Drive
 Washington, D. C. 20008

30. Professor Ralph Hippensteil 1
Code 62Hi
Naval Postgraduate School
Monterey, California 93943-5000
31. Professor James H. Miller 1
Code 62Ml
Naval Postgraduate School
Monterey, California 93943-5000
32. Defense Technical Information Center 2
Cameron Station
Alexandria, Virginia 22304-6145

Thesis
S4385 Shefi
c.1 Passive multipath tar-
get tracking in an in-
homogeneous acoustic
medium.

Thesis
S4385 Shefi
c.1 Passive multipath tar-
get tracking in an in-
homogeneous acoustic
medium.



thesS4385

Passive multipath target tracking in an



3 2768 000 78640 4

DUDLEY KNOX LIBRARY *c.1*